



Delft University of Technology

## Electrochemical stability of the next generation lithium batteries

Arszelewska, Violetta

**DOI**

[10.4233/uuid:c1cfb42d-6472-499d-a41e-7c980058da2c](https://doi.org/10.4233/uuid:c1cfb42d-6472-499d-a41e-7c980058da2c)

**Publication date**

2021

**Document Version**

Final published version

**Citation (APA)**

Arszelewska, V. (2021). *Electrochemical stability of the next generation lithium batteries*.  
<https://doi.org/10.4233/uuid:c1cfb42d-6472-499d-a41e-7c980058da2c>

**Important note**

To cite this publication, please use the final published version (if applicable).  
Please check the document version above.

**Copyright**

Other than for strictly personal use, it is not permitted to download, forward or distribute the text or part of it, without the consent of the author(s) and/or copyright holder(s), unless the work is under an open content license such as Creative Commons.

**Takedown policy**

Please contact us and provide details if you believe this document breaches copyrights.  
We will remove access to the work immediately and investigate your claim.

# Electrochemical stability of next generation lithium batteries

Dissertation

for the purpose of obtaining the degree of doctor

at Delft University of Technology

by the authority of the Rector Magnificus, Prof.dr.ir. T.H.J.J. van der Hagen,

chair of the Board for Doctorates

to be defended publicly on

Wednesday, 24 March 2021 at 12:30

by

**Violetta Arzelewska**

Master in Science, Erasmus Mundus Joint Master Program: Materials for Energy  
Storage and Conversion

University of Picardy Jules Verne, Aix Marseille Université, Université Paul  
Sabatier, Warsaw University of Technology, Universidad de Córdoba

born in Swindon, United Kingdom



This dissertation has been approved by the promotors.

Composition of the doctoral committee:

Rector Magnificus	chairperson
Dr. E.M. Kelder	Delft University of Technology, promotor
Prof. dr. ir. M. Wagemaker	Delft University of Technology, co-promotor

.....

Independent members:

Prof. dr. ir. Władysław Wieczorek	Warsaw University of Technology, Poland
Prof. dr. C. Masquelier	Université de Picardie Jules Verne, France
Prof. dr. ir. M. Huijben	University of Twente, The Netherlands
Prof. dr. F.M. Mulder	Delft University of Technology, The Netherlands
Prof. dr. E.H. Brück	Delft University of Technology, The Netherlands



The research described in this thesis was carried out in the group of Storage of Electrochemical Energy (SEE), Faculty of Applied Sciences, Delft University of Technology. This work was financially supported by ADEM, A Green Deal in Innovative Energy Materials of the Ministry of Economic Affairs of The Netherlands ([www.adem-innovationlab.nl](http://www.adem-innovationlab.nl)).

Keywords: silicon negative electrode, TiO<sub>2</sub> protective coating, solid ionic conductive additive, operando neutron depth profiling, operando X-Ray Diffraction, nuclear magnetic resonance, mechanism of solid electrolyte decomposition, electrochemical stability window of solid electrolytes

ISBN 978-94-6423-188-5

Copyright © 2021 by Violetta Arszewska

Cover design by Carla Robledo

Printed by ProefschriftMaken

An electronic version of this dissertation is available at <http://repository.tudelft.nl/>.

# Contents

<b>Chapter 1: Introduction</b> .....	1
1.1 The importance of batteries .....	2
1.2 Lithium ion batteries .....	4
1.3 The challenges of Si negative electrode and how they are addressed in this thesis.....	8
1.4 The challenges of all solid state batteries, understanding the electrochemical stability window of solid electrolytes and how they are addressed in this thesis...	11
1.5 The outline of thesis: research questions and methods used to answer them.	15
1.6 References: .....	16
<b>Chapter 2: Clarifying the relationship between redox activity and electrochemical stability in solid electrolytes</b> .....	23
2.1 Introduction .....	25
2.2 Results and discussion .....	27
2.2.1 Electrochemical activity of argyrodite $\text{Li}_6\text{PS}_5\text{Cl}$ .....	27
2.2.2 Evaluation of the redox activity of the argyrodite $\text{Li}_6\text{PS}_5\text{Cl}$ with DFT simulations.....	29
2.2.3 Analysis of the argyrodite $\text{Li}_6\text{PS}_5\text{Cl}$ decomposition products using XRD and $^6\text{Li}$ and $^{31}\text{P}$ solid-state NMR .....	35
2.3 Methods.....	44
2.4 References .....	49
<b>Chapter 3: Operando X-ray Diffraction of Silicon Particles Encapsulated in Metal Oxide For Negative Electrode in Lithium-Ion Batteries</b> .....	53
3.1 Introduction .....	55
3.2 Results and discussion .....	57
3.2.1 Deposition method .....	57

3.2.2	Characterisation of TiO <sub>2</sub> coated Si using Inductive Coupled Plasma and Transmission Electron Microscopy .....	57
3.2.3	Electrochemical cycling of Si with different coatings .....	59
3.2.4	Morphological evolution of the coating.....	62
3.2.5	Structural evolution of the coating by operando XRD.....	63
3.2.6	Evolution of stresses of n-Si and Si/a-TiO <sub>2</sub> .....	68
3.2.7	NDP Si with TiO <sub>2</sub> coating with FEC as an electrolyte additive.....	70
3.3	Conclusions .....	75
3.4	Materials and methods .....	75
3.5	References .....	79
<b>Chapter 4: Operando monitoring the Li-ion distribution in Silicon Anodes for Li-ion batteries</b> .....		<b>85</b>
4.1	Introduction .....	87
4.2	Results.....	90
4.2.1	Impact of cycle number on Li concentration distribution .....	90
4.2.2	Impact of VC/FEC on Li concentration distribution .....	92
4.2.3	Effect of VC/FEC on Li capacity and cell capacity .....	95
4.3	Discussion .....	98
4.4	Conclusions .....	99
4.5	Methods.....	100
4.6	References: .....	101
<b>Chapter 5: Operando study of the distribution of activity in silicon electrodes, its relation to the cycle life and the impact of solid additives</b> .....		<b>107</b>
5.1	Introduction .....	109
5.2	Results.....	110
5.2.1	Impact of solid additives on electrochemical cycling .....	110
5.2.2	Effect of solid additive on Li concentration depth distribution.....	113

5.2.3 Effect of solid additive on Li- capacity and electron capacity.....	116
5.2.4 Analysis of the LAGP decomposition (Ge3d, Al2p) and SEI formation (C1s, O1s, F1s) using XPS .....	118
5.3 Discussion .....	122
5.4 Conclusions .....	124
5.6 References: .....	127
<b>6: Appendix</b> .....	132
Supplementary A information of chapter 2 .....	132
Supplementary B Information of chapter 3 .....	143
Supplementary C Information of chapter 5 .....	145
Neutron Depth Profiling.....	148
<b>Summary</b> .....	153
<b>Samenvatting</b> .....	159
<b>Acknowledgments</b> .....	165
<b>List of publications and patent</b> .....	169



---

# Introduction

---



### 1.1 The importance of batteries

Particularly during the last century, human activities demand high energy generation. Currently most of the energy is generated by burning fossil fuels, coal and oil. As a result carbon dioxide (CO<sub>2</sub>) is emitted to the atmosphere. Since CO<sub>2</sub> is a good absorber of heat radiation, accumulation of CO<sub>2</sub> will cause greenhouse effect, accordingly rising the global average temperature<sup>1</sup>. The Paris Agreement aims to limit the temperature increase to 1.5 °C above pre-industrial levels, which would significantly reduce impact of climate change<sup>2,3</sup>. To accomplish this climate goal, governments agreed to ensure sustainable food production, develop technologies to capture and store carbon, and implement different sectors of the energy systems<sup>4</sup>. This then will ultimately must lead to a significant reduction of the emission of CO<sub>2</sub> into the atmosphere. The first step in transforming the energy systems is electricity decarbonisation to reduce emissions from the building, industry and transport sectors, which is required as a near-term goal. Transport particularly is difficult to decarbonise since it is highly dependent on liquid fossil fuels with dispersed combustion. Decarbonisation efforts will inevitably have an effect on the global economy. From a broader perspective, the main issues associated with the generation and usage of the electricity are mainly (1) reliability of the grid, (2) usage of fossil fuels and carbon footprint, (3) development of electric vehicles to replace oil, (4) usage and promotion of renewable energy generation. The solution to overcome those issues need to be affordable with respect to costs. A long-term goal, however, is to replace fossil fuels by renewable energy. The dominant resources for renewable energy today are wind and solar power<sup>5</sup>. These wind and solar plants are connected to the electricity grid to further distribute energy to the utilisation sites. Electrical energy storage devise are essential to improve utilisation and reliability of the grid. Batteries are an excellent energy storage system to integrate with renewable energy generation technology<sup>6</sup>, since copying with varying power generation is

challenging and batteries can prevent the shortage of energy during daily and seasonal fluctuations of solar and wind generation<sup>7</sup>. Usage of the batteries systems for electricity storage is required to have low cost and long cycle life (at least 20–30 years). Different energy systems<sup>8</sup>, commercially available such as lead acid, nickel cadmium (NiCd), sodium sulphur (Na-S) for grid application and Li-ion for electronics, grid storage and electric vehicles, are considered<sup>9</sup>. Portable devices and transportation can have different energy needs, different parameters need to be considered for optimal use. For portable electronics energy density is vital, however for electrical vehicles improvement of power density for charging is also important. The energy density (Wh/kg) represents the energy stored per kg in the system (which can be regarded as equivalent to the driving range for a car), while the power density represents its ability to deliver high power in a short time (seen as equivalent to the acceleration of a car or the time of recharging its battery). Capacitors for example can deliver a very high power (typically between  $10^3$  and  $10^4$  W/kg) but only for a limited time (from a few milliseconds to a few seconds) because of a low energy density (<10 Wh/kg). The advantage of Li-ion batteries is that they are versatile: they can both deliver a high power and a high energy density, which is crucial in an electric car for example where both acceleration and long range are needed. This is the main reason why Li-ion batteries are today the preferred power source for many applications: portable electronics, power tools, plug-in hybrid electric vehicle (PHEV) and electric vehicles (EV), etc. Since, Li-ion batteries offers the highest power and energy density compared to other battery systems, cycle life, and nominal voltage (important since determines the quantity of single cells required) are also in advantage. The cost is still the challenge<sup>10</sup>.

## 1.2 Lithium ion batteries

The Nobel Prize in Chemistry in 2019 has been awarded to the scientists that devoted their work to Li-ion batteries<sup>11</sup>. The concept of intercalation materials<sup>12-15</sup> was firstly introduced by Michael Stanley Whittingham and in 1970s he discovered  $\text{TiS}_2$  structure<sup>16</sup> used as a positive electrode for Li-ion batteries together with Li metal (**Fig. 1b**). In 1980s John Goodenough proposed the battery with intercalation cathode material lithium cobalt oxide ( $\text{LiCoO}_2$  or in short LCO)<sup>17,18</sup>, which is nowadays the most common cathode material for rechargeable Li-ion batteries (**Fig. 1a**). In 1985s Akira Yoshino proposed carbonaceous materials for a negative electrode<sup>19-21</sup>, mainly responsible for the development of graphite (**Fig. 1c**). In 1991s Sony commercialised first Li-ion battery, consisting on those two developments, graphite as a negative electrode and lithium cobalt oxide as a positive electrode. In this thesis, as will be pointed out later on, a further improvement on the negative electrode is being studied, focussing on moving over to silicon to replace the carbonaceous electrode material.

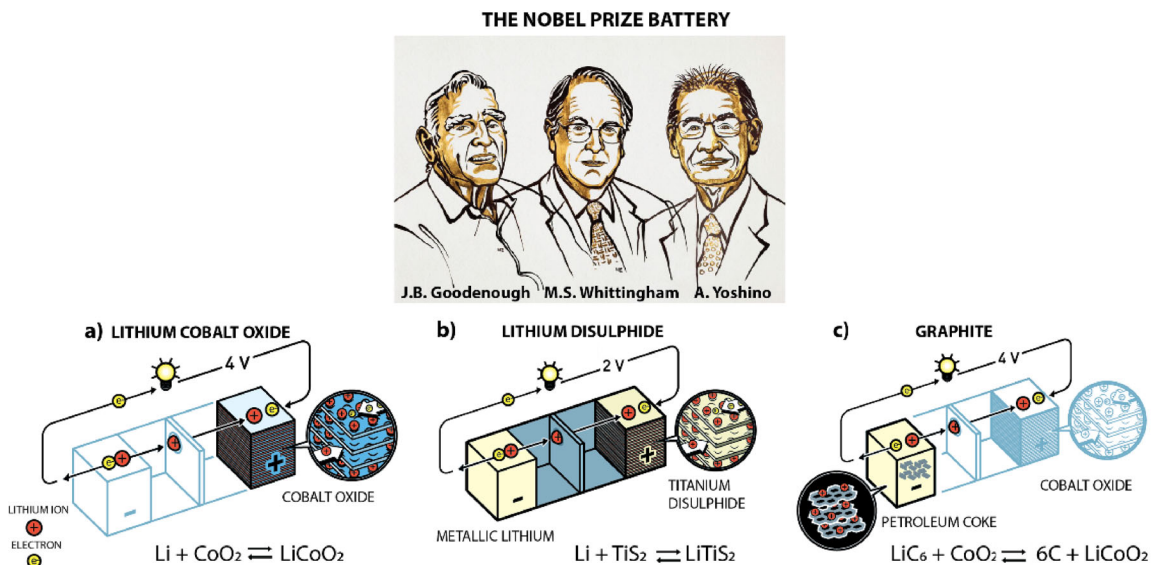


**Figure 1** | Nobel Prize winners in Chemistry awarded for development of Li-ion batteries. **a)** J.B. Goodenough for lithium cobalt oxide, **b)** M.S. Whittingham for lithium disulphide and **c)** A. Yoshino for graphite. © Johan Jarnestad/The Royal Swedish Academy of Sciences

**What is the working principle of the Li-ion battery?** In general, a battery is an electrochemical system that converts and stores electrical energy into chemical energy during charge and converts it back to electrical energy during discharge. It consists of a negative and a positive electrode, erroneously, but usually for simplicity named anode and cathode, respectively. Between the electrodes a separator typically wetted with an ionically conductive electrolyte solution is placed<sup>22</sup>. Every battery requires the exchange of charge carriers between negative and positive electrode, which depends on the type of battery system mentioned at Section 1.1. For the Li-ion batteries however, the most commonly used charge carrier is a Li-ion. The electrolyte allows the Li-ions to flow from one electrode to the other through the separator<sup>9,23</sup>.

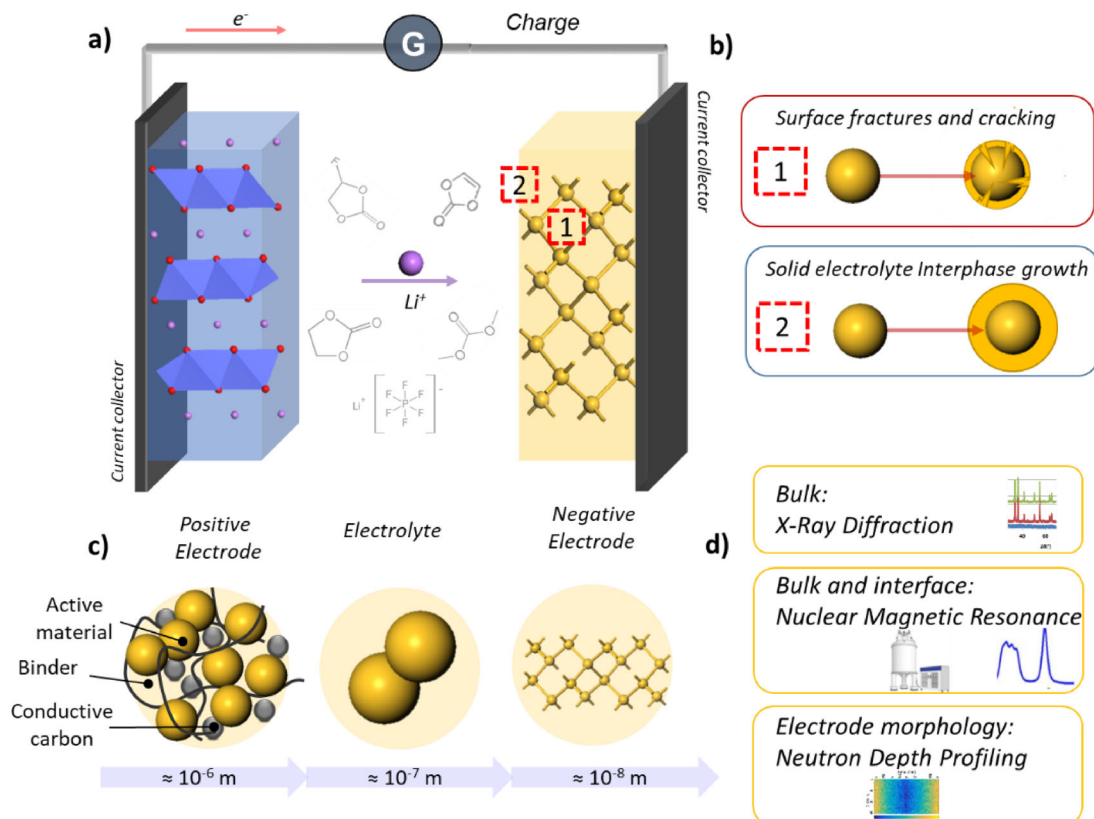
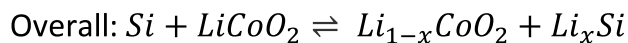
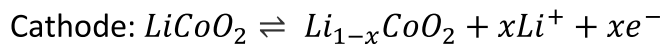


**Figure 2 | a)** Schematic representation of the working principle of a Li-ion battery and **b)** the main issues associated with its usage. **c)** Relevant length scales in the battery and **d)** characterisation techniques used in this thesis to study them.

The principle of the rechargeable Li-ion battery is presented in **Figure 2a**. A rich field of investigation is focused on developing new materials with high performance by increasing both energy and power density in advanced Li-ion batteries. Since the development of the first Li-ion battery, the negative electrode material of choice has been graphite, because it has a very stable behaviour in the battery<sup>24</sup> and gives rise to a high cycle life, compared to other negative electrode materials. Despite its high cycle life, graphite has a big drawback, namely its low specific capacity (372 mAh/g for the end compound  $\text{LiC}_6$ )<sup>25</sup>. This makes it hard to develop batteries with higher energy densities. Silicon (Si) is a very promising candidate for the future applications to replace graphite, due to its relatively low discharge potential ( $< 0.5$  V versus  $\text{Li/Li}^+$ ), a high capacity of 3579 mAh/g<sup>26</sup>, corresponding to the  $\text{Li}_{15}\text{Si}_4$  phase<sup>21</sup> at room temperature and natural abundance of elemental Si, which makes it is relatively cheap to produce<sup>27</sup>. The Li density in the fully lithiated Li-Si alloy ( $\text{Li}_{22}\text{Si}_5$ ) is higher compared to that in metallic Li<sup>28</sup>. The driving force for Li between two electrodes is the difference in Li chemical potential ( $\mu$ ). In the charged battery, where a Si electrode is used and thus is filled with Li-ions and the charge compensating electrons, the difference in Li chemical potential between positive and negative electrode forces Li-ions to move spontaneously from the negative electrode (lithium silicide,  $\text{Li}_{3.75}\text{Si}$ ), through the electrolyte solution to the positive electrode (e.g. a lithium cobalt oxide,  $\text{Li}_{0.5}\text{CoO}_2$ ). To enable electric neutrality, the charge of the Li-ions needs to be compensated with the same amount of electrons which are transported through an external circuit, since the electrolyte has a high electronic resistivity, due to its large electronic bandgap. This process is called discharge. When the chemical potential reaches equilibrium (the potential of the battery becomes zero), the movement of ions and electrons will stop. However, once applying an electrical potential, electrons and ions start to flow in the opposite direction, which process is then called charge. By definition an oxidation reaction takes place at the anode and a reduction reaction occurs at the cathode. Hence during discharge, the anode is the

negative electrode and the positive electrode then is the cathode, and vice versa during charge. However, as indicated earlier, in the battery community, usually the negative electrode is being referred to as the anode. Hence, the processes in a  $\text{LiCoO}_2 \mid \text{Si}$  Li-ion battery can be described by the following reactions:



It is important to realise, that in a charged battery, if *Si* alloyed with electrons and ions ( $\text{Li}_{3.75}\text{Si}$ ) and has the highest chemical potential in contact with delithiated LCO with a lower chemical potential gives a spontaneous reaction. In this situation  $\text{Li}_{3.75}\text{Si}$  is an anode and LCO cathode. However, in a half cell configuration where Li metal is used as counter electrode, the reverse terminology is valid, due to higher chemical potential of Li metal (lower voltage) versus Si. Hence, Li metal will always be regarded as the anode.

The performance of the battery is further dependent on the amount of electrons being transferred between the electrodes referred to as the capacity and measured in mAh/g. The number of ions transported through the battery is controlled by the applied or accepted current. Particularly, high currents require an extra energy to drive the reaction, which is referred to as overpotential so as to overcome energy barriers, better known as the resistance. Since the electrode has to allow a flow of both Li-ions and electrons, the system needs to be both ionically and electronically conductive. Many active materials are poor electronic conductors, so it is important to optimise the particle size to allow a decent power performance. In the same respect, using these particles, they need to have mutual electronic contact, which is achieved by adding certain conductive carbons<sup>29</sup>. Finally, in order to fabricate a complete electrode, these materials needs to be kept together, which is done with a binder<sup>30,31</sup>. This binder is

further important in assisting to resist volumetric changes occurring in the electrodes during insertion / de-insertion and ensure adhesion to the current collector<sup>32,33</sup>.

### 1.3 The challenges of Si negative electrode and how they are addressed in this thesis

**What are the main challenges of the Si electrodes?** The two main issues of Si electrodes, as shown in **Figure 2b**, are structural changes and solid electrolyte interphase (SEI) formation, which shorten the cycle life. Despite the attractive features, including high specific capacity, low costs and low operation potential, Si-based electrodes face significant challenges such as large volume changes (almost 300%) during cycling<sup>34</sup>, which limit the cycle life of the battery. This volume change is caused due the large number of Li atoms that can be inserted into the Si<sup>35</sup>. The volume expansion causes pulverisation of the Si particles and fractures in the electrode which leads to decrease of capacity<sup>36</sup>. Extended fractures in the whole electrode structure lead to a complete loss of electrical contact between active particles, conductive network and current collector<sup>37</sup>. As a results of lithiation and structural changes<sup>38</sup> occurring in the Si due to crystalline-amorphous phase transformation, induces mechanical stresses in the host material<sup>39</sup>. Due to low electrochemical potential of negative electrodes<sup>40</sup>, the surface of the negative electrode is covered by an SEI, which consists of decomposition products of lithium salt and organic electrolyte solvent. The Li in this process is irreversibly consumed, with the electrolyte solvent electrochemically reduced to inorganic crystals (protective function) and oligomers (small polymers), causing lower Coulombic efficiency during the first cycle. In case of a carbonaceous negative electrodes, a stable SEI is formed on the graphite over the first cycles preventing its continuous formation of SEI and further consumption of Li. In this case the SEI allows Li ions movements but prevents the infiltration of solvent. In contrast to graphite negative electrode, due to

the huge volume expansion of Si, the SEI is highly unstable and it will crack during cycling. This will result in fresh Si being exposed to the electrolyte. Hence, to restore the SEI, Li and electrolyte will be consumed again. The SEI will grow thicker during cycling, and this will lead to losses in the electrochemical contact with the particles and capacity fading. The repeated consumption of Li affects the safety, power, capacity and the cycle life of the cell.

**Solution strategies to the mechanical stress induced by volume expansion<sup>41</sup> in Si electrodes.** To prevent fracturing of the surface and cracking of Si particles during cycling<sup>42</sup>, reducing the particle size to approximately 100 nm<sup>43</sup> is essential. To accommodate large volume changes without pulverisation, different morphologies such as nanowires<sup>44,45</sup>, hollow nanospheres<sup>46</sup>, nanotubes<sup>47</sup>, yolk shell structures<sup>48,49</sup> are suggested. Moreover surface modifications, such as various coating strategies are applied<sup>50,51</sup>. To preserve the integrity of the Si electrode during extensive cycling Si particles are dispersed in inactive<sup>52</sup> or conductive composite<sup>53</sup> such as carbon matrix<sup>54,55</sup> have been developed<sup>56</sup>. To further maintain the electrode integrity the usage binders are explored<sup>57</sup>. CMC (carboxymethyl cellulose)<sup>58</sup> made from an acidic solvent (pH = 3) showed better accommodation of volume changes. The aqueous slurry with pH = 3 tends to form hydrogen bonds (Si-OH-COOH) and that promotes formation of covalent bonds (Si-OCO-R) between CMC chains and Si particles. Covalent bonds improve the mechanical strength of the Si electrode<sup>59</sup>. Other binders such as PEFM for Si have different functional groups providing flexibility, mechanical adhesion and high electrical and ionic conductivity<sup>60,61</sup>.

**Solutions to unstable SEI formation in Si electrodes<sup>41</sup>.** Modifying the electrolyte composition is relevant for the Si/electrolyte interface so as to form a stable SEI. Chemical and mechanical stability of the SEI is vital for the long term operation of the battery. The most common electrolyte additive are fluoroethylene carbonate (FEC), vinylene carbonate (VC)<sup>62</sup>, and lithium difluoride(oxalate) borate (LiDFOB)<sup>63-65</sup>. FEC decomposes easier than the



standard solvents (ethylene carbonate (EC)/ diethyl carbonate (DEC) commonly used in liquid electrolytes) forming an artificial protection layer composed of lithium fluoride (LiF). It thus suppresses degradation of the electrolyte solvents as well as it absorbs organic species from SEI by strong bonds of Li-F<sup>66</sup> for further protection of the active electrode material. Hence, such an SEI is desired to separate Si and the electrolyte from continuous decomposition, provided it is a good ion and electron conductor.

In this study, 100 nm Si particles were used (to avoid pulverisation), in combination with a CMC binder in acidic media (to promote structural integrity of the electrode). In **Chapter 3**, we study how an artificial protective coating behaves upon repeated (dis)charging and in **Chapter 4** how in situ formed coatings behave, through FEC and VC electrolyte additives. Finally in **Chapter 5** we study a novel approach, the addition of solid additives, aiming to improve the ionic conductivity of the electrodes and achieve more homogenous (de)lithiation of Si electrodes which is demonstrated to play a key role in the cycle life.

Characterisation tools are explored in order to study the impact of protective coatings on the structural evolution and the lithiation through the depth of the electrode, both information being essential for complete understanding of the system. **How to study at different length scales relevant for the described processes?** Apart from the regular diagnostics such as charge/discharge profiling, cyclic voltammetry and electrochemical impedance spectroscopy, a detailed study is made on smaller length scales monitored with advanced tools. Relevant length scales in the battery are presented in **Figure 2c,d**. The issues associated with Li ion batteries have to be evaluated from an atomistic to the macroscopic level, which requires application of different experimental strategies. Especially in situ/operando are important as the processes are often dynamic in nature, and the reactivity of the systems often compromise the outcomes of ex-situ measurements. In this thesis study studies were performed at different length scales and under operando conditions, including X-ray diffraction and

Neutron Depth Profiling, aiming to gain insight in the relationship between interface properties, homogeneity of the electrode reactions and cycle life.

1.4 The challenges of all solid state batteries, understanding the electrochemical stability window of solid electrolytes and how they are addressed in this thesis

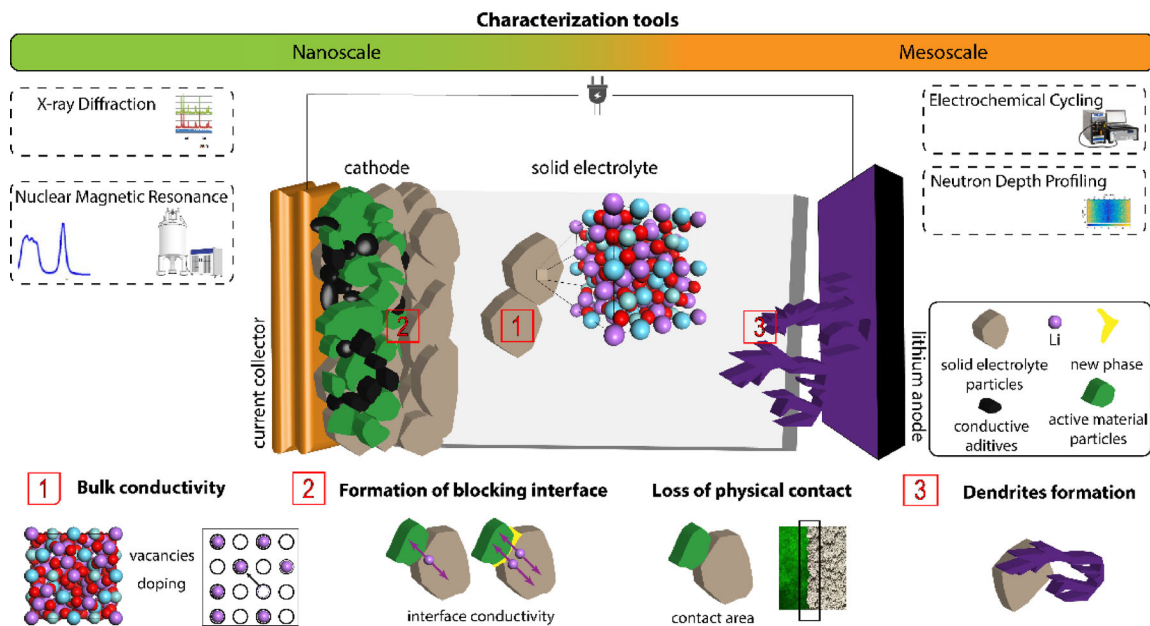


**Figure 3 |** Schematic representation of a solid-state battery and the main issues associated with its usage. Relevant length scales in the battery and characterisation tools used to study them. A first challenge, marked as **1)**, is associated to improvement of bulk conductivity which can be done by doping or creating vacancies in solid electrolyte. At **2)** it shows an electrode/solid electrolyte interface. As a challenge here the formation of new phase is shown which will have an impact on the interface conductivity. Another challenge is contact loss upon volume changes, which is detrimental to the electrode. Last challenge marked in **3)**, is associated with inhomogeneous Li deposition.

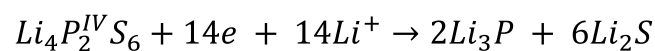
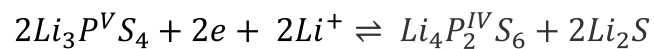
Solid-state batteries have the potential to replace the current Li-ion batteries using a flammable liquid electrolyte so as to improve the safety of the battery. Besides, due to this improved safety, solid state batteries can have a significantly increased energy density as now it is possible to better stack the anode and cathode leading to reduce packaging and weight of non-

active parts in the battery<sup>67</sup>. Recent developments showed that solid electrolytes almost reach the conductivity of liquid electrolytes<sup>68</sup>. Despite the progress of the high bulk conductivity, the rate performance of the solid-state battery remains poor. The **main challenges of solid-state batteries** are illustrated in **Figure 3**, and are described in more detail below. The first challenge is to maintain **mechanical stability** due to volume changes (loss of physical contact is detrimental). The second challenge is related to inhomogeneous deposition of Li through dendrite formation. The third challenge is associated with **stabilisation of the interfaces** by formation of ionically conductive and electronically insulating interphases between all components of the battery (active material, solid electrolyte and conductive additives such as carbons). These newly formed phases originate from electrochemical driven processes at the solid-solid interface creating high internal resistances<sup>69</sup>, and thus inducing high overpotentials allowing several parasitic reactions to occur. The outstanding stability reported for solid electrolyte materials are evaluated using cyclic voltammetry measurements<sup>70,71</sup> and its claimed to be very wide compared to computational studies revealing narrower electrochemical stability window<sup>72,73</sup>. These computational studies, that calculate the electrochemical stability window based on thermodynamic predictions where differences in formation energies of decomposition products are considered, indeed lead to much narrower stability windows<sup>72,73</sup>. Albeit, practical stability windows usually appear to be larger<sup>74-76</sup>. In order to develop future solid-state batteries high ionic conductivity has to be combined with chemical compatibility and electrochemical stability<sup>70,74,77-79</sup>.

**What is the electrochemical stability window of a solid electrolyte and how to determine it?** The stability window of a solid electrolyte is the voltage window where the electrolyte does not allow redox decomposition. At thermodynamic equilibrium, the stability window is defined based on the lowest free energy of the formed decomposition products. Moreover the voltage at which those reactions occur can be determined as was presented

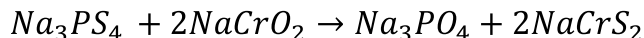
by Richards et al. and Zhu et al. From those predictions, the electrochemical stability window is determined based on the discussed below possible reactions (redox decomposition, chemical reaction, electrochemical stability). Hence, if the electrolyte undergoes a redox reaction, it can be regarded as an electrode material, and thus can be treated as such similar to the electrode materials as presented by Ceder et al. named as topotactic stability. It is however stressed that those predictions are not in thermodynamic equilibrium. In this thesis we aim to extend our current understanding of the electrochemical stability of solid electrolytes, posing a major challenge for all-solid-state-batteries<sup>67,74-76,80,81</sup>. Through computational predictions, in combination with galvanostatic experiments and XRD and NMR analysis, new and general insights are developed in the practical electrochemical stability window, and the formation of the decomposition products.

**What are the possible reactions at the electrolyte/electrode interface in solid-state batteries<sup>67</sup>?** Several parasitic reactions at the electrode/electrolyte interface may happen and these are described below along a typical example. The first possible reaction is **redox decomposition** described by the donation and acceptance of electrons and Li-ions in the solid electrolyte. An example can be the redox decomposition of lithium thiophosphate solid electrolyte ( $\text{Li}_3\text{PS}_4$ ) in contact with Li metal, reducing phosphorous and thus going towards the most stable composition of the decomposition products. The decomposition reaction then can be written as:

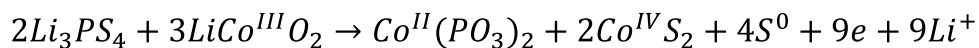


Those reactions can be partially reversible and were reported in the single material battery, where  $\text{Li}_{10}\text{GeP}_2\text{S}_{12}$  (LGPS) was reversibly oxidised and reduced<sup>82</sup>. A second possible reaction is a **chemical reaction**, which leads to the formation of a new composition combining electrode material and solid

electrolyte, often seen as ion exchange. As an example the following reaction is predicted<sup>76,83</sup>:



Hence, at the interface of an oxide cathode and a thiophosphate solid electrolyte a displacement reaction takes place. Here then a sulfur atom is displaced by oxygen. A third possible reaction is a combination of the other two and proceeds via a redox and a chemical reaction and it is typically referred to as **electrochemical stability**. As an example at the interface of an oxide cathode (LiCoO<sub>2</sub>) and a sulfide electrolyte (Li<sub>3</sub>PS<sub>4</sub>), the following reaction may occur<sup>72</sup>:



**What are the different types of functional interfaces in solid-state batteries<sup>67</sup>?** As mentioned above, several reactions may occur that will degrade the battery or more specifically the electrode. In that respect it would be important to figure out how to stabilise these electrode materials against the electrolyte, and vice versa. Here several possibilities are discussed in terms of functional interfaces. The first type is the ideal case of **intrinsic stability** which is associated with no reactions occurring at all at the interface of electrode material and solid electrolyte. How this can be achieved is still under debate. The second type is **kinetic interface stabilisation**, where decomposition products form a functional interphase with desired properties at the interface such as enhanced ionic conduction and restricted electronic conductivity<sup>72</sup>. As an example of kinetic interface stabilisation LiPON is used and it is known to decompose into Li<sub>3</sub>PO<sub>4</sub> and Li<sub>3</sub>N<sup>84</sup>. This thin nanometric layer consisting of decomposition products serves as functional interphase and provides electrochemical stability vital for long-term cycling. Finally, the third type is **artificial protection** acting as protection layer at the electrode and solid electrolyte interface and prevents

redox decomposition. It is achieved by applying a coating typically of acidic oxides such as  $\text{Li}_4\text{Ti}_5\text{O}_{12}$ <sup>85</sup> or  $\text{LiNbO}_3$ <sup>86</sup>.

## 1.5 The outline of thesis: research questions and methods used to answer them

This thesis has two independent main research questions: what is the origin of the electrochemical stability window of solid electrolytes and what is the role of the interface and bulk properties to improve the cycle life of Si negatives electrodes. **Chapter 2** is devoted to the understanding of the electrochemical stability window of solid electrolytes, with emphasis on argyrodite-, garnet- and NASICON type materials. The current understanding of the electrochemical stability window of solid electrolytes is based on the stability of the stable decomposition products. However, measured stability windows deviate from this significantly. In this thesis, new mechanistic insights lead to the formulation of the indirect electrochemical stability window, that is demonstrated to represent the actual stability window of solid electrolytes. The indirect electrochemical stability windows are calculated with thermodynamic predictions based on the formation energies of the various potential decomposition products (calculations performed by Ir. Tammo Schwietert) and analysed by Galvanostatic electrochemistry, XRD and solid state NMR experiments. The fundamental nature of the proposed mechanism suggests that this is a key aspect for solid electrolytes in general, guiding interface and material design for all-solid-state batteries. **Chapters 3-5** deal with the second main research question, what is the role of interface and bulk properties to improve the cycle life of Si electrodes. Local volume expansion due to inhomogeneous Li compositions, the coexistence of different Li-Si phases and poor electronic conductivity of Si are shown to be important contributors to the detrimental operation of Si electrodes. To gain insight in the homogeneity of the (de)lithiation, and in the reversibility of the processes operando Neutron Depth Profiling (NDP) is employed for

the first time for Si electrodes. NDP allows quantitative measurement of the Li density as a function of the electrode depth. Thereby it enables us to determine the utilisation of the Si material and the homogeneity of the (de)lithiation, as well as the distribution of Li decomposition products. Through the Li distribution as a function of the electrode depth, this technique additionally provides insights in the Li-ion and electron transport properties of the Si electrodes. **Chapter 3** focuses on investigation of the role of protective conformal TiO<sub>2</sub> coatings on Si particles for improving its cycle life. Operando NDP is used to study the homogeneity of the lithiation process and quantification of Li containing SEI species together with the lithiation of the protective coating. To gain insight into the structure changes of the anatase TiO<sub>2</sub> coated Si particles, operando X-Ray Diffraction is employed. **Chapter 4** presents the failure mechanisms of Si electrodes and usage of electrolyte additives such as FEC and VC in improving electrochemical performance at the interface by an ionically conducting artificial SEI. This is demonstrated to result in more homogenous lithiation of the Si electrodes, which is suggested to play a critical role in extending the cycle life. Motivated by this result, **Chapter 5** investigates the possibility to use solid additives to improve the ion transport in Si electrodes. These ion-conductive additives are expected to facilitate ion transport via a network vital for high capacity operation, which lowers the internal resistance during the (dis)charge process and thus leads to a more homogenous distribution of Li through the whole electrode.

### 1.6 References:

- 1 Houghton, J. *Global warming: the complete briefing*. (Cambridge university press, 2009).
- 2 Rogelj, J. *et al.* Paris Agreement climate proposals need a boost to keep warming well below 2 degrees C. *Nature* **534**, 631-639 (2016).
- 3 Hallegatte, S. *et al.* Mapping the climate change challenge. *Nature Climate Change* **6**, 663-668 (2016).
- 4 Rogelj, J. *et al.* Energy system transformations for limiting end-of-century warming to below 1.5 °C. *Nature Climate Change* **5**, 519-527 (2015).

- 5 Edenhofer, O. *et al.* *Renewable energy sources and climate change mitigation: Special report of the intergovernmental panel on climate change.* (Cambridge University Press, 2011).
- 6 Whittingham, M. S. Materials challenges facing electrical energy storage. *Mrs Bulletin* **33**, 411-419 (2008).
- 7 Mulder, F. M. Implications of diurnal and seasonal variations in renewable energy generation for large scale energy storage. *Journal of Renewable and Sustainable Energy* **6** (2014).
- 8 Tarascon, J. M. & Armand, M. Issues and challenges facing rechargeable lithium batteries. *Nature* **414**, 359-367 (2001).
- 9 Dunn, B., Kamath, H. & Tarascon, J.-M. Electrical energy storage for the grid: a battery of choices. *Science* **334**, 928-935 (2011).
- 10 Ali, M. U. *et al.* Towards a smarter battery management system for electric vehicle applications: A critical review of lithium-ion battery state of charge estimation. *Energies* **12**, 446 (2019).
- 11 Mazouzi, D. & Hammouti, B. Congratulations to Professors John B Goodenough, M Stanley Whittingham and Akira Yoshino awarded the Nobel Prize in Chemistry 2019 for work on Lithium-ion batteries. (2019).
- 12 Whittingham, M. S. & Gamble Jr, F. R. The lithium intercalates of the transition metal dichalcogenides. *Materials Research Bulletin* **10**, 363-371 (1975).
- 13 Whittingham, M. Batterie à Base de Chalcogénures. *Belgian patent* (1975).
- 14 Whittingham, M. S. Electrical energy storage and intercalation chemistry. *Science* **192**, 1126-1127 (1976).
- 15 Whittingham, M. S. Chemistry of intercalation compounds: metal guests in chalcogenide hosts. *Progress in Solid State Chemistry* **12**, 41-99 (1978).
- 16 Whittingham, M. S., Siu, C. & Ding, J. Can multielectron intercalation reactions be the basis of next generation batteries? *Accounts of chemical research* **51**, 258-264 (2018).
- 17 Mizushima, K., Jones, P., Wiseman, P. & Goodenough, J. B.  $\text{Li}_x\text{CoO}_2$  ( $0 < x < 1$ ): A new cathode material for batteries of high energy density. *Materials Research Bulletin* **15**, 783-789 (1980).
- 18 Goodenough, J. B. & Mizushima, K. (Google Patents, 1982).
- 19 賴威均. 電解沉積二氧化鈦應用於薄膜鋰離子電池陽極之特性研究. (2009).
- 20 Yoshino, A., Sanekika, K. & Nakajima, T. (Google Patents, 1987).
- 21 Yoshino, A. The birth of the lithium-ion battery. *Angewandte Chemie International Edition* **51**, 5798-5800 (2012).
- 22 Armand, M. & Tarascon, J.-M. Building better batteries. *nature* **451**, 652-657 (2008).
- 23 Whittingham, M. S. Lithium batteries and cathode materials. *Chemical reviews* **104**, 4271-4302 (2004).
- 24 Yazami, R. & Touzain, P. A reversible graphite-lithium negative electrode for electrochemical generators. *Journal of Power Sources* **9**, 365-371 (1983).
- 25 Simon, B. *et al.* On the choice of graphite for lithium ion batteries. *Journal of power sources* **81**, 312-316 (1999).



- 26 Obrovac, M., Christensen, L., Le, D. B. & Dahn, J. R. Alloy design for lithium-ion battery anodes. *Journal of The Electrochemical Society* **154**, A849-A855 (2007).
- 27 Wang, W. *et al.* Monodisperse porous silicon spheres as anode materials for lithium ion batteries. *Scientific reports* **5**, 8781 (2015).
- 28 Winter, M. & Besenhard, J. O. Electrochemical lithiation of tin and tin-based intermetallics and composites. *Electrochimica Acta* **45**, 31-50 (1999).
- 29 Dominko, R., Gaberšček, M., Drofenik, J., Bele, M. & Jamnik, J. Influence of carbon black distribution on performance of oxide cathodes for Li ion batteries. *Electrochimica Acta* **48**, 3709-3716 (2003).
- 30 Markevich, E., Salitra, G. & Aurbach, D. Influence of the PVdF binder on the stability of LiCoO<sub>2</sub> electrodes. *Electrochemistry communications* **7**, 1298-1304 (2005).
- 31 Chen, L., Xie, X., Xie, J., Wang, K. & Yang, J. Binder effect on cycling performance of silicon/carbon composite anodes for lithium ion batteries. *Journal of applied electrochemistry* **36**, 1099-1104 (2006).
- 32 Fransson, L., Eriksson, T., Edström, K., Gustafsson, T. & Thomas, J. O. Influence of carbon black and binder on Li-ion batteries. *Journal of power sources* **101**, 1-9 (2001).
- 33 Jeschull, F. *et al.* Influence of inactive electrode components on degradation phenomena in nano-Si electrodes for Li-ion batteries. *Journal of Power Sources* **325**, 513-524 (2016).
- 34 Jerliu, B. *et al.* Volume expansion during lithiation of amorphous silicon thin film electrodes studied by in-operando neutron reflectometry. *The Journal of Physical Chemistry C* **118**, 9395-9399 (2014).
- 35 Beaulieu, L., Eberman, K., Turner, R., Krause, L. & Dahn, J. Colossal reversible volume changes in lithium alloys. *Electrochemical and Solid-State Letters* **4**, A137-A140 (2001).
- 36 Winter, M., Besenhard, J. O., Spahr, M. E. & Novak, P. Insertion electrode materials for rechargeable lithium batteries. *Adv. Mater.* **10**, 725-763 (1998).
- 37 Ryu, J. H., Kim, J. W., Sung, Y.-E. & Oh, S. M. Failure modes of silicon powder negative electrode in lithium secondary batteries. *Electrochemical and Solid State Letters* **7**, A306 (2004).
- 38 Obrovac, M. & Christensen, L. Structural changes in silicon anodes during lithium insertion/extraction. *Electrochemical and Solid State Letters* **7**, A93 (2004).
- 39 Chon, M. J., Sethuraman, V. A., McCormick, A., Srinivasan, V. & Guduru, P. R. Real-time measurement of stress and damage evolution during initial lithiation of crystalline silicon. *Physical Review Letters* **107**, 045503 (2011).
- 40 Xu, K. & Wang, C. Batteries: widening voltage windows. *Nature Energy* **1**, 1-2 (2016).
- 41 Zhu, B., Wang, X., Yao, P., Li, J. & Zhu, J. Towards high energy density lithium battery anodes: silicon and lithium. *Chemical science* **10**, 7132-7148 (2019).
- 42 Bruce, P. G., Scrosati, B. & Tarascon, J. M. Nanomaterials for rechargeable lithium batteries. *Angewandte Chemie International Edition* **47**, 2930-2946 (2008).
- 43 Liu, X. H. *et al.* Size-Dependent Fracture of Silicon Nanoparticles During Lithiation. *Acs Nano* **6**, 1522-1531 (2012).

- 44 Chan, C. K. *et al.* High-performance lithium battery anodes using silicon nanowires. *Nature nanotechnology* **3**, 31 (2008).
- 45 Cui, L.-F., Yang, Y., Hsu, C.-M. & Cui, Y. Carbon– silicon core– shell nanowires as high capacity electrode for lithium ion batteries. *Nano letters* **9**, 3370-3374 (2009).
- 46 Yao, Y. *et al.* Interconnected silicon hollow nanospheres for lithium-ion battery anodes with long cycle life. *Nano letters* **11**, 2949-2954 (2011).
- 47 Wu, H. *et al.* Stable cycling of double-walled silicon nanotube battery anodes through solid–electrolyte interphase control. *Nature nanotechnology* **7**, 310 (2012).
- 48 Liu, N. *et al.* A yolk-shell design for stabilized and scalable Li-ion battery alloy anodes. *Nano letters* **12**, 3315-3321 (2012).
- 49 Li, Y. *et al.* Growth of conformal graphene cages on micrometre-sized silicon particles as stable battery anodes. *Nature Energy* **1**, 1-9 (2016).
- 50 Guan, C. & Wang, J. Recent development of advanced electrode materials by atomic layer deposition for electrochemical energy storage. *Advanced Science* **3**, 1500405 (2016).
- 51 Bai, Y. *et al.* Core-shell Si@ TiO<sub>2</sub> nanosphere anode by atomic layer deposition for Li-ion batteries. *Journal of Power Sources* **308**, 75-82 (2016).
- 52 Kim, I.-s., Blomgren, G. & Kumta, P. Nanostructured Si/TiB<sub>2</sub> composite anodes for Li-ion batteries. *Electrochemical and solid state letters* **6**, A157 (2003).
- 53 Roberts, G., Cairns, E. & Reimer, J. Magnesium silicide as a negative electrode material for lithium-ion batteries. *Journal of power sources* **110**, 424-429 (2002).
- 54 Khomenko, V. G. & Barsukov, V. Z. Characterization of silicon-and carbon-based composite anodes for lithium-ion batteries. *Electrochimica acta* **52**, 2829-2840 (2007).
- 55 Wang, G., Ahn, J., Yao, J., Bewlay, S. & Liu, H. Nanostructured Si–C composite anodes for lithium-ion batteries. *Electrochemistry communications* **6**, 689-692 (2004).
- 56 Mao, O. *et al.* Active/Inactive nanocomposites as anodes for Li-Ion batteries. *Electrochemical and Solid State Letters* **2**, 3 (1998).
- 57 Munao, D., Van Erven, J., Valvo, M., Garcia-Tamayo, E. & Kelder, E. Role of the binder on the failure mechanism of Si nano-composite electrodes for Li-ion batteries. *Journal of Power Sources* **196**, 6695-6702 (2011).
- 58 Lestriez, B., Bahri, S., Sandu, I., Roué, L. & Guyomard, D. On the binding mechanism of CMC in Si negative electrodes for Li-ion batteries. *Electrochemistry Communications* **9**, 2801-2806 (2007).
- 59 Tranchot, A., Idrissi, H., Thivel, P. X. & Roué, L. Impact of the Slurry pH on the Expansion/Contraction Behavior of Silicon/Carbon/Carboxymethylcellulose Electrodes for Li-Ion Batteries. *Journal of The Electrochemical Society* **163**, A1020-A1026, doi:10.1149/2.1071606jes (2016).
- 60 Wu, M. *et al.* Toward an ideal polymer binder design for high-capacity battery anodes. *Journal of the American Chemical Society* **135**, 12048-12056 (2013).
- 61 Choi, N.-S. *et al.* Recent progress on polymeric binders for silicon anodes in lithium-ion batteries. *Journal of Electrochemical Science and Technology* **6**, 35-49 (2015).

- 62 Michan, A. L. *et al.* Fluoroethylene carbonate and vinylene carbonate reduction: understanding lithium-ion battery electrolyte additives and solid electrolyte interphase formation. *Chemistry of Materials* **28**, 8149-8159 (2016).
- 63 Verma, P., Maire, P. & Novák, P. A review of the features and analyses of the solid electrolyte interphase in Li-ion batteries. *Electrochimica Acta* **55**, 6332-6341 (2010).
- 64 Zhang, S. S. A review on electrolyte additives for lithium-ion batteries. *Journal of Power Sources* **162**, 1379-1394 (2006).
- 65 Vogl, U. S. *et al.* The mechanism of SEI formation on a single crystal Si (100) electrode. *Journal of The Electrochemical Society* **162**, A603 (2015).
- 66 Okuno, Y., Ushirogata, K., Sodeyama, K. & Tateyama, Y. Decomposition of the fluoroethylene carbonate additive and the glue effect of lithium fluoride products for the solid electrolyte interphase: an ab initio study. *Physical Chemistry Chemical Physics* **18**, 8643-8653 (2016).
- 67 Famprikis, T., Canepa, P., Dawson, J. A., Islam, M. S. & Masquelier, C. Fundamentals of inorganic solid-state electrolytes for batteries. *Nature materials*, 1-14 (2019).
- 68 Valøen, L. O. & Reimers, J. N. Transport properties of LiPF<sub>6</sub>-based Li-ion battery electrolytes. *Journal of The Electrochemical Society* **152**, A882-A891 (2005).
- 69 Yu, C., van Eijck, L., Ganapathy, S. & Wagemaker, M. Synthesis, structure and electrochemical performance of the argyrodite Li<sub>6</sub>PS<sub>5</sub>Cl solid electrolyte for Li-ion solid state batteries. *Electrochimica Acta* **215**, 93-99 (2016).
- 70 Boulineau, S., Courty, M., Tarascon, J.-M. & Viallet, V. Mechanochemical synthesis of Li-argyrodite Li<sub>6</sub>PS<sub>5</sub>X (X= Cl, Br, I) as sulfur-based solid electrolytes for all solid state batteries application. *Solid State Ionics* **221**, 1-5 (2012).
- 71 Auvergniot, J. *et al.* Interface Stability of Argyrodite Li<sub>6</sub>PS<sub>5</sub>Cl toward LiCoO<sub>2</sub>, LiNi<sub>1/3</sub>Co<sub>1/3</sub>Mn<sub>1/3</sub>O<sub>2</sub>, and LiMn<sub>2</sub>O<sub>4</sub> in Bulk All-Solid-State Batteries. *Chemistry of Materials* **29**, 3883-3890 (2017).
- 72 Richards, W. D., Miara, L. J., Wang, Y., Kim, J. C. & Ceder, G. Interface Stability in Solid-State Batteries. *Chemistry of Materials* **28**, 266-273 (2016).
- 73 Zhu, Y., He, X. & Mo, Y. Origin of Outstanding Stability in the Lithium Solid Electrolyte Materials: Insights from Thermodynamic Analyses Based on First-Principles Calculations. *ACS Applied Materials & Interfaces* **7**, 23685-23693 (2015).
- 74 Zheng, F., Kotobuki, M., Song, S., Lai, M. O. & Lu, L. Review on solid electrolytes for all-solid-state lithium-ion batteries. *Journal of Power Sources* **389**, 198-213 (2018).
- 75 Lotsch, B. V. & Maier, J. Relevance of solid electrolytes for lithium-based batteries: A realistic view. *Journal of Electroceramics* **38**, 128-141 (2017).
- 76 Tian, Y. *et al.* Compatibility issues between electrodes and electrolytes in solid-state batteries. *Energy & Environmental Science* **10**, 1150-1166 (2017).
- 77 Kamaya, N. *et al.* A lithium superionic conductor. *Nature materials* **10**, 682-686 (2011).
- 78 Ohta, S., Kobayashi, T. & Asaoka, T. High lithium ionic conductivity in the garnet-type oxide Li<sub>7-*X*</sub>La<sub>3</sub>(Zr<sub>2-*X*</sub>, Nb<sub>*X*</sub>)O<sub>12</sub> (*X* = 0–2). *Journal of Power Sources* **196**, 3342-3345 (2011).

- 79 Kato, Y. *et al.* High-power all-solid-state batteries using sulfide superionic conductors. *Nature Energy* **1**, 16030 (2016).
- 80 Zhang, Z. *et al.* New horizons for inorganic solid state ion conductors. *Energy & Environmental Science* **11**, 1945-1976, doi:10.1039/c8ee01053f (2018).
- 81 Janek, J. & Zeier, W. G. A solid future for battery development. *Nature Energy* **1**, 16141 (2016).
- 82 Han, F., Gao, T., Zhu, Y., Gaskell, K. J. & Wang, C. A Battery Made from a Single Material. *Advanced Materials* **27**, 3473-3483 (2015).
- 83 Tang, H. *et al.* Probing solid–solid interfacial reactions in all-solid-state sodium-ion batteries with first-principles calculations. *Chemistry of Materials* **30**, 163-173 (2018).
- 84 Schwöbel, A., Hausbrand, R. & Jaegermann, W. Interface reactions between LiPON and lithium studied by in-situ X-ray photoemission. *Solid State Ionics* **273**, 51-54 (2015).
- 85 Ohta, N. *et al.* Enhancement of the high-rate capability of solid-state lithium batteries by nanoscale interfacial modification. *Advanced Materials* **18**, 2226-2229 (2006).
- 86 Ohta, N. *et al.* LiNbO<sub>3</sub>-coated LiCoO<sub>2</sub> as cathode material for all solid-state lithium secondary batteries. *Electrochemistry communications* **9**, 1486-1490 (2007).





# 2

---

## Clarifying relationship between redox activity and electrochemical stability in solid electrolytes

---

**This chapter has been published as: Violetta Arszewska<sup>†</sup>, Tammo Schwietert<sup>†</sup>, Chao Wang, ..., Erik M. Kelder, Swapna Ganapathy, Marnix Wagemaker, Clarifying the relationship between redox activity and electrochemical stability of solid electrolytes, **Nature Materials** 19, no. 4 (2020): 428-435 (<sup>†</sup>co first author).**

### **Abstract**

All-solid-state Li-ion batteries promise safer electrochemical energy storage with larger volumetric and gravimetric energy densities. A major concern is the limited electrochemical stability of solid electrolytes and related detrimental electrochemical reactions, especially because of our restricted understanding. Here it is demonstrated for the argyrodite, garnet and NASICON type solid electrolytes, that the favourable decomposition pathway is indirect rather than direct, via (de)lithiated states of the solid electrolyte, into the thermodynamically stable decomposition products. The consequence is that the electrochemical stability window of the solid electrolyte is significantly larger than predicted for direct decomposition, rationalizing the observed stability window. The observed argyrodite metastable (de)lithiated solid electrolyte phases contribute to the (ir)reversible cycling capacity of all-solid-state batteries, in addition to the contribution of the decomposition products, comprehensively explaining solid electrolyte redox activity. The fundamental nature of the proposed mechanism suggests this is a key aspect for solid electrolytes in general, guiding interface and material design for all-solid-state batteries.

## 2.1 Introduction

All-solid-state-batteries (ASSBs) are attracting ever increasing attention due to their high intrinsic safety, achieved by replacing the flammable and reactive liquid electrolyte by a solid electrolyte<sup>1</sup>. In addition, a higher energy density in ASSBs may be achieved through; (a) bipolar stacking of the electrodes, which reduces the weight of the non-active battery parts and (b) by potentially enabling the use of a Li-metal negative electrode, which possesses the maximum theoretical Li capacity and lowest electrochemical potential (3860 mAhg<sup>-1</sup> and -3.04 V vs. SHE). First of all, the success of ASSBs relies on solid electrolytes with a high Li-ion conductivity<sup>2-5</sup>. A second prerequisite, is the electrochemical stability at the interfaces of the solid electrolyte with the electrode material in the range of their working potential. Any electrochemical decomposition of the solid electrolyte may lead to decomposition products with poor ionic conductivity that increase the internal battery resistance<sup>2-4,6</sup>. Third, ASSBs require mechanical stability as the changes in volume of the electrode materials upon (de)lithiation, as well as decomposition reactions at the electrode-electrolyte interface may lead to contact loss, also increasing the internal resistance and lowering the capacity<sup>2-4,7</sup>.

Initially, for many solid electrolytes wide electrochemical stability windows were reported<sup>4,8-11</sup>, which appeared in practice to be much more limited<sup>4,12,13</sup>. Evaluation of the electrochemical stability, based on differences in formation energies, indeed lead to much narrower stability windows<sup>14,15</sup>, however, practical stability windows typically appeared wider<sup>4,12,13</sup>. As a thermodynamic evaluation does not take into account kinetic barriers for decomposition reactions, which should be expected to play a critical role<sup>13</sup>, the mechanisms of solid electrolyte decomposition are poorly understood, presenting one of the major challenges for ASSBs<sup>2-4,7,12,13</sup>. Another important aspect, directly related to this, is the potentially significant contribution of the typically Li-rich solid electrolytes through



(de)lithiation reactions, either directly or indirectly<sup>16</sup>. In general, redox activity can be expected near the interface between the solid electrolyte and the electronically conductive components of the electrode (electrode active material and carbon additives<sup>17</sup>), but may also extend deep into the solid electrolyte through short range electron conductivity of the electrolyte itself<sup>18</sup>. Understanding the redox activity of solid electrolytes, and its correlation with the electrochemical stability window is thus of fundamental importance for the development of stable solid-solid interfaces in ASSBs.

Here, we demonstrate that the electrochemical stability window of the argyrodite  $\text{Li}_6\text{PS}_5\text{Cl}$  solid electrolyte is determined by the solid electrolyte redox activity *i.e.* lithiation upon reduction of phosphorus and delithiation upon oxidation of sulfur, before decomposing into more stable products. As demonstrated by DFT simulations, this kinetically favourable indirect decomposition pathway effectively widens the electrochemical stability window, compared to direct decomposition into stable products, in excellent agreement with accurate electrochemical measurements. The (de)lithiated argyrodite phases are directly observed with XRD and solid state NMR, providing direct evidence of this indirect decomposition mechanism. As solid electrolytes are designed to provide fast ionic conduction, the indirect decomposition through (de)lithiation is proposed to be relevant for solid electrolytes in general, determining the practical electrochemical stability window. This is further validated by the agreement between the measured and the predicted indirect decomposition mechanism for  $\text{Li}_7\text{La}_3\text{Zr}_2\text{O}_{12}$  (LLZO) garnet type and  $\text{Li}_{1.5}\text{Al}_{0.5}\text{Ge}_{1.5}(\text{PO}_4)_3$  (LAGP) NASICON type solid electrolytes. This mechanism establishes that not only the decomposition products, but also the solid electrolyte structure itself contribute to the reversible capacity in ASSBs, making the present findings highly relevant for the working and development of ASSBs.

## 2.2 Results and discussion

### 2.2.1 Electrochemical activity of argyrodite $\text{Li}_6\text{PS}_5\text{Cl}$

2

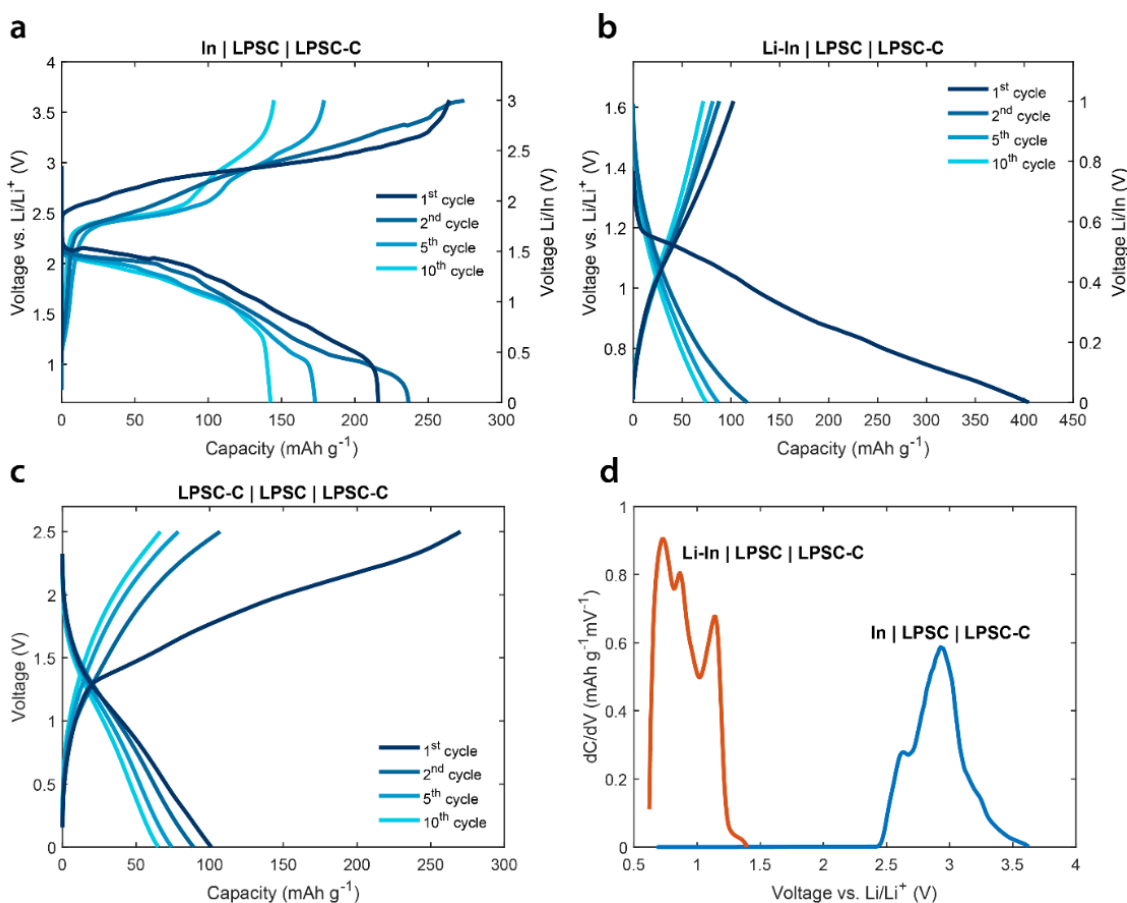


**Figure 1 | Voltage profiles and differential capacity curve of the  $\text{Li}_6\text{PS}_5\text{Cl}$ -C electrode.** a-c, Voltage profile of the 1<sup>st</sup>, 2<sup>nd</sup>, 5<sup>th</sup> and 10<sup>th</sup> cycles of: (a) In|LPSC|LPSC-C ASSB starting from charge and on galvanostatic oxidation, the LPSC-C electrode shows a voltage plateau at 2.5 V, reaching a total charge capacity of 264 mAh g<sub>LPSC</sub><sup>-1</sup> when charged to 3.63 V. (b) Li-In|LPSC|LPSC-C ASSB starting from discharge and on galvanostatic reduction, the LPSC-C electrode shows a voltage plateau at around 1.2 V, with a discharge capacity of 405 mAh g<sub>LPSC</sub><sup>-1</sup> when discharged to 0.63 V. (c) LPSC-C|LPSC|LPSC-C, a one material (LPSC) ASSB, shows an initial charge capacity of 270 mAh g<sub>LPSC</sub><sup>-1</sup>, which drops to 107 mAh g<sub>LPSC</sub><sup>-1</sup> in the second cycle. (d) The differential capacity dC/dV curve of the In|LPSC|LPSC-C (blue) and the Li-In|LPSC|LPSC-C battery (orange) showing the first oxidation and first reduction of LPSC. Electrochemical activity is observed below 1.25 V and above 2.50 V vs. Li/Li<sup>+</sup>, indicating an electrochemical stability window of 1.25 V. Note that these experiments should be expected

to approach thermodynamic conditions, hence the contribution of overpotentials is minimal. This is because the applied current density (see methods section) is distributed over the very large interface area between the conductive carbon additives and the solid electrolyte ( $\gg 1 \text{ m}^2$ ).

The electrochemical stability, especially for thiophosphate solid electrolytes, was shown to be significantly lower than initially expected<sup>10,17,19-22</sup>, where the consequential decomposition reactions have had a large impact on the ASSB performance<sup>11,21-25</sup>. To investigate the electrochemical stability and the role of electrochemical reactions in solid electrolytes, the argyrodite  $\text{Li}_6\text{PS}_5\text{Cl}$  (LPSC), introduced by Deiseroth et al.<sup>26</sup>, is employed both as active material and solid electrolyte in ASSBs. To induce oxidation and reduction reactions of the solid electrolyte, carbon black and carbon nano-fibres are mixed in with the LPSC. The mixture is referred to as the LPSC-C electrode (for details see the methods section). To study the oxidation and reduction independently, while at the same time preventing the redox activity of the decomposition products from interfering with the decomposition itself, individual cells are prepared for the first oxidation and for the first reduction respectively. An  $\text{In}|\text{LPSC}|\text{LPSC-C}$  battery is cycled galvanostatically starting with oxidation, and a  $\text{Li-In}|\text{LPSC}|\text{LPSC-C}$  battery starting with reduction, the resulting voltage curves of which are shown in **Figure 1a and b**. Unless otherwise specified, all voltages are expressed vs.  $\text{Li}/\text{Li}^+$ . The large partially reversible specific capacities demonstrate that LPSC can undergo severe oxidation and reduction reactions, and the low coulombic efficiencies of 70 and 40% upon first oxidation and reduction, respectively, suggest the formation of a significant amount of decomposition products. The decreasing capacity of the initial cycles (**Supplementary A Fig. 1**) indicates that these decomposition reactions increase the impedance. However, upon extended cycling, the reversible capacity remains relatively constant, which could indicate that the decomposition products are able to deliver reversible electrochemical activity, as already suggested for LPSC by Auvergnot et al.<sup>27</sup> and worked out in detail by Tan et al.<sup>25</sup>. Since LPSC can undergo both

oxidation and reduction reactions, it can be used to assemble a one-material-battery, similar to what was reported for the  $\text{Li}_{10}\text{GeP}_2\text{S}_{12}$  solid electrolyte, for which the combination of decomposition products at the cathode and anode provided the reversible redox<sup>16</sup>. During the first charge the activity appears to set in at around 1.25 V, a direct indication of the practical electrochemical stability window. To evaluate the practical electrochemical stability window more accurately, the differential capacity is determined from the 1<sup>st</sup> charge of the  $\text{In}|\text{LPSC}|\text{LPSC-C}$  battery and from the 1<sup>st</sup> discharge of the  $\text{Li-In}|\text{LPSC}|\text{LPSC}$  battery, shown in **Figure. 1d**. Indeed, a practical stability window of 1.25 V is obtained, much larger than that theoretically predicted (0.3 V)<sup>14,15</sup>, and much smaller than initially reported (7 V)<sup>10</sup>. Additionally, the presence of more than one peak, both on reduction and oxidation, indicates subsequent redox activity. This raises the question; what reactions take place and how do these determine the observed electrochemical stability window?

### 2.2.2 Evaluation of the redox activity of the argyrodite $\text{Li}_6\text{PS}_5\text{Cl}$ with DFT simulations

Aiming for a better understanding and prediction of practical electrochemical stability windows, and correlation with solid electrolyte redox activity, we evaluate the formation energies of all possible Li-vacancy configurations at different compositions of argyrodite  $\text{Li}_x\text{PS}_5\text{Cl}$ , within a (charge neutral) single unit cell, similar to how the energetics of electrode materials are evaluated<sup>28</sup>. This appears to be a realistic approach considering that the solid electrolyte is in contact with the conductive additives in a cathodic mixture, and therefore the solid electrolyte can function as an electrode material being oxidised and reduced.

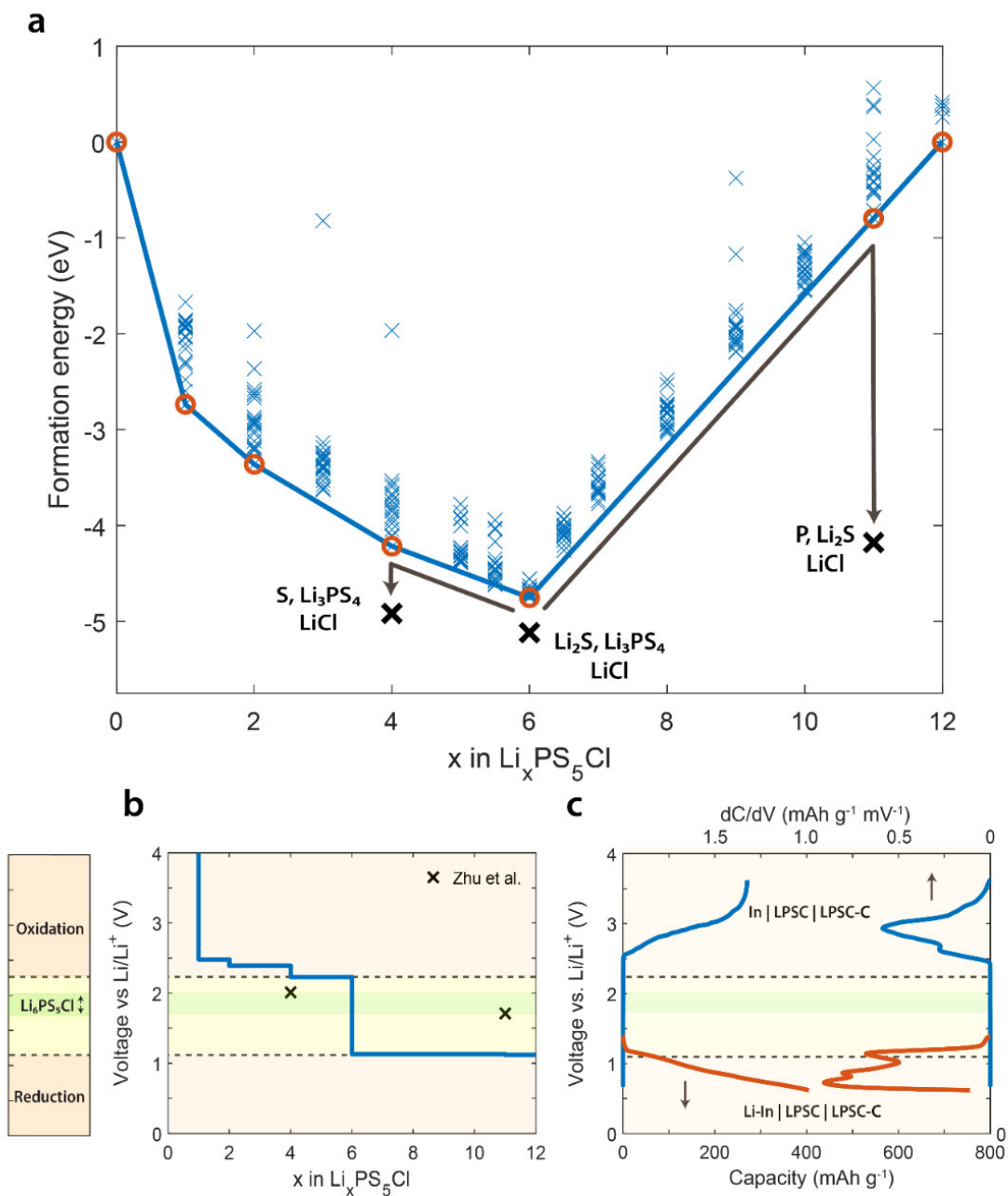


**Figure 2 | Formation energies of Li-vacancy configurations of  $\text{Li}_x\text{PS}_5\text{Cl}$  and comparison of experimental and calculated voltage profiles. a)** Formation energies per formula unit for all Li configurations within one unit cell, versus the composition  $x$  in  $\text{Li}_x\text{PS}_5\text{Cl}$ . The formation energy of the combination of  $\text{Li}_3\text{PS}_4$ ,  $\text{Li}_2\text{S}$  and  $\text{LiCl}$  is shown below the convex hull at  $x = 6$ . At  $x = 4$  and  $x = 11$  the formation energies of the decomposition products upon oxidation ( $\text{S}$ ,  $\text{Li}_3\text{PS}_4$ ,  $\text{LiCl}$ ) and upon reduction ( $\text{P}$ ,  $\text{Li}_2\text{S}$  and  $\text{LiCl}$ ) respectively, are shown, in line with the decomposition products previously reported<sup>14</sup>. **b)** Calculated theoretical voltage profile, vs.

$i/\text{Li}^+$ , of  $\text{Li}_x\text{PS}_5\text{Cl}$  in the compositional range of  $0 < x < 12$ . Reduction and oxidation are expected to occur at 1.08 V and 2.24 V vs.  $\text{Li}/\text{Li}^+$ , respectively. The black crosses indicate the voltages at which the argyrodite is expected to decompose, upon oxidation to S,  $\text{Li}_3\text{PS}_4$ , LiCl, and upon reduction to P,  $\text{Li}_2\text{S}$  and LiCl, previously reported<sup>14</sup>. **c**, First charge of the  $\text{In}|\text{LPSC}|\text{LPSC-C}$  (blue) and first discharge of the  $\text{Li-In}|\text{LPSC}|\text{LPSC-C}$  battery (orange) including the differential capacity from Figure 1d. Above 2.30 V vs.  $\text{Li}/\text{Li}^+$  LPSC is oxidised, and below 1.25 V vs.  $\text{Li}/\text{Li}^+$  LPSC is reduced. The legend compares the stability windows. Yellow: stability window of LPSC based on the oxidation and reduction potentials of  $\text{Li}_4\text{PS}_5\text{Cl}$  and  $\text{Li}_{11}\text{PS}_5\text{Cl}$ , respectively. Green: Predicted window (thermodynamic), based on the stability of the decomposition products for oxidation (S,  $\text{Li}_3\text{PS}_4$ , LiCl) and reduction (P,  $\text{Li}_2\text{S}$  and LiCl)<sup>14,15</sup>.

The resulting formation energies of the argyrodite  $\text{Li}_x\text{PS}_5\text{Cl}$  as a function of Li-composition are shown in **Figure 2a**, where the convex hull connects the most stable configurations. Upon oxidation and reduction of  $\text{Li}_6\text{PS}_5\text{Cl}$  the most stable compositions are  $\text{Li}_4\text{PS}_5\text{Cl}$  and  $\text{Li}_{11}\text{PS}_5\text{Cl}$ , respectively. Upon oxidation of argyrodite, sulfur is redox active ( $\text{S}^{-2} \rightarrow \text{S}^0 + 2\text{e}^-$ ) whereas upon reduction, phosphorous is redox active ( $\text{P}^{5+} \rightarrow \text{P}^0 - 5\text{e}^-$ ). Also indicated in **Figure 2a** are the energies of the thermodynamically more stable combinations of  $\text{Li}_3\text{PS}_4$ ,  $\text{Li}_2\text{S}$  and LiCl species, and the most stable decomposition products of the oxidised and reduced argyrodite. Clearly, a delithiated (oxidised) argyrodite ( $\text{Li}_4\text{PS}_5\text{Cl}$ ) is much less stable than the combination of  $\text{Li}_3\text{PS}_4$ , S and LiCl, and similarly, a lithiated (reduced) argyrodite ( $\text{Li}_{11}\text{PS}_5\text{Cl}$ ) is much less stable than the combination of P,  $\text{Li}_2\text{S}$  and LiCl, as previously predicted<sup>14,15</sup>, which are therefore the expected decomposition products on oxidation.

The average voltages as a function of Li composition  $x$  in  $\text{Li}_x\text{PS}_5\text{Cl}$ , calculated from the convex hull are shown in **Figure 2b**. From the theoretical voltage curve it is expected that the argyrodite LPSC delithiates (oxidises) at 2.24 V and lithiates (reduces) at 1.08 V. This indicates that if the decomposition reactions for oxidation and reduction are determined by the stability of the  $\text{Li}_4\text{PS}_5\text{Cl}$  and  $\text{Li}_{11}\text{PS}_5\text{Cl}$  species respectively, an electrochemical stability window of 1.16 V is expected. Also indicated is the much narrower electrochemical stability window, approximately 0.3 V wide, based on direct

decomposition into  $\text{Li}_3\text{PS}_4$ , S and LiCl (oxidation) and into  $\text{Li}_3\text{PS}_4$ ,  $\text{Li}_2\text{S}$  and LiCl (reduction), in line with previous DFT calculations<sup>14,15</sup>. Which stability window applies, depends on the activation barriers to these decomposition routes. Based on the high Li-ion conductivity of the argyrodite, indicating low kinetic barriers for changes in the Li-composition, we propose that the decomposition occurs indirectly, via the lithiated and delithiated compositions of argyrodite ( $\text{Li}_4\text{PS}_5\text{Cl}$  and  $\text{Li}_{11}\text{PS}_5\text{Cl}$ ), rather than directly into the decomposition products. Upon argyrodite oxidation and reduction, first  $\text{Li}_4\text{PS}_5\text{Cl}$  and  $\text{Li}_{11}\text{PS}_5\text{Cl}$  would form, which are most likely unstable as evaluated below, providing a facile reaction pathway towards the formation of the more stable decomposition products as indicated by the solid black arrows in **Figure 2a**.

The experimental voltage curves obtained on oxidation and reduction of the argyrodite, including their differential capacity, are shown for comparison in **Figure 2c**. Remarkable agreement is found between the predicted electrochemical stability window of 1.16 V (**Fig. 2b**) and the experimentally observed window (**Fig. 2c**), supporting the present hypothesis that the argyrodite stability is determined by its redox activity upon (de)lithiation. The formation of decomposition products can be expected to increase the impedance depending on their location in the electrodes, which is most likely the origin of the broadening of oxidation and reduction peaks in the differential capacity shown in **Figure 2c**. The offset between the measured and predicted stability window is most likely a result of the lower voltages predicted by DFT calculations<sup>29</sup>. Based on this, we propose that the first oxidation peak in the differential capacity, shown in **Figure 1d** and **Figure 2c**, is associated with the decomposition of LPSC at around 2.24 V via  $\text{Li}_4\text{PS}_5\text{Cl}$  into  $\text{Li}_3\text{PS}_4$ , S and LiCl, and the first reduction peak in the differential capacity with the decomposition of LPSC at around 1.08 V via  $\text{Li}_{11}\text{PS}_5\text{Cl}$  into P,  $\text{Li}_2\text{S}$  and LiCl.

Upon further oxidation, after the formation of  $\text{Li}_3\text{PS}_4$  via  $\text{Li}_4\text{PS}_5\text{Cl}$ , thermodynamic evaluation predicts the formation of  $\text{P}_2\text{S}_5$  at 2.3 V<sup>14</sup>. Further

reduction, after formation of P via  $\text{Li}_{11}\text{PS}_5\text{Cl}$ , thermodynamic evaluations predicts the formation of  $\text{Li}_3\text{P}$ , resulting in several voltage plateau's starting from 1.3 V down to approximately 0.87 V. The latter represents 67% of the reduction capacity ( $\text{LiP}$  to  $\text{Li}_3\text{P}$ ) (see Supplementary Table 1, consistent with previous DFT predictions<sup>30</sup>). This provides a complete prediction of the oxidation and reduction potential pathway, via the solid electrolyte to the redox activity of the decomposition products as illustrated by **Supplementary A Figure 2**. For reduction this is consistent with the observed reduction activity measured at around 0.8 V in **Figure 2c**, and with the known reduction potentials associated with the lithiation of phosphorus<sup>31</sup>. However, upon oxidation of the expected  $\text{Li}_3\text{PS}_4$  decomposition product, a peak in the differential capacity is observed around 2.9 V, which is not in agreement with the predicted  $\text{P}_2\text{S}_5$  formation at 2.3 V. As discussed below, formation of  $\text{P}_2\text{S}_7^{4-}$  is observed, consistent with the P-S-P bridging polyhedral suggested by XPS<sup>20</sup>. Moreover,  $\text{Li}_3\text{PS}_4$  has been observed to oxidise at 2.9 V towards of  $\text{P}_2\text{S}_7^{4-}$ <sup>32</sup> consistent with the observed oxidation activity shown in **Figure 1d and 2b**. We anticipate that to predict the oxidation of  $\text{Li}_3\text{PS}_4$  to  $\text{P}_2\text{S}_7^{4-}$  at 2.9 V requires a comprehensive DFT redox activity analysis as done here for LSPC.

Additionally, DFT based molecular dynamics (MD) simulations are performed on the delithiated ( $\text{Li}_4\text{PS}_5\text{Cl}$ ) and lithiated ( $\text{Li}_{11}\text{PS}_5\text{Cl}$ ) phases, showing that the  $\text{Li}_4\text{PS}_5\text{Cl}$  and  $\text{Li}_{11}\text{PS}_5\text{Cl}$  compositions are extremely unstable, having very low activation barriers towards decomposition (**Fig. 3**). This supports the presently proposed indirect decomposition reaction, via the facile oxidation and reduction of the argyrodite towards the  $\text{Li}_4\text{PS}_5\text{Cl}$  and  $\text{Li}_{11}\text{PS}_5\text{Cl}$  phases.



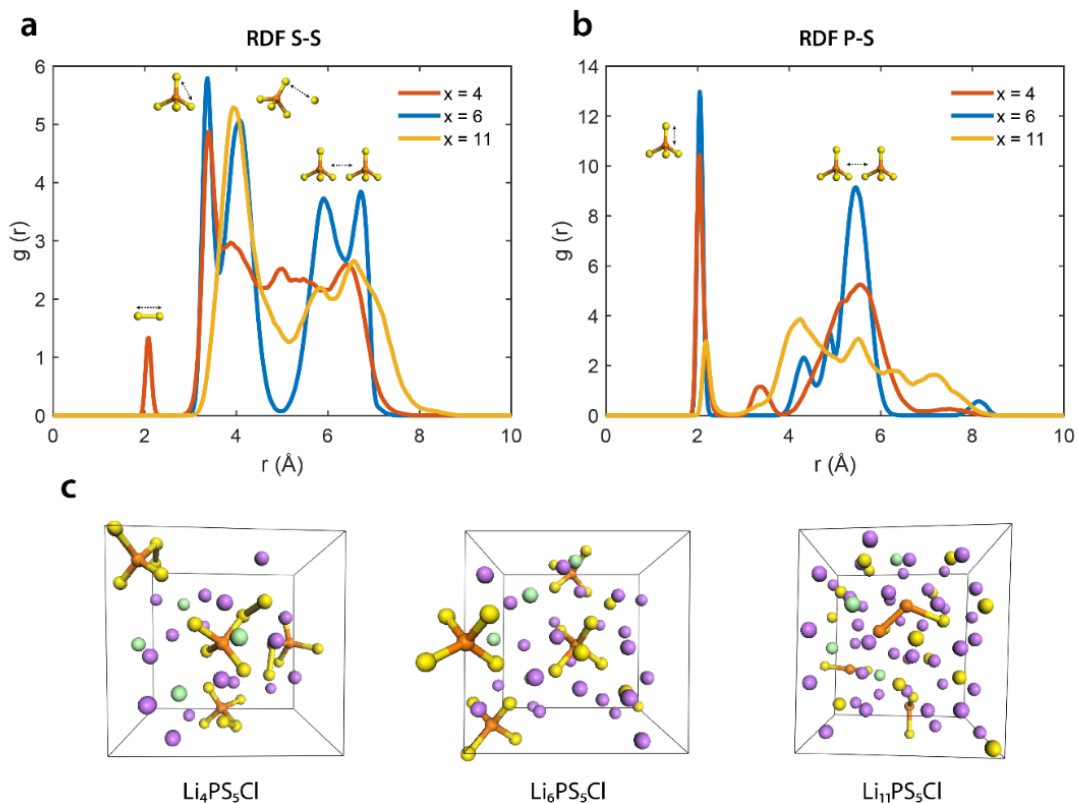


**Figure 3 | Molecular dynamics simulations of  $\text{Li}_4\text{PS}_5\text{Cl}$ ,  $\text{Li}_6\text{PS}_5\text{Cl}$  and  $\text{Li}_{11}\text{PS}_5\text{Cl}$**  **a)** Radial distribution function (RDF) of the S-S bonds in (de)lithiated  $\text{Li}_x\text{PS}_5\text{Cl}$  for  $x = 4, 6$ , and  $11$  during a  $400\text{ K}$  DFT-MD simulation. During delithiation an increase in S-S bonds is seen around  $2.1\text{ \AA}$ , indicating that the formation of S-S bonds originates from the oxidation of S in the argyrodite. On top of the peaks, bonds at corresponding radii are displayed. **b)** Radial distribution function (RDF) of the P-S bonds of (de)lithiated  $\text{Li}_x\text{PS}_5\text{Cl}$  for  $x = 4, 6$  and  $11$  during a  $400\text{ K}$  DFT-MD simulation, showing a decrease of P-S bonds in  $\text{PS}_4$  units, indicating the reduction of P occurs in the argyrodite. **c)** Relaxed structures of  $\text{Li}_x\text{PS}_5\text{Cl}$  for  $x = 4, 6$  and  $11$  after a  $400\text{ K}$  DFT-MD simulation. The violet, orange, yellow and green spheres indicate lithium, phosphorous, sulfur, and chlorine respectively. For the  $\text{Li}_4\text{PS}_5\text{Cl}$  structure S atoms at the  $4a$  and  $4c$  positions form S-S bonds with  $\text{PS}_4$  groups, while for  $\text{Li}_{11}\text{PS}_5\text{Cl}$  P-S bonds break upon reduction of P.

### 2.2.3 Analysis of the argyrodite $\text{Li}_6\text{PS}_5\text{Cl}$ decomposition products using XRD and $^6\text{Li}$ and $^{31}\text{P}$ solid-state NMR

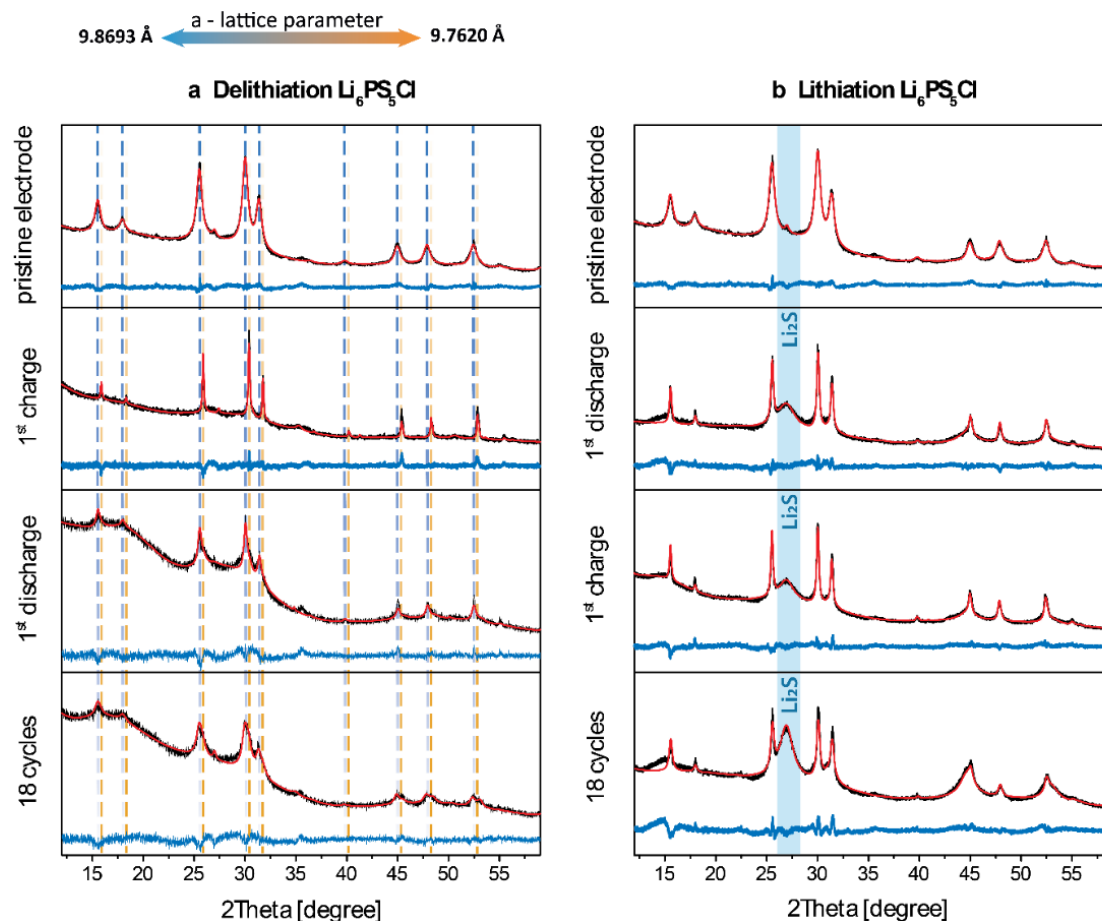


**Figure 4 | XRD patterns and fits of the LPSC-C electrodes before and after cycling.** All the patterns are fit with the Rietveld method as implemented in GSAS<sup>33</sup>, the resulting structural parameters are provided in Supplementary Tables 2-7. **a**, XRD patterns for the In|LPSC|LPSC-C battery after 1<sup>st</sup> charge to 3.63 V vs Li/Li<sup>+</sup>, after subsequent discharge to 0.63 V vs Li/Li<sup>+</sup> and after 18 full cycles. **b**, XRD patterns for the Li-In|LPSC|LPSC-C battery after 1<sup>st</sup> discharge to 0.63 V vs Li/Li<sup>+</sup>, after subsequent charge to 1.63 V vs Li/Li<sup>+</sup> and after 18 full cycles. A growing peak at around 27° reflects the formation of the  $\text{Li}_2\text{S}$  phase, consistent with the predicted decomposition reaction of lithiated (reduced) argyrodite ( $\text{Li}_{11}\text{PS}_5\text{Cl} \rightarrow \text{P} + 5 \text{Li}_2\text{S} + \text{LiCl}$ ). The amount of the  $\text{Li}_2\text{S}$  phase that is formed increases dramatically as a function of cycle number, also indicating the continued decomposition of the argyrodite for low potential cycling. After the 1<sup>st</sup> half cycle, both on oxidation and reduction, a decrease in peak width is observed, indicating an increase in average crystallite size. The average crystallite size increases from 13 nm to 80 nm on delithiation (a) and to 41 nm on lithiation

(b) respectively. An increase in average particle size can be rationalised by the preferential decomposition of smaller particles, most likely due to their large surface areas and resulting shorter electronic pathways for oxidation and reduction. This implies that electronic transport occurs through the argyrodite solid over tens of nanometers (the size of argyrodite particles). Upon subsequent cycling, the argyrodite XRD peaks widen, which may indicate partial decomposition of larger particles as well as a distribution of argyrodite lattice parameters as discussed below.

To monitor the structural changes of the LPSC-C electrodes, XRD measurements are performed at different stages during the cycling (following the same cycling strategy as in **Fig. 1a,b**) of both the In|LPSC|LPSC-C and Li-In|LPSC|LPSC-C batteries as shown in **Figure 4**. During the oxidation (delithiation) of the LPSC-C electrode to 3.63 V, the LPSC peak positions shift (**Fig. 4a**), corresponding to a decrease in the average cubic lattice parameter from 9.87 Å to 9.76 Å. This can be attributed to the partial delithiation of the LPSC phase, consistent with the lattice volume changes predicted by DFT for the compositional range  $6 \geq x \geq 4$  for  $\text{Li}_x\text{PS}_5\text{Cl}$  (**Supplementary A Fig. 3**). Interestingly, several argyrodite compositions between  $\text{Li}_4\text{PS}_5\text{Cl}$  and  $\text{Li}_{11}\text{PS}_5\text{Cl}$  are located slightly above the convex hull (only 7.5 meV per atom for  $\text{Li}_5\text{PS}_5\text{Cl}$ ) as seen in **Figure 2a**. Based on the convex hull in **Figure 2a**, these metastable phases  $6 \geq x \geq 4$  should disproportionate into  $\text{Li}_4\text{PS}_5\text{Cl}$  (which would decompose immediately) and  $\text{Li}_6\text{PS}_5\text{Cl}$ . However, in reality, the system will not be in thermodynamic equilibrium as some parts of the electrodes are, or can become, more isolated through poor ionic and/or electronic contact. This makes it reasonable to suggest that parts of the electrode can be captured in  $6 \geq x \geq 4$  metastable phases (which are kinetically more stable as compared to the  $\text{Li}_4\text{PS}_5\text{Cl}$  and  $\text{Li}_{11}\text{PS}_5\text{Cl}$  phases). Importantly, the presence of these phases in the composition range  $6 \geq x \geq 4$ , provides experimental support for the proposed indirect decomposition mechanism via (de)lithiation of the solid electrolyte. After subsequent reduction, hence after one complete charge-discharge cycle, two different phases of argyrodite appear to be present,

indicated by the dashed lines in **Figure 4a**. The  $2\theta$  position of the first phase (blue line) shifts back to the pristine argyrodite position, indicating that at least a partially reversible (de)lithiation of LPSC occurs. The second phase (orange line) remains at the position representing the delithiated argyrodite phases, the amount of which appears to grow upon cycling, indicating an increasing amount of oxidised argyrodite phases are formed upon cycling. The total amount of crystalline argyrodite decreases as indicated by the increasing background that appears over cycling, indicating the concomitant formation of amorphous sulfide and phosphorous sulfide decomposition products. During the first reduction (lithiation) of the LPSC-C electrode to 0.63 V, the XRD patterns (**Fig. 4b**) do not display an obvious peak shift, as would be expected for the lithiated phases of argyrodite (**Supplementary A Fig. 3**). A growing peak at around  $27^\circ$  reflects the formation of the  $\text{Li}_2\text{S}$  phase, consistent with the predicted decomposition reaction of lithiated (reduced) argyrodite ( $\text{Li}_{11}\text{PS}_5\text{Cl} \rightarrow \text{P} + 5 \text{Li}_2\text{S} + \text{LiCl}$ ). The amount of the  $\text{Li}_2\text{S}$  phase that is formed increases dramatically as a function of cycle number, also indicating the continuous decomposition of the argyrodite for low potential cycling.

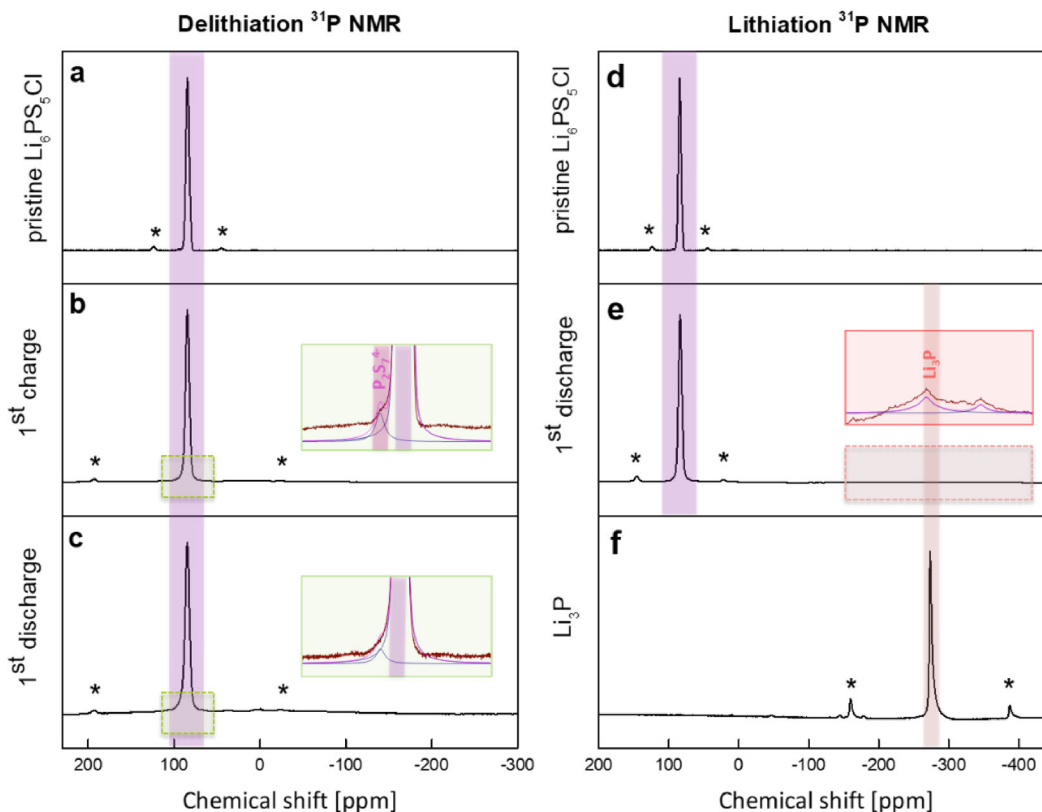


**Fig. 5 | Solid-state  $^{31}\text{P}$  NMR spectra of pristine, oxidised and reduced LPSC-C.** a-f,  $^{31}\text{P}$  MAS NMR of oxidative (a–c) and reductive (d–f) activity of LPSC in In|LPSC|LPSC-C and Li-In|LPSC|LPSC-C ASSBs respectively. After the first charge,  $\text{P}_2\text{S}_7^{4-}$  is found in the cathodic mixture, and after first discharge  $\text{Li}_3\text{P}$  is present in the anodic mixture, in agreement with DFT and thermodynamic predictions. Spinning sidebands are indicated with an asterisk.

Complementary to the XRD measurements, solid-state  $^6\text{Li}$  and  $^{31}\text{P}$  MAS NMR measurements are performed to analyse the decomposition products formed upon cycling. For pristine argyrodite, the  $^{31}\text{P}$  resonance at 85 ppm, shown in **Figure 5a and d**, can be assigned to the P environment in the  $\text{PS}_4$  tetrahedral units<sup>34</sup>. After the 1<sup>st</sup> oxidation (delithiation) to 3.63 V of the LPSC-C electrode, an additional shoulder is observed at 95 ppm (**Fig. 5b**) which can be assigned to the  $^{31}\text{P}$  environment of  $\text{P}_2\text{S}_7^{4-}$  species<sup>35–37</sup>. This indicates the formation of S-S bonds between  $\text{PS}_4$  tetrahedral units (P-S-S-P), which undergoes a disproportionation reaction leading to the formation of  $\text{P}_2\text{S}_7^{4-}$

and  $S^0$ , with P-S-P bridging polyhedra<sup>20</sup>. Upon 1<sup>st</sup> oxidation, the  $^6\text{Li}$  NMR spectrum (**Fig. 6b**) shows the formation of an additional shoulder at around -1.1 ppm consistent with the formation of  $\text{LiCl}$ <sup>38</sup>. This supports the decomposition products observed by XPS<sup>23,27</sup>, in line with the MD simulations that indicate the bonding of S to  $\text{PS}_4$  units. Note that the oxidation to  $\text{Li}_3\text{PS}_4$ , S and  $\text{LiCl}$  is proposed at 2.24 V, via the intermediate formation of  $\text{Li}_4\text{PS}_5\text{Cl}$ , whereas at around 2.9 V the oxidation towards  $\text{P}_2\text{S}_7^{4-}$  and  $S^0$  can be expected (**Fig. 2b**), all due to the  $S/S^{-2}$  redox, represented by the first and second oxidation peaks of the differential capacity (**Fig. 1d**). The line broadening of the  $^{31}\text{P}$  and  $^6\text{Li}$  resonances of LPSC may originate from a distribution in bond angles and Li-deficient phases observed with XRD (**Fig. 4a**). After a full cycle i.e. 1<sup>st</sup> oxidation to 3.63 V followed by reduction to 0.63 V, the intensity of the amount of  $\text{P}_2\text{S}_7^{4-}$  decreases, whereas in the  $^6\text{Li}$  NMR spectrum, a new Li-environment appears at 0.44 ppm which can be assigned to  $\text{Li}_3\text{PS}_4$  (**Figs. 6c,d**). This indicates that the P-S-P bridges connecting the  $\text{PS}_4$  units, forming upon oxidation, break upon reduction transforming them back to isolated  $\text{PS}_4$  units, similar to what was reported for the  $\text{Li}_3\text{PS}_4$  electrolyte<sup>20,21,39</sup>.

Upon the 1<sup>st</sup> reduction (lithiation) to 0.63 V of the LPSC-C electrode, a new  $^{31}\text{P}$  environment appears at -220 ppm (**Fig. 5e**) which can be assigned to  $\text{Li}_3\text{P}$  (**Fig. 5f**). The  $^6\text{Li}$  NMR spectrum (**Fig. 6f**), shows the appearance a Li chemical environment very similar to that of Li in the argyrodite. Although the  $^6\text{Li}$  chemical shift of this environment is close to that of  $\text{Li}_2\text{PS}_3$  (**Supplementary A Fig. 4**), the associated phosphorus environment at 109 ppm is not observed in **Figure 5e**. We suggest that this Li environment may represent disordered lithiated argyrodite phases, which are suggested to form as metastable phases, occurring just above the convex hull in **Figure 2a**. Also, an additional peak appears at 2.3 ppm in the  $^6\text{Li}$  spectrum (**Fig. 6f**), which can be assigned to the formation of  $\text{Li}_2\text{S}$ , consistent with the XRD pattern in **Figure 4b**. After a full cycle i.e. 1<sup>st</sup> reduction to 0.63 V followed by oxidation to 1.63 V,  $\text{Li}_3\text{P}$  disappears (**Supplementary A Fig. 5**), indicating that

in this voltage range phosphorous is redox active, reversibly transforming  $\text{Li}_3\text{PS}_4$  to  $\text{Li}_3\text{P}$ . The observed formation of  $\text{Li}_3\text{P}$  and  $\text{Li}_2\text{S}$  in the LPSC-C electrodes reduced to 0.63 V, is consistent with XPS observations showing the formation of  $\text{Li}_3\text{P}$ ,  $\text{Li}_2\text{S}$  and  $\text{LiCl}$  species, at the interface of LPSC with Li-metal<sup>22</sup>. The formation of P,  $\text{Li}_2\text{S}$  and  $\text{LiCl}$ , through the decomposition of the intermediate  $\text{Li}_{11}\text{PS}_5\text{Cl}$ , is expected to occur at 1.08 V, and further reduction up to 0.63 V will result in the formation of  $\text{Li}_3\text{P}$  at around 0.8 V<sup>31</sup> as observed (Fig. 1d) and predicted (Fig. 2b).

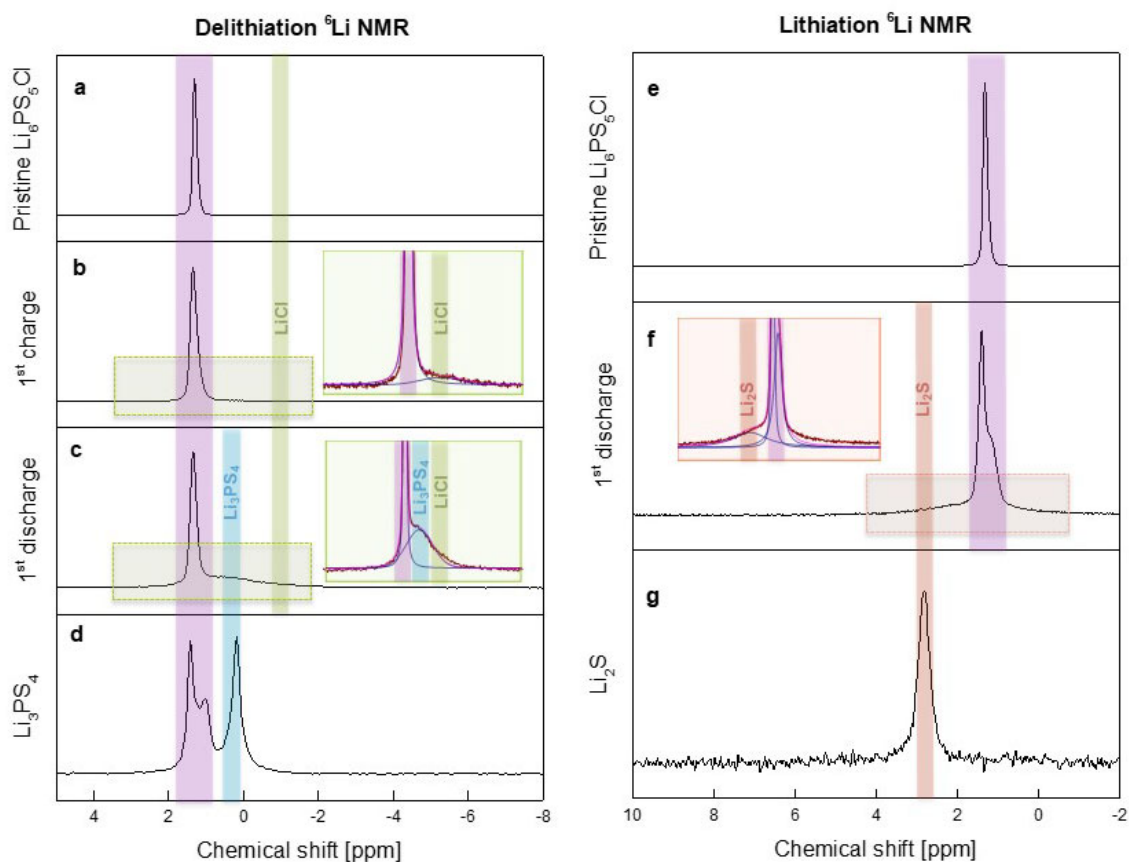


**Figure 6 |  $^6\text{Li}$  MAS NMR spectra of the cathodic mixtures (a-d) and anodic mixtures (e-g) of  $\text{Li}_6\text{PS}_5\text{Cl}$  in the In|LPSC|LPSC-C and Li-In|LPSC|LPSC-C solid-state batteries respectively. After first charge of the In|LPSC|LPSC-C solid state cell, formation of  $\text{LiCl}$  is observed (b). First discharge shows formation at a new resonance frequency corresponding to  $\text{Li}_3\text{PS}_4$  (c, d). The solid state cell, which starts from lithiation process (f), results in formation of  $\text{Li}_2\text{S}$ , confirmed with the spectrum of the reference  $\text{Li}_2\text{S}$  (g).**

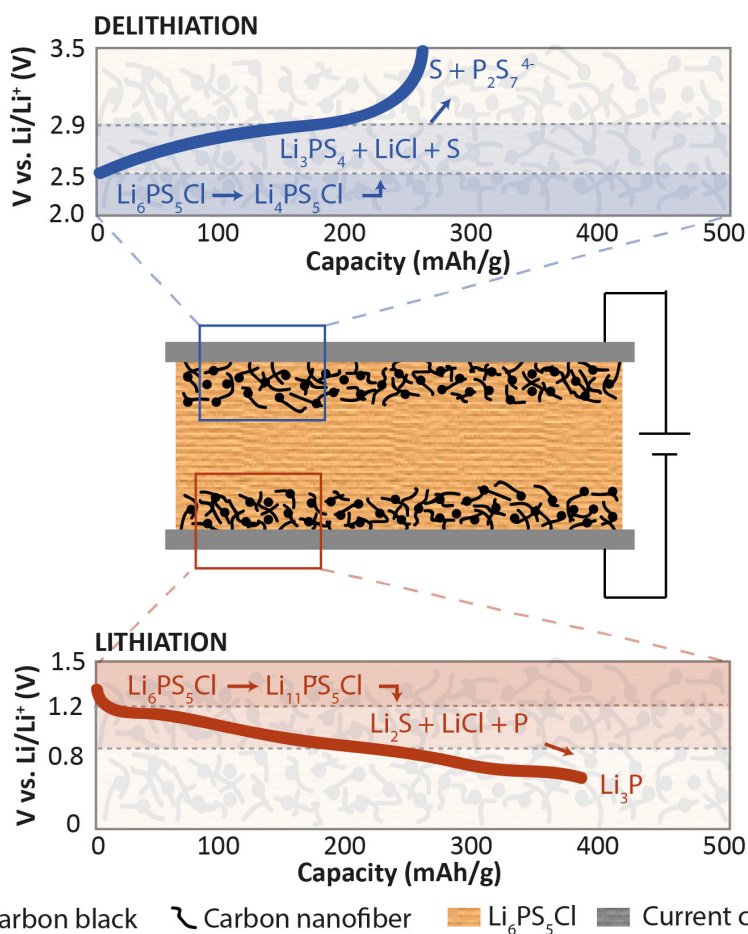


**Figure 7 | Schematic of the electrochemical activity of  $\text{Li}_6\text{PS}_5\text{Cl}$  upon oxidation (delithiation) and reduction (lithiation)** The electrochemical stability window is determined by the oxidation and reduction potentials of  $\text{Li}_4\text{PS}_5\text{Cl}$  ( $\text{S}/\text{S}^{2-}$  redox, at 2.24 V) and  $\text{Li}_{11}\text{PS}_5\text{Cl}$  (through the  $\text{P}/\text{P}^{5+}$  redox, at 1.08 V), respectively, here shown schematically, where the activation barriers to form these compositions are expected to be very low based on the high Li-ion conductivity. These redox potentials of the argyrodite solid electrolyte determine the practical electrochemical stability window, as expressed by the first oxidation and reduction reactions observed in the cycling (Fig. 1a,b), and in the differential capacity (Fig. 1d), consistent with the predicted redox activity (Fig. 2). The unstable argyrodite phases rapidly decompose into the expected stable  $\text{Li}_3\text{PS}_4$ , S and LiCl species after oxidation, and P,  $\text{Li}_2\text{S}$ , and LiCl species after reduction. These decompose upon further oxidation and reduction to  $\text{P}_2\text{S}_7^{4-}$  and  $\text{S}^0$  at 2.9 V<sup>32</sup> and  $\text{Li}_3\text{P}$  around 0.8 V<sup>14,15</sup> respectively, as observed by XPS<sup>20,21</sup> and the present XRD and NMR analysis. XRD and NMR also demonstrate the presence of metastable (de)lithiated argyrodite phases. This provides strong support for the



proposed kinetically most favourable decomposition route, via the redox activity of the argyrodite solid electrolyte, thereby determining the electrochemical stability window.

The proposed indirect oxidative and reductive decomposition mechanism of the argyrodite LPSC solid electrolyte, via the unstable  $\text{Li}_4\text{PS}_5\text{Cl}$  ( $\text{S}/\text{S}^{2-}$  redox) and unstable  $\text{Li}_{11}\text{PS}_5\text{Cl}$  ( $\text{P}/\text{P}^{5+}$  redox), is schematically shown in **Figure 7**. Both the redox activity of the solid electrolyte and of the decomposition products are responsible for the observed cycling capacity at anodic and cathodic potentials. In ASSBs this implies that both contributions of the solid electrolyte, will add to the cycling capacity based on the active electrode materials and the specified potential ranges. Moreover, the poor ionic conductivity of the decomposition products, especially S,  $\text{Li}_2\text{S}$  and  $\text{LiCl}$ , as well as the change in volume can be expected to be responsible for the large increase in interfacial resistance upon cycling<sup>22,40,41</sup>. In addition to the observed decomposition reactions, specific active materials can result in additional decomposition reactions, for instance  $\text{Ni}_3\text{S}_4$  upon cycling LPCS in combination with a NCM622 ( $\text{LiNi}_{0.6}\text{Co}_{0.2}\text{Mn}_{0.2}\text{O}_2$ ) cathode (**Supplementary A Fig. 6**).

To support the general nature of the indirect decomposition mechanism, the Li insertion/extraction potentials are also determined computationally and experimentally for two different families of solid electrolytes i.e. garnet LLZO and NASICON LAGP, shown in **Figure 8**. For LLZO, the predicted and measured oxidation are both located just above 3.5 V, significantly larger than the direct decomposition at 2.91 V towards the predicted stable decomposition products  $\text{Li}_2\text{O}_2$ ,  $\text{La}_2\text{O}_3$  and  $\text{Li}_6\text{Zr}_2\text{O}_7$ <sup>14</sup>. For LAGP, the predicted and measured oxidation occur close to 2.31 V, which is lower than direct decomposition at 2.70 V based on the stability of the predicted decomposition products Ge,  $\text{GeO}_2$ ,  $\text{Li}_4\text{P}_2\text{O}_7$  and  $\text{AlPO}_4$ <sup>14</sup>. These results support that the proposed indirect, kinetically favourable decomposition, via the (de)lithiation of the solid electrolyte is a general mechanism, in practice widening the solid electrolyte stability window.

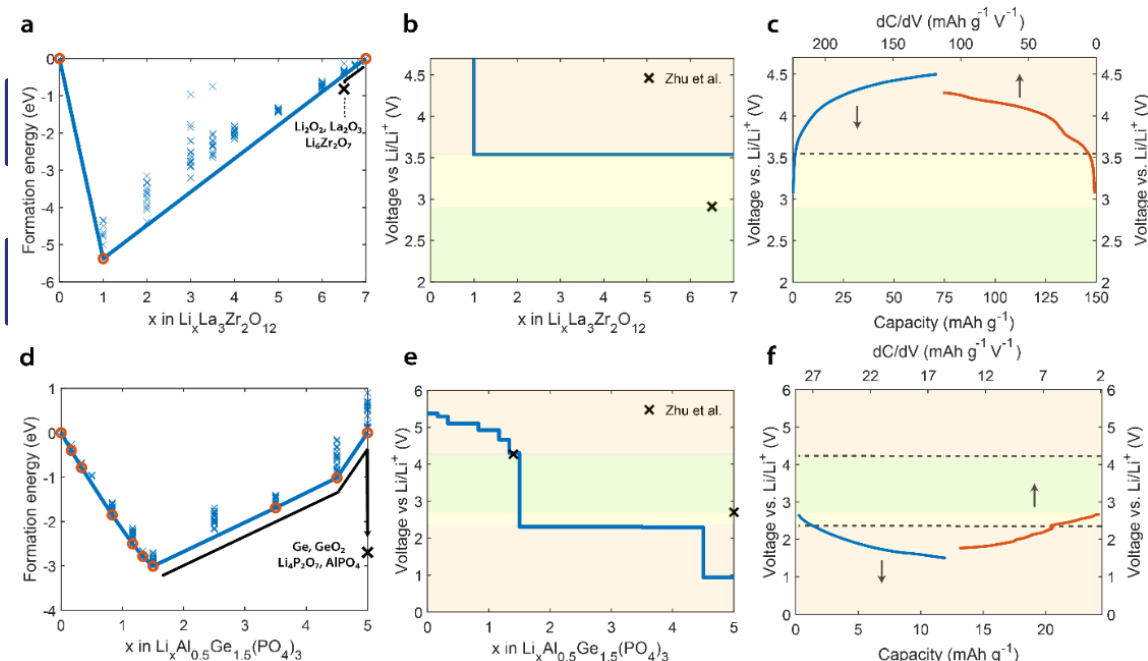


**Figure 8 | Formation energies of Li-vacancy configurations of garnet  $\text{Li}_x\text{La}_3\text{Zr}_2\text{O}_{12}$  (LLZO) and NASICON  $\text{Li}_{1.5}\text{Al}_{0.5}\text{Ge}_{1.5}(\text{PO}_4)_3$  (LAGP) solid electrolytes and comparison of experimental and calculated oxidation potentials.** **a,d** Formation energies per formula unit of  $\text{Li}_x\text{La}_3\text{Zr}_2\text{O}_{12}$  for  $0 \leq x \leq 7$  and for  $\text{Li}_x\text{Al}_{0.5}\text{Ge}_{1.5}(\text{PO}_4)_3$   $0 \leq x \leq 5$ . The formation energy of the decomposition products are indicated with a black cross. It is unlikely that oxidation will proceed to  $\text{Li}_1\text{La}_3\text{Zr}_2\text{O}_{12}$  as suggested by the convex hull, because several compositions between  $x=7$  and  $x=6$  (in  $\text{Li}_x\text{La}_3\text{Zr}_2\text{O}_{12}$ ) are located marginally above the convex hull. This suggests that in the presence of slightly higher potentials ( $>3.54$  V), oxidation will lead to indirect decomposition via  $x=6.5$ , towards the predicted stable decomposition products  $\text{Li}_2\text{O}_2$ ,  $\text{La}_2\text{O}_3$  and  $\text{Li}_6\text{Zr}_2\text{O}_7$ <sup>14</sup>. **b,e** The calculated voltage based on the convex hull of  $\text{Li}_x\text{La}_3\text{Zr}_2\text{O}_{12}$  and  $\text{Li}_x\text{Al}_{0.5}\text{Ge}_{1.5}(\text{PO}_4)_3$ . The blue line represents the redox potentials of the solid electrolytes, and the potentials for direct oxidation/reduction into the decomposition products are indicated with a black cross<sup>14</sup>. The green area indicates the stability window assuming direct decomposition, defined by the black cross, and yellow the extended stability window based on the presently proposed indirect decomposition via (de)lithiation of the solid electrolyte. **c,f** Experimental voltage curve and differential capacity upon first oxidation of a Li|Liquid-Electrolyte|LLZO-C battery and first reduction of a Li|Liquid-Electrolyte|LAGP-C battery. The differential capacity shows that oxidation of LLZO occurs around 3.6 V and reduction of LAGP occurs around 2.4 V, both in good agreement with the predicted stability window based on the indirect decomposition via (de)lithiation of the solid electrolytes. The specific capacities are calculated based on the weight of LLZO and LAGP respectively. Notably, the reduction of LLZO and the oxidation of LAGP are not

considered at present because both the indirect and direct reduction result in practically the same potential, making it impossible to discriminate between the two different mechanisms.

As solid electrolytes are designed for high ionic conductivity, the activation energies for oxidation and reduction reactions, associated with delithiation and lithiation respectively, can be expected to be small. The resulting metastable solid electrolyte compositions provide a kinetically facile reaction intermediate, providing an indirect pathway towards the more stable solid electrolyte decomposition products. As a consequence, the electrochemical stability window is determined by the solid electrolyte oxidation and reduction potentials (S and P redox for argyrodite and several other thiophosphate based solid electrolytes, O and Zr redox for LLZO and O and P redox for LAGP), and not by the stability of the most stable solid electrolyte decomposition products. The consequence of this indirect thermodynamic pathway, is that the electrochemical stability window is generally wider than that based on only on the stability of the decomposition products. Based on this mechanism, the design of stable solid electrolytes and their interfaces should focus on maximizing (de)lithiation redox potentials of the solid electrolytes. The demonstrated relation between the solid electrolyte electrochemical stability window and the redox reactions of the electrolyte, are decisive for the performance of solid state batteries and provide understanding that will contribute to the design electrolyte-electrode interfaces in ASSBs.

### 2.3 Methods

**Synthesis of materials:** Argyrodite  $\text{Li}_6\text{PS}_5\text{Cl}$  (LPSC) was synthesised as described in detail elsewhere<sup>42</sup>. Appropriate amounts of  $\text{Li}_2\text{S}$  (99.9%, Alfa Aesar),  $\text{P}_2\text{S}_5$  (99%, Sigma-Aldrich) and  $\text{LiCl}$  (99.0%, Sigma-Aldrich) were ball-milled at 110 rpm for 2 h under argon atmosphere. The mixture was then transferred to quartz tubes and annealed at 550 °C for 15 h in order to get the pure phase of the argyrodite  $\text{Li}_6\text{PS}_5\text{Cl}$  (Supplementary Fig. 8).

**Solid-state battery assembly and electrochemical cycling:** The electrode mixture was prepared by ball milling argyrodite with carbon (Super P, TIMCAL) and carbon nanofibers (Sigma Aldrich) in a weight ratio of 0.70 : 0.15 : 0.15 for 6 h at 450 rpm in a ZrO<sub>2</sub> coated stainless steel jar with 8 ZrO<sub>2</sub> balls. The solid electrolyte and electrodes were then cold pressed under 4 tons/cm<sup>2</sup> in a solid-state cell. In a cell, 10 mg of LPSC-C electrode was used and pressed against 180 mg of electrolyte<sup>42,43</sup>. Cycling was performed in an argon filled glove box, in order to avoid reactions with oxygen and moisture. The ASSBs were cycled galvanostatically with a current density of 5.5 mA/cm<sup>2</sup> within a voltage window of 0 – 3 V vs. In for In|LPSC|LPSC-C, 0 – 1 V vs. Li/In for Li-In|LPSC|LPSC-C and 0 – 2.5 V for LPSC-C|LPSC|LPSC-C respectively. To evaluate the practical electrochemical stability window more accurately, the differential capacity is determined from the 1<sup>st</sup> charge of the In|LPSC|LPSC-C battery and from the 1<sup>st</sup> discharge of the Li-In|LPSC|LPSC-C battery. Often cyclic voltammetry (CV) is used to determine the experimental stability window. However, the relatively short exposure time to the decomposition potentials in combination with the typically sluggish decomposition reactions make it challenging to evaluate the electrochemical stability window with CV cycling. In contrast, the differential capacity, determined from the slow galvanostatic charge and discharge profiles of individual oxidation and reduction processes is effective in determining the practical electrochemical stability window, in particular when the solid electrolyte is used as an active electrode material. To measure the oxidative and reductive stability of LLZO and LAGP an NMP (Sigma Aldrich) based electrode slurry was prepared by ball-milling active material (LLZO Ta-doped, D50 = 400 – 600 nm, Ampcera™, LAGP, Ampcera™), with carbon black (Super P, TIMCAL), PVDF binder (polyvinylidene fluoride, Solef® PVDF, Solvay ) in weight ratio 0.4 : 0.5 : 0.1 for 90 min at 250 rpm in ZrO<sub>2</sub> coated stainless steel jar with 8 ZrO<sub>2</sub> balls. A blank test was prepared using carbon black (Super P, TIMCAL) as active material and PVDF as a binder in the weight ratio 0.9 : 0.1 to result in the

same carbon black loading as the LLZO and LAGP electrodes. The slurry was cast on Al foil with a thickness of 100  $\mu\text{m}$  and dried at 60°C in vacuum oven for 12h. The loading of the LLZO, LAGP and carbon electrodes was 1.6  $\text{mg}/\text{cm}^2$ , 1.0  $\text{mg}/\text{cm}^2$  and 0.6  $\text{mg}/\text{cm}^2$  respectively. The coin cells were assembled in an argon filled glove box, in order to avoid reactions with oxygen and moisture (< 0.1 ppm  $\text{O}_2$  and < 2 ppm  $\text{H}_2\text{O}$ ) using both a polymer (Celgard 2250) and glass fiber (Whatman) separator and lithium metal as a counter electrode (Sigma Aldrich), which is washed with dimethyl carbonate (DMC) to remove the oxide layer and 400  $\mu\text{l}$  of 1.0 M  $\text{LiPF}_6$  in 1:1 v/v ethylene carbonate (EC) and diethyl carbonate (DEC) (<15 ppm  $\text{H}_2\text{O}$ , Sigma Aldrich) was added as an electrolyte for wetting both working and counter electrode surfaces. Galvanostatic oxidation was performed with cut-off voltage of 4.5 V (vs.  $\text{Li}/\text{Li}^+$ ) for first oxidation (LLZO-C) and 1.5 V (vs.  $\text{Li}/\text{Li}^+$ ) for first reduction (LAGP-C) with 12 hours of rest and charge/discharge current of 7.0  $\mu\text{A}$ . Comparison of the galvanostatic oxidation and reduction of the LLZO-C and LAGP-C electrodes and blank electrode are provided in Supplementary Fig. 7a,b. With the solid electrolyte – carbon mixtures, very large interface areas are achieved (for the current particle sizes  $\gg 1 \text{ m}^2$ ) making the effective current densities at least 4 orders of magnitude lower than the current densities based on the electrode diameter.

**X-ray diffraction:** In order to identify the crystalline phases of the prepared materials, powder XRD patterns were collected in the  $2\theta$  range of 10–120° using  $\text{Cu K}\alpha$  X-rays (1.5406 Å at 45 kV and 40 mA) on an X'Pert Pro X-ray diffractometer (Panalytical). The samples were tested in an airtight sample holder, filled with argon, to prevent exposure to oxygen and moisture.

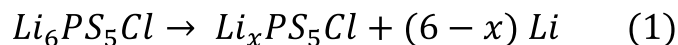
**Solid state nuclear magnetic resonance:** NMR measurements were performed using a Bruker Ascend 500 MHz spectrometer equipped with two and three channel 4.0 mm and 3.2 mm Magic Angle Spinning (MAS) probes respectively. The operating frequencies for  $^{31}\text{P}$  and  $^6\text{Li}$  were 202.47 and 73.60 MHz respectively, and all measurements were performed within a

spinning speed range of 8 to 23 kHz and  $\pi/2$  pulse lengths of 4 – 5  $\mu\text{s}$  were determined for  $^6\text{Li}$  and  $^{31}\text{P}$ . The chemical shifts of  $^6\text{Li}$  spectra were referenced with respect to a 0.1M LiCl solution, and  $^{31}\text{P}$  spectra with respect to an 85%  $\text{H}_3\text{PO}_4$  solution. Based on the  $T_1$  relaxation time, recycle delays of 5-10000 s were utilised collecting between 128 and 11264 scans for each sample.

**Computational details: (all this part done by Tammo Schwietert):**

Argyrodite  $\text{Li}_x\text{PS}_5\text{Cl}$  crystallises in the  $F\bar{4}3m$  space group and at  $x = 6$  has 50 % of the 48h crystallographic Li positions randomly occupied<sup>6</sup>. The starting structure of the argyrodite was obtained from literature, where a thorough investigation of the most stable configuration was performed taking into account the halogen disorder<sup>44</sup>. By calculating the energies of the symmetrically non-equivalent Li configurations, the most stable  $\text{Li}_x\text{PS}_5\text{Cl}$  configurations are obtained, from which the voltage at which these phases are formed can be determined.

To determine the energy properties of crystalline phases, Density Functional Theory (DFT) relaxations were performed with the Vienna Ab-Initio Simulation Package (VASP)<sup>45</sup>. The PBE exchange correlation functional of Perdew et al. was implemented<sup>46</sup>, and core electrons were probed with the projected-augmented wave approach (PAW)<sup>47</sup>. A cut-off value of 280 eV and a 4 x 4 x 4 k-point mesh were used. For the argyrodite, the following reaction is considered:



If  $x < 6$  Li  $\text{Li}_6\text{PS}_5\text{Cl}$  is oxidised, if  $x > 6$   $\text{Li}_6\text{PS}_5\text{Cl}$  is reduced. Then, by calculating the energies on both sides of the reaction and taking the electrochemical potential of Li into account,

$$\bar{\mu}_{\text{Li}} = \mu_{\text{Li}} - \phi \quad (2)$$

with  $\bar{\mu}_{\text{Li}}$  the electrochemical potential of Li,  $\mu_{\text{Li}}$  the chemical potential of Li, and  $\phi$  the electrical potential. Therefore, the average electrical potential at which oxidation/reduction takes place can be determined by:

$$\bar{\phi} = - \frac{E(\text{Li}_6\text{PS}_5\text{Cl}) - E(\text{Li}_x\text{PS}_5\text{Cl}) - (6 - x) E(\text{Li})}{6 - x} \quad (3)$$

Where  $E(\text{Li}_x\text{PS}_5\text{Cl})$  represents the composition of the most stable configurations on the convex hull. DFT based Molecular Dynamics (MD) simulations were performed using the same cut-off value as in DFT simulations. The ab initio MD simulations were executed in the NVT ensemble, where the temperature scales every 1000 time steps. The simulations use periodic boundary conditions with time steps of 2 fs, the total time of the MD simulations being 100 ps. The number of k-points was reduced from 4 x 4 x 4 used in the DFT simulations to 1 x 1 x 1 for the MD simulations. The lattice parameters and positions of all atoms were allowed to relax during relaxation.

The argyrodite structure was obtained from previous work<sup>44</sup>. There the Cl-S disorder over the 4a and 4c sites was investigated, and the thermodynamically most favourable configuration was obtained. Note that the Cl-S disorder is kept constant in the presented convex hull and thus the oxidation and reduction voltages are not affected. For determination of configurations as a function of the Li-concentration, 10000 structures are created by placing the appropriate amount of Li-ions randomly at the 48h-positions. To quickly scan these for possible low-energy structures only the electrostatic energies in these structures were calculated, using the Undamped Shifted Force method with a cut-off radius of 15 Angstrom<sup>48</sup>. For the 20 lowest energy configurations of the electrostatic calculations the structure was optimised and the energy was calculated using VASP. For  $\text{Li}_x\text{PS}_5\text{Cl}$   $12 \leq x \leq 15$  extra Li atoms are inserted on the 16e position.

All DFT calculations are performed on charge-neutral cells, thus taking into account the true oxidation and reduction of solid electrolytes, and thus behaving similar to an electrode material. The formation energies of the thermodynamic decomposition products are taken from the Materials Project database<sup>49</sup>. The structure of LLZO is obtained from the Materials

Project database<sup>49</sup>. For LLZO a 1 x 1 x 1 k-point mesh was used with a cut-off value of 500 eV. The structure of LAGP is taken from literature<sup>50</sup> and was relaxed using a 3 x 3 x 1 k-point mesh with a cut-off value of 500 eV.

## 2.4 References

- 1 Kim, J. G. *et al.* A review of lithium and non-lithium based solid state batteries. *Journal of Power Sources* **282**, 299-322, doi:10.1016/j.jpowsour.2015.02.054 (2015).
- 2 Zhang, Z. *et al.* New horizons for inorganic solid state ion conductors. *Energy & Environmental Science* **11**, 1945-1976, doi:10.1039/c8ee01053f (2018).
- 3 Janek, J. & Zeier, W. G. A solid future for battery development. *Nature Energy* **1**, 16141 (2016).
- 4 Zheng, F., Kotobuki, M., Song, S., Lai, M. O. & Lu, L. Review on solid electrolytes for all-solid-state lithium-ion batteries. *J. Power Sources* **389**, 198-213 (2018).
- 5 Fergus, J. W. Ceramic and polymeric solid electrolytes for lithium-ion batteries. *Journal of Power Sources* **195**, 4554-4569 (2010).
- 6 Yu, C., van Eijck, L., Ganapathy, S. & Wagemaker, M. Synthesis, structure and electrochemical performance of the argyrodite Li<sub>6</sub>PS<sub>5</sub>Cl solid electrolyte for Li-ion solid state batteries. *Electrochimica Acta* **215**, 93-99 (2016).
- 7 Famprakis, T., Canepa, P., Dawson, J. A., Islam, M. S. & Masquelier, C. Fundamentals of inorganic solid-state electrolytes for batteries. *Nat. Mater* (2019).
- 8 Kamaya, N. *et al.* A lithium superionic conductor. *Nature Materials* **10**, 682-686 (2011).
- 9 Ohta, S., Kobayashi, T. & Asaoka, T. High lithium ionic conductivity in the garnet-type oxide Li<sub>7-X</sub>La<sub>3</sub>(Zr<sub>2-X</sub>, NbX)O<sub>12</sub> (X = 0-2). *Journal of Power Sources* **196**, 3342-3345 (2011).
- 10 Boulineau, S., Courty, M., Tarascon, J.-M. & Viallet, V. Mechanochemical synthesis of Li-argyrodite Li<sub>6</sub>PS<sub>5</sub>X (X = Cl, Br, I) as sulfur-based solid electrolytes for all solid state batteries application. *Solid State Ionics* **221**, 1-5 (2012).
- 11 Kato, Y. *et al.* High-power all-solid-state batteries using sulfide superionic conductors. *Nature Energy* **1**, 16030 (2016).
- 12 Lotsch, B. V. & Maier, J. Relevance of solid electrolytes for lithium-based batteries: A realistic view. *J. Electroceram.* **38**, 128-141 (2017).
- 13 Tian, Y. *et al.* Compatibility issues between electrodes and electrolytes in solid-state batteries. *Energy Environ. Sci.* **10**, 1150-1166 (2017).
- 14 Zhu, Y., He, X. & Mo, Y. Origin of Outstanding Stability in the Lithium Solid Electrolyte Materials: Insights from Thermodynamic Analyses Based on First-Principles Calculations. *ACS Applied Materials & Interfaces* **7**, 23685-23693 (2015).
- 15 Richards, W. D., Miara, L. J., Wang, Y., Kim, J. C. & Ceder, G. Interface Stability in Solid-State Batteries. *Chemistry of Materials* **28**, 266-273 (2016).
- 16 Han, F., Gao, T., Zhu, Y., Gaskell, K. J. & Wang, C. A Battery Made from a Single Material. *Advanced Materials* **27**, 3473-3483 (2015).



- 17 Zhang, W. *et al.* The Detrimental Effects of Carbon Additives in Li<sub>10</sub>GeP<sub>2</sub>S<sub>12</sub>-Based Solid-State Batteries. *ACS Appl. Mater. Interfaces* **9**, 35888-35896 (2017).
- 18 Han, F. *et al.* High electronic conductivity as the origin of lithium dendrite formation within solid electrolytes. *Nature Energy* **4**, 187-196 (2019).
- 19 Han, F., Zhu, Y., He, X., Mo, Y. & Wang, C. Electrochemical Stability of Li<sub>10</sub>GeP<sub>2</sub>S<sub>12</sub> and Li<sub>7</sub>La<sub>3</sub>Zr<sub>2</sub>O<sub>12</sub> Solid Electrolytes. *Advanced Energy Materials* **6**, 1501590 (2016).
- 20 Koerver, R. *et al.* Redox-active cathode interphases in solid-state batteries. *Journal of Materials Chemistry A* **5**, 22750-22760 (2017).
- 21 Hakari, T. *et al.* Structural and Electronic-State Changes of a Sulfide Solid Electrolyte during the Li Deinsertion–Insertion Processes. *Chemistry of Materials* **29**, 4768-4774 (2017).
- 22 Wenzel, S., Sedlmaier, S. J., Dietrich, C., Zeier, W. G. & Janek, J. Interfacial reactivity and interphase growth of argyrodite solid electrolytes at lithium metal electrodes. *Solid State Ionics* **318**, 102-112 (2018).
- 23 Auvergniot, J. *et al.* Interface Stability of Argyrodite Li<sub>6</sub>PS<sub>5</sub>Cl toward LiCoO<sub>2</sub>, LiNi<sub>1/3</sub>Co<sub>1/3</sub>Mn<sub>1/3</sub>O<sub>2</sub>, and LiMn<sub>2</sub>O<sub>4</sub> in Bulk All-Solid-State Batteries. *Chemistry of Materials* **29**, 3883-3890 (2017).
- 24 Lau, J. *et al.* Sulfide Solid Electrolytes for Lithium Battery Applications. *Advanced Energy Materials* **8** (2018).
- 25 Tan, D. H. S. *et al.* Elucidating Reversible Electrochemical Redox of Li<sub>6</sub>PS<sub>5</sub>Cl Solid Electrolyte. *ACS Energy Letters* **4**, 2418-2427 (2019).
- 26 Deiseroth, H.-J. *et al.* Li<sub>6</sub>PS<sub>5</sub>X: A class of crystalline Li-rich solids with an unusually high Li<sup>+</sup> mobility. *Angew. Chem.* **47**, 755-758 (2008).
- 27 Auvergniot, J. *et al.* Redox activity of argyrodite Li<sub>6</sub>PS<sub>5</sub>Cl electrolyte in all-solid-state Li-ion battery: An XPS study. *Solid State Ionics* **300**, 78-85 (2017).
- 28 Aydinol, M. K., Kohan, A. F. & Ceder, G. Ab initio calculation of the intercalation voltage of lithium-transition-metal oxide electrodes for rechargeable batteries. *Journal of Power Sources* **68**, 664-668 (1997).
- 29 Aydinol, M. K., Kohan, A. F., Ceder, G., Cho, K. & Joannopoulos, J. Ab initio study of lithium intercalation in metal oxides and metal dichalcogenides. *Physical Review B* **56**, 1354-1365 (1997).
- 30 Mayo, M., Griffith, K. J., Pickard, C. J. & Morris, A. J. Ab Initio Study of Phosphorus Anodes for Lithium- and Sodium-Ion Batteries. *Chemistry of Materials* **28**, 2011-2021 (2016).
- 31 Ramireddy, T. *et al.* Phosphorus–carbon nanocomposite anodes for lithium-ion and sodium-ion batteries. *Journal of Materials Chemistry A* **3**, 5572-5584 (2015).
- 32 Hakari, T., Nagao, M., Hayashi, A. & Tatsumisago, M. All-solid-state lithium batteries with Li<sub>3</sub>PS<sub>4</sub> glass as active material. *Journal of Power Sources* **293**, 721-725 (2015).
- 33 Larson, A. C. & Von Dreele, R. B. General Structure Analysis System (GSAS). (Los Alamos National Laboratory, Los Alamos, NM 87545, 2004).
- 34 Deiseroth, H. J. *et al.* Li<sub>6</sub>PS<sub>5</sub>X: A Class of Crystalline Li-Rich Solids With an Unusually High Li<sup>+</sup> Mobility. *Angewandte Chemie International Edition* **47**, 755-758 (2008).

- 35 Dietrich, C. *et al.* Local Structural Investigations, Defect Formation, and Ionic Conductivity of the Lithium Ionic Conductor  $\text{Li}_4\text{P}_2\text{S}_6$ . *Chem. Mater.* **28**, 8764-8773 (2016).
- 36 Dietrich, C. *et al.* Lithium ion conductivity in  $\text{Li}_2\text{S}-\text{P}_2\text{S}_5$  glasses – building units and local structure evolution during the crystallization of superionic conductors  $\text{Li}_3\text{PS}_4$ ,  $\text{Li}_7\text{P}_3\text{S}_{11}$  and  $\text{Li}_4\text{P}_2\text{S}_7$ . *J. Mater. Chem. A* **5**, 18111-18119 (2017).
- 37 Murakami, M. *et al.* Dynamical Origin of Ionic Conductivity for  $\text{Li}_7\text{P}_3\text{S}_{11}$  Metastable Crystal As Studied by  $^6/7\text{Li}$  and  $^{31}\text{P}$  Solid-State NMR. *J. Phys. Chem. C* **119**, 24248-24254 (2015).
- 38 Meyer, B. M., Leifer, N., Sakamoto, S., Greenbaum, S. G. & Grey, C. P. High field multinuclear NMR investigation of the SEI layer in lithium rechargeable batteries. *Electrochem. Solid State Lett.* **8**, A145-A148 (2005).
- 39 Stöfler, H. *et al.* Amorphous versus Crystalline  $\text{Li}_3\text{PS}_4$ : Local Structural Changes during Synthesis and Li Ion Mobility. *The Journal of Physical Chemistry C* **123**, 10280-10290 (2019).
- 40 Yu, C. *et al.* Accessing the bottleneck in all-solid state batteries, lithium-ion transport over the solid-electrolyte-electrode interface. *Nature Communications* **8** (2017).
- 41 Zhang, W. *et al.* (Electro)chemical expansion during cycling: monitoring the pressure changes in operating solid-state lithium batteries. *Journal of Materials Chemistry A* **5**, 9929-9936 (2017).
- 42 Yu, C. *et al.* Facile Synthesis toward the Optimal Structure-Conductivity Characteristics of the Argyrodite  $\text{Li}_6\text{PS}_5\text{Cl}$  Solid-State Electrolyte. *ACS applied materials & interfaces* **10**, 33296-33306 (2018).
- 43 Yu, C. *et al.* Tailoring  $\text{Li}_6\text{PS}_5\text{Br}$  ionic conductivity and understanding of its role in cathode mixtures for high performance all-solid-state Li-S batteries. *J. Mater. Chem. A* **7**, 10412-10421 (2019).
- 44 de Klerk, N. J. J., Rostóń, I. & Wagemaker, M. Diffusion Mechanism of Li Argyrodite Solid Electrolytes for Li-Ion Batteries and Prediction of Optimized Halogen Doping: The Effect of Li Vacancies, Halogens, and Halogen Disorder. *Chemistry of Materials* **28**, 7955-7963 (2016).
- 45 Kresse, G. & Hafner, J. Ab initio molecular dynamics for liquid metals. *Physical Review B* **47**, 558-561 (1993).
- 46 Perdew, J. P., Burke, K. & Wang, Y. Generalized gradient approximation for the exchange-correlation hole of a many-electron system. *Physical Review B* **54**, 16533-16539 (1996).
- 47 Blöchl, P. E. Projector augmented-wave method. *Physical Review B* **50**, 17953-17979 (1994).
- 48 Fennell, C. J. & Gezelter, J. D. Is the Ewald summation still necessary? Pairwise alternatives to the accepted standard for long-range electrostatics. *J. Chem. Phys.* **124**, 234104 (2006).
- 49 Jain, A. *et al.* Commentary: The Materials Project: A materials genome approach to accelerating materials innovation. **1**, 011002 (2013).

- 50 Kang, J., Chung, H., Doh, C., Kang, B. & Han, B. Integrated study of first principles calculations and experimental measurements for Li-ionic conductivity in Al-doped solid-state  $\text{LiGe}_2(\text{PO}_4)_3$  electrolyte. *Journal of Power Sources* **293**, 11-16 (2015).



# 3

---

Operando X-ray diffraction of Si particles in metal oxides for negative electrodes in Li-ion batteries

---

### Abstract

The challenge of high capacity Si negative electrodes for Li-ion batteries is to achieve a long cycle life. One of the detrimental processes that shortens the cycle life is electrolyte decomposition. This is a result of continuous solid electrolyte interphase formation, due to large volumetric changes upon (de)lithiation, effectively resulting in contact loss and mechanical failure. A less known factor is the homogeneity of the Li storage throughout the Si electrodes. Inhomogeneous lithiation will lead to large local volumetric changes, that can be expected to accelerate the detrimental processes. In this study we investigate the role of protective conformal TiO<sub>2</sub> coatings on Si particles in improving its cycle life. Si nanoparticles are coated with a conformal 5 nm TiO<sub>2</sub> coating through Atomic Layer Deposition. Operando X-Ray Diffraction during deep discharge of Si reveals that the reduction of the TiO<sub>2</sub> coating is restricted, resulting in a solid solution composition of Li<sub>x</sub>TiO<sub>2</sub>, with  $x \approx 0.12$ . The reasonable Li-ion conductivity of this phase is beneficial for Li-ion transport through the electrodes, whereas its limited electronic conductivity is expected to suppress SEI formation. With TEM, the TiO<sub>2</sub> coating is observed to become amorphous, which appears to suppress crack formation upon the volumetric changes of the Si electrode. With operando neutron depth profiling, it is demonstrated that in the uncoated Si, the lithiation takes place inhomogeneously throughout the Si electrodes, whereas the Li<sub>0.12</sub>TiO<sub>2</sub> coating results in a more homogeneous lithiation as a function of electrode depth. Thus, the results suggest that the improved performance and more homogeneous lithiation of the coated Si is not only a consequence of acting as artificial SEI, but also a result of its Li-conducting properties resulting in more homogeneous lithiation of the Si electrode.

### 3.1 Introduction

In order to meet today's energy needs, it is important to develop higher energy density materials to replace graphite at the negative electrode of Li-ion batteries. Si is a promising candidate given its high theoretical energy density of  $3579 \text{ mAhg}^{-1}$ <sup>1,2</sup>. Nonetheless, the commercial use of Si is limited due to several issues, such as pulverisation of the Si particles caused by the volume expansion when it is repeatedly (de)lithiated<sup>3</sup>, the high irreversible capacity loss<sup>4,5</sup>, and isolation of the particles caused by the formation of the solid electrolyte interphase (SEI) due to the decomposition of the electrolyte at the surface of the Si particles<sup>6,7</sup>. To mitigate the mechanical effects associated with electrochemical lithiation, nanostructured Si has been intensively studied, showing improved performance. It has been established that a particle diameter of  $\sim 150 \text{ nm}$  is optimal, balancing detrimental surface reactions with faster Li transport and facile strain relaxation<sup>8</sup>. Another approach to mitigate the issues of volume expansion and high reactivity with the liquid electrolyte is the use of protective coatings. They function as an artificial SEI that should be conductive both for electrons and Li-ions<sup>9</sup>. Evidently, the improvements are related to the nature of the formed SEI layer. However, it is unclear how the SEI is preserved and survives the stress induced by the volume changes occurring during cycling to unequivocally prove the buffering effect of such coatings<sup>10,11</sup>. Anatase  $\text{TiO}_2$  has been studied both as a negative electrode material, as well as a potential coating material for Li-ion battery electrodes due to its high structural stability. This is a consequence of the small volume changes it undergoes upon lithiation and delithiation ( $<4\%$ ). This is beneficial for example, for the adhesion of a  $\text{TiO}_2$  coating on a Si nanoparticle. Additionally,  $\text{TiO}_2$  coatings on Si have been reported to passivate detrimental reactions, resulting in better cyclability and significantly lower electrolyte decomposition compared to bare Si<sup>12</sup>. The redox potential of  $\text{TiO}_2$  towards (de)lithiation is between 1 and 3 V vs.  $\text{Li/Li}^+$  and it was previously reported that the cycling

stability of  $\text{TiO}_2$  is not affected by extending the potential range down to 0.1 V<sup>13-15</sup>. Li intercalation in the anatase phase of  $\text{TiO}_2$  is usually restricted to  $\text{Li}_{x=0.55}\text{TiO}_2$ , but it has been shown to reach  $x = 1$  for amorphous  $\text{TiO}_2$  and for very small anatase particles ( $\approx 7$  nm), turning the material from an insulator into an electronic conductor and to a very poor Li-ion conductor<sup>16,17</sup>.

In this chapter, we try to understand the mechanism by which thin conformal anatase  $\text{TiO}_2$  coatings on Si nanoparticles improve its performance in Li-ion batteries in comparison with bare uncoated Si. During discharge, lithiation of the 5 nm thin  $\text{TiO}_2$  coatings is expected to lead to blocking of the Li-ion transport<sup>16,17</sup>. From this perspective, it is surprising that thin  $\text{TiO}_2$  coatings lead to improved Si electrode cycling performance in combination with a reasonable composite diffusivity of  $10^{-12}$ – $10^{-13}$   $\text{cm}^2 \text{s}^{-1}$ <sup>18,19</sup>. To better understand this phenomenon we investigate the nature of the lithiated state of the  $\text{TiO}_2$  coating on Si with operando Neutron Depth Profiling (NDP) and X-ray diffraction (XRD). Operando NDP<sup>20,21</sup> offers the possibility to monitor the Li distribution quantitatively and non-destructively and to monitor Li-ion transport, electrode activity and irreversible capacity loss as a function of electrode depth<sup>22-24</sup>. This allows the investigation of the homogeneity of the lithiation of the electrode as a function of depth, reflecting the charge transport within the electrode, as well as the distribution of Li-containing decomposition products. The findings demonstrate that the  $\text{TiO}_2$  coating results in a more homogeneous activity of the Si electrode material and less formation of irreversible Li-species in the SEI. From operando XRD it can be determined that the Li-composition of the  $\text{TiO}_2$  coating is restricted to  $\text{Li}_{0.12}\text{TiO}_2$  which is suggested to be the a consequence of the interface constraints posed by the Si particles. This composition is known to be an reasonable Li-conducting phase<sup>25</sup>, providing Li-ion diffusion paths through the electrode, rationalizing the more homogeneous activation of the Si electrode material, which is argued to play a prominent role in the improved cycle life of the  $\text{TiO}_2$  coated materials.

## 3.2 Results and discussion

### 3.2.1 Deposition method

As discussed above, for this study, titanium dioxide ( $\text{TiO}_2$ ) is applied as a coating material for Si nanoparticles ( $\text{n-Si}$ )<sup>15,26</sup>. Atomic Layer Deposition (ALD) is utilised for the surface modification of  $\text{n-Si}$  in order to get thin and conformal  $\text{TiO}_2$  coatings<sup>27</sup>. The thickness of the coating can be controlled by setting the number of deposition cycles. Moreover, ALD is a low temperature process, resulting in the deposition of amorphous  $\text{TiO}_2$  coatings. Here various coated  $\text{n-Si}$  samples are prepared using an increasing number of ALD cycles corresponding to coating thicknesses of 0.5, 1, 3, 5 and 20 nm. Henceforth the samples will be referred as  $\text{n-Si/a-TiO}_2\text{-ALD-x}$ , i.e. Si nanoparticles coated with x nm amorphous  $\text{TiO}_2$  using ALD deposition.

3

### 3.2.2 Characterisation of $\text{TiO}_2$ coated Si using Inductive Coupled Plasma and Transmission Electron Microscopy

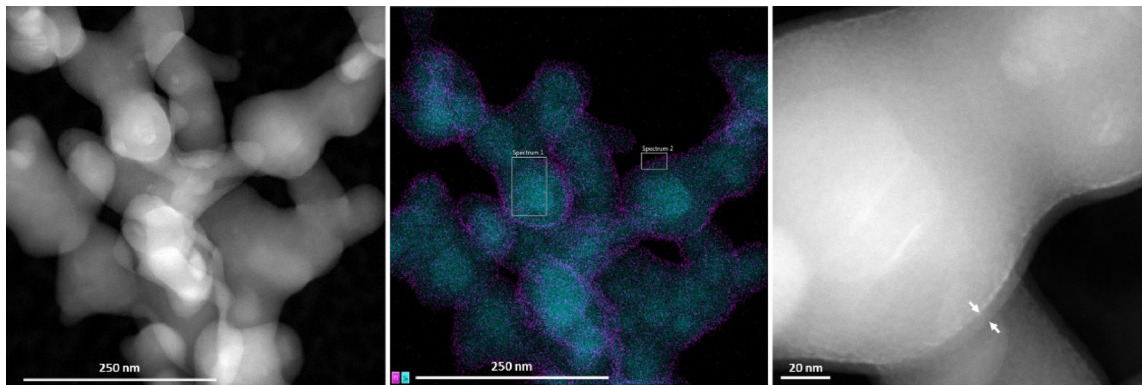


**Figure 1 | a)** Transmission electron microscopy image of ALD coated samples ( $\text{n-Si/a-TiO}_2\text{-ALD-5}$ ) **b)** and corresponding EDX mapping images of elemental Si, Ti shown in blue and magenta respectively **c)** Magnified image of  $\text{TiO}_2$  coating having thickness of around 4 nm.

To characterise the uniformity of the coating, Transmission Electron Microscopy (TEM) with Energy Dispersive X-Ray Analysis (EDX) was applied (**Fig. 1**). As shown in **Figure 1a**, the particle size distribution for  $\text{n-Si}$  is  $\sim 80$



nm. From the EDX map given in **Figure 1b**, it can be seen that the signal corresponding to Ti at the surface, encapsulates Si, clearly demonstrating a core-shell structure with a homogeneous distribution of thin a TiO<sub>2</sub> layer on the Si surface. A magnified Si particle with a visible coating (n-Si/a-TiO<sub>2</sub>-ALD-5) is shown in **Figure 1c**, where a ~4 nm coating thickness can be seen. That is close to the 5 nm thickness of the TiO<sub>2</sub> coating expected from the number of ALD cycles.

To verify that the crystallinity of Si after the ALD process is preserved, XRD measurements were conducted. The diffractogram's of bare n-Si and n-Si/a-TiO<sub>2</sub>-ALD1, -3, and -5 obtained are given in **Supplementary B Figure 1**. All the samples have identical diffraction peaks at  $2\theta = 28.3, 47.3, 56.1, 69.2, 76.6^\circ$ , indexed as (111), (220), (311), (400), and (331) planes of cubic Si. The absence of visible changes of Si diffraction peaks suggest that TiO<sub>2</sub> does not influence the Si structure. Rietveld refinement of the diffraction patterns was also performed (**Supplementary B Figure 1, Supplementary B Table 1**), where the lattice parameters, fractional atomic coordinates, isotropic atomic displacement and site occupancies were refined at room temperature for n-Si and n-Si/a-TiO<sub>2</sub>-ALD-1, -3 and -5. No significant changes in the lattice parameters and the average crystallite size (determined from the peak width) were observed after the coating process. In addition, no diffraction peaks of any crystalline TiO<sub>2</sub> polymorph were observed. This indicates that the crystallinity and/or content of the TiO<sub>2</sub> coating is low. Nevertheless for all the XRD patterns an underlying background is seen at low diffraction angles. This is a typical indication of the presence of amorphous phases, which in this case could be either amorphous TiO<sub>2</sub> or silica.

## 3.2.3 Electrochemical cycling of Si with different coatings

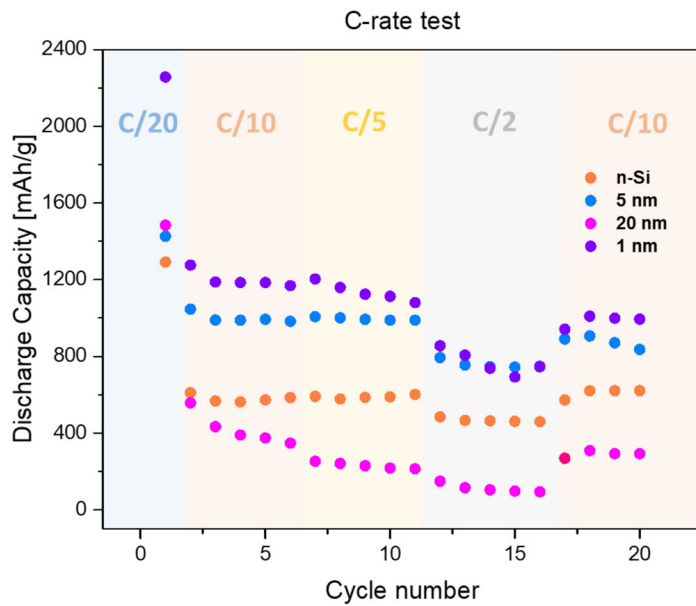


**Figure 2 | Comparison of rate capabilities** of n-Si and n-Si/a-TiO<sub>2</sub>-ALD-1, -5, and -20. Increasing C-rates ranging from C/20 to C/2 were applied, to study the electrode response on increasing polarisation. Amorphous TiO<sub>2</sub> coatings of 1 and 5 nm are found to be optimal, giving the best cycling performance and reaching up to 1200 mAhg<sup>-1</sup>. Capacities were calculated based on Si weight, and a capacity of 1500 mAhg<sup>-1</sup>.

To evaluate the effect of the TiO<sub>2</sub> coating and its various thicknesses on the electrochemical cycling performance, coin cells were assembled according to the details given in the experimental section. Galvanostatic cycling tests at various C-rates were conducted. The specific discharge capacities obtained for different TiO<sub>2</sub> coating thicknesses at these C-rates are presented in **Figure 2**. It can be seen that the electrode always delivers a 1<sup>st</sup> irreversible capacity loss on discharge, irrespective of the coating thickness. At a low initial C-rate of C/10, n-Si with a 1 nm TiO<sub>2</sub> coating exhibits the highest specific capacity of ~1200 mAhg<sup>-1</sup> followed by n-Si with a 5 nm coating which exhibits a ~900 mAhg<sup>-1</sup> capacity. There is an appreciable drop in capacity at a higher C/2 rate, but the capacity recovers when a subsequent C/10 rate is applied, with a retained capacity of ~1000 and ~800 mAhg<sup>-1</sup> for the 1 nm and 5 nm coatings respectively after 20 cycles. The thicker 20 nm

TiO<sub>2</sub> coating on n-Si, even at slow C/10 cycling, results in a much lower specific capacity of  $\sim 600 \text{ mAhg}^{-1}$ , similar to bare uncoated n-Si. However, unlike the bare n-Si which retains its capacity on further cycling at C/5, the 20 nm TiO<sub>2</sub> coated n-Si shows a steady decline in capacity. The thickness of the coating is determined by the number of ALD cycles. The TiO<sub>2</sub> coating thickness may limit the Li-ion transport, through the limited conductivity of the TiO<sub>2</sub>, and cause the worse electrochemical performance of the n-Si with the 20 nm TiO<sub>2</sub> coating.

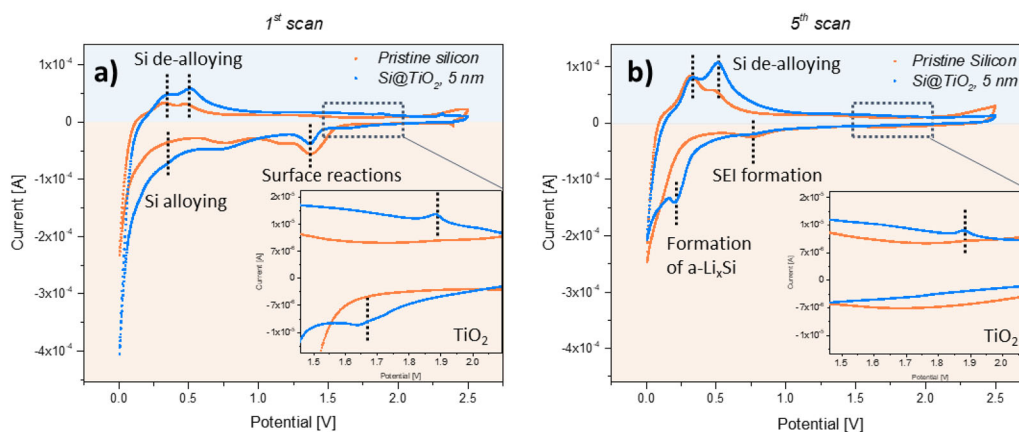


**Figure 3 | Cyclic voltammetry curves** for the a) first and b) fifth cycle of n-Si and n-Si/a-TiO<sub>2</sub>-ALD-5 at the scan rate of 0.1 mV/s between 0 – 2.5 V vs. Li/Li<sup>+</sup>.

Cyclic voltammetry was performed to understand the impact of the TiO<sub>2</sub> coating on the first (**Fig. 3a**) and fifth (**Fig. 3b**) reduction and oxidation of the n-Si and n-Si/a-TiO<sub>2</sub>-ALD-5 samples and the reductive decomposition of the electrolyte. Furthermore, the oxidation and reduction of the TiO<sub>2</sub> coating itself can be captured. By following the curve from the start of measurement (orange region), the first interesting features are observed at 1.9 and 1.7 V vs. Li/Li<sup>+</sup> (inset of **Fig. 3a**), corresponding to the lithiation and delithiation of TiO<sub>2</sub> respectively. That proves the redox activity of the anatase TiO<sub>2</sub> phase. However, as seen from the inset in **Figure 3b**, in the 5<sup>th</sup> scan, no redox activity upon TiO<sub>2</sub> lithiation. Furthermore, in **Figure 3a**, a reduction peak at 1.4 V vs. Li/Li<sup>+</sup> for both n-Si and n-Si/a-TiO<sub>2</sub>-ALD-5 is observed (however

larger for n-Si). That indicates charge consumption due to surface reactivity of metal oxides in the current collector ( $\text{Cu}_2\text{O}/\text{CuO}$ ) with Li and leads to formation of metallic  $\text{Cu}^0$  and  $\text{Li}_2\text{O}^{28}$  (indicated on the figure as surface reactions). Copper oxide reduction is only observed for the first cycle (seen from **Fig. 3a**), but not detected in 5<sup>th</sup> cycle (**Fig. 3b**). Another interesting feature in **Figure 3b** is a broad reduction peak at  $\sim 0.8$  V vs.  $\text{Li}/\text{Li}^+$ , which indicates large charge consumption due to the reduction of diethyl carbonate and ethylene carbonate, corresponding to the continuous formation of the SEI<sup>29</sup> for n-Si at 5<sup>th</sup> cycle. Hence, it can be deduced that the  $\text{TiO}_2$  layers reduce the continuous formation of an SEI due to the absence of reduction peak in the 5<sup>th</sup> cycle. Following the reduction curve, at 0.2 V vs.  $\text{Li}/\text{Li}^+$  redox activity is observed which is associated to alloying of  $\text{Si}^2$ . In the 5<sup>th</sup> scan, a distinctive reduction peak appears at around 0.2 V vs.  $\text{Li}/\text{Li}^+$  and it is attributed to the formation of an amorphous phase of  $\text{Li}_x\text{Si}$  ( $x \leq 3.75$ ) and gradual breakage of the crystalline Si framework<sup>10,30,31</sup>. The increase in the intensity of the current means that more electrons participated in this reaction, so that more Si particles became accessible for alloying.

Following an oxidation curve (blue area), a peak at 0.3 and 0.5 V vs.  $\text{Li}/\text{Li}^+$  is present and represents delithiation of  $\text{Si}^2$ . Moreover, n-Si/a- $\text{TiO}_2$ -ALD-5 after the 5<sup>th</sup> cycle, seen as an increase in the oxidation peak area at 0.5 V vs.  $\text{Li}/\text{Li}^+$  which means more electrons involved in the reaction, thus probably better activity of Si.

## 3.2.4 Morphological evolution of the coating

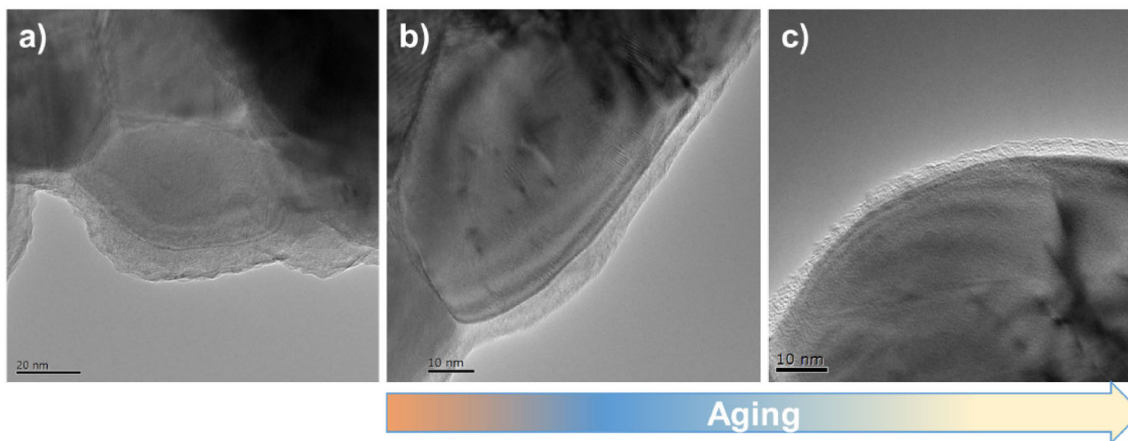


**Figure 4 | Transmission electron microscopy images of cycled electrodes** a) n-Si after 20 cycles b) n-Si/a-TiO<sub>2</sub>-ALD-5 after 1 complete cycle c) n-Si/a-TiO<sub>2</sub>-ALD-5 after 20 cycles. All images show structural integrity and no morphological changes upon cycling.

In order to assess the effect of extended electrochemical cycling on the structure and morphology of the TiO<sub>2</sub> coating, post mortem TEM measurements are performed. Images are recorded of the coated electrode (n-Si/a-TiO<sub>2</sub>-ALD-5) particles after undergoing 5 and 20 complete (dis)charge cycles and the uncoated n-Si particles after 20 (dis)charge cycles for comparison. These are shown in **Figure 4**. It can be observed from **Figure 4a**, that the surface of uncoated n-Si particles becomes rougher upon cycling. The surface of the n-Si particles are covered with nano-meter sized smaller particles, most likely corresponding to decomposition products. However, no cracks are observed on the Si surface. This can be attributed to the nano-structured nature of these Si particles which are ~ 80 nm (**Fig. 1a**), consistent with previously reported work, where it was found that 100 nm is the critical particle size needed to avoid fractures on the surface of the particle<sup>8</sup>. It can be seen from **Figure 4b and c** that the a-TiO<sub>2</sub> coating on n-Si shows robust structural stability upon cycling. No morphological changes are detected, even after 20 cycles, unlike for the uncoated n-Si, which demonstrates the integrity of the coating with the Si particle.

### 3.2.5 Structural evolution of the coating by operando XRD

The usage of Si as an electrode requires an effective charge transport network, for both electrons and Li-ions. This implies that the coating itself should also have good ionic conductivity and provide conductivity for the charge compensating electrons. The Li diffusion coefficient in Si nanoparticles coated with  $\text{TiO}_2$  has been estimated to be  $10^{-12}$ – $10^{-13}$   $\text{cm}^2 \text{s}^{-1}$ <sup>18,19</sup>. As mentioned in the introduction,  $\text{TiO}_2$  is also a potential negative electrode material for Li-ion batteries, able to intercalate Li reversibly with very small volume changes. The degree of Li insertion in the anatase phase i.e.  $\text{Li}_x\text{TiO}_2$  is usually found to be  $x < 0.55$ , but can be close to  $x = 1$  for amorphous  $\text{TiO}_2$  and for very small anatase  $\text{TiO}_2$  particles ( $\sim 7$  nm). On lithiation  $\text{TiO}_2$  turns from an insulator into an electronic conductor ( $x = 1$ ), albeit with very slow Li ion diffusion in its fully lithiated state<sup>16</sup>. This was also seen in a study performed by Wagemaker and co-workers, where the ionic conductivity of Li in lithiated anatase  $\text{Li}_x\text{TiO}_2$  was probed with NMR relaxation experiments<sup>32,33</sup>. They found that  $\text{Li}_1\text{TiO}_2$  has a reduced Li-ion mobility, based on the low hopping frequency observed,  $10^4 \text{ s}^{-1}$ , compared to  $\text{Li}_{0.5}\text{TiO}_2$  with a jump frequency of  $10^5 \text{ s}^{-1}$  at 300 K. Thereby, the  $\text{Li}_1\text{TiO}_2$  phase is limiting large anatase particles to reach their full theoretical capacity. This raises the question how the  $\text{TiO}_2$  coating deposited on Si behaves during cycling<sup>17</sup>. Cyclic voltammetry tests already demonstrated the electrochemical activity of the  $\text{TiO}_2$  coating, observed by small reduction and oxidation peaks (**Fig. 3**). However, it is not known what the composition is of the  $\text{Li}_x\text{TiO}_2$  ( $x = 0$  to 1) coating during cycling. To determine this, operando XRD is applied to monitor the structural changes of the electrode particles during electrochemical cycling. For the optimal coating thickness with respect to the cycling performance (1 to 5 nm), the reflections of the  $\text{TiO}_2$  phase were practically invisible due to the small phase fraction in the electrode. For this reason, the operando XRD experiment was performed utilizing a 20 nm coating. Moreover, as the  $\text{TiO}_2$  coating deposited with ALD

on n-Si is amorphous, it is not possible to attain any structural information with operando XRD in this polymorph. Therefore to observe structural changes both in the Si and TiO<sub>2</sub> phases, the n-Si/a-TiO<sub>2</sub>-ALD-20 was first annealed under an argon atmosphere at 450°C for 5h in order to crystallise the amorphous TiO<sub>2</sub> coating phase. The XRD pattern of the annealed sample presented in **Supplementary B Figure 2**, confirms the formation of crystalline TiO<sub>2</sub> which can be indexed to the anatase phase (referred to as n-Si/Anatase-ALD-20). Additional crystallographic details obtained from the Rietveld refinement of the XRD pattern are given in **Supplementary B Table 2**.

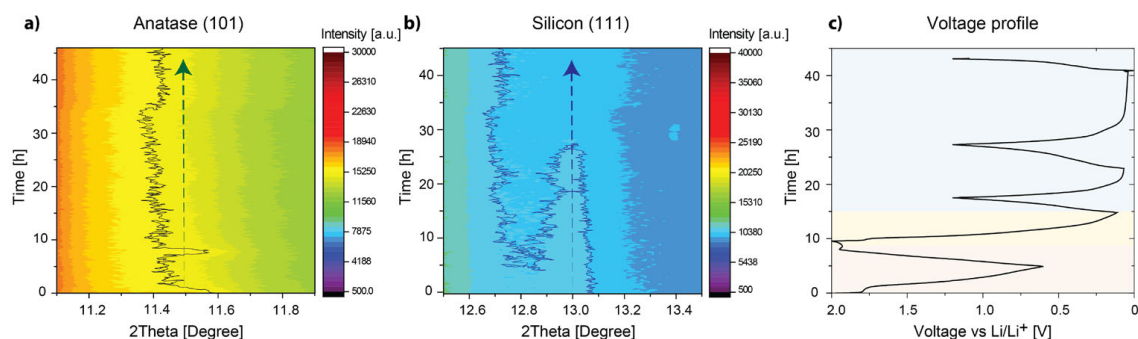


**Figure 5 | The time evolution of the operando XRD patterns** at room temperature measured with Mo source (K-alpha: 17.45 keV,  $\lambda = 0.7107 \text{ \AA}$ ) for n-Si/Anatase-ALD-20 at different stages of lithiation and delithiation. The colour bar is representing changes in the reflection intensity. **a)** Only the (101) reflection at 11.5 2Theta of anatase upon alloying of Si to the fully lithiated phase  $\text{Li}_x\text{Si}$   $x < 3.75$  and subsequent delithiation is shown. The (101) reflection at 11.5 2Theta shifts towards lower angle during Si alloying and goes back to its original position during delithiation. **b)** The (111) reflection of Si is shown, slowly disappearing due to amorphisation of Si **c)** The corresponding electrochemical profile is presented on the graph on the right. Firstly, the electrochemical activity of anatase within a voltage window of 0.6 V to 2V vs. Li/Li<sup>+</sup> was tested (indicated in light orange, 0-10 h). The second stage involves lithiation of TiO<sub>2</sub> and Si respectively with limited capacity ( $x = 0.1$ ,  $\text{Li}_x\text{Si}$ ) and voltage cut-off at 5 mV (indicated in light yellow, 10-15 h). The measurement was followed by progressive Li alloying of Si for two cycles from  $x = 0.2$  to fully lithiated phase of  $x = 3.75$  for  $\text{Li}_x\text{Si}$  within the working potential of Si with discharge down to 5 mV and charge until 1.2 V vs. Li/Li<sup>+</sup> (indicated in light blue, 15-43 h), to exclude the changes associated to the electrochemical activity of anatase.

In **Figure 5a and b**, the time evolution of the operando XRD patterns measured at room temperature for the n-Si/Anatase-ALD-20 electrode in a pouch cell at different stage of lithiation is shown. The colour bar represents changes in the reflection intensity. The corresponding electrochemical profile is presented in **Figure 5c**. The experiment was carried out in three stages. Firstly, the electrochemical activity of anatase within voltage window of 0.6 V to 2V vs.  $\text{Li}/\text{Li}^+$  was tested (light orange, 0-10 h). This was followed by lithiation of  $\text{TiO}_2$  and Si ( $x = 0.1$ ,  $\text{Li}_x\text{Si}$ ) within working potential of Si with discharge down to 5 mV (light yellow, ~10-15h). Finally, subsequent delithiation and lithiation of only the Si phase to  $x = 0.2$  and to fully lithiated phase of  $x = 3.75$  for  $\text{Li}_x\text{Si}$  was performed by limiting the voltage window to between 5 mV and 1.2 V for two cycles (light blue, ~15-43h).

Anatase  $\text{TiO}_2$  has a tetragonal phase with space group  $I41/amd$ , number 141, where titanium is surrounded by distorted oxygen octahedron with lattice parameters of  $a = 3.785 \text{ \AA}$ ,  $c = 9.506 \text{ \AA}$  (**Supplementary B Table 2**) upon lithiation, anatase  $\text{TiO}_2$  undergoes a phase transformation from tetragonal into an orthorhombic structure (lithium titanate,  $\text{Li}_{0.5}\text{TiO}_2$ , space group  $Imma$ , number 74,  $a = 3.808 \text{ \AA}$ ,  $b = 4.077 \text{ \AA}$ ,  $c = 9.053 \text{ \AA}$ )<sup>34,35</sup> where the octahedra become more regular and the Li ions are randomly distributed occupying 50% of the interstitial octahedral 4e sites. This structure has been previously determined by neutron diffraction. This change in symmetry upon lithiation is accompanied by a decrease of the unit cell dimensions along the c-axis and an increase along the b-axis, resulting in an increase of the volume of the unit cell by about 4%. The initial (101) reflection of anatase  $\text{TiO}_2$  (**Fig. 5a**) and the (111) reflection of Si (**Fig. 5b**) are indicated with an arrow.

During the first stage of this experiment, where only the lithiation of anatase  $\text{TiO}_2$  is expected, the (011) reflection of  $\text{TiO}_2$ , is expected to appear as the lithiated phase  $x = 0.5 \text{ Li}_x\text{TiO}_2$  is formed. However, as observed in **Figure 5a**, at the beginning of discharge, the (101) reflection of anatase (Li-poor phase) at  $11.5 \text{ } 2\theta$  shifts towards a lower angle, which is an

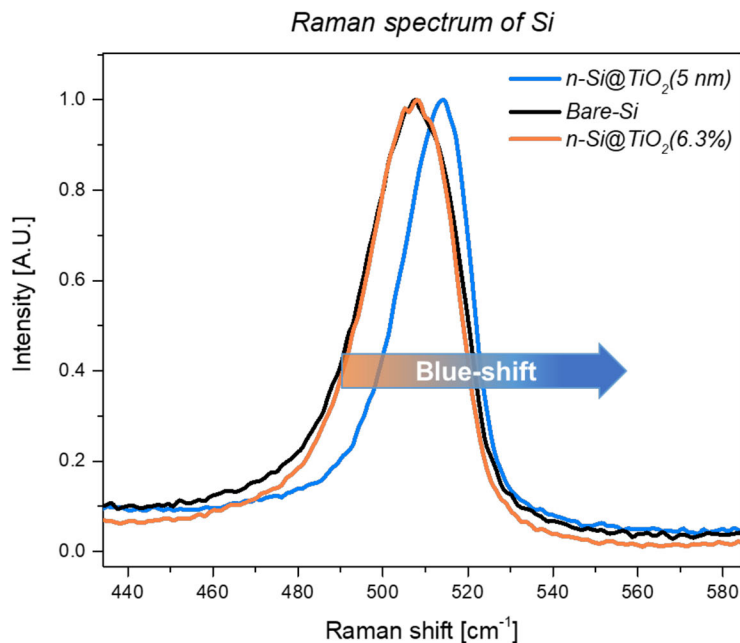


indication that the lithiation proceeds via a single phase reaction<sup>36</sup>. Further lithiation to Li-rich phase ( $x > 0.5 \text{ Li}_x\text{TiO}_2$ ) cannot be confirmed as only a decrease in intensity of the (101) peak is observed. This could be an indication of a growing (011) reflection at the expense of (101) (**Fig. 5a**). Moreover, in these measurements, the (011) reflection was hardly detectable due to high background and packaging of the cell. Another explanation for the decrease in intensity of the (101) reflection is the presence of non-uniform strain in the coating material during lithiation, which would result in peak broadening (strain broadening), thus a decrease in intensity. Upon delithiation (charge), the (101) reflection corresponding to anatase  $\text{TiO}_2$  is restored, proving the reversible electrochemical activity of anatase. Moreover, based on the calculated capacity of anatase at the end of discharge ( $> 0.6 \text{ V vs. Li/Li}^+$ ), the degree of lithiation corresponds to Li-poor phase of  $\text{Li}_{0.12}\text{TiO}_2$ , in contrast to what would be expected on a full discharge of  $\text{TiO}_2$  ( $\text{Li}_{0.55}\text{TiO}_2$  for 20 nm particles up to  $\text{Li}_1\text{TiO}_2$  for 5 nm particles). This is in agreement with the shift in peak position of the (101) reflection, corresponding to the evolution of the lattice parameters in a Li-poor anatase phase as previously reported<sup>17</sup>, where in the regime of initial lithiation, a steep increase in *a*- and decrease in *c*-lattice parameter (for overall composition of  $\text{Li}_{0.1}\text{TiO}_2$ ) was observed.

In the second stage of the measurement, followed by subsequent (de)lithiation over two cycles in the third stage, a (111) reflection corresponding to the Si is presented in **Figure 5b** with the arrow. Si has a cubic structure with space group *Fd-3m* and lattice parameter 5.427 Å (**Supplementary B Table 1**). At the same time, during the third stage, upon lithiation of Si up to the  $\text{Li}_{3.75}\text{Si}$  phase at 0.1 V vs.  $\text{Li/Li}^+$ , the XRD reflections are slowly fading, and a long plateau is observed<sup>2</sup>. During alloying, Si will undergo amorphisation forming  $\text{Li}_x\text{Si}$   $x < 3.75$ , diminishing the crystalline phase of Si<sup>37,38</sup>. On the contrary, there is no significant change in the peak width observed in the XRD pattern of n-Si (**Fig. 5b**), which indicates that the coated Si particles do not undergo pulverisation.

To better observe changes occurring in anatase on lithiation in the second stage of the measurement, followed by subsequent (de)lithiation over two cycles in the third stage, the (101) reflection corresponding to the anatase is presented in **Figure 5a**. The measurement was limited to a voltage of 1.2 V vs.  $\text{Li}/\text{Li}^+$ , to exclude the changes associated to the electrochemical activity of Anatase. As presented in the figure, the black intensity line at  $11.5^\circ$   $2\theta$  is moving towards lower  $2\theta$  angle during deep lithiation (started after 27 h, followed by long plateau from 31 to 41 h), which implies an increasing unit cell volume. It is going towards original position during delithiation of Si (from 41 to 43 h). This can be understood as stretching of the bonds of Si particles.

Summarizing, the operando XRD measurement indicates that during the lithiation and delithiation of n-Si/Anatase- $\text{TiO}_2$ -ALD-20, the lithiation of the  $\text{TiO}_2$  coating goes via a single phase reaction up to  $\text{Li}_{0.12}\text{TiO}_2$ . The reasonable Li-ion conductivity of this phase<sup>25</sup> is expected to be a key factor in the improved performance of the  $\text{TiO}_2$  coated Si particles. The appearance of a solid solution  $\text{Li}_{0.12}\text{TiO}_2$  composition in the 20 nm thin coating is consistent with the previously reported phase diagram, relating the Li composition of anatase to the particle size, where particle sizes below 20 nm can be expected to display a solid solution at this composition. This thus prevents a two-phase coexistence,<sup>16</sup> which has been demonstrated to be the rate limiting factor in the Li-ion transport in lithiated  $\text{TiO}_2$ , posing a large diffusional barrier (0.5 eV) as compared to the barrier in the Li-poor phase (0.2 eV) and the Li-rich phase (0.09 eV)<sup>33</sup>.

3.2.6 Evolution of stresses of n-Si and Si/a-TiO<sub>2</sub>

**Figure 6 | Raman spectrum** of bare n-Si (black line), Si nanoparticles encapsulated in amorphous shell of TiO<sub>2</sub> (n-Si/a-TiO<sub>2</sub>-ALD-5) (blue line) and Si nanoparticles mechanically mixed with amorphous TiO<sub>2</sub> (n-Si+a-TiO<sub>2</sub>, 6.3 wt. % of TiO<sub>2</sub>) (orange line). As a result the Raman shift is observed for n-Si/a-TiO<sub>2</sub>-ALD-5, compared to Si mixed mechanically with a-TiO<sub>2</sub> since there is stress-induced on the Si surface of the particle from the a-TiO<sub>2</sub>.

To determine the changes in bond angles, bond strength and bond energy in the Si before and after coating deposition, Raman Spectroscopy measurements were performed. The changes in Raman shift are an indication of tensile to compressive transition of the stress in the Si, before and after coating deposition, similar what happens during the lithiation which was previously reported<sup>39</sup>. The Raman spectrum of n-Si is presented in **Figure 6** (black line) and shows the characteristic vibrational mode at about 507 cm<sup>-1</sup>, which can be assigned to nano-crystalline Si (shift value could relate to the nanometre scale of Si crystallites)<sup>10</sup>. After applying the a-TiO<sub>2</sub> coating (n-Si/a-TiO<sub>2</sub>-ALD-5), the Si peak shifted toward higher wavenumbers by 7 cm<sup>-1</sup> and is accompanied by a peak width decrease of 7

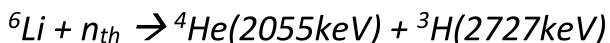
$\text{cm}^{-1}$  (Fig. 6, blue line). Peak narrowing indicates lower difference in the distribution of the bond lengths in the coated samples<sup>40</sup>. The shift indicates changes in the Si-Si bond lengths i.e. being compressed and deformation of the crystal lattice occurring (higher density of lattice defects). The observed blue-shift (shift toward lower wavenumber) is therefore assigned to a tensile to compressive transition of the stress in the Si core of the nanoparticles which are coated (n-Si/a-TiO<sub>2</sub>-ALD-5)<sup>41</sup>. As a comparison n-Si was also mechanically mixed with amorphous TiO<sub>2</sub> (a-TiO<sub>2</sub>) indicated and the Raman spectrum was recorded of this sample, given in Figure 6 as orange line. It can be clearly seen that the shift of the Raman spectrum of mechanical mixture of n-Si and a-TiO<sub>2</sub> is comparable to that of n-Si alone, indicating that there is no stress-induced from the a-TiO<sub>2</sub> on n-Si in the mixture.

The bond strength between the atoms depends on the thermal expansion coefficient (TEC). Covalent materials such as Si have strong bonds between atoms, resulting in low coefficients of thermal expansion being  $2.75\text{-}3.75 \times 10^{-6} \text{ K}^{-1}$ <sup>42</sup>. In contrast, amorphous TiO<sub>2</sub> possess weaker bonds between atoms, resulting in higher coefficients, estimated to be 3 times larger,  $6 \times 10^{-6} \text{ K}^{-1}$  for low temperature deposition<sup>43</sup>. High difference in TEC between materials induces chemical stresses<sup>44</sup>, which were previously reported being around 133 MPa<sup>45</sup>, caused by strong interaction (covalent bonding) leading to lattice mismatch. That will result in high energy vibrations seen as blue-shift in Raman spectrum. Thus, the observed high energy vibrations can originate from that. The blue shift observed for the n-Si/a-TiO<sub>2</sub>-ALD-5 can therefore be attributed to the stress introduced by covalent bonds between n-Si and a-TiO<sub>2</sub>, which is absent in the mechanical mixture of the two. The stresses of the material are calculated according to the following equation<sup>39</sup>:  $\Delta w = -4.4\sigma$ , where  $\Delta w$  is the difference in Raman shift in  $\text{cm}^{-1}$  and  $\sigma$  the compressive stress in GPa. Increasing the layer thickness of the TiO<sub>2</sub> coating, slowly increases the stress of the material, giving  $\sigma = 1.5 \text{ GPa}$ , for 5 nm deposition layer. Therefore the a-TiO<sub>2</sub> coating

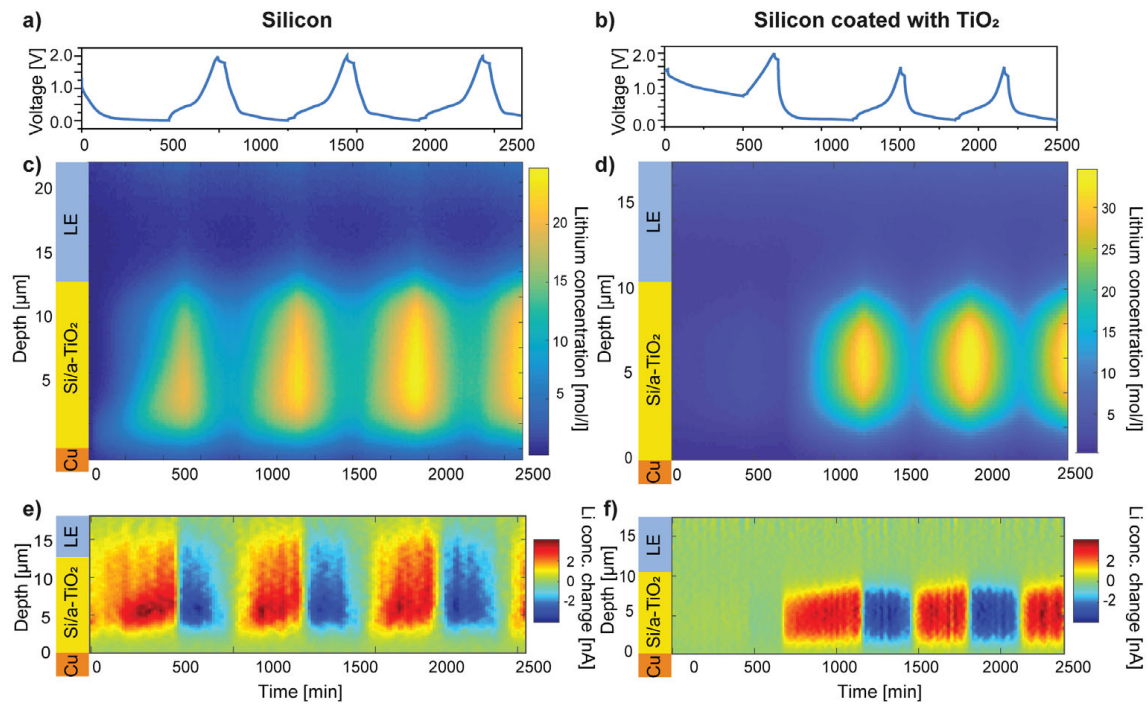
on Si nanoparticles does not influence the bulk crystallinity, but introduces changes on the surface related to the stress in the material.

### 3.2.7 NDP Si with TiO<sub>2</sub> coating with FEC as an electrolyte additive

The homogeneity of the Li storage throughout the Si electrode, can be a critical factor in the cycle life of the battery. Inhomogeneous lithiation will lead to large local volumetric changes, that can be expected to accelerate the detrimental processes. The a-TiO<sub>2</sub> coating has been found to improve the electrochemical performance of n-Si, where the artificial SEI layer, which has a composition of Li<sub>0.12</sub>TiO<sub>2</sub> determined with operando XRD, could be beneficial for the electron and Li transport to the Si nanoparticle. The hypothesis is that this 'artificial SEI' this may facilitate more homogeneous lithiation of the Si electrode. NDP is used to investigate it, since can quantify Li density as a function of electrode depth<sup>20,21</sup>. NDP utilises the neutron capture reaction<sup>46</sup>, where incoming thermal neutrons are captured by the <sup>6</sup>Li (natural abundance around 7.5%) which will generate <sup>3</sup>H and <sup>4</sup>He ions with a specific kinetic starting energy according to following reaction:



The tritium ions have sufficient energy to transmit through roughly 30 μm of Cu. By measuring their energy when reaching the detector, the depth at which the caption reaction took place (location of Li-ions) can be determined. Through the number of ions that reach the detector, the Li concentration can be determined after the data normalisation and background correction. As a result, the Li concentration profile as a function of depth is established.



3

**Figure 7 | Impact of the Si nanoparticles coated with  $\text{TiO}_2$  on the Li concentration depth distribution compared to uncoated Si electrode. (a, c, e) Voltage profile of cells cycled for 4 cycles at  $0.5 \text{ mA/cm}^2$ , Li distribution, the changes in Li distribution during each 10 min of measurement of Si electrode (n-Si|1M  $\text{LiPF}_6$  EC:DEC (1:1), 2 wt. % VC, 25 wt. % FEC|Li) (b, d, f) Voltage profile, Li distribution, the changes in Li distribution during each 10 min of measurement of Si coated with a- $\text{TiO}_2$  electrode (n-Si/a- $\text{TiO}_2$ -5|1M  $\text{LiPF}_6$  EC:DEC (1:1), 2 wt. % VC, 25 wt. % FEC|Li).**

All the NDP measurements are performed on the 4 initial cycles of the assembled cells, including uncoated n-Si and coated n-Si/a- $\text{TiO}_2$ -ALD-5 electrodes with the voltage limit of 10 mV. The initial (de)lithiation for n-Si/a- $\text{TiO}_2$ -ALD-5 was performed by setting up a voltage limit to 0.6 V vs.  $\text{Li/Li}^+$  to exclude Si activity. In that way it was possible to monitor changes in Li concentration as a function of depth for a- $\text{TiO}_2$ . That was followed by subsequent (de)lithiation of Si.

**Figure 7a, b** represent the voltage profiles corresponding to the n-Si|LE+VC+FEC|Li and n-Si/a- $\text{TiO}_2$ |LE+VC+FEC|Li cells during operando NDP measurements. **Figure 7c and d** show the Li concentration, indicated by the colour scale, as a function of electrode depth. The surface of the Cu foil is

used both as a current collector and window, and its set as zero  $\mu\text{m}$  depth in the Li concentration profile. It can be observed in **Figure 7d** that the initial lithiation and delithiation occurs homogeneously as a function of depth across the n-Si/a-TiO<sub>2</sub>-ALD-5 electrode. This is in clear contrast to the lithiation in Si without a coating, as here the Si is in direct contact with the liquid electrolyte. As shown in **Figure 7c**, the Si is alloying inhomogeneously with Li, observed as an accumulation of Li close to the current collector. This non-homogeneous lithiation of Si based electrodes can be regarded as a possible origin of the fast degradation of Si electrodes<sup>47</sup>.

The activity of lithiation and delithiation is demonstrated in **Figure 7e and f** representing the difference between two subsequent measurements for each time step (each measurement is 10 min). This provides further insight into homogeneity of the lithiation, where red represents positive change in Li concentration during lithiation of the Si electrode and blue corresponds to negative change in Li concentration during delithiation. As shown in **Figure 7e** for the uncoated Si electrode, a higher Li concentration at the beginning of lithiation is observed. This can be ascribed to the surface reactions of the current collector, and as a result formation of Li<sub>2</sub>O. This is consistent with the cathodic peak shown in **Figure 4** at 1.4 V vs. Li/Li<sup>+</sup> indicating charge consumption due to reactivity of metal oxides (Cu<sub>2</sub>O/CuO) with Li and formation of metallic Cu<sup>0</sup> and Li<sub>2</sub>O<sup>28</sup>. Before any activity of Si is expected, a higher Li concentration is observed at 1.2 – 0.8 V vs. Li/Li<sup>+</sup>, which corresponds to SEI formation (also seen in the CV plot, **Fig. 4**). The decomposition of FEC electrolyte additive occurs at 1.2 V vs. Li/Li<sup>+</sup>, followed by decomposition of electrolyte solvents at 0.8 V vs. Li/Li<sup>+</sup>, as a result creating a passivating layer of LiF<sup>48-52</sup>. Notwithstanding in **Figure 7f**, a very small amount of Li is observed in the first cycle, where electrochemical activity of Si was excluded by limiting potential ( $\geq 0.6$  V vs. Li/Li<sup>+</sup>). Moreover, no Li contribution from SEI formation was observed, consistent with the CV plot (**Fig. 3b**) where n-Si/a-TiO<sub>2</sub>-ALD-5 showed absence of the SEI peak at 0.8 V vs. Li/Li<sup>+</sup>. This can be explained from the limited electronic conductivity of

the Li-poor phase of  $\text{TiO}_2$  which is expected to suppress SEI formation. Once the lithiation of Si started in the next cycles, homogenous distribution of Li is observed.

Lithiation of the Si electrode occurs preferentially close to the current collector (**Fig. 7c**), and progresses slowly across the complete electrode. This may indicate a limited electronic conductivity of the electrode<sup>53</sup>, which in case of Si improves as it alloys with Li, and that will be discussed in details in **chapter 4**. In comparison, the n-Si/a- $\text{TiO}_2$ -ALD-5, demonstrates very homogenous Li distribution (**Fig. 7d**). As discussed, this can be attributed to the enhanced Li-ion conductivity of lithiated  $\text{Li}_{0.12}\text{TiO}_2$  coating phase that forms before the lithiation of n-Si commences.

**Figure 8a** illustrates evolution of the Li capacity and irreversible reactions upon cycling, which are determined by integrating the Li concentration depth profile from NDP over the complete depth as a function of time. **Figure 8 and b** shows integrated Li concentration throughout n-Si electrode compared to n-Si/a- $\text{TiO}_2$ -ALD-5 respectively. The results demonstrate higher Li capacity for the n-Si/a- $\text{TiO}_2$ -ALD-5 and better reversibility upon cycling (**Fig. 8b**) compared to the n-Si electrode (**Fig. 8a**). Moreover, a smaller amount of irreversible Li builds up upon cycling. However, the chemical nature of Li cannot be distinguished with NDP.



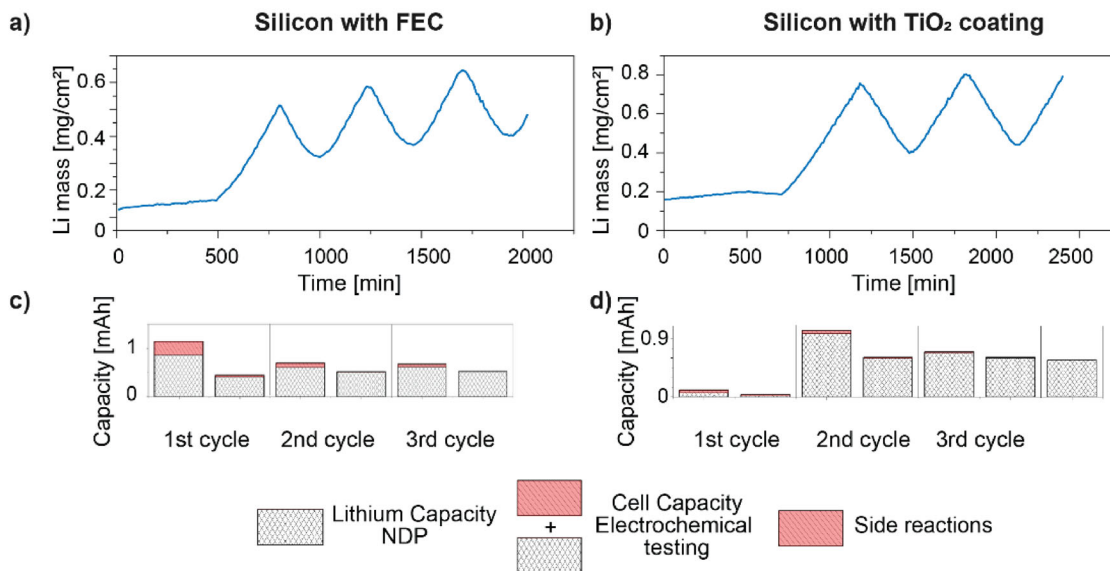


**Figure 8 | Impact of the Si nanoparticles coated with TiO<sub>2</sub> on the Li mass, Li capacity, cell capacity compared to uncoated Si electrode.** (a, c) Illustrates integrated NDP data over the complete depth as a function of time, and Li capacity from operando NDP and cell capacity from electrochemical data indicated as a column chart of the Si electrode (n-Si|1M LiPF<sub>6</sub> EC:DEC (1:1), 2 wt. % VC, 25 wt. % FEC|Li) (b, d) Integrated NDP data, Li capacity, cell capacity of Si coated with TiO<sub>2</sub> (n-Si/a-TiO<sub>2</sub>|1M LiPF<sub>6</sub> EC:DEC (1:1), 2 wt. % VC, 25 wt. % FEC|Li).

The difference between the Li capacity from NDP and the cell capacity from electrochemical cycling reflects the amount of irreversible reactions that only involves electron transfer, such as direct electrolyte reduction and chemical dissolution of Li from the SEI. Both capacities are represented in a single column for each (dis)charge step and their difference is shown in red (Figs. 8c, d). Clearly this red part is relatively large for the Si electrode during initial discharge (Fig. 8c), when, due to the SEI formation, most of the side reactions are expected to occur. In Figure 8d it is demonstrated that contribution of side reactions is low. Moreover a difference is observed at all electrochemical steps, including charge. This is a direct indication that irreversible reactions mainly involve electrons. Such changes can be associated to chemical dissolution of LiF or other Li species from SEI layer or oxidation reaction of electrolyte<sup>54,55</sup>.

### 3.3 Conclusions

Here the role of protective  $\text{TiO}_2$  coatings was investigated on Si nanoparticles and the distribution of Li as a function of electrode depth during cycling. The protective artificial SEI was successfully synthesised using ALD. The optimal coating thickness appears to be 5 nm, which balances the conductivity of the charges and the buffering effect of the coating, explaining the improved electrochemical reversibility observed. Operando XRD was performed to evaluate the behaviour of  $\text{TiO}_2$  during deep discharge of Si, indicating that the lithiation proceeds via a solid solution resulting in a composition of  $\text{Li}_{x \sim 0.12}\text{TiO}_2$ . The reasonable Li-ion conductivity of this phase is beneficial for the Li-ion transport through the electrodes, whereas the limited electronic conductivity is expected to suppress SEI formation as well as crack formation. Restricted lithiation may be explained by the stress-induced on the Si particles by applying the coating, as indicated by the blue-shift in the Raman spectrum. Additionally, operando NDP demonstrates that in the uncoated Si, the lithiation proceeds inhomogeneously as a function of electrode depth, whereas the  $\text{Li}_{0.12}\text{TiO}_2$  coating results in a more homogeneous lithiation as a function of electrode depth. Thus, the results suggest that the improved performance of the coated Si is not only a consequence of the protective function of the coating, but also because of more homogeneous lithiation as a result of the Li-conducting properties of the coating.

3

### 3.4 Materials and methods

**Synthesis of materials:** Si particles (100 nm) were conformally coated with  $\text{TiO}_2$  with various thicknesses of 0.5, 1, 3, 5, 20 nm. The  $\text{TiO}_2$  coating on the Si particles were prepared via Atomic Layer Deposition by the company **Delft-IMP**. Here, ALD was performed in a fluidised bed reactor operated at atmospheric pressure, using titanium isopropoxide (TTIP) as a precursor and  $\text{H}_2\text{O}$  as a co-reactant at  $150^\circ\text{C}$ . The carrier gas used to purge the reactor in

order to remove the by-products was nitrogen ( $N_2$ ) and the exposure sequence applied was 3-6-1-4 min (for TTIP- $N_2$ - $H_2O$ - $N_2$ , respectively). By setting the number of cycles (2, 5, 15, 25, 125 cycles in order to achieve 0.5, 1, 3, 5, 20 nm of coating respectively), the thickness of  $TiO_2$  was controlled. The n-Si coated with the thick layer of  $TiO_2$  (20 nm) was sintered in argon at 450 °C for 5h in order to get crystalline phase of anatase prior to the operando XRD measurements.

**Electrode preparation for C-rate test, CV and ex-situ TEM:** An electrode slurry was prepared by ball-milling active material (crystalline silicon powder, mean particle size distribution of 100 nm, 99% purity, Alfa Aesar), with carbon black (Super P, TIMCAL) and binder (carboxymethyl cellulose, Mw = 90,000 g/mol, Sigma Aldrich) in a weight ratio of 0.6 : 0.2 : 0.2 for 90 min at 250 rpm in an agate jar with 3 agate balls. As a solvent, 2 ml of buffer solution of citric acid/sodium hydroxide/sodium chloride solution with fungicide (pH = 3, Fluka) was used. The slurry was casted on copper foil (cleaned with 0.1M oxalic acid and ethanol) with wet thickness of 100  $\mu$ m and dried at 60°C under vacuum for 12h and cold-pressed under 2 tons for 1 minute. The coin cells were assembled in an argon filled glove box, in order to avoid reactions with oxygen and moisture (< 0.1 ppm  $O_2$  and < 2 ppm  $H_2O$ ) using a polymer separator (Celgard 2250) and Li metal as a counter electrode (Sigma-Aldrich), which was washed with dimethyl carbonate (DMC) to remove the oxide layer. Finally, 140  $\mu$ l of 1.0 M  $LiPF_6$  in 1:1 v/v ethylene carbonate (EC) and diethyl carbonate (DEC) (<15 ppm  $H_2O$ , Sigma Aldrich) was added as an electrolyte for wetting both working and counter electrode surfaces. The electrodes after cycling for the ex-situ TEM were washed with diethylene carbonate (DEC) and dried under vacuum at 80 °C, overnight.

**Pouch cells for operando NDP and XRD:** The results are based on measurements in pouch cells<sup>56-59</sup>, also known as coffee bag cells<sup>60</sup>, which are common practice in industrial applications<sup>61</sup>. **For NDP measurements** pouch cell<sup>56-59</sup> was made with one copper window with a diameter of 18 mm and

thickness of 6  $\mu\text{m}$ . A picture and schematic illustration of the pouch cell are provided in **Figure 1**.

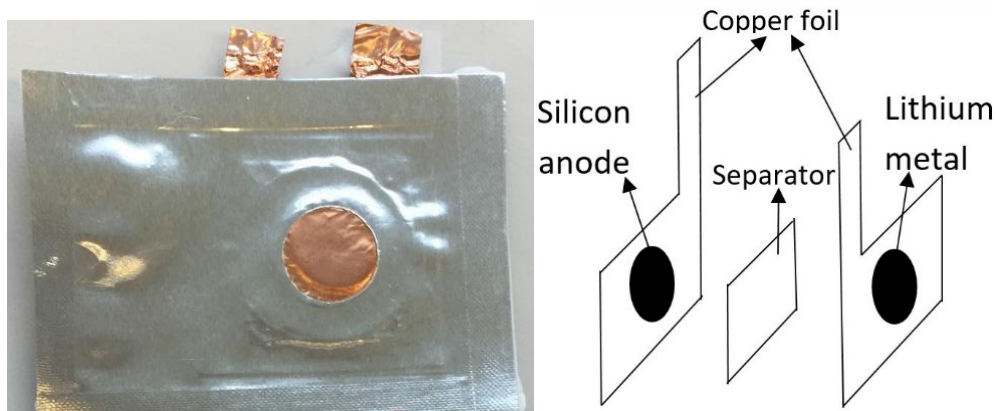


**Figure 1** | Image and schematic representation of the pouch cell.

A window was cut in the outer layer of coffee bag and the Si coated copper current collector substrate was heat-sealed to form a window<sup>62</sup>. Note that the current collector has a second function as a window to separate the in- from the outside, while being as thin as possible to limit parasitic energy loss<sup>22</sup>. In operando cells should be simple and use limited materials, as neutron activation instigate stable isotopes to emit radiation. The pouch cells introduce negligible background by other isotopes as they consist of plastic coated aluminum foil. For these samples, relevant activating elements are isotopes of Cu, Si and Al. The Cu foil however activates significantly through the neutron capture forming  $^{64}\text{Cu}$  and  $^{66}\text{Cu}$ , which have a half-life of 12.7 h and 5 min, respectively. Therefore, prior to disposal, samples are stored for  $\sim 1$  week<sup>63</sup>. The other activated isotopes produced will have decayed within this time.

The electrode slurry was prepared in the same way as for coin-cells, but casted in circular shape with wet thickness of 25  $\mu\text{m}$ . After sealing both current collectors and placing separators: 25  $\mu\text{m}$  PE (Celgard 2250) against the working electrode and 300  $\mu\text{m}$  glass fibre (Whatman), in size of 40x80 mm) and Teflon plate below working electrode (to ensure more pressure), pouch cells were dried overnight at 60°C. Pouch cells were assembled inside

the glove box, in order to avoid reactions with oxygen and moisture (< 0.1 ppm O<sub>2</sub> and < 2 ppm H<sub>2</sub>O). <sup>6</sup>Li metal was used as a counter electrode (Aldrich, 95 wt. % <sup>6</sup>Li, 5 wt. % <sup>7</sup>Li, density 0.47 g cm<sup>-3</sup>). Standard electrolyte 140 μl of 1.0 M LiPF<sub>6</sub> in 1:1 v/v ethylene carbonate (EC) and diethyl carbonate (DEC) (<15 ppm H<sub>2</sub>O, Sigma Aldrich) with 2 wt. % VC and 25 wt. % FEC was used. In order to increase the count rate in the NDP experiments, the electrolyte was enriched with <sup>6</sup>Li metal by adding an excess of <sup>6</sup>Li metal with natural <sup>6</sup>Li abundancy of 7.5% in the electrolyte overnight. This increased the count rate by a factor of 13 as <sup>7</sup>Li is replaced by <sup>6</sup>Li<sup>64</sup>. After wetting the separator from both sides, the cell was left for 30 min to ensure wetting, afterwards the cell was sealed in sealer with vacuum (Audionvac VMS 153).

For **XRD measurements** the cells were cycled in the pouch cells without windows to prevent reaction with moisture and oxygen.

**Electrochemical test:** Galvanostatic cycling was performed within cut-off voltage of 0.005 V to 1.2 V (vs. Li/Li<sup>+</sup>) at C/20 C-rate. The current was calculated based on the Si with the capacity of 1500 mAhg<sup>-1</sup>. For NDP measurements the current was calculated based on the Si with a capacity of 800 mAh/g and voltage limit of 10 mV. The initial (de)lithiation n-Si/a-TiO<sub>2</sub>-ALD-5 was performed by excluding Si activity by setting up a voltage limit from 0.6 V vs. Li/Li<sup>+</sup> to 2V.

**Cyclic voltammetry:** CV measurements were performed using a Metrohm Autolab B.V. at a scanning rate of 0.1 mV/s.

**Operando X-ray diffraction:** Measurements were performed using X-Ray Diffraction in transmission mode. Powder XRD patterns were collected in the 2θ range of 6.0-17.0° to identify changes in lattice parameters of crystalline phases of the prepared materials using Mo K<sub>α</sub> X-rays (0.7107 Å at 60 kV and 40 mA) on an Empyrean X-ray powder diffractometer (Malvern Panalytical).

**Ex-situ transmission electron microscopy:** The TEM measurements were carried out in a Cs corrected FEI TITAN microscope operating at HAADF STEM mode equipped with an EDX detector.

**Raman Spectroscopy:** The Raman experiments were carried out with a Nicolet Almega XR Raman microscope using the 633 nm line from a He–Ne laser. Ex situ Raman mapping was done in an area of  $10 \times 10 \mu\text{m}^2$  on the pressed powders. Spectra were recorded over a Raman shift range of 400 to  $600 \text{ cm}^{-1}$  using an integration time of 100 s per spectrum.

### 3.5 References

- 1 M. N. Obrovac, L. C., Dinh Ba Le, J. R. Dahn. Alloy Design for Lithium-Ion Battery Anodes. *Journal of The Electrochemical Society* (2007).
- 2 Obrovac, M. & Krause, L. Reversible cycling of crystalline silicon powder. *Journal of The Electrochemical Society* **154**, A103-A108 (2007).
- 3 Chon, M. J., Sethuraman, V. A., McCormick, A., Srinivasan, V. & Guduru, P. R. Real-time measurement of stress and damage evolution during initial lithiation of crystalline silicon. *Physical Review Letters* **107**, 045503 (2011).
- 4 Liu, X. H. *et al.* Size-Dependent Fracture of Silicon Nanoparticles During Lithiation. *Acs Nano* **6**, 1522-1531 (2012).
- 5 Ji Heon Ryu, J. W. K., Yung-Eun Sung, and Seung M. Oh. Failure Modes of Silicon Powder Negative Electrode in Lithium Secondary Batteries. *Electrochemical and Solid-State Letters* (2004).
- 6 Oumellal, Y. *et al.* The failure mechanism of nano-sized Si-based negative electrodes for lithium ion batteries. *Journal of Materials Chemistry* **21** (2011).
- 7 Chan, C. K., Ruffo, R., Hong, S. S. & Cui, Y. Surface chemistry and morphology of the solid electrolyte interphase on silicon nanowire lithium-ion battery anodes. *Journal of Power Sources* **189**, 1132-1140 (2009).
- 8 Xiao Hua Liu, L. Z., Shan Huang, Scott X. Mao, Ting Zhu, and Jian Yu Huang. Size-Dependent Fracture of Silicon Nanoparticles During Lithiation. *American Chemical Society* (2012).
- 9 Jin, Y. *et al.* Self-healing SEI enables full-cell cycling of a silicon-majority anode with a coulombic efficiency exceeding 99.9%. *Energy & Environmental Science* **10**, 580-592 (2017).
- 10 Maroni, F., Carbonari, G., Croce, F., Tossici, R. & Nobili, F. Anatase  $\text{TiO}_2$  as a Cheap and Sustainable Buffering Filler for Silicon Nanoparticles in Lithium-Ion Battery Anodes. *ChemSusChem* **10**, 4771-4777 (2017).
- 11 Yang, J. *et al.* Amorphous  $\text{TiO}_2$  Shells: A Vital Elastic Buffering Layer on Silicon Nanoparticles for High-Performance and Safe Lithium Storage. *Adv Mater* **29** (2017).

- 12 Lotfabad, E. M. *et al.* ALD TiO<sub>2</sub> coated silicon nanowires for lithium ion battery anodes with enhanced cycling stability and coulombic efficiency. *Physical Chemistry Chemical Physics* **15**, 13646-13657 (2013).
- 13 Pfanzelt, M., Kubiak, P., Fleischhammer, M. & Wohlfahrt-Mehrens, M. TiO<sub>2</sub> rutile—an alternative anode material for safe lithium-ion batteries. *Journal of Power Sources* **196**, 6815-6821 (2011).
- 14 Luo, W. *et al.* Silicon/mesoporous carbon/crystalline TiO<sub>2</sub> nanoparticles for highly stable lithium storage. *ACS nano* **10**, 10524-10532 (2016).
- 15 Feng, K. *et al.* Conformal formation of Carbon-TiOX matrix encapsulating silicon for high-performance lithium-ion battery anode. *Journal of Power Sources* **399**, 98-104 (2018).
- 16 Wagemaker, M., Borghols, W. J. H. & Mulder, F. M. Large Impact of Particle Size on Insertion Reactions. A Case for Anatase Li<sub>x</sub>TiO<sub>2</sub>. *Journal of the American Chemical Society* **129**, 4323-4327 (2007).
- 17 Liu, H. & Grey, C. P. Influence of particle size, cycling rate and temperature on the lithiation process of anatase TiO<sub>2</sub>. *Journal of Materials Chemistry A* **4**, 6433-6446 (2016).
- 18 Zeng, Z. *et al.* Electrochemical Properties of a Mesoporous Si/TiO<sub>2</sub> Nanocomposite Film Anode for Lithium-Ion Batteries. *Electrochemical and Solid-State Letters* **11**, A105-A107 (2008).
- 19 Liu, Y. & Yang, Y. Recent progress of TiO<sub>2</sub>-based anodes for Li ion batteries. *Journal of Nanomaterials* **2016**, 2 (2016).
- 20 Whitney, S. M., Biegalski, S. R. F. & Downing, G. Benchmarking and analysis of 6Li neutron depth profiling of lithium ion cell electrodes. *Journal of Radioanalytical and Nuclear Chemistry* **282**, 173 (2009).
- 21 Oudenhoven, J. F. M. *et al.* In Situ Neutron Depth Profiling: A Powerful Method to Probe Lithium Transport in Micro-Batteries. *Advanced Materials* **23**, 4103-+ (2011).
- 22 Harks, P.-P. R. M. L. *et al.* Spatiotemporal Quantification of Lithium both in Electrode and in Electrolyte with Atomic Precision via Operando Neutron Absorption. *Journal of the American Chemical Society* **141**, 14280-14287 (2019).
- 23 Ziegler, J. F., Cole, G. W. & Baglin, J. E. E. Technique for determining concentration profiles of boron impurities in substrates. *Journal of Applied Physics* **43**, 3809-3815 (1972).
- 24 Liu, M. *et al.* Efficient Li-Metal Plating/Stripping in Carbonate Electrolytes Using a LiNO<sub>3</sub>-Gel Polymer Electrolyte, Monitored by Operando Neutron Depth Profiling. *Chemistry of Materials* **31**, 4564-4574 (2019).
- 25 Shen, K., Chen, H., Klaver, F., Mulder, F. M. & Wagemaker, M. Impact of particle size on the non-equilibrium phase transition of lithium-inserted anatase TiO<sub>2</sub>. *Chemistry of Materials* **26**, 1608-1615 (2014).
- 26 Bai, Y. *et al.* Core-shell Si@TiO<sub>2</sub> nanosphere anode by atomic layer deposition for Li-ion batteries. *Journal of Power Sources* **308**, 75-82 (2016).
- 27 Guan, C. & Wang, J. Recent Development of Advanced Electrode Materials by Atomic Layer Deposition for Electrochemical Energy Storage. *Adv Sci (Weinh)* **3**, 1500405 (2016).

- 28 Ferraresi, G., Czornomaz, L., Villevieille, C., Novak, P. & El Kazzi, M. Elucidating the Surface Reactions of an Amorphous Si Thin Film as a Model Electrode for Li-Ion Batteries. *ACS Appl Mater Interfaces* **8**, 29791-29798 (2016).
- 29 Jin, Y. *et al.* Identifying the Structural Basis for the Increased Stability of the Solid Electrolyte Interphase Formed on Silicon with the Additive Fluoroethylene Carbonate. *J Am Chem Soc* **139**, 14992-15004 (2017).
- 30 Key, B., Morcrette, M., Tarascon, J.-M. & Grey, C. P. Pair distribution function analysis and solid state NMR studies of silicon electrodes for lithium ion batteries: understanding the (de) lithiation mechanisms. *Journal of the American Chemical Society* **133**, 503-512 (2011).
- 31 Ogata, K. *et al.* Revealing lithium–silicide phase transformations in nano-structured silicon-based lithium ion batteries via in situ NMR spectroscopy. *Nature communications* **5**, 1-11 (2014).
- 32 Borghols, W. J. H. *et al.* The electronic structure and ionic diffusion of nanoscale  $\text{LiTiO}_2$  anatase. *Physical Chemistry Chemical Physics* **11**, 5742-5748 (2009).
- 33 Wagemaker, M., van de Krol, R., Kentgens, A. P. M., van Well, A. A. & Mulder, F. M. Two phase morphology limits lithium diffusion in  $\text{TiO}_2$  (anatase): A Li-7 MAS NMR study. *J. Am. Chem. Soc.* **123**, 11454-11461 (2001).
- 34 Murphy, D., Cava, R. J., Zahurak, S. & Santoro, A. Ternary  $\text{Li}_x\text{TiO}_2$  phases from insertion reactions. *Solid State Ionics* **9**, 413-417 (1983).
- 35 Cava, R. J., Murphy, D. W., Zahurak, S., Santoro, A. & Roth, R. S. The Crystal-Structures of the Lithium-Inserted Metal-Oxides  $\text{Li}_{0.5}\text{TiO}_2$  Anatase,  $\text{Li}_2\text{O}_4$  Spinel, and  $\text{Li}_2\text{Ti}_2\text{O}_4$ . *J. Solid State Chem.* **53**, 64-75 (1984).
- 36 Wagemaker, M., Borghols, W. J. H. & Mulder, F. M. Large impact of particle size on insertion reactions, A case of anatase  $\text{Li}_x\text{TiO}_2$ . *J. Am. Chem. Soc.* **129**, 4323 (2007).
- 37 Li, J. & Dahn, J. An in situ X-ray diffraction study of the reaction of Li with crystalline Si. *Journal of The Electrochemical Society* **154**, A156-A161 (2007).
- 38 Obrovac, M. & Christensen, L. Structural changes in silicon anodes during lithium insertion/extraction. *Electrochemical and Solid State Letters* **7**, A93 (2004).
- 39 Zeng, Z. *et al.* In situ measurement of lithiation-induced stress in silicon nanoparticles using micro-Raman spectroscopy. *Nano Energy* **22**, 105-110 (2016).
- 40 Unifantowicz, P., Vaucher, S., Lewandowska, M. & Kurzydłowski, K. J. Structural changes of silicon upon high-energy milling investigated by Raman spectroscopy. *Journal of Physics: Condensed Matter* **20** (2008).
- 41 Y Gogotsi, C. B. a. F. K. Raman microspectroscopy study of processing-induced phase transformations and residual stress in silicon. *Semiconductor Science and Technology* (1999).
- 42 Okada, Y. & Tokumaru, Y. Precise determination of lattice parameter and thermal expansion coefficient of silicon between 300 and 1500 K. *Journal of Applied Physics* **56**, 314-320 (1984).
- 43 Hanada, T. Thermal expansion and coordination state of cations in amorphous films in the system  $\text{Al}_2\text{O}_3\text{-TiO}_2$ . (1986).



- 44 Memarzadeh Lotfabad, E. *et al.* ALD TiO<sub>2</sub> coated silicon nanowires for lithium ion battery anodes with enhanced cycling stability and coulombic efficiency. *Phys Chem Chem Phys* **15**, 13646-13657 (2013).
- 45 Huang, Y., Pandraud, G. & Sarro, P. M. Characterization of low temperature deposited atomic layer deposition TiO<sub>2</sub> for MEMS applications. *Journal of Vacuum Science & Technology A: Vacuum, Surfaces, and Films* **31** (2013).
- 46 Verhallen, T. W., Lv, S. & Wagemaker, M. Operando neutron depth profiling to determine the spatial distribution of Li in Li-ion Batteries. *Frontiers in Energy Research* **6**, 62 (2018).
- 47 Oumellal, Y. *et al.* The failure mechanism of nano-sized Si-based negative electrodes for lithium ion batteries. *Journal of Materials Chemistry* **21**, 6201-6208 (2011).
- 48 Lin, Y. M. *et al.* High performance silicon nanoparticle anode in fluoroethylene carbonate-based electrolyte for Li-ion batteries. *Chem Commun (Camb)* **48**, 7268-7270 (2012).
- 49 Etacheri, V. *et al.* Effect of fluoroethylene carbonate (FEC) on the performance and surface chemistry of Si-nanowire Li-ion battery anodes. *Langmuir* **28**, 965-976 (2012).
- 50 Dalavi, S., Guduru, P. & Lucht, B. L. Performance Enhancing Electrolyte Additives for Lithium Ion Batteries with Silicon Anodes. *Journal of The Electrochemical Society* **159**, A642-A646 (2012).
- 51 Jaumann, T. *et al.* Lifetime vs. rate capability: Understanding the role of FEC and VC in high-energy Li-ion batteries with nano-silicon anodes. *Energy Storage Materials* **6**, 26-35 (2017).
- 52 Li, Q. *et al.* Identification of the Solid Electrolyte Interface on the Si/C Composite Anode with FEC as the Additive. *ACS Appl Mater Interfaces* **11**, 14066-14075 (2019).
- 53 Zhang, X., Verhallen, T. W., Labohm, F. & Wagemaker, M. Direct Observation of Li-Ion Transport in Electrodes under Nonequilibrium Conditions Using Neutron Depth Profiling. *Advanced Energy Materials* **5**, 1500498 (2015).
- 54 Dupré, N. *et al.* Multiprobe study of the solid electrolyte interphase on silicon-based electrodes in full-cell configuration. *Chemistry of Materials* **28**, 2557-2572 (2016).
- 55 Marino, C. *et al.* Study of the Electrode/Electrolyte Interface on Cycling of a Conversion Type Electrode Material in Li Batteries. *The Journal of Physical Chemistry C* **117**, 19302-19313 (2013).
- 56 Yu, D. Y. W., Donoue, K., Inoue, T., Fujimoto, M. & Fujitani, S. Effect of electrode parameters on LiFePO<sub>4</sub> cathodes. *Journal of the Electrochemical Society* **153**, A835-A839 (2006).
- 57 Lv, S. *et al.* Operando monitoring the Lithium spatial distribution of Li-metal anodes. *Nature Communications*, in press (2018).
- 58 Mohanty, D. *et al.* Structural transformation of a lithium-rich Li<sub>1.2</sub>Co<sub>0.1</sub>Mn<sub>0.55</sub>Ni<sub>0.15</sub>O<sub>2</sub> cathode during high voltage cycling resolved by in situ X-ray diffraction. *Journal of Power Sources* **229**, 239-248 (2013).

- 59 Gustafsson, T., Thomas, J. O., Koksang, R. & Farrington, G. C. The polymer battery as an environment for in situ X-ray diffraction studies of solid-state electrochemical processes. *Electrochimica Acta* **37**, 1639-1643 (1992).
- 60 Singh, M., Kaiser, J. & Hahn, H. Thick Electrodes for High Energy Lithium Ion Batteries. *Journal of The Electrochemical Society* **162**, A1196-A1201, (2015).
- 61 Trask, S. E. *et al.* From coin cells to 400 mAh pouch cells: Enhancing performance of high-capacity lithium-ion cells via modifications in electrode constitution and fabrication. *Journal of Power Sources* **259**, 233-244, (2014).
- 62 Villevieille, C. 183-232 (Elsevier, 2015).
- 63 Liu, M. *et al.* Efficient Li-Metal Plating/Stripping in Carbonate Electrolytes Using a  $\text{LiNO}_3$ -Gel Polymer Electrolyte, Monitored by Operando Neutron Depth Profiling. *Chemistry of Materials*, (2019).
- 64 Verhallen, T. W., Lv, S. & Wagemaker, M. Operando Neutron Depth Profiling to Determine the Spatial Distribution of Li in Li-ion Batteries. *Frontiers in Energy Research* **6**, (2018).





# 4

---

Operando monitoring the Li  
distribution in Si negative electrodes  
for Li-ion batteries

---

### Abstract

Silicon is a promising candidate to replace graphite at the negative electrode of Li-ion batteries given its high theoretical capacity of  $3579 \text{ mAhg}^{-1}$ . Nonetheless, the commercial use of Si is limited due to high volume expansion during lithiation and consequential pulverisation of the Si particles and extensive growth of SEI. Here, atmospheric operando NDP is employed to understand the role of the reaction homogeneity on cycle life and how this is affected by the nature of the SEI. Si electrodes are tested with standard electrolyte (1 M  $\text{LiPF}_6$  EC/DEC) and in the combination with VC/FEC additives. For the Si in standard electrolyte a large Li concentration gradient as a function of depth is observed. That indicates inhomogeneous lithiation which results in local volumetric changes that can contribute to the capacity loss upon cycling. The electrochemical activity and the highest Li concentration is observed in the region near the current collector, as a consequence of relatively poor electronic conductivity of Si particles at the beginning of cycling. It is expected that lithiation will proceed towards separator, however inhomogeneous lithiation is apparent for a number of cycles, clearly indicating that poor passivation layer of the Si surface inhibits the complete utilisation of the active material. Addition of FEC and VC electrolyte additives, is well known to result in a more stable, electronically resistive and flexible SEI that improves cycling efficiency of Si electrodes and as a consequence effectively homogeneous (de)lithiation. Based on these results we propose that the properties of SEI has an impact on the homogeneity of the lithiation and reversible capacity of Si electrodes.

## 4.1 Introduction

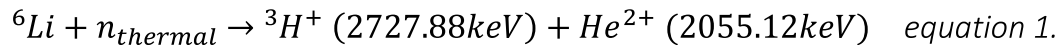
For increasing demands of portable electronic devices Li-ion battery research focuses on increasing the energy density, while ensuring a stable, long cycle life<sup>1,2</sup>. A high energy density requires high Li capacities of the electrode materials and a large difference in potential between negative and positive electrode<sup>3</sup>. For its high theoretical capacity, Si is an intensively studied material for negative electrode<sup>4-7</sup>. However, the large volumetric expansion of Si, up to 400% upon lithiation, makes commercialisation challenging. Repetitive (dis)charge cycles, induce mechanical stresses that leads to pulverisation of Si particles and loss of contact and thus limiting the utilisation of active electrode material<sup>8,9</sup>. Consequently, rupture of the passivating solid electrolyte interphase (SEI), induces progressive electrolyte decomposition<sup>10,11</sup>. This results in capacity loss over cycling and thus causing an insufficient cycle life of Si electrodes. In addition, in Si electrodes, the semiconducting properties of Si hinder electron conductivity and the crystalline framework does not allow facile ion transport through the solid state<sup>12</sup>. However, when Si is lithiated this rapidly changes, causing Si to become amorphous<sup>13</sup> and the electronic and ionic conductivities rise, lowering the internal resistance of (partially) cycled batteries<sup>14,15</sup>. Moreover, continuous degradation of electrolyte progressively decrease the porosity<sup>16,17</sup> within the electrode, leading to increase of the tortuosity and as a result lithiation becomes kinetically limited. This will result in pore clogging and non-homogeneous Li alloying<sup>18</sup>. As a consequence Si particles will be lithiated preferentially near the electrode/separator interface compared to the Si grains close to current collector. Thus, the resulting high local Li compositions will promote lower utilisation of active material. Therefore, in this case degradation of the ionic wiring, caused by SEI formation, plays an important role in the cycle life of the Si negative electrode<sup>19</sup>. Other studies stress the importance of electronic wiring<sup>20</sup> and homogenous dispersion of the conductive additive as a key parameter that

determines the degradation mechanism. These results indicate that the homogeneity of lithiation is an important aspect that determines the cycle life of Si electrodes. Thus charge transport, both ionic and electronic conductivity, will play an important role in addition to the stability of the SEI.

The most widely used strategy to improve the cycle life of Si electrode is to modify the electrolyte composition such that it stabilises SEI, by preventing further electrolyte decomposition due to high resistivity of the SEI components and to create flexible SEI with host upon volumetric changes<sup>21</sup>. Common electrolyte additives for Si negative electrode are vinylene carbonate (VC) and fluoroethylene carbonate (FEC)<sup>22-25</sup> since they modify the nature of the SEI. VC possess double bond and polymerises upon first reduction and forms oligomers and insoluble polymers. FEC decomposes upon reduction at higher potentials (1.3 V vs. Li/Li<sup>+</sup>) than those commonly used in liquid electrolyte solvents (ethylene carbonate (EC)/ diethyl carbonate (DEC)) forming an artificial protection layer composed of lithium fluoride (LiF) and other organic species (–CHF–OCO<sub>2</sub>-type compounds)<sup>15</sup>. SEI formed in VC/FEC electrolyte additives consists on cross-linked polyethylene oxides (PEO)<sup>26</sup> and aliphatic chain functionalities. The presence of those species correlates to improved cycling<sup>27</sup>. It thus suppresses degradation of the electrolyte solvents as well as it absorbs organic species from SEI by strong bonds of Li-F<sup>28,29</sup> for further protection of the active electrode material.

Given the instability of the system and the reactivity towards oxygen and moisture, the formation of these layers are preferably studied using in operando methodologies. Furthermore the technique used should be able to discriminate processes involving Li products from electrochemical decomposition of organic compounds. Here, NDP is used which allows to follow in operando Li-ion movement during (dis)charge in Li-ion batteries providing unprecedented insights regarding diffusion, transfer and cycling efficiency of ions in batteries<sup>30-32</sup>. Based on a neutron capture reaction, this

non-destructive technique allows the quantitative determination of  ${}^6\text{Li}$  isotope with respect to depth<sup>33</sup> with a resolution of  $1\mu\text{m}$ . In the case of  ${}^6\text{Li}$ , this reaction energy is distributed between a triton ( ${}^3\text{H}$ ) and alpha particle ( $\text{He}^{2+}$ ) according to **Equation 1**<sup>33,34</sup>. The kinetic energy of the lighter  ${}^3\text{H}$  is high enough to reach an energy sensitive detector placed at a distance such that the recorded particles have a trajectory perpendicular to the sample plane, enforcing the relation between particle energy loss and isotope depth.



Neutrons penetrate the entire battery pack while their low energy avoids the risk of beam damage<sup>35</sup>. Moreover as these capture reactions are unique and  ${}^6\text{Li}$  isotope specific, intrinsically allowing high selectivity and low noise, leaving the other battery components unperturbed<sup>36</sup>. However, measurements previously reported are done at low pressure and even vacuum, making liquid electrolyte battery operation extremely challenging<sup>37,38</sup>, forcing researchers to search for ex-situ measurements instead<sup>11,39</sup>.

Herein, we demonstrate measurements using a bespoke helium filled chamber to allow ambient pressure operation without excessive compromises to the set-up resolution<sup>40</sup>. Detailed analysis of NDP provide insights into the homogeneity of the (de)lithiation during first cycles of Si electrode in the standard electrolyte and how this is effected by VC and FEC electrolyte additives. The results indicate that the nature of the SEI strongly influences the homogeneity of the lithiation of Si electrodes. Since inhomogeneous lithiation and delithiation of Si electrodes. Inhomogeneous lithiation of Si will result in locally high Li compositions, together with the large volumetric changes, this will promote lower utilisation of active material. Thus, this represents a secondary effect of the electrolyte composition that leads to capacity loss.



## 4.2 Results

### 4.2.1 Impact of cycle number on Li concentration distribution

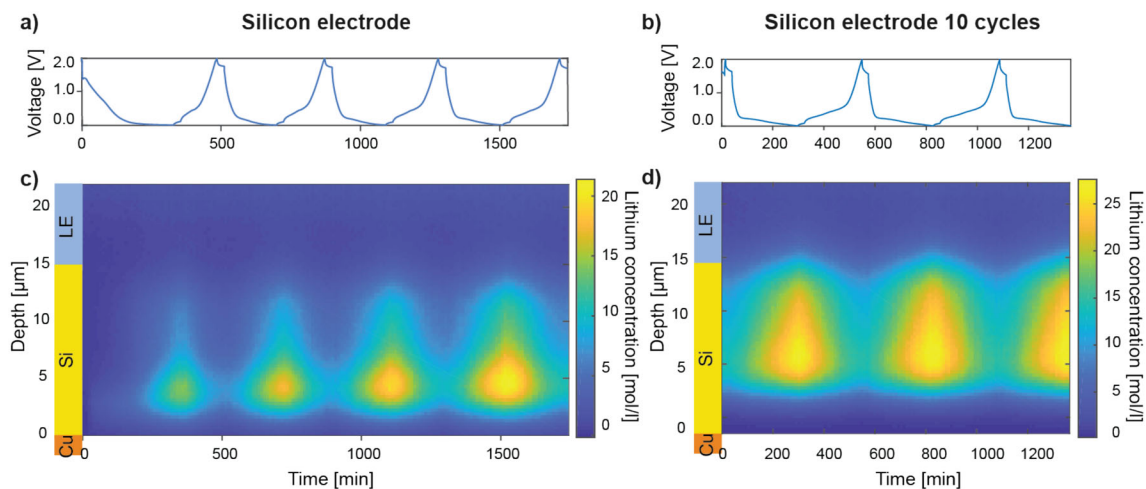


**Figure 1 | The impact of cycling on the Li concentration depth distribution.** Operando NDP results obtained of a Si electrode without any electrolyte additive upon the first cycles, i.e. 1-4<sup>th</sup> cycle and after 10 cycles, all measured at a C/8 rate. **a) and b)** The electrochemical response obtained during the measurement. **c) and d)** The measured Li concentration as a function of depth and experiment time.

To investigate the homogeneity of lithiation in Si electrodes as a function of cycle number, in operando NDP<sup>30,31,37</sup> is employed during the first 17 discharge-charge cycles. In **Figures 1a and b** the cell potential is plotted versus measurement time for the 1<sup>st</sup> to 4<sup>th</sup> cycles and the 15-17<sup>th</sup> cycles, respectively. The corresponding **Figures 1c and d**, show the Li concentration in mole per litre as a function of depth perpendicular to the Si electrode into the cell and as a function of cycling time. In terms of cycling performance, the characteristic voltage profile with a long voltage plateau at 0.1 V vs. Li/Li<sup>+</sup> is observed<sup>4,41</sup> for both cells (related to amorphisation of Si), see **Figures 1a and b**. This then is further governed by a sloping behaviour indicating electrolyte decomposition reactions<sup>15,42</sup>. As the delithiation capacity increases with the cycle number, the coulombic efficiency of the cell increases, and after 10 cycles (cycled outside the NDP set-up), the cell shows

largely reversible (de)lithiation. At the beginning of the measurement, the 1.0 M electrolyte is the sole Li source resulting in a homogeneous background signal. Once the current is applied, the Si electrode located in the region of 1-14  $\mu\text{m}$  (thickness of the coating) displays a cyclic increase and decrease of the Li concentration. However, the original, fully delithiated state at 2 V vs.  $\text{Li}/\text{Li}^+$ , is never recovered as observed from the evolution of Li concentration. On the contrary, with each cycle the measured Li concentration increases, indicating an accumulation of irreversible Li during charge. As NDP is not able to distinguish the chemical state of the detected Li, the origin of the irreversible stored Li may be either in the SEI or as deactivated Li in Si ( $\text{Li}_x\text{Si}$ ) or both. During the first cycles, a large gradient of Li concentration within the Si electrode can be discerned, reflecting large inhomogeneity in the  $\text{Li}_x\text{Si}$  composition as a function of depth. Previous reports suggested that clogging of the pores by SEI formation after 50 cycles promotes inhomogeneous lithiation close to the separator/electrode interface, contributing to the Si electrode failure mechanism<sup>19,43,44</sup>. The present results, focusing on the early cycles, indicate a larger Li concentration close to the current collector. This may be explained by the initially poor electronic conductivity of the Si electrode ( $6.7 \cdot 10^{-4} \text{ S cm}^{-1}$ )<sup>20</sup>, which has previously been shown for LFP positive electrodes to result in (de)lithiation near the current collector<sup>37</sup>. Therefore, limited electronic conductivity of crystalline Si particles at the beginning of cycling can be the root of preferential lithiation near the current collector. The Li concentration progressively increases throughout the electrode upon cycling which can be attributed to the improved electronic conductivity of the amorphised Si particles upon lithiation. In **Figures 1b and d** the operando NDP results obtained at cycles 15, 16 and 17 are presented. The electrochemical response shown in **Figure 1b** shows higher coulombic efficiency compared to the previous cell in **Figure 1a**, and the (de)lithiation now occurs throughout the complete electrode, although the current collector/electrode interface remains more active (**Fig. 1d**). At the end of charge, the NDP results indicate

an average Li concentration of 15 mol/L representing irreversible capture Li-species, which was less than 1 mol/L at the beginning of the measurement. This result is an indication of the large amount Li-containing SEI products and immobilised Li in the Si<sup>10,45</sup>, which contribute to the total capacity loss upon cycling.

### 4.2.2 Impact of VC/FEC on Li concentration distribution

To improve the stability of the SEI formed on Si, FEC and VC are commonly used as additives<sup>15</sup>. As shown in **Figure 2**, the evolution of the Li concentration profile measured by NDP reflects this impact. In terms of cycling performance small differences are observed in **Figure 2a**. Although the fully delithiated state at 2 V vs. Li/Li<sup>+</sup> is not achieved, the coulombic efficiency increases more rapidly with cycle number as compared to electrolyte without VC/FEC additives. The Li concentration profile obtained during the initial discharge is similar to that in the Si electrode in combination with standard electrolyte without VC/FEC additives. However, comparing **Figure 2b** with **Figure 1c**, a much higher Li concentration is reached for Si electrode with VC/FEC electrolyte additives. Moreover, in the subsequent cycles the Li concentration rapidly homogenises over the electrode depth in the presence of the VC/FEC additives. At the end of the charge the Li concentration is 10 mol/L and in the subsequent cycles increased to 12 mol/L, representing SEI species and/or deactivated Li-Si. Nevertheless higher utilisation of the Si electrode is achieved faster and coulombic efficiency is higher. Clearly, the VC/FEC electrolyte additives minimise the Li gradient in the Si electrodes as a function of depth. **Figure 2c** demonstrates the time derivative of Li concentration (each measurement is 10 min), which is referred to as the (de)lithiation activity. Notice that a red colour corresponds to a positive change in Li concentration in the Si electrode and a blue colour corresponds to negative change in Li concentration during delithiation, indicating where Li is inserted or extracted at each stage of the cycling.

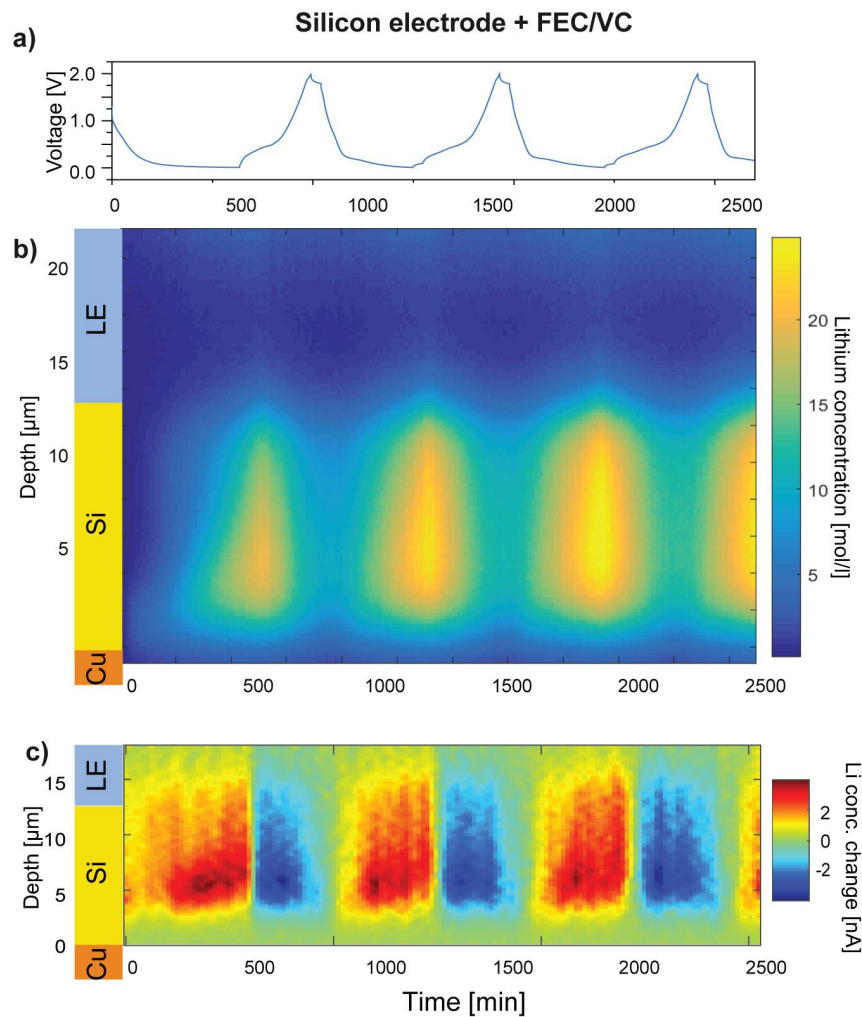


**Figure 2 | Effect of electrolyte additive VC and FEC on Li concentration depth distribution.** Operando NDP results of a Si electrode without and with FEC and VC electrolyte additives during the first 5 cycles measured at a C/8 rate. **a)** The electrochemical response of the Si electrode. **b)** The measured Li concentration as a function of depth and experiment time. **c)** Changes in Li distribution between each measurement.

In this representation, it is more clear that during the first stages of discharge the activity is mainly near the current collector. For the sample without additives (**Fig. 3a**), the lithiation stops here. However, in the case of the VC/FEC additive (**Fig. 2c**), is observed that the discharge process continues and in more homogeneous way. Moreover, upon charge the reverse is observed, in the case without additives, only the region close to the current collector is active, whereas a homogenous activity is observed for the

sample with additives. Hence, a lithiation and delithiation process that is homogenous throughout the electrode depth is reached within a limited number of cycles.

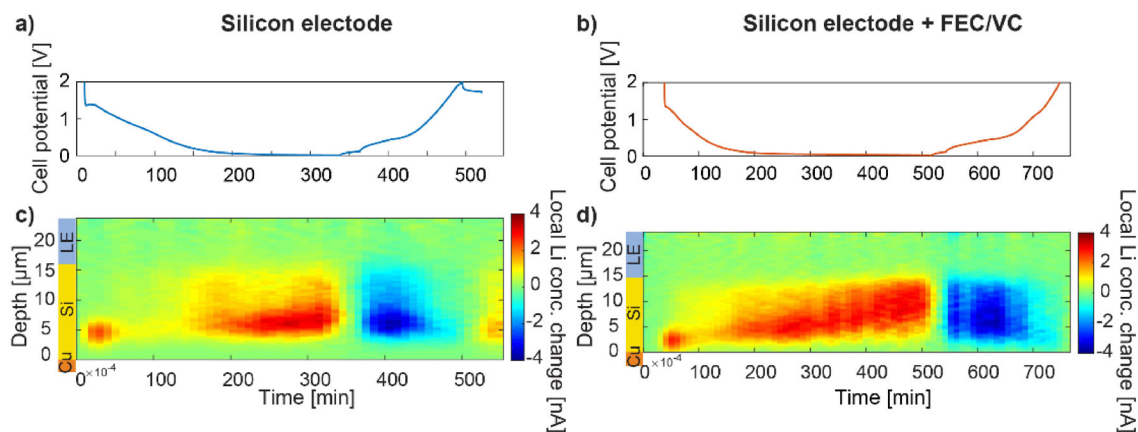


**Figure 3. | Impact of electrolyte additive VC and FEC on change in Li distribution during the first electrochemical cycle. a) and b)** Demonstrated the electrochemical profile of a Si electrode without and with VC and FEC electrolyte additives, respectively. **c) and d)** Changes of Li distribution, in nA, during the first cycle for both electrodes.

To gain more insight in the impact of the VC and FEC electrolyte additives on the homogeneity during the first cycle, the (de)lithiation activity compared between the Si electrode with and without VC/FEC electrolyte additive, shown in **Figures 3c and 3d**, with the corresponding voltage profiles shown in **Figures 3a and 3b**, respectively. For both cases the first increase in positive change in Li concentration is detected at 1.4 V vs. Li/Li<sup>+</sup>. This is a consequence of charge consumption on the surface of the current collector which is covered with copper oxides (Cu<sub>2</sub>O/CuO). At this potential, they react with Li, leading to formation of metallic Cu<sup>0</sup> and Li<sub>2</sub>O<sup>46</sup>. For the Si electrode without VC/FEC additives, at 0.8 V vs. Li/Li<sup>+</sup> the decomposition of electrolyte solvents starts as reflected by the raise in local Li concentration change (1 nA) as can be seen in **Figure 3c**. This is followed by lithiation of Si, clearly demonstrated by accumulation of Li close to the current collector. In the presence of the VC/FEC electrolyte additive, shown in **Figure 3d**, a continuously increasing change in Li concentration is observed during

discharge. Moreover, this process already starts at approximately 1.2 V vs. Li/Li<sup>+</sup>. That is consistent with the decomposition of the FEC additive, creating a passivating layer of LiF<sup>47-51</sup>. This will suppress decomposition of the solvents at 0.8 V vs. Li/Li<sup>+</sup> and, instead, it is followed by the lithiation of Si. This process starts near the current collector, and progressively becomes more homogeneous the end of discharge. The presence of the VC/FEC electrolyte additives, as a result of a better passivating and thinner SEI layer appears to promote more homogeneous (de)lithiation as a function of electrode depth during the first cycles. Additionally, in the presence of VC/FEC additives, the reduced overpotential is observed, thereby allowing a larger discharge capacity before reaching voltage cut-off, which is in line with significantly larger Li concentrations achieved.

4

#### 4.2.3 Effect of VC/FEC on Li capacity and cell capacity

**Figures 4a and b** demonstrate the evolution of the Li mass measured with NDP, which is determined by integrating the Li amount over complete depth as a function of measurement time for Si electrode without and with VC/FEC electrolyte additive respectively. Initially, for both cases, the total amount of Li mass increases with each cycle, indicating incomplete charging and continued SEI formation. Overall, no difference in terms of Li accumulation in SEI in latter cycles. Additionally, the total amount of irreversible Li builds up upon each charge, indicating inactive Li in the Si electrode. Addition of VC/FEC results in a higher Li mass (**Fig. 4b**) compared to the bare electrolyte (**Fig. 4a**).

The capacity measured with NDP (Li capacity) is compared to the capacity measured by electrochemical cycling (cell capacity) and their difference is represented in a single column for each (dis)charge step (**Figs. 4c and d**). The red part is the difference between the two and thus represents the amount of electrons that are not associated with Li addition or extraction (redox reactions), thus reflecting a side reactions involving electrons. This could reflect electrolyte reduction during lithiation or

electrolyte oxidation during delithiation that does not involve Li, or alternatively it could indicate Li-loss during lithiation, or Li-gain during delithiation via another process. Spontaneous reactions, that do not involve electron transfer, may originate from the surface reaction of Si with the liquid electrolyte<sup>52</sup> or by partial dissolution upon cycling<sup>53</sup>. The results clearly indicate that more parasitic reactions occur upon in absence of electrolyte additives (**Fig. 4c**). Such changes can be associated with chemical dissolution of LiF or other Li species from the SEI layer<sup>54,55</sup>. More research is required to use the ability of NDP and pin down the exact mechanism. Most strikingly, the VC/FEC electrolyte additives (**Fig. 4d**) suppress these parasitic reactions, the chemical dissolution of SEI components as the difference between the Li capacity measured by NDP and the one electrochemically measured (cell capacity) disappears within a few cycles. The difference in cell capacity and Li capacity between lithiation and delithiation is observed at each cycle, and it is a direct indication that partially SEI components upon reduction are oxidation are reversible<sup>56</sup> or/and can be related to SEI “breathing”, as an origin of continuous consumption of electrolyte<sup>57</sup>. Previously reported fluctuations of this dynamic SEI were associated with varying Li<sup>+</sup>/EC concentration which was measured by changes in viscosity of the electrolyte and shear storage modulus. During lithiation and reduction of electrolyte a large part of side reactions that involves electrons may initiate dissolution and diffusion of SEI species into the electrolyte. Dissolved products are most likely diffuse out of the NDP observed window and potentially a reason for the increased viscosity previously reported<sup>56</sup>. Upon delithiation the higher cell capacity compared to Li capacity can be caused by (partial) oxidation of the electrolyte ( $\sim 2$  V vs. Li/Li<sup>+</sup>), and formation of a mixture of LiF and other species such as polymeric<sup>57</sup> and their solubility is lower (locally the Li-concentration increases in the electrolyte and SEI species within the electrode region seen by NDP).

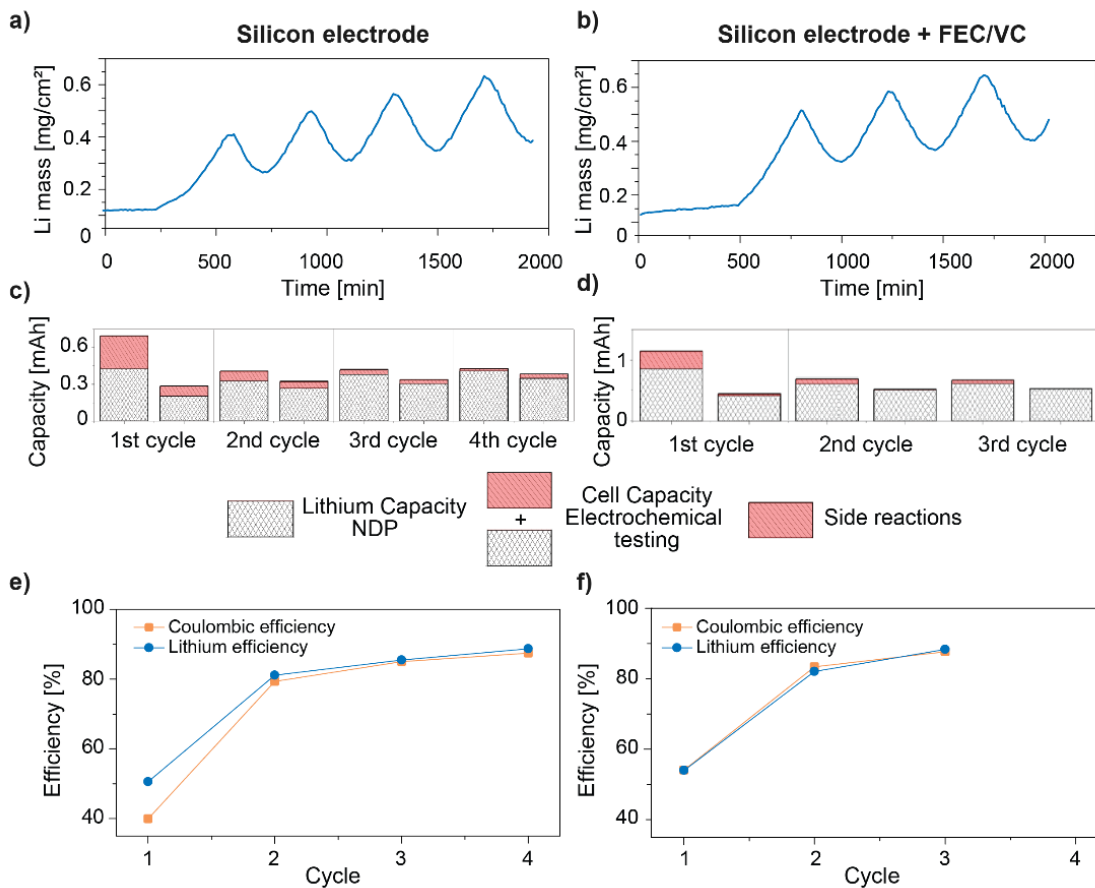


**Figure 4 | Impact of the electrolyte additive VC and FEC on evolution of Li mass, Li capacity, cell capacity, Li efficiency and coulombic efficiency. a) and b) Demonstrate integrated NDP data over complete depth as a function of time for electrodes without and with VC/FEC electrolyte additive respectively. c) and d) Illustrate Li capacity change from operando NDP compared to capacity from electrochemical data indicated as a column chart each representing one electrochemical step. Difference indicated in red, relates to contribution of electrons involved in the reaction. e) and f) Show the Li efficiency with coulombic efficiency of Si electrode and Si with VC/FEC electrolyte additive for the first cycles.**

The ratio of the total amount of Li during discharge and charge quantifies the Li efficiency of a single cycle (Figs. 4e and f). Because the chemical nature of Li cannot be distinguished by NDP, the Li efficiency reflects the amount of Li that is irreversibly captured by the Si and or SEI. Complementary to the Li efficiency, the coulombic efficiency is determined from the difference from



the measured charge and discharge capacities during cycling (**Figs. 4e and f**). As observed, both Li efficiency and coulombic efficiency are low in the first cycle in the absence of the electrolyte additives (**Fig. 4e**) compared to Si with VC/FEC electrolyte additive (**Fig. 4f**). Subsequent cycles shows comparable Li and coulombic efficiency. These results support the well-known impact of the VC/FEC electrolyte additives on the cycling stability of Si electrodes. The additives allow to utilise a much larger fraction of Si capacity which reduces overall stress gradient in the electrode by homogenising the large local volume expansion. This large difference in (de)lithiation homogeneity as a function of electrode depth during the initial cycles as observed in **Figure 1c** and **Figure 2b**, explains the improvement in electrochemical cycling.

### 4.3 Discussion

We propose that the high Li concentration near the current collector during the initial discharge is due to the initially poor electronic conductivity of the Si electrode. This will lead to an increasing potential moving from the current collector through the electrode towards the interface with the electrolyte/separator. Consequently, also the initial SEI formation will be initiated near the current collector, consistent with the Li concentration increase near the current collector above 0.8 V vs. Li/Li<sup>+</sup> seen in **Figure 3c**. In absence of electrolyte additives, uncontrolled SEI formation compromises the electronic contacts between Si/C and that supports the local lithiation near the current collector, and limits lithiation of the Si near separator. This local (inhomogeneous) lithiation enhances local Si degradation. Upon cycling, a combination of clogging of the porosity near the current collector and lithiation of the Si will promote lithiation progressively through the complete electrode, explaining the more homogenous lithiation that is observed upon cycling in **Figure 1c**, however still more located near current collector. Note that upon longer cycling, not investigated at present, the opposite mechanism is reported to become dominant, where clogging

compromises the ionic transport pathway, thus pushing the electrochemical activity towards the electrolyte/separator region. Thus, it is suggested that there exists an additional mechanism that comprises the cycling capacity, where the localised activity near the current collector deactivates part of the Si material during the initial cycles.

Upon addition of the FEC and VC additives, comparable inhomogeneous activity near the current collector is observed in **Figure 2b**, in line with the initially poor electronic conductivity of the Si electrode. However, the nature of the SEI is strongly affected by the FEC and VC electrolyte additive, which is well known to result in a more stable, electronically resistive and flexible SEI that improves cycling efficiency of Si negative electrodes. The higher resistivity of the SEI ( $1.4 \cdot 10^{10} \Omega \text{ cm}$ , 5 orders of magnitude higher)<sup>58</sup>, as compared to the SEI without FEC and VC ( $4.8 \cdot 10^5 \Omega \text{ cm}$ ), will prevent acceleration of SEI formation near the current collector. Moreover, the reduced overpotential will allow a large discharge capacity before reaching voltage cut-off, which is in line with larger Li concentrations achieved. As a consequence, the promotion of local SEI formation and lithiation of the Si, resulting in the strongly inhomogeneous lithiation, is circumvented. This can be expected to result in faster homogenisation of the lithiation activity, which is a self-supporting process as lithiation increases the electronic conduction of the Si. Based on these results it has been proposed that the nature of the SEI has a secondary effect in addition to the better quality SEI, namely the homogeneity of the lithiation during the initial cycling of Si negative electrodes, which contributes to a total irreversible capacity of Si electrodes.

## 4.4 Conclusions

Operando NDP is performed to gain insight into the role of homogeneity on the (de)lithiation in Si electrodes and its relation to SEI build up and on the cycle life. The Si electrode without any electrolyte additive demonstrated a Li gradient as function of depth, which gives an inhomogeneous Li

concentration profile in the first cycles. More inhomogeneous lithiation results in large volumetric changes being detrimental for the operation of Si electrodes. The highest Li concentration is observed close to the current collector, pinpointing limited electronic conductivity of Si particles at the beginning of the cycling. It is suggested that during the initial stages of cycling, that uncontrolled, larger amount of poorly electronically conductive SEI layer, compromises the electronic contacts between Si/carbons and that supports the local lithiation near the current collector and limits lithiation of Si near separator. This local inhomogeneous lithiation enhances local Si degradation. Addition of FEC and VC to the electrolyte is well-known to improve the cycling efficiency of Si electrodes due to the protective behaviour of LiF formed at the surface, because this LiF is more thermodynamically and kinetically stable and has a high electronic resistivity. This controlled and limited SEI growth allows more homogenous (de)lithiation, thus supporting a longer cycle life. Herein, the correlation between properties of SEI and homogeneity of the lithiation is suggested to play an important role in the cycle life. It is strongly suggested that the electronic conductivity in the initial cycling is a key parameter in determining longer cycle life of Si electrodes.

### 4.5 Methods

**Pouch cells for NDP measurements:** NDP measurements were conducted using pouch cells<sup>60-63</sup> with one copper window with a diameter of 18 mm and a thickness of 6  $\mu\text{m}$ . A window was cut in the outer layer of a coffee bag and the Si coated copper current collector substrate was heat-sealed to form a window<sup>64</sup>. Note that the current collector has a second function, functioning as a window to separate the in- from the outside, while being as thin as possible to limit parasitic energy losses<sup>65</sup>. In operando cells should be simple and use limited materials, as neutron activation instigate stable isotopes to emit radiation. The pouch cells introduce negligible background by other isotopes as they consist of plastic-coated aluminum foil. For these samples, relevant activating elements are isotopes of copper, silicon and aluminum. The copper foil however activates significantly through the neutron capture forming  $^{64}\text{Cu}$  and  $^{66}\text{Cu}$ , which have a half-life of 12.7 hours and 5 minutes,

respectively. Therefore, prior to disposal, samples are stored for 1 week<sup>32</sup>, giving these and other activated isotopes time to decay. Electrodes were prepared using a conventional slurry casting method. The dry components; active material (crystalline silicon powder with mean particle size distribution of 100 nm and 99% purity as specified by Alfa Aesar), carbon black (Super P, TIMCAL) and CMC binder (carboxymethyl cellulose, Sigma Aldrich) were mixed in a weight ratio of 0.6 : 0.2 : 0.2. All components were ball-milled at 250 rpm for 90 min in SiN<sub>4</sub> jar with 10 SiN<sub>4</sub> balls. 2 ml of buffer solution of citric acid/sodium hydroxide/sodium chloride solution with fungicide (pH = 3, Fluka) was used as a solvent to form a viscous slurry. The slurry was casted on a clean copper foil, cleaned with 0.1M oxalic acid and ethanol in circular shape with wet thickness of 25 μm. After sealing both current collectors and placing separators: 25 μm PE (Celgard 2250) against the working electrode and 300 μm glass fibre (Whatman), in size of 40x80 mm) and Teflon plate below working electrode (to ensure more pressure), pouch cells were dried overnight at 60°C. Pouch cells were assembled inside the glove box, in order to avoid reactions with oxygen and moisture (< 0.1 ppm O<sub>2</sub> and < 2 ppm H<sub>2</sub>O). <sup>6</sup>Li metal was used as a counter electrode (Aldrich, 95 wt. % <sup>6</sup>Li, 5 wt. % <sup>7</sup>Li, density 0.47 g cm<sup>-3</sup>). Two electrolytes were used for this experiment. Standard electrolyte 140 μl of 1.0 M LiPF<sub>6</sub> in 1:1 v/v ethylene carbonate (EC) and diethyl carbonate (DEC) (<15 ppm H<sub>2</sub>O, Sigma Aldrich) and 140 μl of 1.0 M LiPF<sub>6</sub> in 1:1 v/v EC:DEC 2 wt. % VC and 25 wt. % FEC. In order to increase count rate in the NDP experiments, the electrolyte was enriched with <sup>6</sup>Li metal by adding an excess of <sup>6</sup>Li metal with natural <sup>6</sup>Li abundancy of 7.5% in the electrolyte overnight. This increased the count rate by a factor of 13 as <sup>7</sup>Li is replaced by <sup>6</sup>Li<sup>38</sup>. After wetting the separator from both sides, the cell was left for 30 min to ensure wetting, afterwards the cell was sealed in sealer with vacuum (Audionvac VMS 153). Pouch cells were cycling from 0.01 to 2 V vs. Li/Li<sup>+</sup> at C/8. Current was calculated based on 800 mAh/g.

## 4.6 References:

- 1 Etacheri, V., Marom, R., Elazari, R., Salitra, G. & Aurbach, D. Challenges in the development of advanced Li-ion batteries: a review. *Energy & Environmental Science* **4**, 3243-3262 (2011).
- 2 Tarascon, J.-M. & Armand, M. in *Materials for Sustainable Energy* 171-179.
- 3 Liu, C., Neale, Z. G. & Cao, G. Understanding electrochemical potentials of cathode materials in rechargeable batteries. *Materials Today* **19**, 109-123 (2016).

- 4 Zuo, X., Zhu, J., Müller-Buschbaum, P. & Cheng, Y.-J. Silicon based lithium-ion battery anodes: A chronicle perspective review. *Nano Energy* **31**, 113-143 (2017).
- 5 Franco Gonzalez, A., Yang, N.-H. & Liu, R.-S. Silicon Anode Design for Lithium-Ion Batteries: Progress and Perspectives. *The Journal of Physical Chemistry C* **121**, 27775-27787 (2017).
- 6 Chen, C. *et al.* Origin of Degradation in Si-Based All-Solid-State Li-Ion Microbatteries. *Adv Energy Mater* **8**, 1801430 (2018).
- 7 Xu, Y. *et al.* A High-performance Li-ion Anode from Direct Deposition of Si Nanoparticles. *Nano Energy* **38** (2017).
- 8 Yu, C. *et al.* Silicon Thin Films as Anodes for High-Performance Lithium-Ion Batteries with Effective Stress Relaxation. *Adv Energy Mater* **2**, 68-73 (2012).
- 9 McDowell, M. T., Lee, S. W., Nix, W. D. & Cui, Y. 25th anniversary article: understanding the lithiation of silicon and other alloying anodes for lithium-ion batteries. *Advanced Materials* **25**, 4966-4985 (2013).
- 10 Wetjen, M. *et al.* Quantifying the Distribution of Electrolyte Decomposition Products in Silicon-Graphite Electrodes by Neutron Depth Profiling. *Journal of The Electrochemical Society* **165**, A2340-A2348 (2018).
- 11 Wetjen, M. *et al.* Monitoring the Lithium Concentration across the Thickness of Silicon-Graphite Electrodes during the First (De-)Lithiation. *Journal of The Electrochemical Society* **166**, A1408-A1411 (2019).
- 12 Balke, N. *et al.* Real Space Mapping of Li-Ion Transport in Amorphous Si Anodes with Nanometer Resolution. *Nano Letters* **10**, 3420-3425 (2010).
- 13 Obrovac, M. & Christensen, L. Structural changes in silicon anodes during lithium insertion/extraction. *Electrochemical and Solid State Letters* **7**, A93 (2004).
- 14 Ding, N. *et al.* Determination of the diffusion coefficient of lithium ions in nano-Si. *Solid State Ionics* **180**, 222-225 (2009).
- 15 Xu, C. *et al.* Improved Performance of the Silicon Anode for Li-Ion Batteries: Understanding the Surface Modification Mechanism of Fluoroethylene Carbonate as an Effective Electrolyte Additive. *Chemistry of Materials* **27**, 2591-2599 (2015).
- 16 Paul, N., Wetjen, M., Busch, S., Gasteiger, H. & Gilles, R. Contrast Matched SANS for Observing SEI and Pore Clogging in Silicon-Graphite Anodes. *Journal of The Electrochemical Society* **166**, A1051-A1054 (2019).
- 17 Pietsch, P., Hess, M., Ludwig, W., Eller, J. & Wood, V. Combining operando synchrotron X-ray tomographic microscopy and scanning X-ray diffraction to study lithium ion batteries. *Scientific reports* **6**, 27994 (2016).
- 18 Oumellal, Y. *et al.* The failure mechanism of nano-sized Si-based negative electrodes for lithium ion batteries. *Journal of Materials Chemistry* **21**, 6201-6208 (2011).
- 19 Radvanyi, E. *et al.* Failure mechanisms of nano-silicon anodes upon cycling: an electrode porosity evolution model. *Physical Chemistry Chemical Physics* **16**, 17142-17153 (2014).
- 20 Ryu, J. H., Kim, J. W., Sung, Y.-E. & Oh, S. M. Failure modes of silicon powder negative electrode in lithium secondary batteries. *Electrochemical and Solid State Letters* **7**, A306 (2004).

- 21 Zhu, B., Wang, X., Yao, P., Li, J. & Zhu, J. Towards high energy density lithium battery anodes: silicon and lithium. *Chemical science* **10**, 7132-7148 (2019).
- 22 Verma, P., Maire, P. & Novák, P. A review of the features and analyses of the solid electrolyte interphase in Li-ion batteries. *Electrochimica Acta* **55**, 6332-6341 (2010).
- 23 Zhang, S. S. A review on electrolyte additives for lithium-ion batteries. *Journal of Power Sources* **162**, 1379-1394 (2006).
- 24 Vogl, U. S. *et al.* The mechanism of SEI formation on a single crystal Si (100) electrode. *Journal of The Electrochemical Society* **162**, A603 (2015).
- 25 Michan, A. L. *et al.* Fluoroethylene carbonate and vinylene carbonate reduction: understanding lithium-ion battery electrolyte additives and solid electrolyte interphase formation. *Chemistry of Materials* **28**, 8149-8159 (2016).
- 26 Jin, Y. *et al.* Identifying the Structural Basis for the Increased Stability of the Solid Electrolyte Interphase Formed on Silicon with the Additive Fluoroethylene Carbonate. *J Am Chem Soc* **139**, 14992-15004 (2017).
- 27 Jin, Y. *et al.* Understanding Fluoroethylene Carbonate and Vinylene Carbonate Based Electrolytes for Si Anodes in Lithium Ion Batteries with NMR Spectroscopy. *J Am Chem Soc* **140**, 9854-9867 (2018).
- 28 Okuno, Y., Ushirogata, K., Sodeyama, K. & Tateyama, Y. Decomposition of the fluoroethylene carbonate additive and the glue effect of lithium fluoride products for the solid electrolyte interphase: an ab initio study. *Physical Chemistry Chemical Physics* **18**, 8643-8653 (2016).
- 29 Choi, N.-S. *et al.* Effect of fluoroethylene carbonate additive on interfacial properties of silicon thin-film electrode. *Journal of Power Sources* **161**, 1254-1259 (2006).
- 30 Whitney, S. M., Biegalski, S. R. F. & Downing, G. Benchmarking and analysis of 6Li neutron depth profiling of lithium ion cell electrodes. *Journal of Radioanalytical and Nuclear Chemistry* **282**, 173 (2009).
- 31 Oudenhoven, J. F. M. *et al.* In Situ Neutron Depth Profiling: A Powerful Method to Probe Lithium Transport in Micro-Batteries. *Advanced Materials* **23**, 4103-+ (2011).
- 32 Liu, M. *et al.* Efficient Li-Metal Plating/Stripping in Carbonate Electrolytes Using a LiNO<sub>3</sub>-Gel Polymer Electrolyte, Monitored by Operando Neutron Depth Profiling. *Chemistry of Materials* (2019).
- 33 Ziegler, J. F., Cole, G. W. & Baglin, J. E. E. Technique for determining concentration profiles of boron impurities in substrates. *Journal of Applied Physics* **43**, 3809-3815 (1972).
- 34 Fink, D. *Neutron Depth Profiling*. (Hahn-Meitner Institute fur Kernforschung, 1996).
- 35 Biersack, J. P., Fink, D., Henkelmann, R. & Müller, K. The use of neutron induced reactions for light element profiling and lattice localization. *Nuclear Instruments and Methods* **149**, 93-97 (1978).
- 36 Downing, R. *NIST Neutron Depth Profiling Facility: 2013*. Vol. 109 (2013).
- 37 Zhang, X. Y., Verhallen, T. W., Labohm, F. & Wagemaker, M. Direct Observation of Li-Ion Transport in Electrodes under Nonequilibrium Conditions Using Neutron Depth Profiling. *Adv Energy Mater* **5**, 1500498 (2015).

- 38 Verhallen, T. W., Lv, S. & Wagemaker, M. Operando Neutron Depth Profiling to Determine the Spatial Distribution of Li in Li-ion Batteries. *Frontiers in Energy Research* **6** (2018).
- 39 Liu, Z. *et al.* Relating the 3D electrode morphology to Li-ion battery performance; a case for LiFePO<sub>4</sub>. *Journal of Power Sources* **324**, 358-367 (2016).
- 40 Nagpure, S. C., Mulligan, P., Canova, M. & Cao, L. R. Neutron depth profiling of Li-ion cell electrodes with a gas-controlled environment. *Journal of Power Sources* **248**, 489-497 (2014).
- 41 Limthongkul, P., Jang, Y.-I., Dudney, N. J. & Chiang, Y.-M. Electrochemically-driven solid-state amorphization in lithium–metal anodes. *Journal of Power Sources* **119-121**, 604-609 (2003).
- 42 Zhang, J. *et al.* High-Coulombic-Efficiency Lithium Battery Based on Silicon Particle Materials. *Nanoscale Research Letters* **10**, 395 (2015).
- 43 Etacheri, V., Marom, R., Elazari, R., Salitra, G. & Aurbach, D. Challenges in the development of advanced Li-ion batteries: A review. *Energy and Environmental Science* **4**, 3243-3262 (2011).
- 44 Michan, A. L. *et al.* Solid electrolyte interphase growth and capacity loss in silicon electrodes. *Journal of the American Chemical Society* **138**, 7918-7931 (2016).
- 45 Lee, P.-K., Li, Y. & Denis, Y. Insights from studying the origins of reversible and irreversible capacities on silicon electrodes. *Journal of The Electrochemical Society* **164**, A6206-A6212 (2017).
- 46 Ferraresi, G., Czornomaz, L., Villevieille, C., Novak, P. & El Kazzi, M. Elucidating the Surface Reactions of an Amorphous Si Thin Film as a Model Electrode for Li-Ion Batteries. *ACS Appl Mater Interfaces* **8**, 29791-29798 (2016).
- 47 Lin, Y. M. *et al.* High performance silicon nanoparticle anode in fluoroethylene carbonate-based electrolyte for Li-ion batteries. *Chem Commun (Camb)* **48**, 7268-7270 (2012).
- 48 Etacheri, V. *et al.* Effect of fluoroethylene carbonate (FEC) on the performance and surface chemistry of Si-nanowire Li-ion battery anodes. *Langmuir* **28**, 965-976 (2012).
- 49 Dalavi, S., Guduru, P. & Lucht, B. L. Performance Enhancing Electrolyte Additives for Lithium Ion Batteries with Silicon Anodes. *Journal of The Electrochemical Society* **159**, A642-A646 (2012).
- 50 Jaumann, T. *et al.* Lifetime vs. rate capability: Understanding the role of FEC and VC in high-energy Li-ion batteries with nano-silicon anodes. *Energy Storage Materials* **6**, 26-35 (2017).
- 51 Li, Q. *et al.* Identification of the Solid Electrolyte Interface on the Si/C Composite Anode with FEC as the Additive. *ACS Appl Mater Interfaces* **11**, 14066-14075 (2019).
- 52 Veith, G. M. *et al.* Direct measurement of the chemical reactivity of silicon electrodes with LiPF<sub>6</sub>-based battery electrolytes. *Chemical Communications* **50**, 3081-3084 (2014).
- 53 Seidlhofer, B.-K. *et al.* Lithiation of Crystalline Silicon As Analyzed by Operando Neutron Reflectivity. *ACS Nano* **10**, 7458-7466 (2016).

- 54 Dupré, N. *et al.* Multiprobe study of the solid electrolyte interphase on silicon-based electrodes in full-cell configuration. *Chemistry of Materials* **28**, 2557-2572 (2016).
- 55 Marino, C. *et al.* Study of the Electrode/Electrolyte Interface on Cycling of a Conversion Type Electrode Material in Li Batteries. *The Journal of Physical Chemistry C* **117**, 19302-19313 (2013).
- 56 Kitz, P. G., Lacey, M. J., Novák, P. & Berg, E. J. Operando EQCM-D with Simultaneous in Situ EIS: New Insights into Interphase Formation in Li Ion Batteries. *Analytical Chemistry* **91**, 2296-2303 (2019).
- 57 Veith, G. M. *et al.* Direct determination of solid-electrolyte interphase thickness and composition as a function of state of charge on a silicon anode. *The Journal of Physical Chemistry C* **119**, 20339-20349 (2015).
- 58 Stetson, C. *et al.* Three-dimensional electronic resistivity mapping of solid electrolyte interphase on Si anode materials. *Nano Energy* **55**, 477-485 (2019).
- 59 Chen, Z., Danilov, D. L., Eichel, R.-A. & Notten, P. H. On the reaction rate distribution in porous electrodes. *Electrochemistry communications* **121**, 106865 (2020).
- 60 Yu, D. Y. W., Donoue, K., Inoue, T., Fujimoto, M. & Fujitani, S. Effect of electrode parameters on LiFePO<sub>4</sub> cathodes. *Journal of the Electrochemical Society* **153**, A835-A839 (2006).
- 61 Lv, S. *et al.* Operando monitoring the Lithium spatial distribution of Li-metal anodes. *Nature Communications*, in press (2018).
- 62 Mohanty, D. *et al.* Structural transformation of a lithium-rich Li<sub>1.2</sub>Co<sub>0.1</sub>Mn<sub>0.55</sub>Ni<sub>0.15</sub>O<sub>2</sub> cathode during high voltage cycling resolved by in situ X-ray diffraction. *Journal of Power Sources* **229**, 239-248 (2013).
- 63 Gustafsson, T., Thomas, J. O., Koksang, R. & Farrington, G. C. The polymer battery as an environment for in situ X-ray diffraction studies of solid-state electrochemical processes. *Electrochimica Acta* **37**, 1639-1643 (1992).
- 64 Villevieille, C. 183-232 (Elsevier, 2015).
- 65 Harks, P.-P. R. M. L. *et al.* Spatiotemporal Quantification of Lithium both in Electrode and in Electrolyte with Atomic Precision via Operando Neutron Absorption. *Journal of the American Chemical Society* **141**, 14280-14287 (2019).







# 5

---

Operando study of the performance  
of Si containing electrodes:  
its relation to the cycle life and the  
impact of various solid additives

---

### Abstract

Silicon is a promising candidate as a negative electrode owing to its high theoretical energy density of  $3579 \text{ mAhg}^{-1}$ . Nonetheless, the commercial use of Si is limited, in particular as a result of local volume expansion, poor electronic conductivity of Si and continuous growth of the SEI. Especially for Si negative electrodes, inhomogeneous lithiation challenges the cycle life and drives the degradation reactions. Inhomogeneous lithiation is related to the ability of the electrode to conduct ions and electrons. The electrode pores filled by the electrolyte can be considered as the ionic wiring and the solid components, the Si and the conductive additive as the electronic wiring. In this work solid additives are introduced into the Si electrode to improve the charge transport properties. We demonstrate through galvanostatic cycling that a Li-ion conductive solid additive such as  $\text{Li}_{1.5}\text{Al}_{0.5}\text{Ge}_{1.5}(\text{PO}_4)_3$  enhances the utilised capacity upon repeated cycling, and results in lower overpotentials with respect to bare Si. Using in operando NDP measurements we demonstrate that the solid additive results in a uniform distribution of Li across the electrode, and thus results in more reversible utilisation of the Si. Hence, this provides a high Li efficiency and thus less accumulation of decomposition products formed upon cycling. XPS analysis indicates that the solid additive decomposes before the decomposition of the electrolyte, forming Li-Ge, Li-P, and Li-Al. These decomposition products are suggested to provide ionic and electronic pathways that supports the charge transport from and towards the Si grains, therefore improving Li and electron capacity and efficiency. In a wider perspective, this research pinpoints the critical role of an ionic and electronic network on the performance of Si electrodes which can be manipulated by operando formation of solid electrolyte interphases.

## 5.1 Introduction

Driven by the electrification of mobile transport and the increasing demand for portable electronic devices, there is a growing need for battery materials with an increased energy density. Of further importance is the power density<sup>1</sup>, i.e. the rate at which this energy can be extracted, which requires facile charge transport of both ions and electrons through the battery electrode morphological structure and the active material<sup>2,3</sup>. This is especially critical for high capacity active materials since (dis)charging within the same C-rate requires much higher current densities. One of the most promising high capacity materials is Si. Owing to its high theoretical capacity of 3579 mAhg<sup>-1</sup>, its natural abundance and being environmentally benign, Si is an intensively studied negative electrode<sup>4-7</sup>. In practice however, the large volumetric expansion of up to 400% upon lithiation makes commercialisation of Si electrodes challenging. During repetitive (dis)charge cycles, the expansion of Si leads to the rupture of the passivating SEI and contact loss of active material, thereby inducing progressive electrolyte decomposition. Ultimately, this results in an increase of the impedance and capacity fading, which is problematic as facile ionic and electronic transport needs to be maintained during all stages of (dis)charge<sup>8,9</sup>. Nevertheless, little is known about the inhomogeneous activity in realistic Si negative electrodes, although it is expected that charge transport plays an important role. More homogeneous activity will reduce strain and thus the detrimental reactions that limit the cycle life. The common approach to mitigate this issue is by protecting the active material with oversized carbon or metal oxide cages to allow expansion and contraction while cycling<sup>10,11</sup>. It should be noted that despite the risk of electrochemical induced fracture, conformal coatings have shown appreciable cyclability<sup>12,13</sup>. Hence it could be argued that the introduction of electrochemically inactive components, i.e. a fractured coating, can be beneficial to the cycle life and electrode integrity.

The purpose of this chapter is to study the effect of solid additives to Si electrodes and in particular on electronic and ionic transport. In line with this, the importance of homogeneous lithiation it is shown as a critical factor for extending cycle life of Si electrodes. First, it is shown by using electrochemical measurements that adding a solid electrolyte substantially improves the capacity and charge efficiency. The ability to monitor the evolution of Li distribution upon cycling, as well as Li-ion transport is crucial, this is however experimentally challenging as it inherently requires operando measurements, and preferably direct probing of Li. In operando NDP measurements on electrodes with the state-of-the-art (best performing) additive,  $\text{Li}_{1.5}\text{Al}_{0.5}\text{Ge}_{1.5}(\text{PO}_4)_3$  (LAGP), reveal that the improved performance is related to a more uniform distribution of Li in the electrode with additive as compared to the reference Si electrode. In addition, the NDP measurements indicate reversible utilisation of the Si electrode and less SEI layer growth. Using XPS we show that commonly observed resistive decomposition products are not present in the electrode with the LAGP solid electrolyte additive. Most importantly, the XPS results after etching, i.e. the bulk of the electrode, reveal that LAGP decomposes, which is suggested to result in an improved SEI. As such, this chapter focusses on the understanding of the role of charge transport by addition of inorganic materials to Si electrodes, so as to achieve homogeneous lithiation as a criterion in extending the cycle life of Si electrodes.

## 5.2 Results

### 5.2.1 Impact of solid additives on electrochemical cycling

To test whether Si electrodes mixed with additives in the electrode can significantly improve charge transport properties, C-rate tests are performed. The additives are chosen based on different charge transport properties, as they have been used as coating materials, such as electron conductive copper (Cu)<sup>12,14</sup>, electron insulating alumina ( $\text{Al}_2\text{O}_3$ )<sup>15</sup>, electron

and ion conductive  $\text{Li}_4\text{Ti}_5\text{O}_{12}$  (LTO)<sup>16</sup> and titanium oxide ( $\text{TiO}_2$ ). Notice that  $\text{TiO}_2$  is a semiconductor but a poor ionic conductor<sup>11,17</sup>, nevertheless after lithiation it is capable to conduct Li-ions. In addition, a far superior ion conductor ( $10^{-4}$ – $10^{-3}$   $\text{S}\cdot\text{cm}^{-1}$ )<sup>18</sup> but poor electronic conductor  $\text{Li}_{1.5}\text{Al}_{0.5}\text{Ge}_{1.5}(\text{PO}_4)_3$  (LAGP) is used as additive. Because of its high ionic conductivity and low electronic conductivity LAGP is often used as solid electrolyte in all solid state batteries<sup>19-21</sup>. The electrodes with additives are tested at varying C-rates and compared to a sample without additives to determine whether the additives have beneficial influence on the performance.

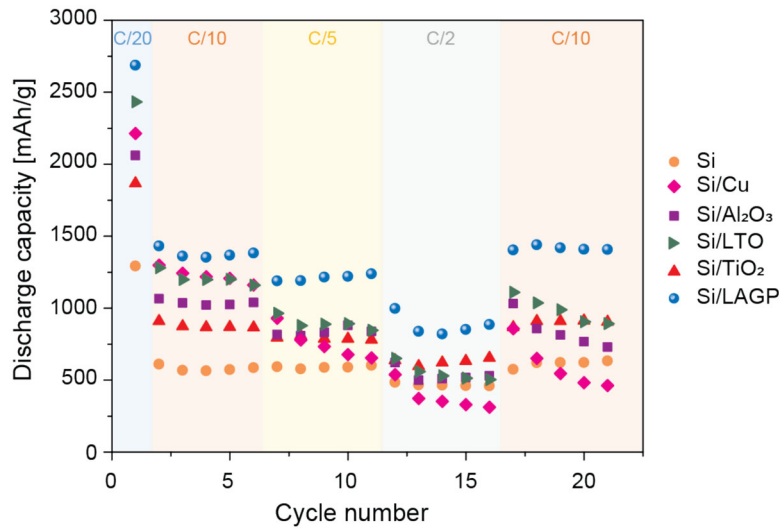


**Figure 1 | Impact of solid additives on the cycling performance.** Rate capability of Si electrodes with solid additives. All additives such as  $\text{TiO}_2$ ,  $\text{Al}_2\text{O}_3$ , Cu, LTO exhibited improved cycling performance compare to bare Si. The electrode with LAGP has the highest capacity of  $1400 \text{ mAhg}^{-1}$ . Capacities are calculated based on Si weight and capacity of  $1500 \text{ mAhg}^{-1}$ , and recorded in a voltage window from 0.01 V and 1.2 V vs.  $\text{Li}/\text{Li}^+$ .

**Figure 1** displays the results of the electrochemical tests and shows that all additives show improvement at low C-rates with respect to bare Si. The copper composite (Si/Cu) exhibits an especially high capacity in the first few cycles, when electrodes were cycled at C-rates of C/20 and C/10, but performs no better than bare Si from cycle 12 onwards when higher C-rates

were used ( $C/2$ ). The electronic conductivity of this electrode is expected to be superior<sup>12</sup>, due to electron conductive network on the Si surface formed by the Cu additive, but can also lead to an increase in electrolyte decomposition rate, thereby instigating cell failure. The alumina composite (Si/ $\text{Al}_2\text{O}_3$ ) retains a lower capacity of  $1000 \text{ mAhg}^{-1}$  compared to other additives. Even though alumina is an inert additive, research on its use as a coating indicates that it improves cycling performance due to lower reactivity between electrode and electrolyte, preventing side reactions<sup>15</sup>. With the exception of the first cycle, the electrochemical response of the electrodes with LTO and  $\text{TiO}_2$  is similar: in both cases the performance is slightly better than that of the other additives. During the initial cycling Si/LTO has been superior, likely related to its higher electronic and ionic conductivity<sup>16</sup>. Most interesting, the biggest improvement is observed for the ionic conductive additive LAGP (Si/LAGP) delivering  $\sim 1400 \text{ mAhg}^{-1}$  after 20 cycles. This is approximately 1.5 times larger than for the second-best additives and 3 times larger than the bare Si electrode, thus indicating a substantially better performance. Even when the capacity drops to  $900 \text{ mAh/g}$  when the electrode is cycled at higher rates (cycle 11 – 16) ( $C/2$ ), the capacity recovers when the electrode is subsequently cycled at a lower rate of  $C/10$  reaching capacity of  $1400 \text{ mAhg}^{-1}$ . As the performance of the electrode with LAGP additive is superior compared to the electrodes with other additives, the focus is on the remainder of the analysis of this electrode. In order to get better understanding of the electrochemical processes involved upon the first cycles and their reversibility, the differential capacity curve is plotted in **Figure 2a and b** of the Si electrode, with and without LAGP solid additive for the first and third cycle, respectively.

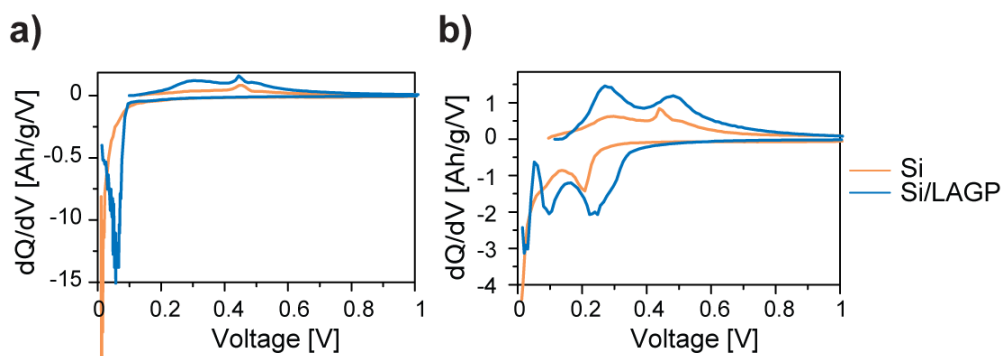


**Figure 2 | Evolution of lower (100 mV) and higher (250 mV) voltage process of Si electrode in comparison to Si electrode with LAGP solid additive. a) and b)** Differential capacity curves of Si electrode and Si/LAGP in 1M LiPF<sub>6</sub> in EC/DEC electrolyte with electrolyte additives (2 wt. % VC, 25 wt. % FEC) for the first and third cycle respectively.

The Si/LAGP electrode provides much higher capacity than the bare Si electrode and the two main processes, typical for lithiation of Si, can be clearly observed. The first process is the higher voltage process (250 mV), which is related to breaking the Si network and cluster formation ( $a\text{-Si} + 2\text{Li} \rightarrow a\text{-Li}_2\text{Si}$ ). The second process is a low voltage process (100 mV) and associated with the breakage of clusters and formation of isolated Si anions ( $a\text{-Li}_2\text{Si} + 1.5\text{Li} \rightarrow a\text{-Li}_{3.5}\text{Si}$ ). The decay in capacity of the electrode is the result of decreased capacity of higher voltage process at 250 mV<sup>22</sup> and that was observed for the Si electrode by the absence of higher voltage process. Si/LAGP electrodes provide reversible cycling of both phases, being a reason for improved performance for those cells.

5

### 5.2.2 Effect of solid additive on Li-density depth distribution

To further understand the limiting charge transport step in the Si electrodes with (Figs. 3b and d) and without LAGP solid additives (Figs. 3a and c), these two systems are studied with NDP<sup>23-25</sup>. NDP is a unique method that allows in operando quantification of the <sup>6</sup>Li concentration with approximately 1 μm resolution in depth (see Methods and Appendix)<sup>26</sup>. Figure 3a displays the NDP together with the simultaneously performed electrochemical



measurements on the Si reference electrode. In this figure, both the cell potential and the Li concentration profile in mol/L as a function of depth into the cell are plotted versus measurement time. A characteristic electrochemical response for crystalline Si is observed for both cells<sup>4,27</sup>. However, the Si electrode (**Fig. 3a**) presents gradual change in voltage associated with electrolyte decomposition reactions<sup>28,29</sup>.

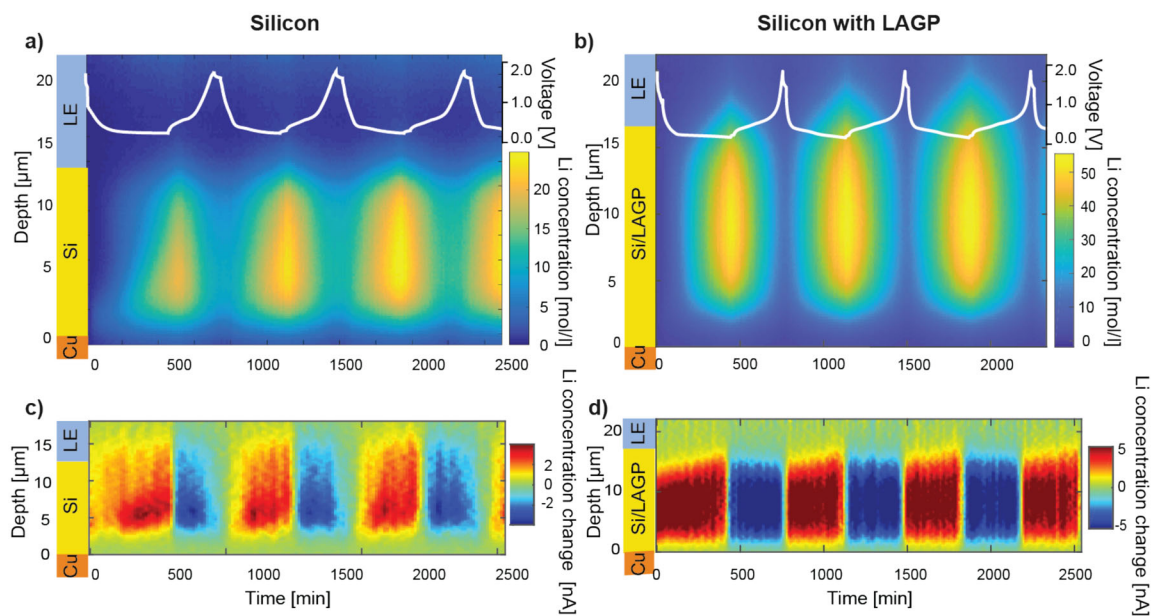


**Figure 3 | Operando NDP results showing the effect of solid additive on Li concentration depth distribution.** In operando NDP results obtained on bare Si electrode vs. Si electrode with LAGP solid additive referred as Si/LAGP. **a) and b)** The electrochemical response obtained during the measurement of Si electrode and Si/LAGP respectively, together with the measured Li concentration as a function of depth (average Li density integrated over  $1\text{cm}^2$ ). **c) and d)** Changes of  $^6\text{Li}$  distribution during each measurement of Si and Si/LAGP electrode respectively .

At the beginning of the measurement, the active material, i.e. pristine Si, is completely free of Li, hence the electrolyte is the sole Li source. In the Si electrode region (**Fig. 3a**), i.e. 1-14  $\mu\text{m}$ , a repeated increase/decrease of the Li concentration upon lithiation/delithiation is observed. Within the Si electrode, a gradient of Li concentrations can be discerned. The Si electrode exhibits a large Li concentration gradient and preferential lithiation close to the current collector, which is correlated with the limited electronic

conductivity of Si at the beginning of lithiation. Moreover, the Si electrode is not completely delithiated in each cycle. On the contrary, at each charge, the measured Li concentration increases, indicating an accumulation of dead Li, and thus can no longer be utilised. At the end of the charge the Li concentration is 10 mol/L and increases during subsequent cycling to 12 mol/L. The results on the Si/LAGP electrode shown in **Figure 3b** are strikingly different as compared with the Si electrode. The first difference is that lithiation occurs homogeneously throughout the depth of the electrode, the concentration gradient is practically absent within 1 – 16  $\mu\text{m}$  which indicates that lithiation of the electrode in this case proceeds via a single stage. In addition a higher Li concentration is reached (50 mol/l), homogeneously distributed, as clearly observed in **Figure 3b**. The higher and homogeneous Li-uptake appears also more reversible, as less dead Li accumulates after each charge. **Figure 3c and d** represents the time derivative of the Li concentration (each measurement is 10 min). The red colour signifies a positive change in Li concentration during lithiation (alloying of Si or SEI formation) of the electrode and blue corresponds to negative change in Li concentration (de-alloying of Si) during delithiation. As displayed in **Figure 3c**, a high positive concentration change is observed at 1.4 V vs. Li/Li<sup>+</sup>, which can be ascribed to surface reactions at the current collector, due to the formation of Li<sub>2</sub>O<sup>30</sup>. At the onset of discharge more Li is accumulated close to the current collector. The addition of LAGP is presented in **Figure 3d**, displaying homogeneous lithiation and delithiation, and thus suggesting that the volumetric changes of Si occur homogeneously throughout the electrode<sup>31,32</sup>. This then can explain the improved performance of the Si/LAGP electrodes, because large local volumetric changes associated with inhomogeneous lithiation drives the degradation reactions of Si electrodes. Another important aspect is the homogenous distribution of the decomposition products and LAGP itself in the electrode. That is shown in **Supplementary C Figure 1** with SEM/EDX.

## 5.2.3 Effect of solid additive on Li- capacity and electron capacity

The evolution of the total amount of Li in  $\text{Li}_x\text{Si}$  alloy upon cycling and Li build-up in SEI is evaluated for the Si electrode (**Fig. 4a**) and the Si/LAGP electrode (**Fig. 4b**). The evolution of the Li mass is determined by integrating the Li-density in **Figure 3a and 3b** over the complete depth as a function of measurement time.

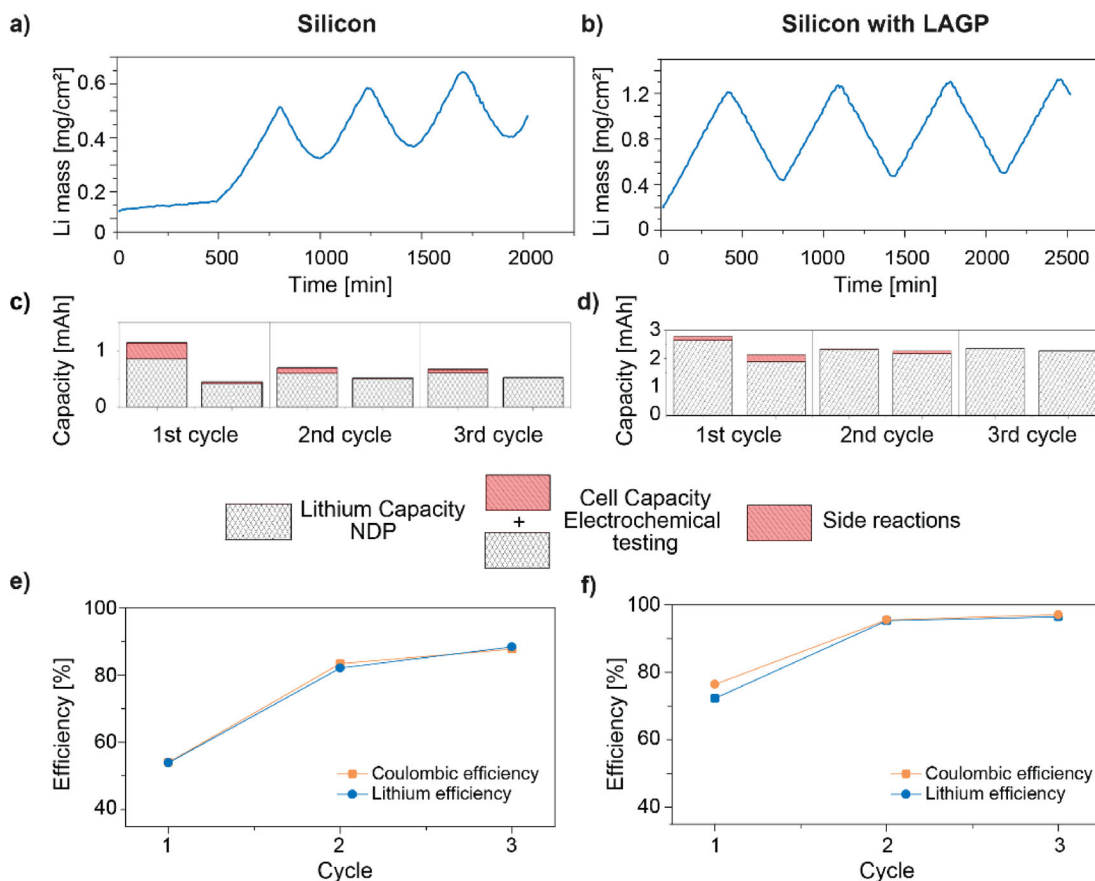


**Figure 4 | Impact of the solid additive to Si electrode on the Li mass, Li capacity and cell capacity.** **a) and b)** Demonstrates integrated NDP data over the complete depth as a function of time for the Si electrode and the Si/LAGP electrode respectively, and **c) and d)** Li capacity from operando NDP and capacity from electrochemical data indicated as a column chart of the Si electrode and Si/LAGP directly. **e) and f)** Li efficiency and Coulombic efficiency of Si and Si/LAGP electrode.

For the Si electrode (**Fig. 4a**), a large irreversible build-up of inactive Li is observed upon delithiation (especially in the first cycle). As a consequence

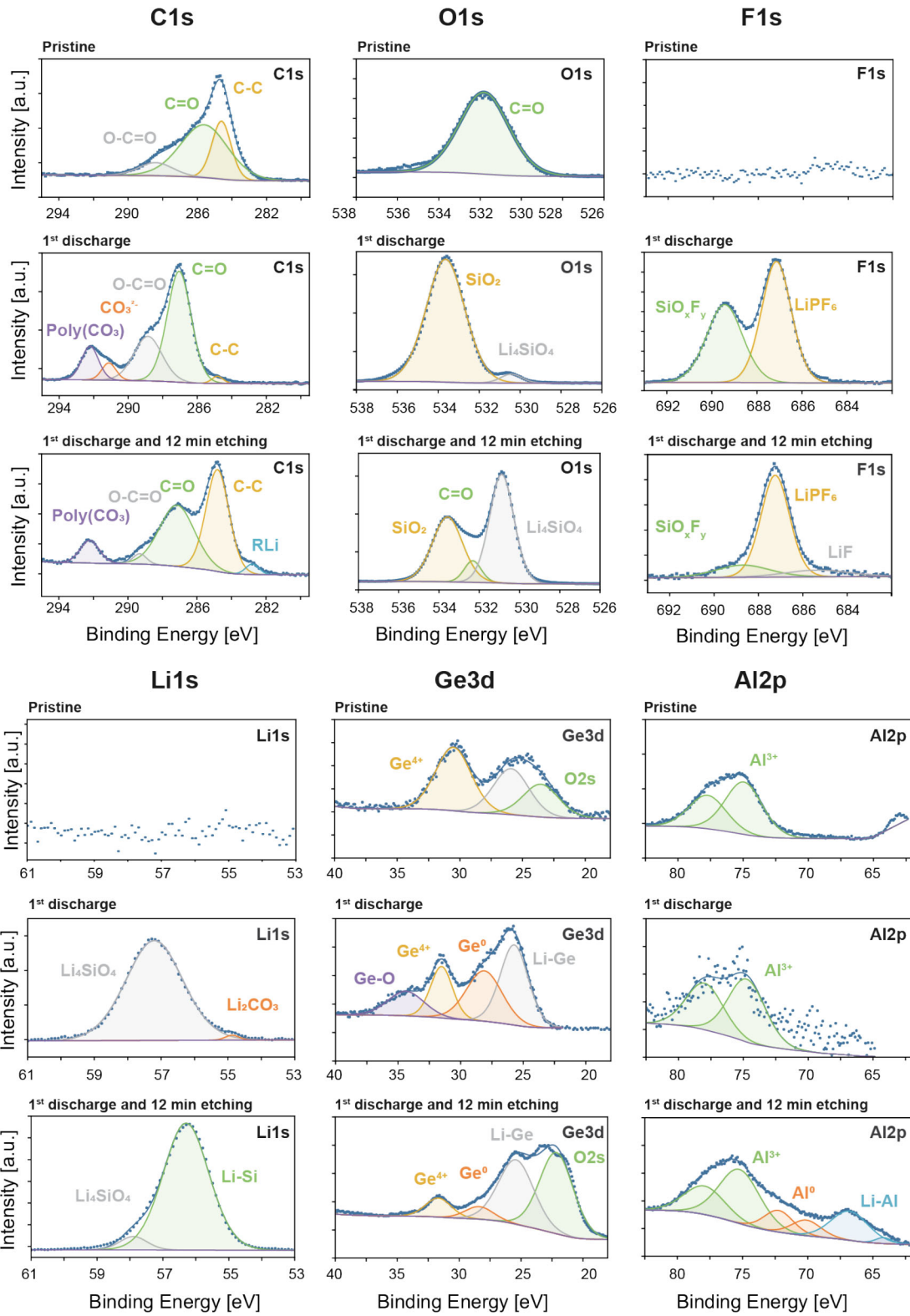
this results in a low Li efficiency as shown in **Figure 4e**. This continues upon each lithiation, reflecting the continuous build-up of SEI species upon cycling. The Si/LAGP electrode (**Fig. 4b**) displays much less build-up of inactive Li, resulting in a higher Li efficiency as can be seen in **Figure 4f**. The utilisation of Si is improved in line with less accumulation of irreversible Li-containing species upon cycling, all in line with the improved cycling observed as was already shown in **Figure 1**.

We compare the lithiation and delithiation capacity as measured with NDP (Li-capacity) and through electrochemical testing (cell capacity) in **Figure 4c, d**, where the difference between both capacities is indicated in red. During lithiation, the larger electron capacity may reflect direct electrolyte reduction reactions that do not involve Li, however typical electrolyte reduction reactions reported consume as much Li-ions as electrons<sup>33</sup>. Another possibility is dissolution of Li-containing SEI species, diffusion of which outside the volume observed by NDP can explain the lower Li-capacity. Also during delithiation the Li-capacity is smaller than the electron capacity, in this case potentially explained by partial oxidation of the electrolyte ( $\sim 2$  V vs. Li/Li<sup>+</sup>)<sup>34</sup>, or back diffusion of Li-containing species. Ex-situ methods have previously reported that LiF exposed to the electrolyte might redissolve during oxidation<sup>35</sup>, also reported by <sup>7</sup>Li NMR analysis<sup>36</sup>. In contrast, the present results indicate loss of Li-species during reduction, and gain in Li-species during oxidation (much less but similar to LiS electrodes where this is caused by dissolution/oxidation of polysulfides<sup>37</sup>, which demands detailed future investigations to unravel this mechanism). The smaller differences between electron and Li capacities demonstrate that this plays a much smaller role for Si/LAGP, as shown in **Figure 4d**. The ratio of the total amount of Li during discharge and charge quantifies the Li efficiency of a single cycle and additionally, the Coulombic efficiency is determined from the charge and discharge capacities upon cycling. (**Figure 4e, f**). Both efficiencies are higher upon adding LAGP, thus reflecting less SEI formation, which is the origin of the improved cycling performance.

### 5.2.4 Analysis of the LAGP decomposition (Ge3d, Al2p) and SEI formation (C1s, O1s, F1s) using XPS

We employ X-ray photoelectron spectroscopy (XPS) to gain a more detailed understanding on how LAGP solid electrolyte added into Si electrodes can improve the homogeneity of the lithiation. XPS measurements were performed on the pristine electrode (i.e. without electrolyte) and the same sample after being first discharge. In the latter case, we measured the sample after washing i.e. probing the SEI layer and after an additional etching of 2, 12, 22 minutes corresponding to approximately 60, 360, 660 nm. All etching procedures yielded similar results, indicating that all correspond to the bulk of the electrode, hence we focus our discussion on the measurements without etching and after 12 min of etching. **Figure 4** displays the XPS results. The C1s, O1s, F1s spectra demonstrate surface and bulk of the electrode components together with changes in the electrolyte after first discharge. Changes of the electrode and LAGP decomposition are presented based on Ge3d, Al2p and Li1s lines.

In the pristine electrode, the **C1s** lines corresponds to commonly observed species consisting of carbon black (C-C bond,  $E_{\text{bin}} \approx 284.6$  eV) and CMC binder (C=O,  $E_{\text{bin}} \approx 285.6$  eV and O-C=O,  $E_{\text{bin}} \approx 288.4$  eV)<sup>38</sup>. In the **O1s** spectra a peak at  $E_{\text{bin}} \approx 531.9$  eV corresponds to C=O groups present in CMC binder. **F1s** lines are not present since there is no electrolyte yet. In the **Ge3d** spectra, a sharp peak at  $E_{\text{bin}} \approx 30.5$  eV and another peak at  $E_{\text{bin}} \approx 25.9$  eV are observed, attributed to reduced Ge. The peak at  $E_{\text{bin}} \approx 23.5$  eV corresponds to O2s of LAGP. In the **Al2p** spectra is described by two components indicating Al2p composed of Al2p<sub>1/2</sub> and Al2p<sub>3/2</sub> due to spin-orbit coupling. Al2p<sub>1/2</sub> and Al2p<sub>3/2</sub> are observed at  $E_{\text{bin}} \approx 74.9$  and 77.7 eV binding energy corresponding to Al<sup>3+</sup> which is consistent with the primary LAGP reported previously<sup>39</sup>. The **Li1s** lines are not detected, due to very low Li contents in the sample.



5

Figure 5 | Degradation components on the surface of Si electrode with LAGP solid electrolyte additive, pristine and after first discharge Li both at the surface and at the bulk

**(12 min etching).** X-ray Photoelectron Spectroscopy (XPS) profiles of C1s, O1s, F1s spectra which focus on the electrolyte decomposition and Li1s, Ge3d, Al2p spectra with emphasis on LAGP decomposition.

The XPS results on the non-etched sample after the first discharge indicate that many of the commonly observed decomposition products ( $\text{Li}_2\text{O}$ ,  $\text{LiF}$ ) are not present in the electrode with LAGP solid electrolyte additive. Although the XPS results reveal the presence of small amount  $\text{Li}_2\text{CO}_3$ <sup>38</sup> on **C1s**, **Li1s** spectra (**C1s**,  $E_{\text{bin}} \approx 291.1$  eV and **Li1s**,  $E_{\text{bin}} \approx 54.87$  eV, 54.3 eV reported) as a result of EC-based solvents decomposition, the **O1s**, **F1s** spectra do not show any signal at 528 eV, 685 eV position where products such as  $\text{Li}_2\text{O}$  and  $\text{LiF}$  are to be expected.

In addition, the XPS measurements do show in the **C1s** spectra at  $E_{\text{bin}} \approx 292.2$  eV the presence of polyethylene carbonate  $(\text{CH}_2\text{CH}_2\text{OCOO})_n$ , referred to as poly( $\text{CO}_3$ )<sup>40,41</sup>. Ethylene carbonate (EC) molecules are likely to polymerise and as a result SEI is enriched with Poly( $\text{CO}_3$ ). Poly(EC) has fairly high molecular weight, so it may act as a flexible polymeric network which keeps all ionically conductive SEI components together<sup>41</sup>. This SEI layer enriched with poly(EC) can suppress the reactivity with electrolyte and promotes Li ion transport<sup>42</sup>. In the cycled electrode, on the **C1s** spectra, a peak corresponding to C-C is barely visible, due to coverage of the carbon surface with SEI products, so that higher photon energy (etching) is required to for deeper analysis. Moreover, the surface of Si covered with  $\text{SiO}_2$  ( $E_{\text{bin}} \approx 533.6$  eV), after first discharge, **O1s**, **Li1s**, **F1s**, **Si2p** spectra reveal the presence of lithiated surface  $\text{Li}_4\text{SiO}_4$  (**O1s**,  $E_{\text{bin}} \approx 530.4$  eV<sup>38</sup>, and **Li1s**,  $E_{\text{bin}} \approx 57.2$  eV), residue of the salt  $\text{LiPF}_6$  (**F1s**,  $E_{\text{bin}} \approx 687.1$  eV)<sup>29,38</sup> and fluorinated silicon oxide  $\text{SiO}_x\text{F}_y$  (**F1s**,  $E_{\text{bin}} \approx 689.4$  eV<sup>43</sup> and **Si2p**,  $E_{\text{bin}} \approx 105.5$  eV<sup>44</sup>). As a confirmation in **Si2p** lines presented in (**Supplementary C Fig. 2**) are observed, indicating formation of  $\text{SiO}_x\text{F}_y$  and they are in agreement with previous reports ( $E_{\text{bin}} = 106.5$  eV)<sup>45</sup>.  $\text{Li}_4\text{SiO}_4$  is formed as a result of lithiation of  $\text{SiO}_2$  ( $2\text{SiO}_2 + 4\text{Li} \rightarrow \text{Si} + \text{Li}_4\text{SiO}_4$ )<sup>46</sup>. And  $\text{SiO}_x\text{F}_y$  are formed due to reaction of  $\text{SiO}_2$  with  $\text{HF}$ <sup>44</sup>. And presence of  $\text{HF}$  resulted from hydrolysis of

the salt  $\text{LiPF}_6$ <sup>29</sup>. ( $\text{LiPF}_6 \leftrightarrow \text{LiF} + \text{PF}_5$ )( $\text{PF}_5 + \text{H}_2\text{O} \rightarrow \text{POF}_3 + 2\text{HF}$ ) . Presence of  $\text{LiPF}_6$  ensures the formation of HF and the consumption of  $\text{Li}_2\text{O}$  from the surface. In order to prevent these reactions, the main strategy is to replace the salt with one that is more stable towards hydrolysis, such as  $\text{LiFSI}$ <sup>45</sup>. Another strategy is to use VC additive as it may protect the surface of the Si particles from side reactions<sup>45</sup>. It has been shown that on graphite electrodes VC polymerises, form poly alkyl Li carbonate species which prevent salt anion reduction and solvent degradation<sup>47</sup>. In our case the fluorinated species have disappeared after the addition of VC, FEC electrolyte additive (**Supplementary C Fig. 3**).

In addition, the XPS results also show that after first discharge clear **Ge3d** lines can be assigned to unreacted  $\text{Ge}^{4+}$  at  $E_{\text{bin}} \approx 31.52$  eV, reduced Ge to  $\text{Ge}^0$  at  $E_{\text{bin}} \approx 28.1$  eV and even more reduced Li-Ge alloy at  $E_{\text{bin}} \approx 25.7$  eV. Similar peaks at  $E_{\text{bin}}$  28.5, 25.6, 23.5 eV observed in other reports<sup>48,49</sup>. The valence of Ge is the same as  $\text{Si}^{38}$  so we expect that formation of a Li-Ge alloy will result in lower binding energies<sup>18</sup>. The appearance of the line at higher binding energy of  $E_{\text{bin}} \approx 34.4$  eV, indicates the formation of a Ge compound in a different environment, perhaps Ge-O bond. Moreover, in the **Al2p** lines the intensity of the  $\text{Al}^{3+}$  species decreased strongly, which implies that Al present in LAGP reacted.

Notably, the XPS results after 12 min etching, i.e. roughly corresponding to the bulk of the electrode, **reveal that LAGP decomposes**. **Ge3d** lines are present at  $E_{\text{bin}} \approx 31.7$  eV ( $\text{Ge}^{4+}$ ),  $E_{\text{bin}} \approx 28.4$  eV ( $\text{Ge}^0$ ),  $E_{\text{bin}} \approx 25.4$  eV (Li-Ge), whereas  $E_{\text{bin}} \approx 22.2$  eV ( $\text{O}2s$ ) represents oxygen present in LAGP. The ratio of  $\text{Ge}^0$  and Li-Ge changed, indicating that  $\text{Ge}^0$  dominates at the surface and that most of the Ge from LAGP is reduced in the bulk through Li-Ge alloy. In the **Al2p** spectra, new Al components are detected at lower binding energies. The lines at  $E_{\text{bin}} \approx 72.2$  and 70.1 eV ( $\text{Al}2p_{1/2}$ ,  $\text{Al}2p_{3/2}$ ) can be attributed to the Al in a lower oxidation state ( $\text{Al}^0$ )<sup>50</sup>. Another new Al line at  $E_{\text{bin}} \approx 66.8$  and 64.2 eV ( $\text{Al}2p_{1/2}$ ,  $\text{Al}2p_{3/2}$ ) is likely to be correlated to a Li-Al alloy, since reduction will lead to lower binding energies as previously



mentioned. Cycled sample shows **P2p** line at  $E_{\text{bin}} \approx 138$  eV attributed to the residue of the salt  $\text{LiPF}_6$ <sup>51</sup>. At  $E_{\text{bin}} \approx 134$  eV lines are assigned to phosphate groups present in LAGP<sup>48</sup>. New lines of **P2p** at  $E_{\text{bin}} \approx 129$  eV that are an indication of P with the lower oxidation state and perhaps forms phosphides<sup>51,52</sup>.

In addition, SEI components present in the **C1s** spectra ( $E_{\text{bin}} \approx 282.8$  eV) include a small amount of carbide species (RLi) such as  $\text{LiCH}_2\text{CH}_2\text{OCO}_2\text{Li}$ <sup>42</sup>, a reduction product of ethylene carbonate<sup>47,53,54</sup>. The absence of  $\text{Li}_2\text{CO}_3$ , with higher photon energy means that it is not located deeper in the electrode (decomposition of  $\text{Li}_2\text{CO}_3$  occurred just on the surface). **O1s**, **Li1s**, **F1s**, spectra indicates the presence of C=O groups (**O1s**,  $E_{\text{bin}} \approx 532.3$  eV),  $\text{Li}_4\text{SiO}_4$  (**O1s**,  $E_{\text{bin}} \approx 530.9$  eV and **Li1s**,  $E_{\text{bin}} \approx 57.9$  eV) and  $\text{SiO}_2$  (**O1s**,  $E_{\text{bin}} \approx 533.6$  eV), presence of residual  $\text{LiPF}_6$  (**F1s**,  $E_{\text{bin}} \approx 687.4$  eV) originates from salt remaining in the porous of the electrode, the amount of  $\text{SiO}_x\text{F}_y$  species (**F1s**,  $E_{\text{bin}} \approx 689$  eV) decreased, signifying that those species are not present in the bulk. No peak at 685 eV (**F1s**) indicates the absence of LiF in the SEI, which contributes to the improved performance. And as we see more intensity in the bulk at the 56.29 eV **Li1s** peak, corresponding to a Li-Si alloy<sup>55</sup>. **Summarizing**, the SEI layer formed on the surface of the Si/LAGP is thin and **free from the main ion resistive decomposition products** of EC-based solvents such as  $\text{Li}_2\text{CO}_3$ ,  $\text{Li}_2\text{O}$  and decomposition of the salt such as LiF, having low ionic conductivities in the range of  $10^{-8} \text{ Scm}^{-1}$ <sup>56</sup>.

### 5.3 Discussion

The SEI in the Si/LAGP electrode is based on decomposition products of  $\text{Li}_{1.5}\text{Al}_{0.5}\text{Ge}_{1.5}(\text{PO}_4)_3$  formed at higher potentials than the SEI that forms upon reduction of the liquid electrolyte (1.0 M  $\text{LiPF}_6$  in 1:1 v/v EC:DEC) around 1V vs. Li/Li<sup>+</sup>. The amount of  $\text{Li}_{1.5}\text{Al}_{0.5}\text{Ge}_{1.5}(\text{PO}_4)_3$  used in the electrode material is relatively small (5 wt. %), resulting in a thin solid electrolyte interface containing LAGP decomposition products. This is demonstrated by XPS,

providing the chemical composition of the SEI by measuring C1s, O1s, F1s, of not etched samples and resulting in a solid electrolyte interface practically free from decomposition of the solvents, such as LiF, Li<sub>2</sub>O and Li<sub>2</sub>CO<sub>3</sub>. Moreover, XPS results prove complete reduction of LAGP, a consequence of the low applied potentials (down to 10 mV). Li<sub>1.5</sub>Al<sub>0.5</sub>Ge<sub>1.5</sub>(PO<sub>4</sub>)<sub>3</sub> will decompose towards Li<sub>15</sub>Ge<sub>4</sub>, Li<sub>3</sub>P, Li<sub>9</sub>Al<sub>4</sub>, Li<sub>2</sub>O<sup>57</sup> (based on the computational predictions of the formation energy of these products)<sup>48,49</sup>. Additional lines of Ge3d and Al2p at lower binding energy show the formation of Li-Ge and Li-Al alloys after deep discharge. The schematic degradation mechanism is shown in **Figure 6**. The degradation models of Si as previously described<sup>22,58,59</sup> are based on the decreased accessibility of Si grains and degradation of the ionic network. The limited cycled life is correlated to inhomogeneous lithiation, and Li accumulation close to the separator due to sluggish Li ion diffusion through clogged pores. However, from our studies based on NDP, inhomogeneous lithiation starts close to the current collector during the first cycles. This mechanism is presented in the **Figure 6a**. Addition of LAGP solid additive shows an improvement in uniform lithiation during the first cycles, schematically shown in **Figure 6b**, which is correlated with the infiltrated decomposition products in the SEI which are electron (Li-Al, Li-Ge) and ion (Li-P) conductors. We suggest that this is responsible for the homogenous lithiation throughout the electrode, improving both electron and Li efficiency. Thereby this research pinpoints the critical role of an ionic and electronic network on the performance of Si electrode, which effects the homogeneity of activity that dictates cycle life. This plays an important role already during the initial cycles, which can be improved by guided solid electrolyte interface formation.

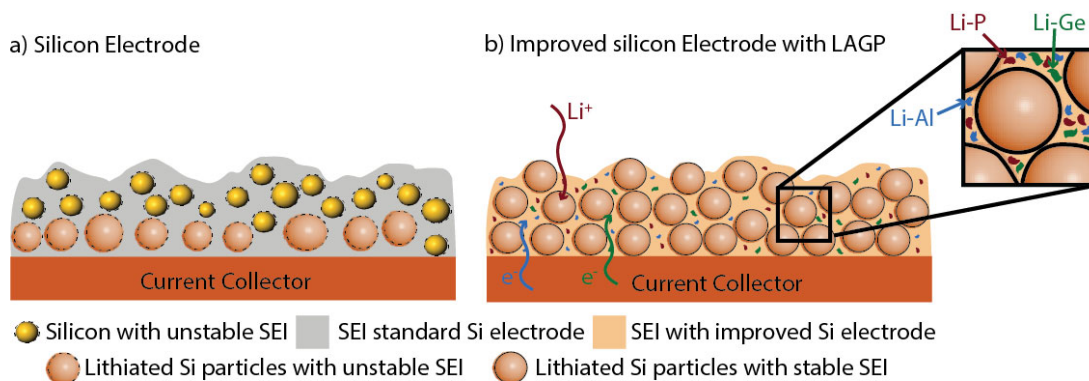


**Figure 6 | Schematic representation of degradation mechanism of Si electrode and its improvement with the solid inorganic additive. a)** Si electrode, where Si particles loose ionic contact, causing inhomogeneous lithiation which is responsible for degradation of Si electrodes. Lithiation starts from the current collector due to limited electronic conductivity of the pristine Si electrode, resulting in Li-rich alloys close to current collector. **b)** Morphology and charge transport has been improved due to the addition of the solid electrolyte LAGP additive to the electrode. This promotes the ionic and electronic wiring leading to homogeneous lithiation throughout the Si electrode.

## 5.4 Conclusions

In summary, to enable better ionic and electronic conduction, solid additives were introduced to Si electrodes, all showing improved cycling performance. The electrodes with Li-ion conductive solid additives such as LAGP demonstrate the highest capacity, charge efficiency and lowest overpotential. The solid electrolyte will decompose before decomposition of the electrolyte, which will introduce decomposition products of LAGP such as Li-Ge and Li-Al alloys into the SEI. These conductive materials are proposed to be vital for the transport network and improved cycle life. Operando NDP revealed that this is mainly attributed to the more homogenous distribution of Li through the whole electrode. This research pinpoints the critical role of the ionic network given by inorganic additive that promotes homogeneous activity throughout the electrodes, therefore improving Li capacity and charge efficiency.

## 5.5 Methods and Materials

### Preparation of Si electrodes - Coin-cells for C-rate test and XPS analysis:

The electrochemical measurements were conducted using coin-cells assembled in a glove-box filled with argon. The electrode slurry was prepared by ball-milling active material (crystalline silicon powder, mean particle size distribution of 100 nm, 99% purity, Alfa Aesar), with carbon black (Super P, TIMCAL) and binder (carboxymethyl cellulose, Mw = 90,000 g/mol, Sigma Aldrich) in a weight ratio of 0.6 : 0.2 : 0.2. For the electrode with solid additive the weight ratio was 0.54 : 0.06 : 0.2 : 0.2 Silicon : Solid additive : Carbon black : binder. Solid additives used for slurry were crystalline TiO<sub>2</sub> powder (< 1 μm) aluminum oxide (Al<sub>2</sub>O<sub>3</sub>, 99.99% purity, Sigma-Aldrich), copper powder (Sigma-Aldrich), lithium titanium oxide (LTO, Li<sub>4</sub>Ti<sub>5</sub>O<sub>12</sub> – grade EXM, SUD CHEMIE, size = 1-10 μm), and Li<sub>1.5</sub>Al<sub>0.5</sub>Ge<sub>1.5</sub>(PO<sub>4</sub>)<sub>3</sub> (LAGP, size = ~10 μm). All the components were ball-milled for 90 min at 250 rpm in SiN<sub>4</sub> jar with 10 SiN<sub>4</sub> balls. As a solvent, 2 ml of buffer solution of citric acid/sodium hydroxide/sodium chloride solution with fungicide (pH = 3, Fluka) was used. Slurry was casted on copper foil (cleaned with 0.1M oxalic acid and ethanol) with wet thickness of 100 μm and dried for 12h at 60°C in vacuum oven and subsequently cold-pressed under 2 tons for 1 minute. The coin-cells were assembled in an argon filled glove box, in order to avoid reactions with oxygen and moisture (< 0.1 ppm O<sub>2</sub> and < 2 ppm H<sub>2</sub>O) using polymer separator (Celgard 2250) and Li metal as a counter electrode (Sigma-Aldrich), which is washed with dimethyl carbonate (DMC) to remove the oxide layer and a 140 μl of 1.0 M LiPF<sub>6</sub> in 1:1 v/v ethylene carbonate (EC) and diethyl carbonate (DEC) (<15 ppm H<sub>2</sub>O, Sigma Aldrich) was added as an electrolyte for wetting both working and counter electrode surfaces.

**Pouch cells for NDP measurements:** Pouch cell<sup>60-63</sup> was made with one copper window with a diameter of 18 mm and thickness of 6 μm. The electrode slurry was prepared in the same way as for coin-cells, but casted in circular shape with wet thickness of 25 μm. A window was cut in the outer

layer of coffee bag and the Si coated copper current collector substrate was heat-sealed to form a window<sup>64</sup>. After sealing both current collectors and placing separators: 25  $\mu\text{m}$  PE (Celgard 2250) against the working electrode and 300  $\mu\text{m}$  glass fibre (Whatman), in size of 40x80 mm) and Teflon plate below working electrode (to ensure more pressure), pouch cells were dried overnight at 60°C. Pouch cells were assembled inside the glove box, in order to avoid reactions with oxygen and moisture (< 0.1 ppm O<sub>2</sub> and < 2 ppm H<sub>2</sub>O). <sup>6</sup>Li metal was used as a counter electrode (Aldrich, 95 wt. % <sup>6</sup>Li, 5 wt. % <sup>7</sup>Li, density 0.47 g cm<sup>-3</sup>). Two electrolytes were used for this experiment. Standard electrolyte 140  $\mu\text{l}$  of 1.0 M LiPF<sub>6</sub> in 1:1 v/v ethylene carbonate (EC) and diethyl carbonate (DEC) (<15 ppm H<sub>2</sub>O, Sigma Aldrich) and 140  $\mu\text{l}$  of 1.0 M LiPF<sub>6</sub> in 1:1 v/v EC:DEC 2 wt. % VC and 25 wt. % FEC. In order to increase count rate in the NDP experiments, the electrolyte was enriched with <sup>6</sup>Li metal by adding an excess of <sup>6</sup>Li metal with natural <sup>6</sup>Li abundance of 7.5% in the electrolyte overnight. This increased the count rate by factor of 13 by replacing <sup>7</sup>Li to <sup>6</sup>Li<sup>65</sup>. After wetting the separator from both sides, the cell was left for 30 min to ensure wetting, afterwards the cell was sealed in sealer with vacuum (Audionvac VMS 153).

**Synthesis of LAGP:** The solid electrolyte LAGP was synthesized by a conventional solid-state reaction method. The starting materials Li<sub>2</sub>CO<sub>3</sub> (99%, Alfa Aesar), Al<sub>2</sub>O<sub>3</sub> (AR, Nanjing Chemical Reagent Co. P. R. China), GeO<sub>2</sub> (99.999%, Sinopharm Chemical Reagent Beijing Co., P. R. China) and NH<sub>4</sub>H<sub>2</sub>PO<sub>4</sub> (99%, Aladdin) were first ball milled in ZrO<sub>2</sub> jar at 400 rpm for 4 h. Then the mixture was sintered at 600 °C for 1 h and 900 °C for 6 h, respectively. After each sintering process the same ball milling process was carried out<sup>66</sup>.

**Electrochemical cycling:** The battery performance was evaluated using Maccor 4000A battery cycler. Cells were cycled between 0.005 V and 1.5 V vs. Li/Li<sup>+</sup>. In the next cycles, the cut-off voltages were 0.01 V and 1.2 V. In the C-rate test, the cells were discharged in 0.1C, 0.2C, 0.5C, and back to 0.1C

for 5 cycles in each C-rate. For NDP measurements the current was calculated based on the silicon with the capacity of 800 mAh/g and voltage limit of 10 mV vs. Li/Li<sup>+</sup> to 2V at C/8.

**X-Ray Photoelectron Spectroscopy:** XPS spectrometer (K-Alpha ThermoFisher) equipped with a monochromatic (1486.6eV) anode operating at 36W (12 kV, 3mA) and flood gun operating at 1V, 100 $\mu$ . Al  $\alpha$  source and a spot-size of approx. 770 x 380  $\mu$ m<sup>2</sup> was used. The pressure in the chamber was 6.5 $\times$ 10<sup>-7</sup> mbar. Etching was done with a 3kV Ar<sup>+</sup> ion gun, with etching rate 0.5 nm s<sup>-1</sup>. The etching was done for 2, 12 and 22 min which corresponds to 60, 360 and 660 nm. Since 2, 12 and 22 min etching yielded in similar results, corresponding to the bulk of the electrode, just 12 min etching is presented. Cycled electrodes were washed with diethyl carbonate (DEC), dried in vacuum and placed in a XPS airtight sample holder inside the glove box to prevent air and moisture exposure and transferred within 10 minutes to the XPS spectrometer. The primary C1s peak was fixed at E<sub>bin</sub> = 284.8 eV as correction factor of the BE for the charge shift<sup>71</sup>. The peaks were fitted using 70% Gaussian and 30% Lorentzian line shapes (weighted least-squares fitting method) and nonlinear Shirley-type background.

## 5.6 References:

- 1 Jiang, Y. *et al.* Suitability of representative electrochemical energy storage technologies for ramp-rate control of photovoltaic power. *Journal of Power Sources* **384**, 396-407 (2018).
- 2 Liu, Z. *et al.* Relating the 3D electrode morphology to Li-ion battery performance; a case for LiFePO<sub>4</sub>. *Journal of Power Sources* **324**, 358-367 (2016).
- 3 Lennon, A. *et al.* High-rate lithium ion energy storage to facilitate increased penetration of photovoltaic systems in electricity grids. *MRS Energy & Sustainability* **6**, E2 (2019).
- 4 Zuo, X., Zhu, J., Müller-Buschbaum, P. & Cheng, Y.-J. Silicon based lithium-ion battery anodes: A chronicle perspective review. *Nano Energy* **31**, 113-143 (2017).
- 5 Franco Gonzalez, A., Yang, N.-H. & Liu, R.-S. Silicon Anode Design for Lithium-Ion Batteries: Progress and Perspectives. *The Journal of Physical Chemistry C* **121**, 27775-27787 (2017).
- 6 Chen, C. *et al.* Origin of Degradation in Si-Based All-Solid-State Li-Ion Microbatteries. *Adv Energy Mater* **8**, 1801430 (2018).

- 7 Xu, Y. *et al.* A High-performance Li-ion Anode from Direct Deposition of Si Nanoparticles. *Nano Energy* **38** (2017).
- 8 Wetjen, M. *et al.* Quantifying the Distribution of Electrolyte Decomposition Products in Silicon-Graphite Electrodes by Neutron Depth Profiling. *Journal of The Electrochemical Society* **165**, A2340-A2348 (2018).
- 9 Wetjen, M. *et al.* Monitoring the Lithium Concentration across the Thickness of Silicon-Graphite Electrodes during the First (De-)Lithiation. *Journal of The Electrochemical Society* **166**, A1408-A1411 (2019).
- 10 Zhang, Y. *et al.* Porous silicon in carbon cages as high-performance lithium-ion battery anode Materials. *Electrochimica Acta* **252**, 438-445 (2017).
- 11 Jeong, G. *et al.* Core-Shell Structured Silicon Nanoparticles@TiO<sub>2</sub>-x/Carbon Mesoporous Microfiber Composite as a Safe and High-Performance Lithium-Ion Battery Anode. *ACS Nano* **8**, 2977-2985 (2014).
- 12 Murugesan, S., Harris, J. T., Korgel, B. A. & Stevenson, K. J. Copper-Coated Amorphous Silicon Particles as an Anode Material for Lithium-Ion Batteries. *Chemistry of Materials* **24**, 1306-1315 (2012).
- 13 Lu, Z. *et al.* Nonfilling Carbon Coating of Porous Silicon Micrometer-Sized Particles for High-Performance Lithium Battery Anodes. *ACS Nano* **9**, 2540-2547 (2015).
- 14 Zhang, H. *et al.* In situ synthesis of multilayer carbon matrix decorated with copper particles: enhancing the performance of Si as anode for Li-ion batteries. *Acs Nano* **13**, 3054-3062 (2019).
- 15 He, Y., Yu, X., Wang, Y., Li, H. & Huang, X. Alumina-Coated Patterned Amorphous Silicon as the Anode for a Lithium-Ion Battery with High Coulombic Efficiency. *Advanced Materials* **23**, 4938-4941 (2011).
- 16 Babu, B. V. *et al.* Structural and electrical properties of Li<sub>4</sub>Ti<sub>5</sub>O<sub>12</sub> anode material for lithium-ion batteries. *Results in Physics* **9**, 284-289 (2018).
- 17 de Klerk, N., Vasileiadis, A., Smith, R., Bazant, M. & Wagemaker, M. Explaining key properties of lithiation in TiO<sub>2</sub> -anatase Li-ion battery electrodes using phase-field modeling. *Physical Review Materials* **1** (2017).
- 18 Liu, Y. *et al.* Germanium Thin Film Protected Lithium Aluminum Germanium Phosphate for Solid-State Li Batteries. *Advanced Energy Materials* **8**, 1702374 (2018).
- 19 DeWees, R. & Wang, H. Synthesis and Properties of NaSICON-type LATP and LAGP Solid Electrolytes. *ChemSusChem* **12**, 3713-3725 (2019).
- 20 Feng, J., Lu, L. & Lai, M. Lithium storage capability of lithium ion conductor Li<sub>1.5</sub>Al<sub>0.5</sub>Ge<sub>1.5</sub>(PO<sub>4</sub>)<sub>3</sub>. *Journal of Alloys and Compounds* **501**, 255-258 (2010).
- 21 Schwietert, T. *et al.* *The relationship between the redox activity and electrochemical stability of solid electrolytes for solid-state batteries.* (2019).
- 22 Michan, A. L. *et al.* Solid electrolyte interphase growth and capacity loss in silicon electrodes. *Journal of the American Chemical Society* **138**, 7918-7931 (2016).
- 23 Zhang, X. Y., Verhallen, T. W., Labohm, F. & Wagemaker, M. Direct Observation of Li-Ion Transport in Electrodes under Nonequilibrium Conditions Using Neutron Depth Profiling. *Adv Energy Mater* **5**, 1500498 (2015).

- 24 Whitney, S. M., Biegalski, S. R. F. & Downing, G. Benchmarking and analysis of 6Li neutron depth profiling of lithium ion cell electrodes. *Journal of Radioanalytical and Nuclear Chemistry* **282**, 173 (2009).
- 25 Oudenhoven, J. F. M. *et al.* In Situ Neutron Depth Profiling: A Powerful Method to Probe Lithium Transport in Micro-Batteries. *Advanced Materials* **23**, 4103-+ (2011).
- 26 Ziegler, J. F., Cole, G. W. & Baglin, J. E. E. Technique for determining concentration profiles of boron impurities in substrates. *Journal of Applied Physics* **43**, 3809-3815 (1972).
- 27 Limthongkul, P., Jang, Y.-I., Dudney, N. J. & Chiang, Y.-M. Electrochemically-driven solid-state amorphization in lithium–metal anodes. *Journal of Power Sources* **119-121**, 604-609 (2003).
- 28 Zhang, J. *et al.* High-Coulombic-Efficiency Lithium Battery Based on Silicon Particle Materials. *Nanoscale Research Letters* **10**, 395 (2015).
- 29 Xu, C. *et al.* Improved Performance of the Silicon Anode for Li-Ion Batteries: Understanding the Surface Modification Mechanism of Fluoroethylene Carbonate as an Effective Electrolyte Additive. *Chemistry of Materials* **27**, 2591-2599 (2015).
- 30 Ferraresi, G., Czornomaz, L., Villevieille, C., Novák, P. & El Kazzi, M. Elucidating the surface reactions of an amorphous Si thin film as a model electrode for Li-ion batteries. *ACS applied materials & interfaces* **8**, 29791-29798 (2016).
- 31 Jerliu, B. *et al.* Volume expansion during lithiation of amorphous silicon thin film electrodes studied by in-operando neutron reflectometry. *The Journal of Physical Chemistry C* **118**, 9395-9399 (2014).
- 32 Key, B., Morcrette, M., Tarascon, J.-M. & Grey, C. P. Pair distribution function analysis and solid state NMR studies of silicon electrodes for lithium ion batteries: understanding the (de) lithiation mechanisms. *Journal of the American Chemical Society* **133**, 503-512 (2011).
- 33 Seidlhofer, B.-K. *et al.* Lithiation of Crystalline Silicon As Analyzed by Operando Neutron Reflectivity. *ACS Nano* **10**, 7458-7466 (2016).
- 34 Kitz, P. G., Lacey, M. J., Novák, P. & Berg, E. J. Operando EQCM-D with Simultaneous in Situ EIS: New Insights into Interphase Formation in Li Ion Batteries. *Analytical chemistry* **91**, 2296-2303 (2018).
- 35 Marino, C. *et al.* Study of the Electrode/Electrolyte Interface on Cycling of a Conversion Type Electrode Material in Li Batteries. *The Journal of Physical Chemistry C* **117**, 19302-19313 (2013).
- 36 Dupré, N. *et al.* Multiprobe study of the solid electrolyte interphase on silicon-based electrodes in full-cell configuration. *Chemistry of Materials* **28**, 2557-2572 (2016).
- 37 Harks, P.-P. R. *et al.* Spatiotemporal Quantification of Lithium both in Electrode and in Electrolyte with Atomic Precision via Operando Neutron Absorption. *Journal of the American Chemical Society* **141**, 14280-14287 (2019).
- 38 Philippe, B. *et al.* Nanosilicon electrodes for lithium-ion batteries: interfacial mechanisms studied by hard and soft X-ray photoelectron spectroscopy. *Chemistry of Materials* **24**, 1107-1115 (2012).



- 39 Hartmann, P. *et al.* Degradation of NASICON-type materials in contact with lithium metal: formation of mixed conducting interphases (MCI) on solid electrolytes. *The Journal of Physical Chemistry C* **117**, 21064-21074 (2013).
- 40 Wang, Q. *et al.* Interface chemistry of an amide electrolyte for highly reversible lithium metal batteries. *Nature Communications* **11**, 1-11 (2020).
- 41 Zheng, J. *et al.* Electrolyte additive enabled fast charging and stable cycling lithium metal batteries. *Nature Energy* **2**, 1-8 (2017).
- 42 Zheng, J. *et al.* Highly stable operation of lithium metal batteries enabled by the formation of a transient high-concentration electrolyte layer. *Advanced Energy Materials* **6**, 1502151 (2016).
- 43 Pereira, J. *et al.* In situ x-ray photoelectron spectroscopy analysis of SiO<sub>x</sub>F<sub>y</sub> passivation layer obtained in a SF<sub>6</sub>/O<sub>2</sub> cryoetching process. *Applied Physics Letters* **94**, 071501 (2009).
- 44 Philippe, B. *et al.* Improved performances of nanosilicon electrodes using the salt LiFSI: a photoelectron spectroscopy study. *Journal of the American Chemical Society* **135**, 9829-9842 (2013).
- 45 Philippe, B. *et al.* Photoelectron spectroscopy for lithium battery interface studies. *Journal of The Electrochemical Society* **163**, A178 (2015).
- 46 Guo, B. *et al.* Electrochemical reduction of nano-SiO<sub>2</sub> in hard carbon as anode material for lithium ion batteries. *Electrochemistry Communications* **10**, 1876-1878 (2008).
- 47 Aurbach, D. *et al.* On the use of vinylene carbonate (VC) as an additive to electrolyte solutions for Li-ion batteries. *Electrochimica Acta* **47**, 1423-1439 (2002).
- 48 He, L. *et al.* Failure mechanism and interface engineering for NASICON-structured all-solid-state lithium metal batteries. *ACS applied materials & interfaces* **11**, 20895-20904 (2019).
- 49 Wang, L., Liu, D., Huang, T., Geng, Z. & Yu, A. Reducing interfacial resistance of a Li<sub>1.5</sub>Al<sub>0.5</sub>Ge<sub>1.5</sub>(PO<sub>4</sub>)<sub>3</sub> solid electrolyte/electrode interface by polymer interlayer protection. *RSC Advances* **10**, 10038-10045 (2020).
- 50 Bagus, P., Pacchioni, G. & Parmigiani, F. Surface core-level spectroscopy of Cu (100) and Al (100). *Physical Review B* **43**, 5172 (1991).
- 51 Reinhold, R. *et al.* Surface and Electrochemical Studies on Silicon Diphosphide as Easy-to-Handle Anode Material for Lithium-Based Batteries —the Phosphorus Path. *ACS applied materials & interfaces* **10**, 7096-7106 (2018).
- 52 Lin, L. *et al.* Lithium phosphide/lithium chloride coating on lithium for advanced lithium metal anode. *Journal of Materials Chemistry A* **6**, 15859-15867 (2018).
- 53 Aurbach, D., Markovsky, B., Weissman, I., Levi, E. & Ein-Eli, Y. On the correlation between surface chemistry and performance of graphite negative electrodes for Li ion batteries. *Electrochim. Acta* **45**, 67-86 (1999).
- 54 Ota, H. *et al.* Structural and functional analysis of surface film on Li anode in vinylene carbonate-containing electrolyte. *Journal of the Electrochemical Society* **151**, A1778 (2004).

- 55 Grehk, T., Johansson, L., Gray, S., Johansson, M. & Flodström, A. Absorption of Li on the Si (100)  $2 \times 1$  surface studied with high-resolution core-level spectroscopy. *Physical Review B* **52**, 16593 (1995).
- 56 Jiao, S. *et al.* Behavior of lithium metal anodes under various capacity utilization and high current density in lithium metal batteries. *Joule* **2**, 110-124 (2018).
- 57 Zhu, Y., He, X. & Mo, Y. Origin of Outstanding Stability in the Lithium Solid Electrolyte Materials: Insights from Thermodynamic Analyses Based on First-Principles Calculations. *ACS Applied Materials & Interfaces* **7**, 23685-23693 (2015).
- 58 Radvanyi, E. *et al.* Failure mechanisms of nano-silicon anodes upon cycling: an electrode porosity evolution model. *Physical Chemistry Chemical Physics* **16**, 17142-17153 (2014).
- 59 Oumellal, Y. *et al.* The failure mechanism of nano-sized Si-based negative electrodes for lithium ion batteries. *Journal of Materials Chemistry* **21**, 6201-6208 (2011).
- 60 Yu, D. Y. W., Donoue, K., Inoue, T., Fujimoto, M. & Fujitani, S. Effect of electrode parameters on LiFePO<sub>4</sub> cathodes. *Journal of the Electrochemical Society* **153**, A835-A839 (2006).
- 61 Lv, S. *et al.* Operando monitoring the Lithium spatial distribution of Li-metal anodes. *Nature Communications*, in press (2018).
- 62 Mohanty, D. *et al.* Structural transformation of a lithium-rich Li<sub>1.2</sub>Co<sub>0.1</sub>Mn<sub>0.55</sub>Ni<sub>0.15</sub>O<sub>2</sub> cathode during high voltage cycling resolved by in situ X-ray diffraction. *Journal of Power Sources* **229**, 239-248 (2013).
- 63 Gustafsson, T., Thomas, J. O., Koksang, R. & Farrington, G. C. The polymer battery as an environment for in situ X-ray diffraction studies of solid-state electrochemical processes. *Electrochimica Acta* **37**, 1639-1643 (1992).
- 64 Villevieille, C. 183-232 (Elsevier, 2015).
- 65 Verhallen, T. W., Lv, S. & Wagemaker, M. Operando Neutron Depth Profiling to Determine the Spatial Distribution of Li in Li-ion Batteries. *Frontiers in Energy Research* **6** (2018).
- 66 Cheng, Z. *et al.* Revealing the Impact of Space-Charge Layers on the Li-Ion Transport in All-Solid-State Batteries. *Joule* (2020).
- 67 Tabet, N., Faiz, M., Hamdan, N. & Hussain, Z. High resolution XPS study of oxide layers grown on Ge substrates. *Surface science* **523**, 68-72 (2003).

## 6 Appendix

## Supplementary A information of chapter 2

**Supplementary A Table 1** | Reduction voltages of elemental phosphorus towards  $\text{Li}_3\text{P}$  calculated from the stable configurations on the P convex hull. All energies are taken from the Materials Project database.

Phase	Voltage (V)
<b>P</b>	-
<b><math>\text{LiP}_7</math></b>	1.27
<b><math>\text{Li}_3\text{P}_7</math></b>	1.17
<b><math>\text{LiP}</math></b>	0.94
<b><math>\text{Li}_3\text{P}</math></b>	0.87

**Supplementary A Table 2** | Rietveld refinement of pristine  $\text{Li}_6\text{PS}_5\text{Cl}$  as at room temperature. Lattice parameter, fractional atomic coordinates, isotropic atomic displacement and site occupancies are refined.

$\text{Li}_6\text{PS}_5\text{Cl}$	Atom	X	Y	Z	Wyckoff	Occ.	Uiso ( $\text{\AA}^2$ )
<b>F-43m</b>	Li	0.1630	0.1630	-0.0082	48h	0.47	0.055
<b>a = 9.853</b>	P	0.5	0.5	0.5	4b	1.00	0.027
	S1	0.6223	0.6223	0.6223	16e	1.00	0.044
	S2	0.0	0.0	0.0	4c	0.53	0.040
	S3	0.25	0.25	0.25	4a	0.32	0.038
	Cl1	0.0	0.0	0.0	4c	0.47	0.028
	Cl2	0.25	0.25	0.25	4a	0.68	0.026

**Supplementary A Table 3** | Rietveld refinement of  $\text{Li}_6\text{PS}_5\text{Cl}$  in the LPSC-C electrode mixture at room temperature. Lattice parameter, fractional atomic coordinates, isotropic atomic displacement and site occupancies are refined.

$\text{Li}_6\text{PS}_5\text{Cl} - \text{C}$	Atom	X	Y	Z	Wyckoff	Occ.	Uiso ( $\text{\AA}^2$ )
<b>F-43m</b>	Li	0.1540	0.1540	0.0042	48h	0.47	0.663
<b>a = 9.869 \text{\AA}</b>	P	0.5	0.5	0.5	4b	1.00	0.128
	S1	0.6223	0.6223	0.6223	16e	1.00	0.056
	S2	0.0	0.0	0.0	4c	0.53	0.070
	S3	0.25	0.25	0.25	4a	0.32	0.040
	Cl1	0.0	0.0	0.0	4c	0.47	0.070
	Cl2	0.25	0.25	0.25	4a	0.68	0.040

**Supplementary A Table 4** | Refinements of the  $\text{Li}_6\text{PS}_5\text{Cl}$  structure in a  $\text{In}|\text{LPSC}|\text{LPSC-C}$  battery after 1<sup>st</sup> charge to 3.63 V vs  $\text{Li}/\text{Li}^+$ , as shown in Fig. 4. The **a**, cubic  $\text{Li}_6\text{PS}_5\text{Cl}$  structure and **b**, cubic  $\text{Li}_6\text{PS}_5\text{Cl}$  with a smaller lattice parameter are refined.

**Supplementary A Table 4a**

$\text{Li}_6\text{PS}_5\text{Cl}$ (1)	Atom	X	Y	Z	Wyckoff	Occ.	Uiso ( $\text{\AA}^2$ )
<b>F-43m</b>	Li	0.1257	0.1257	0.0334	48h	0.47	0.614
<b>a = 9.846 \AA</b>	P	0.5	0.5	0.5	4b	1.00	0.078
	S1	0.6299	0.6299	0.6299	16e	1.00	0.068
	S2	0.0	0.0	0.0	4c	0.53	0.020
	S3	0.25	0.25	0.25	4a	0.32	0.019
	Cl1	0.0	0.0	0.0	4c	0.47	0.020
	Cl2	0.25	0.25	0.25	4a	0.68	0.019

**Supplementary A Table 4b**

$\text{Li}_6\text{PS}_5\text{Cl}$ (2)	Atom	X	Y	Z	Wyckoff	Occ.	Uiso ( $\text{\AA}^2$ )
<b>F-43m</b>	Li	0.1540	0.1540	0.0042	48h	0.47	0.663
<b>a = 9.750 \AA</b>	P	0.5	0.5	0.5	4b	1.00	0.128
	S1	0.6223	0.6223	0.6223	16e	1.00	0.056
	S2	0.0	0.0	0.0	4c	0.53	0.070
	S3	0.25	0.25	0.25	4a	0.32	0.040
	Cl1	0.0	0.0	0.0	4c	0.47	0.070
	Cl2	0.25	0.25	0.25	4a	0.68	0.040

**Supplementary A Table 5** | Refinements of the  $\text{Li}_6\text{PS}_5\text{Cl}$  structure in a  $\text{In}|\text{LPSC}|\text{LPSC-C}$  battery after subsequent discharge to 0.63 V vs  $\text{Li}/\text{Li}^+$ , as shown in Fig. 4. The **a**, cubic  $\text{Li}_6\text{PS}_5\text{Cl}$  structure and **b**, cubic  $\text{Li}_6\text{PS}_5\text{Cl}$  with a smaller lattice parameter are refined.

**Supplementary A Table 5a**

$\text{Li}_6\text{PS}_5\text{Cl}$ (1)	Atom	X	Y	Z	Wyckoff	Occ.	Uiso ( $\text{\AA}^2$ )
<b>F-43m</b>	Li	0.1540	0.1540	0.0042	48h	0.47	0.620
<b>a = 9.857 \AA</b>	P	0.5	0.5	0.5	4b	1.00	0.085
	S1	0.6223	0.6223	0.6223	16e	1.00	0.129
	S2	0.0	0.0	0.0	4c	0.32	0.026
	S3	0.25	0.25	0.25	4a	0.47	0.025
	Cl1	0.0	0.0	0.0	4c	0.32	0.026
	Cl2	0.25	0.25	0.25	4a	0.68	0.025

Supplementary A Table 5b

Li <sub>6</sub> PS <sub>5</sub> Cl (2)	Atom	X	Y	Z	Wyckoff	Occ.	Uiso (Å <sup>2</sup> )
<b>F-43m</b>	Li	0.1540	0.1540	0.0042	48h	0.47	0.663
<b>a = 9.725 Å</b>	P	0.5	0.5	0.5	4b	1.00	0.128
	S1	0.6223	0.6223	0.6223	16e	1.00	0.056
	S2	0.0	0.0	0.0	4c	0.53	0.070
	S3	0.25	0.25	0.25	4a	0.32	0.040
	Cl1	0.0	0.0	0.0	4c	0.47	0.070
	Cl2	0.25	0.25	0.25	4a	0.68	0.040

**Supplementary A Table 6** | Refinements of the Li<sub>6</sub>PS<sub>5</sub>Cl structure in a In|LPSC|LPSC-C battery after 18 cycles, as shown in Fig. 4. The **a**, cubic Li<sub>6</sub>PS<sub>5</sub>Cl structure and **b**, cubic Li<sub>6</sub>PS<sub>5</sub>Cl with a smaller lattice parameter are refined.

Supplementary A Table 6a

Li <sub>6</sub> PS <sub>5</sub> Cl	Atom	X	Y	Z	Wyckoff	Occ.	Uiso (Å <sup>2</sup> )
<b>F-43m</b>	Li	0.1281	0.1281	-0.0398	48h	0.47	0.247
<b>a = 9.885 Å</b>	P	0.5	0.5	0.5	4b	1.00	0.135
	S1	0.6232	0.6232	0.6232	16e	1.00	0.052
	S2	0.0	0.0	0.0	4c	0.53	0.059
	S3	0.25	0.25	0.25	4a	0.32	0.030
	Cl1	0.0	0.0	0.0	4c	0.47	0.059
	Cl2	0.25	0.25	0.25	4a	0.68	0.036

Supplementary A Table 6a

Li <sub>6</sub> PS <sub>5</sub> Cl	Atom	X	Y	Z	Wyckoff	Occ.	Uiso (Å <sup>2</sup> )
<b>F-43m</b>	Li	0.1254	0.1254	0.0073	48h	0.47	0.329
<b>a = 9.720 Å</b>	P	0.5	0.5	0.5	4b	1.00	0.270
	S1	0.6234	0.6234	0.6234	16e	1.00	0.045
	S2	0.0	0.0	0.0	4c	0.53	0.026
	S3	0.25	0.25	0.25	4a	0.32	0.025
	Cl1	0.0	0.0	0.0	4c	0.47	0.026
	Cl2	0.25	0.25	0.25	4a	0.68	0.025

**Supplementary A Table 7a** | Refinements of the cubic  $\text{Li}_6\text{PS}_5\text{Cl}$  structure in a Li-In|LPSC|LPSC-C battery after **a**, 1<sup>st</sup> discharge to 0.63 V vs Li/Li<sup>+</sup>.

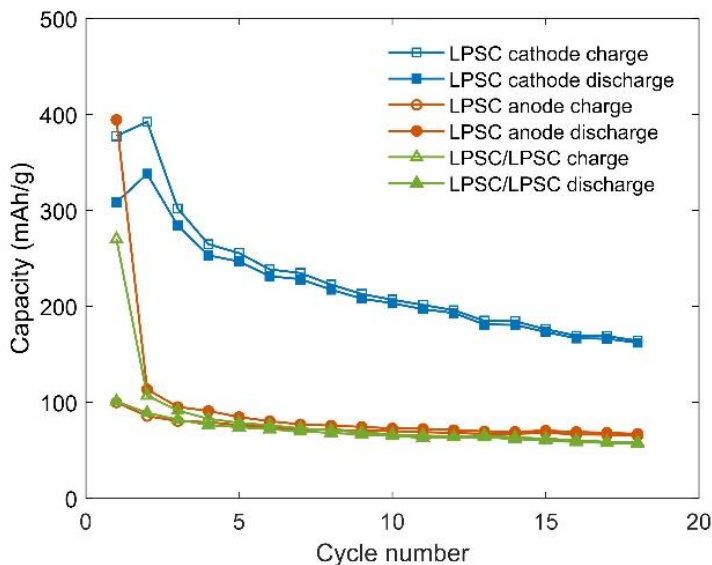
$\text{Li}_6\text{PS}_5\text{Cl}$	Atom	X	Y	Z	Wyckoff	Occ.	Uiso ( $\text{\AA}^2$ )
<b>F-43m</b>	Li	0.1947	0.1947	-0.0002	48h	0.44	0.014
<b>a = 9.861 \AA</b>	P	0.5	0.5	0.5	4b	1.00	0.105
	S1	0.6235	0.6235	0.6235	16e	1.00	0.058
	S2	0.0	0.0	0.0	4c	0.63	0.021
	S3	0.25	0.25	0.25	4a	0.37	0.025
	Cl1	0.0	0.0	0.0	4c	0.63	0.006
	Cl2	0.25	0.25	0.25	4a	0.37	0.128

**Supplementary A Table 7b** | Refinements of the cubic  $\text{Li}_6\text{PS}_5\text{Cl}$  structure in a Li-In|LPSC|LPSC-C battery after subsequent charge to 1.63 V vs Li/Li<sup>+</sup>.

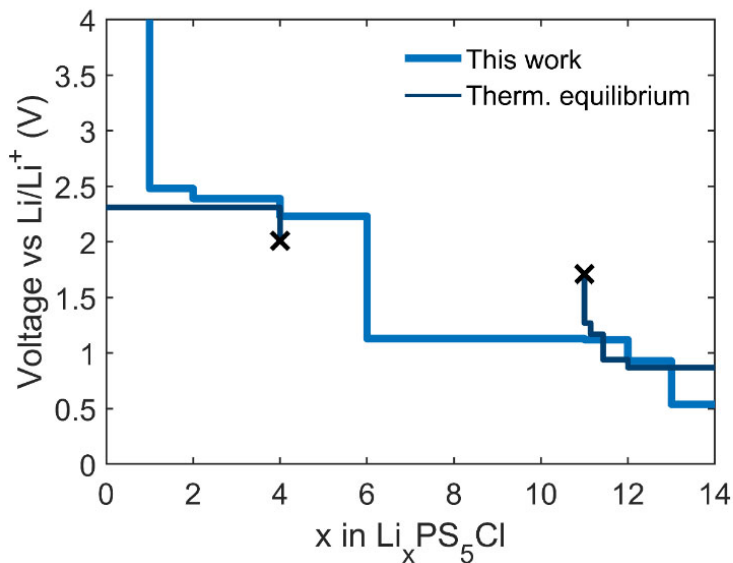
$\text{Li}_6\text{PS}_5\text{Cl}$	Atom	X	Y	Z	Wyckoff	Occ.	Uiso ( $\text{\AA}^2$ )
<b>F-43m</b>	Li	0.1860	0.1860	-0.0023	48h	0.44	0.025
<b>a = 9.871 \AA</b>	P	0.5	0.5	0.5	4b	1.00	0.050
	S1	0.6259	0.6259	0.6259	16e	1.00	0.039
	S2	0.0	0.0	0.0	4c	0.63	0.033
	S3	0.25	0.25	0.25	4a	0.37	0.021
	Cl1	0.0	0.0	0.0	4c	0.63	0.025
	Cl2	0.25	0.25	0.25	4a	0.37	0.007

**Supplementary A Table 7c** | Refinements of the cubic  $\text{Li}_6\text{PS}_5\text{Cl}$  structure in a Li-In|LPSC|LPSC-C battery after 18 full cycles.

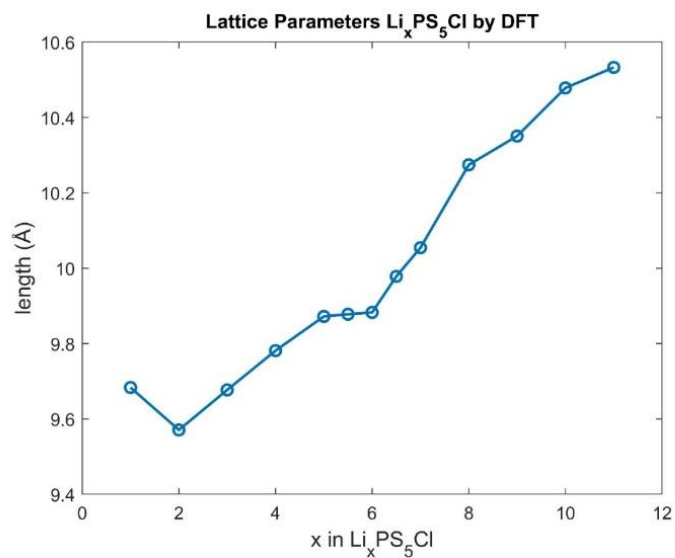
$\text{Li}_6\text{PS}_5\text{Cl}$ – C after 18 cycles	Atom	X	Y	Z	Wyckoff	Occ.	Uiso ( $\text{\AA}^2$ )
<b>F-43m</b>	Li	0.1996	0.1996	-0.0100	48h	0.44	0.001
<b>a = 9.855 \AA</b>	P	0.5	0.5	0.5	4b	1.00	0.130
	S1	0.6232	0.6232	0.6232	16e	1.00	0.100
	S2	0.0	0.0	0.0	4c	0.63	0.069
	S3	0.25	0.25	0.25	4a	0.37	0.296
	Cl1	0.0	0.0	0.0	4c	0.63	0.100
	Cl2	0.25	0.25	0.25	4a	0.37	0.014



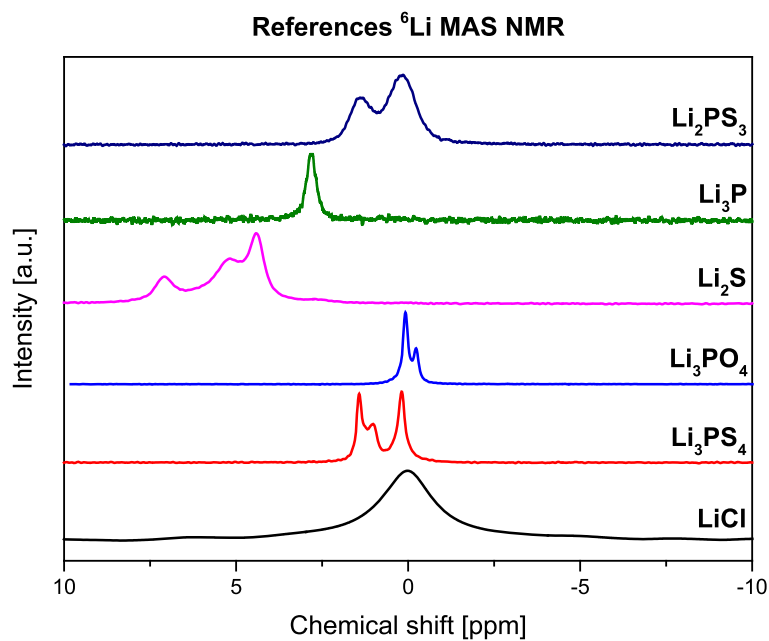
**Supplementary A Figure 1** | Cycling performance of In|LPSC|LPSC-C, Li-In|LPSC|LPSC-C and one material battery LPSC-C|LPSC|LPSC-C ASSBs.



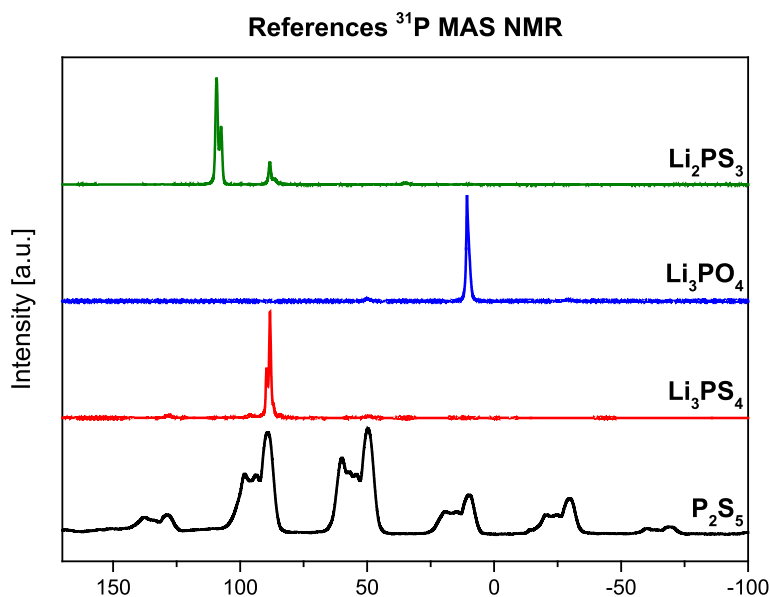
**Supplementary A Figure 2** | Calculated theoretical voltage profile, vs.  $\text{Li}/\text{Li}^+$ , of  $\text{Li}_x\text{PS}_5\text{Cl}$  in the compositional range of  $0 < x < 14$  and the theoretical voltage profile calculated at thermal equilibrium. The voltage window calculated in this work determines the initial voltage window achieving metastable decomposition (de)lithiated phases of  $\text{Li}_x\text{PS}_5\text{Cl}$ . The decomposition products i.e. P can follow the thermodynamic equilibrium voltages for further lithiation towards  $\text{Li}_3\text{P}$ .



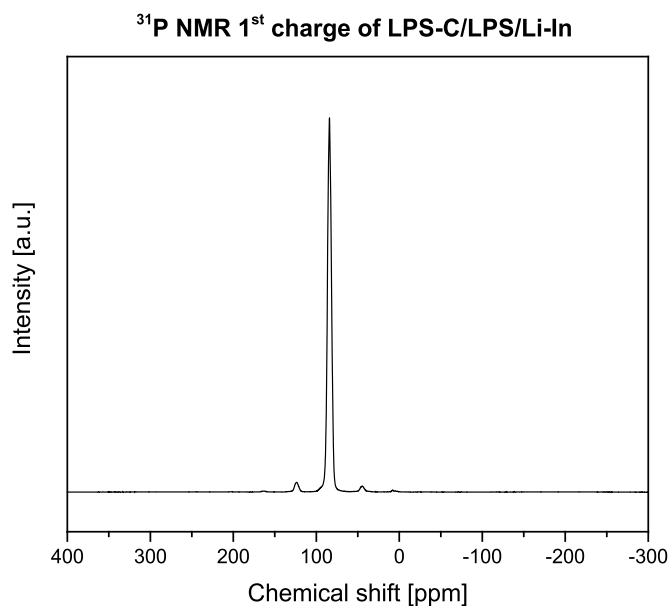
**Supplementary A Figure 3** | Lattice parameters of structures  $\text{Li}_x\text{PS}_5\text{Cl}$  ( $1 < x < 12$ ) calculated by DFT.



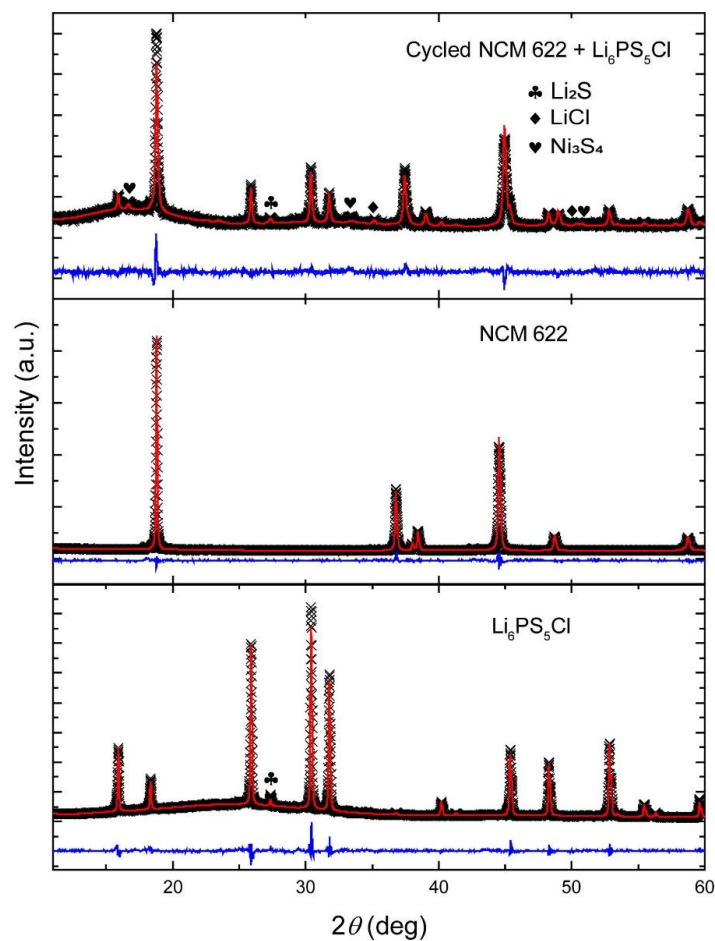




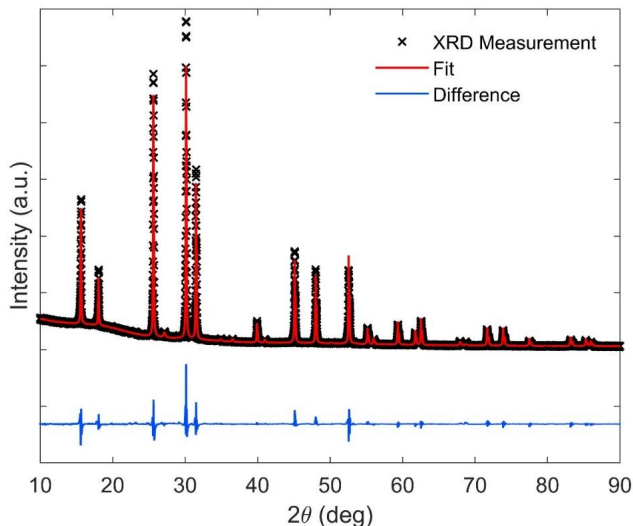
**Supplementary A Figure 4** |  $^6\text{Li}$  MAS NMR spectra of  $\text{LiCl}$ ,  $\text{Li}_3\text{PS}_4$ ,  $\text{Li}_3\text{PO}_4$ ,  $\text{Li}_2\text{S}$ ,  $\text{Li}_3\text{P}$ ,  $\text{Li}_2\text{PS}_3$  and  $^{31}\text{P}$  MAS NMR of  $\text{P}_2\text{S}_5$ ,  $\text{Li}_3\text{PS}_4$ ,  $\text{Li}_3\text{PO}_4$ ,  $\text{Li}_2\text{PS}_3$ .



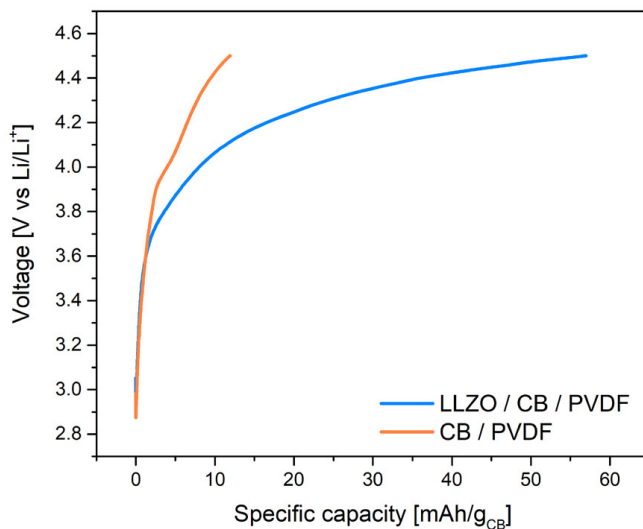
**Supplementary A Figure 5** |  $^{31}\text{P}$  MAS NMR spectra of anodic mixture of  $\text{Li}_6\text{PS}_5\text{Cl}$  in the  $\text{Li-In|LPSC|LPSC-C}$  solid-state batteries. The solid state cell, after complete cycle (discharge-charge) results in consumption of  $\text{Li}_3\text{P}$ , where no evidence of  $\text{Li}_3\text{P}$  was found at 220ppm.



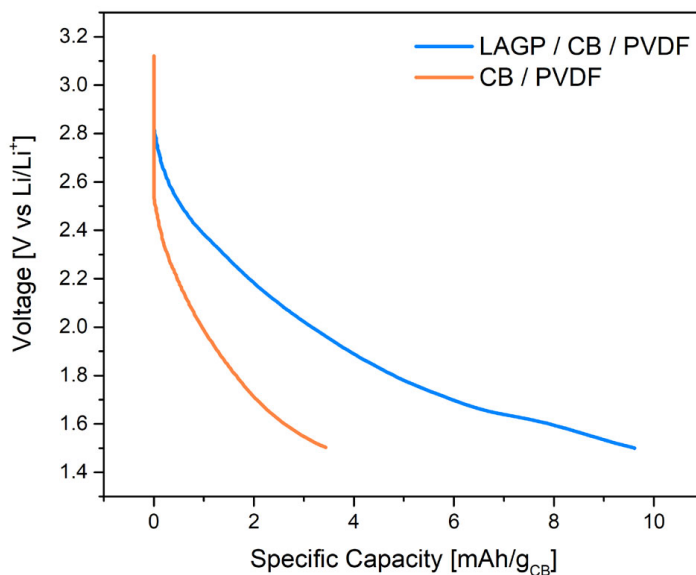
**Supplementary A Figure 6** | Post mortem XRD pattern and Rietveld refinement of an NCM622-cathode (47.5% NCM622 + 47.5%  $\text{Li}_6\text{PS}_5\text{Cl}$  + 5% Super P) after 50 cycles. Galvanostatic cycling was performed at a C/20 rate for a cathode| $\text{Li}_6\text{PS}_5\text{Cl}$ |In ASSB in the voltage range from 2.5 to 4.2 V vs.  $\text{Li}/\text{Li}^+$ . Diffractogram's with refinement of pristine NCM622 and  $\text{Li}_6\text{PS}_5\text{Cl}$  have been included for comparison. The  $\text{Ni}_3\text{S}_4$  phase that forms on cycling has been indicated in the figure.



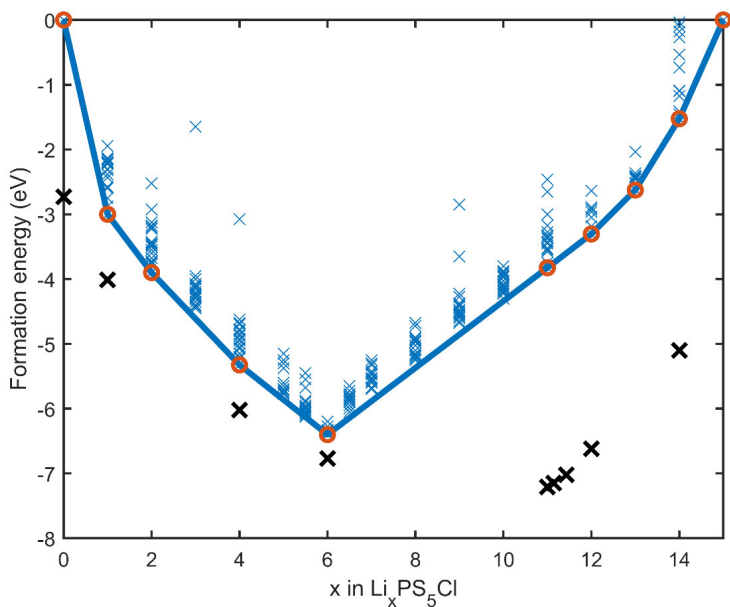
**Supplementary A Figure 7** | Rietveld refinement of the X-ray powder diffraction data of pristine  $\text{Li}_6\text{PS}_5\text{Cl}$  at room temperature.



**Supplementary A Figure 8a** | Voltage profiles during oxidation up to 4.5 V vs  $\text{Li}/\text{Li}^+$  with current of  $7.0 \mu\text{A}$  of the LLZO-C electrode and the blank carbon electrode. Electrochemical activity is observed above 3.6 V vs.  $\text{Li}/\text{Li}^+$ , indicating the oxidation of LLZO, consistent with previously redox activity observed<sup>1</sup>. The specific capacity is calculated based on weight of carbon black, which results in similar carbon black loading for LLZO-C and blank electrode. Blank test shows the capacity contribution of the side reactions and the additional capacity indicates the activity of LLZO.



**Supplementary A Figure 8b** | Voltage profiles during reduction up to 1.5 V vs Li/Li<sup>+</sup> with current of 7.0  $\mu$ A of the LAGP-C electrode and the blank carbon electrode. Electrochemical activity is observed below 2.4 V vs. Li/Li<sup>+</sup>, indicating the reduction of LAGP. The specific capacity is calculated based on weight of carbon black, which results in similar carbon black loading for LAGP-C and blank electrode. The blank test shows the capacity contribution of the side reactions and the additional capacity indicates the activity of LAGP.



**Supplementary A Figure 9** | Formation energies of Li-vacancy configurations of  $\text{Li}_x\text{PS}_5\text{Cl}$  (extended to  $x = 15$ ) and comparison of experimental and calculated voltage profiles. Formation energies per formula unit for all symmetrically non-equivalent Li configurations within one unit cell, versus the composition  $x$  in  $\text{Li}_x\text{PS}_5\text{Cl}$ . The formation energy of the combination of thermodynamically favourable decomposition are shown, in line with the decomposition products previously reported. The theoretical voltages are shown in Supplementary Figure 2.

Reference:

1 Han, F., Zhu, Y., He, X., Mo, Y. & Wang, C. Electrochemical Stability of  $\text{Li}_{10}\text{GeP}_2\text{S}_{12}$  and  $\text{Li}_7\text{La}_3\text{Zr}_2\text{O}_{12}$  Solid Electrolytes. *Adv. Energy Mater.* **6**, 1501590 (2016).

## Supplementary B Information of chapter 3

**Supplementary B Table 1** | Rietveld refinement of pristine Si and ALD-coated with TiO<sub>2</sub> at room temperature. Lattice parameter, fractional atomic coordinates, isotropic atomic displacement and site occupancies are refined.

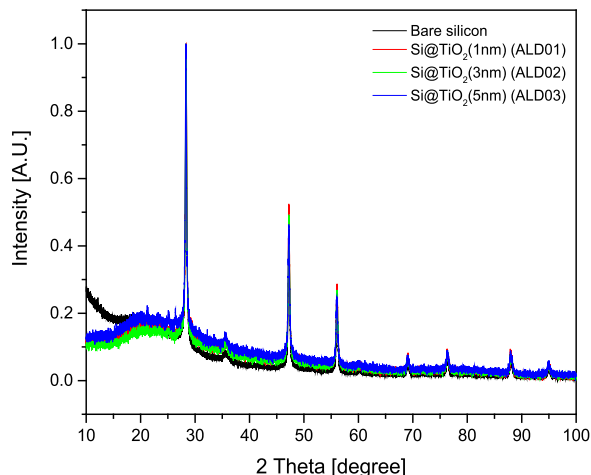
	Atom	X	Y	Z	Wyckoff	Occ.	Uiso (Å <sup>2</sup> )
<b>n-Si</b>	Si	0.125	0.125	0.125	8a	1.00	0.043220
<b>Fd-3m O2</b>							
<b>a = 5.427</b>							
<b>n-Si/a-TiO<sub>2</sub>-ALD-1</b>	Si	0.125	0.125	0.125	8a	1.00	0.043220
<b>Fd-3m O2</b>							
<b>a = 5.427</b>							
<b>n-Si/a-TiO<sub>2</sub>-ALD-3</b>	Si	0.125	0.125	0.125	8a	1.00	0.043220
<b>Fd-3m O2</b>							
<b>a = 5.427</b>							
<b>n-Si/a-TiO<sub>2</sub>-ALD-5</b>	Si	0.125	0.125	0.125	8a	1.00	0.043220
<b>Fd-3m O2</b>							
<b>a = 5.425</b>							

**Supplementary B Table 2** | Rietveld refinement of pristine Si coated with TiO<sub>2</sub> (Anatase) as at room temperature. Lattice parameter, fractional atomic coordinates, isotropic atomic displacement and site occupancies are refined.

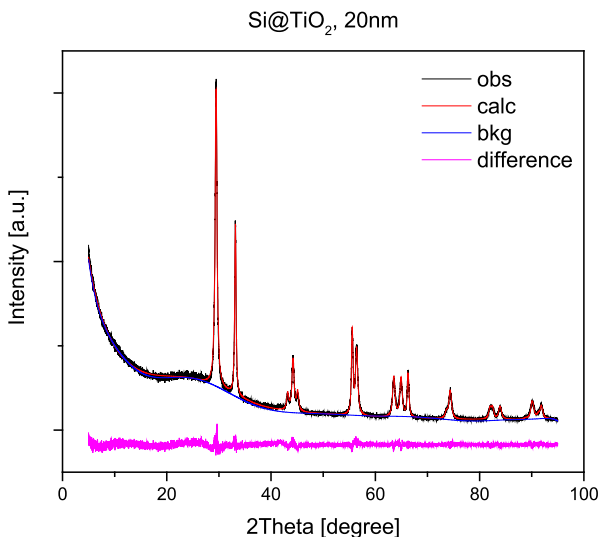
Si	Atom	X	Y	Z	Wyckoff	Occ.	Uiso (Å <sup>2</sup> )
<b>Fd-3m O2</b>	Si	0.125	0.125	0.125	8a	1.00	0.043220
<b>a = 5.427141</b>							

TiO <sub>2</sub>	Atom	X	Y	Z	Wyckoff	Occ.	Uiso (Å <sup>2</sup> )
<b>I41/amd O2</b>	O	0	0.25	0.167	8e	1.00	0.03013
<b>a = b = 3.784923</b>	Ti	0	0.25	0.375	4b	1.00	0.03013
<b>c = 9.506351</b>							

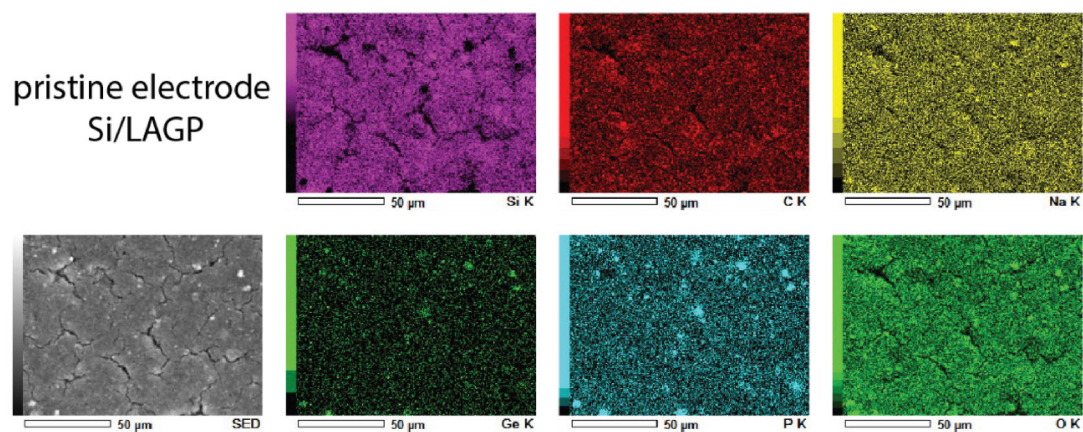
**Supplementary B Figure 1** | XRD pattern of Si coated with TiO<sub>2</sub> using ALD method. No visible changes of Si diffraction peaks suggest that TiO<sub>2</sub> does not influence the Si structure. The crystallinity and content of deposited TiO<sub>2</sub> is low – and thus not detected by XRD. Some amorphous phases are visible and correspond to silica. No changes in the lattice parameters and crystallite size were obtained (XRD refinement).



**Supplementary B Figure 2** | XRD pattern of Si coated with 20 nm TiO<sub>2</sub> layer and annealed under argon atmosphere at 450°C for 5h. Calculated particle size of Si is 35 nm, and particle size of Anatase is 21 nm.

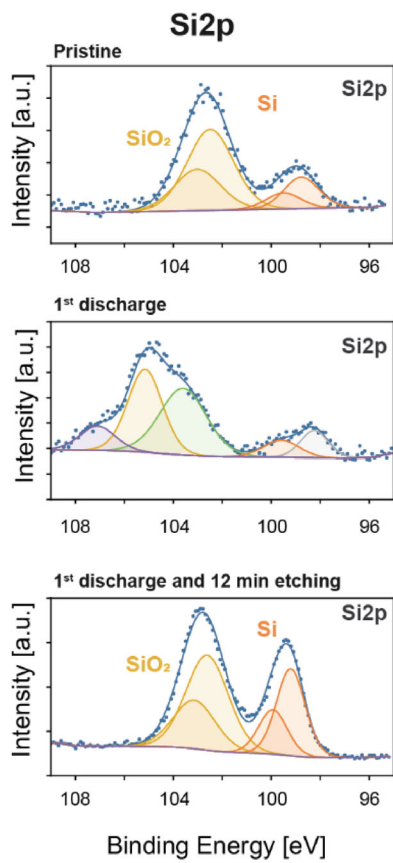


## Supplementary C Information of chapter 5

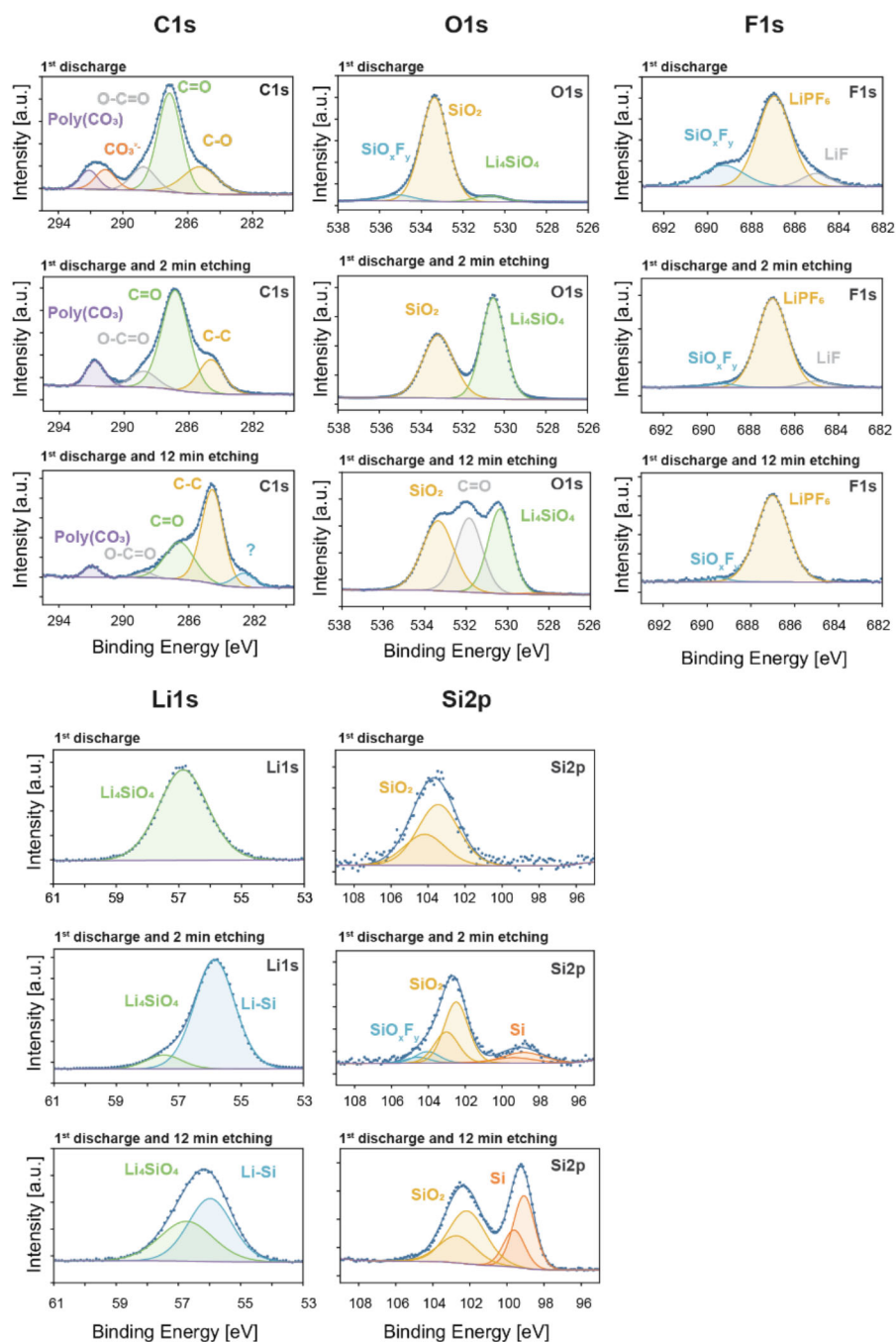


**Supplementary C Figure 1 | Redistribution of LAGP in Si electrode.** SEM/EDX images of pristine electrode Si/LAGP/CB/CMC 54/6/20/20.





**Supplementary C Figure 2 | Degradation components on the surface of Si electrode with LAGP solid additive, pristine and after first discharge both at the surface and at the bulk (12 min etching). X-ray Photoelectron Spectroscopy (XPS) profiles of Si<sub>2</sub>p (surface reactions).**

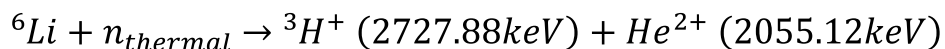


**Supplementary C Figure 3 | Degradation components on the surface of Si electrode with LAGP solid additive with VC/FEC electrolyte additive, pristine and after first discharge both at the surface and at the bulk (2, 12 min etching).** X-ray Photoelectron Spectroscopy (XPS) profiles of C1s, O1s, F1s spectra which focus on the electrolyte decomposition and Li1s, Si2p, lithiation of Si and surface reactions.

## Neutron Depth Profiling

Measurements were performed at the dedicated NDP beamline at the Reactor Institute in Delft, with a neutron flux of approximately  $10^7$  neutrons/cm<sup>2</sup>/s. The NDP measurements are ideally performed in vacuum to minimize particle energy loss of triton (<sup>3</sup>H) through air<sup>1-3</sup>. However, reduced pressure conditions are the main obstacle for operation of battery which contains liquid electrolyte. New experimental setup was designed for operando NDP measurements where pouch cell is placed in stainless-steel chamber with the He gas filled atmosphere (flushed for 10 min with fresh He) at 1 bar<sup>4</sup> in 30° angle towards neutron beam. Working near electrolyte vapour pressure (for EC:DEC vapour pressure = 0.02 bar), allows particles to reach detector with reasonable loss in kinetic energy (0.1 bar). That chamber is placed in the set-up consisting of an aluminum vacuum chamber with detector (Canberra PIPS) with resolution 3.3 keV. The cells are placed perpendicular to the detector at 3 centimeter distance, to detect particles that are leaving the pouch cell and to measure the energy of the emitted <sup>3</sup>H particles. The energy is collected by a Multi-Channel Analyzer. The consequences for the resolution are quantified using a Monte Carlo based algorithm in a separate publication. Schematic representation of the set-up is illustrated in **Figure 1**.

The incoming thermal neutrons undergo capture reaction with the <sup>6</sup>Li isotope (natural abundance around 7.5%). This reaction of neutron with atom core generates <sup>3</sup>H and <sup>4</sup>He ions emitted in all directions with a specific kinetic starting energy according to following reaction<sup>5,6</sup>:



Conversion between measured particle energy and depth of the original isotope is done using the method specified in an earlier publication<sup>3</sup> which relies on stopping powers calculated using SRIM<sup>7</sup>. The interaction of <sup>3</sup>H with the electron environment of the material, gives specific stopping power that can be determined based on the chemical composition. The stopping power

is defined as  ${}^3\text{H}$  loss of energy per unit path length, which is a function of energy. The kinetic energy of  ${}^3\text{H}^+$  is high enough and with perpendicular trajectories to reach detector placed at a specific distance to the sample. By measuring their energy when reaching the detector, the depth at which the capture reaction took place (location of Li-ions) can be determined. Through the number of ions that reach the detector, the concentration can be determined after the data normalization and background correction. As a result, the Li atom density profile as a function of depth is established.

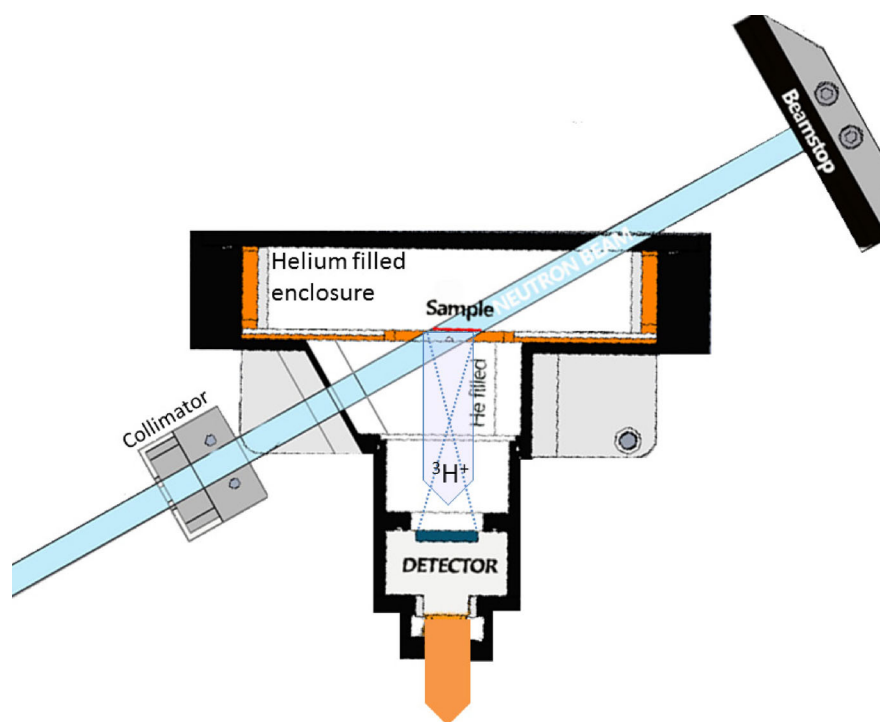


**Figure 1** | Schematic representing the set-up. To prevent electrolyte evaporation the vacuum chamber is in fact filled with helium. Neutron beam is continuously monitored as reactor power and, consequently, the neutron flux is fluctuating.

**Stopping power determination:** As mentioned, the stopping power determines the rate of energy loss as a function of particle energy given by the surrounding material. It is a material property as it depends on the density of charges, associated with the atoms. It is independent of the chemical nature of the surroundings, thus the stopping power of a mixture

of materials is equal to the sum of the stopping power of the components times their volume ratio:

$$S_t = \frac{\partial E(E_n)}{\partial x} = \sum_{i=1}^n v_i \cdot S_i \quad \text{S.1}$$

Where  $S$  represents the stopping power,  $v$  the volume fraction and  $i$  the different components, which in a Li-ion battery electrode would typically be carbon black, binder, electrolyte and active material. Electrons make up most of the matter volume and therefore the electron density dominates the stopping power, especially at high particle energies. An accurate approximation of the stopping power of the porous electrode is necessary to measure representative Li concentration. In this complex system three considerations deserve attention. First, during discharge to 800 mAh/g the material is expected to expand 1.5 fold<sup>8</sup>, hence, due to the decreasing charge density, the stopping power is expected to decrease. Second, assuming isotropic expansion and a rigid connection to the current collector, the porosity is expected and observed to decrease during lithiation<sup>9</sup>. The electrolyte phase has the lowest stopping power in this system. Lastly, a SEI will form on the electrode surface from the electrolyte decomposition products. Composed of similar elements and replacing space once occupied by electrolyte, there is no reason to consider this as a contribution to the stopping power. In short we will assume this contribution of this layer to be equal to that of the electrolyte itself. Note that, furthermore as the electrolyte penetrates the porous electrode layer, we can expect the SEI layer to be present throughout the electrode. The stopping power determines how energy resolution of the detector can be translated in depth resolution. The measurement accuracy is further determined by the sample roughness, the energy resolution of the detector, straggling and small angle scattering of the particles, the set up geometry and alignment<sup>10,11</sup>. The energy resolution of the detector is approximately 14 keV<sup>12</sup>. The consequences of straggling, small scattering and the geometry can be

derived analytically or computationally<sup>10,13,14</sup>. The contribution from the sample roughness is characterised through lithiation of the native copper oxide layer. The counts from this thin layer are spread, the full width at half maximum (FWHM) is good indication of the depth resolution. This value is 183 keV or 4.2 micron.

## References:

- 1 Oudenhoven, J. F. M. *et al.* In Situ Neutron Depth Profiling: A Powerful Method to Probe Lithium Transport in Micro-Batteries. *Advanced Materials* **23**, 4103-+, (2011).
- 2 Downing, R. G., Lamaze, G. P., Langland, J. K. & Hwang, S. T. Neutron Depth Profiling: Overview and Description of NIST Facilities. *Journal of Research of the National Institute of Standards and Technology* **98**, 109-126, (1993).
- 3 Verhallen, T. W., Lv, S. & Wagemaker, M. Operando Neutron Depth Profiling to Determine the Spatial Distribution of Li in Li-ion Batteries. *Frontiers in Energy Research* **6**, (2018).
- 4 Nagpure, S. C., Mulligan, P., Canova, M. & Cao, L. R. Neutron depth profiling of Li-ion cell electrodes with a gas-controlled environment. *Journal of Power Sources* **248**, 489-497, (2014).
- 5 Fink, D. *Neutron Depth Profiling* (Hahn-Meitner Institute fur Kernforschung, 1996).
- 6 Ziegler, J. F., Cole, G. W. & Baglin, J. E. E. Technique for determining concentration profiles of boron impurities in substrates. *Journal of Applied Physics* **43**, 3809-3815, (1972).
- 7 Ziegler, J. F., Ziegler, M. D. & Biersack, J. P. SRIM - The stopping and range of ions in matter (2010). *Nuclear Instruments & Methods in Physics Research Section B-Beam Interactions with Materials and Atoms* **268**, 1818-1823, (2010).
- 8 Kim, H., Chou, C.-Y., Ekerdt, J. G. & Hwang, G. S. Structure and properties of Li-Si alloys: a first-principles study. *The Journal of Physical Chemistry C* **115**, 2514-2521 (2011).
- 9 Paul, N., Wetjen, M., Busch, S., Gasteiger, H. & Gilles, R. Contrast Matched SANS for Observing SEI and Pore Clogging in Silicon-Graphite Anodes. *Journal of The Electrochemical Society* **166**, A1051-A1054, (2019).
- 10 Maki, J. T., Fleming, R. F. & Vincent, D. H. Deconvolution of neutron depth profiling spectra. *Nuclear Instruments and Methods in Physics Research Section B: Beam Interactions with Materials and Atoms* **17**, 147-155, (1986).
- 11 Downing, R., Maki, J. & Fleming, R. Analytical applications of neutron depth profiling. *Journal of Radioanalytical and Nuclear Chemistry* **112**, 33-46, (1987).
- 12 Chanjuan, T. *et al.* Neutron depth profiling system at CARR. *Applied Radiation and Isotopes* **148**, 102-107, (2019).
- 13 Shi, C. *et al.* Inverse iteration algorithm for neutron depth profiling. *Journal of Radioanalytical and Nuclear Chemistry* **317**, 81-85, (2018).

- 14 Yang, X. *et al.* A Monte Carlo code to get response spectrum of ions for Neutron Depth Profiling. *Journal of Radioanalytical and Nuclear Chemistry* **301**, 213-220, (2014).

## Summary

Batteries gained a lot of attention due to a raising demand for energy storage, as required for renewable energy generation systems, portable electronics and transport applications (**Chapter 1**). For the development of new battery materials understanding of fundamental processes is essential, which often relies on the development of new characterisation techniques and tools that enable to study the underlying electrochemical processes at the relevant length scales, i.e. from an atomistic to a macroscopic level as described in **Chapter 1**. Future batteries should be able to store more energy (per unit mass and or volume) and should be safer. Battery material solutions to achieve this are in principle known, where this thesis focusses on: (1) Si being one of the most promising negative electrode based on its large Li storage capacity (ten times higher than current graphite) and (2) solid electrolytes, replacing liquid electrolytes, which would practically annihilate safety concerns of Li batteries. However, for these new battery materials the challenge is to achieve a long cycle life by slowing down, or even preventing degradation reactions at the interfaces between the electrode and the electrolyte. This is the binding theme, and the topic of the main research questions of this thesis are thus: What are these degradation mechanisms and what is the impact of strategies to prevent it and achieve a long cycle life. The focus in this thesis is on Si negative electrodes (**Chapters 3, 4 and 5**) in combination with liquid electrolytes in general, and for solid electrolytes in particular (**Chapter 2**).

**Chapter 2** is devoted to the understanding of the electrochemical stability window of solid electrolytes, with emphasis on argyrodite-, garnet- and NASICON type materials. Current understanding of the electrochemical window is based on the stability of the decomposition products which is calculated based on thermodynamic predictions where differences in formation energies of decomposition products are considered. In this chapter we propose an indirect mechanism of solid electrolyte



decomposition and its relation to the electrochemical stability window. The hereby predicted electrochemical stability window is verified using slow galvanostatic cycling. X-Ray Diffraction and solid-state Nuclear Magnetic Resonance are utilised to study the electrochemical activity of argyrodite itself and their decomposition products respectively. The proposed indirect oxidative and reductive decomposition mechanism of the argyrodite solid electrolyte, via the unstable  $\text{Li}_4\text{PS}_5\text{Cl}$  ( $\text{S}/\text{S}^{2-}$  redox) at 2.24 V vs.  $\text{Li}/\text{Li}^+$  and unstable  $\text{Li}_{11}\text{PS}_5\text{Cl}$  (through the  $\text{P}/\text{P}^{5+}$  redox) at 1.08 V vs.  $\text{Li}/\text{Li}^+$ . The reported redox potentials of the argyrodite solid electrolyte determine the practical electrochemical stability window, as expressed by the first oxidation and reduction reactions observed in the cycling and in the differential capacity, consistent with the predicted redox activity. As a consequence unstable argyrodite phases rapidly decompose into the expected stable  $\text{Li}_3\text{PS}_4$ , S and LiCl species after oxidation, and P,  $\text{Li}_2\text{S}$ , and LiCl species after reduction. Further decomposition upon oxidation and reduction will occur towards  $\text{P}_2\text{S}_7^{4-}$  and  $\text{S}^0$  at 2.9 V vs.  $\text{Li}/\text{Li}^+$  and  $\text{Li}_3\text{P}$  around 0.8 V vs.  $\text{Li}/\text{Li}^+$  respectively. X-Ray Diffraction and solid-state Nuclear Magnetic Resonance also demonstrate the presence of metastable (de)lithiated argyrodite phases. This provides strong support for the proposed kinetically most favourable decomposition route, via the redox activity of the argyrodite solid electrolyte, thereby determining the electrochemical stability window. In all-solid-state batteries this implies that both contributions of the solid electrolyte, will add to the cycling capacity based on the active electrode materials and the specified potential ranges. Moreover, the poor ionic conductivity of the decomposition products, especially S,  $\text{Li}_2\text{S}$  and LiCl, as well as the change in volume can be expected to be responsible for the large increase in interfacial resistance upon cycling. To support the general nature of the indirect decomposition mechanism, the Li insertion/extraction potentials are also determined computationally and experimentally for two different families of solid electrolytes i.e. garnet  $\text{Li}_x\text{La}_3\text{Zr}_2\text{O}_{12}$  and NASICON  $\text{Li}_{1.5}\text{Al}_{0.5}\text{Ge}_{1.5}(\text{PO}_4)_3$ . For the garnets, the predicted and measured oxidation potential are both

located just above 3.54 V vs. Li/Li<sup>+</sup>, (O and Zr redox) significantly larger than the direct decomposition at 2.91 V vs. Li/Li<sup>+</sup> towards the predicted stable decomposition products Li<sub>2</sub>O<sub>2</sub>, La<sub>2</sub>O<sub>3</sub> and Li<sub>6</sub>Zr<sub>2</sub>O<sub>7</sub>. For NASICON type electrolytes, the predicted and measured oxidation occurs close to 2.31 V vs. Li/Li<sup>+</sup> (O and P redox), which is lower than direct decomposition at 2.70 V vs. Li/Li<sup>+</sup> based on the stability of the predicted decomposition products Ge, GeO<sub>2</sub>, Li<sub>4</sub>P<sub>2</sub>O<sub>7</sub> and AlPO<sub>4</sub>. These results support that the proposed indirect, kinetically favourable decomposition, via the (de)lithiation of the solid electrolyte is a general mechanism, in practice widening the solid electrolyte stability window as compared to predictions based on the stability of the decomposition products. The fundamental nature of the proposed mechanism suggests this is a key aspect for solid electrolytes in general, guiding interface and material design for all-solid-state batteries.

**Chapter 3** focuses on the role of a protective coating of TiO<sub>2</sub> on Si particles improving the cycle life of the battery by reducing parasitic reactions at the interface, and, thereby, allowing the interesting bulk properties to be maintained. The optimal coating thickness appears to be 5 nm, which balances the ionic conductivity and the flexibility of the coating, explaining the improved electrochemical reversibility observed. Operando X-Ray Diffraction is performed to evaluate the behaviour of the TiO<sub>2</sub> coating during deep discharge of Si, indicating that the lithiation proceeds via a solid solution resulting in a composition of Li<sub>x</sub>~0.12TiO<sub>2</sub>. The reasonable Li-ion conductivity of this phase is beneficial for the Li-ion transport through the electrodes, whereas the limited electronic conductivity is expected to suppress solid electrolyte interface formation as well as crack formation. Additionally, operando neutron depth profiling demonstrates that in the uncoated Si electrode, the lithiation proceeds inhomogeneously as a function of electrode depth, whereas the Li<sub>0.12</sub>TiO<sub>2</sub> coating results in a more homogeneous lithiation as a function of electrode depth. Thus, the results suggest that the improved performance of the coated Si is not only a consequence of the protective function of the coating, but also because of

more homogeneous lithiation as a result of the Li-conducting properties of the coating.

To gain insight into the degradation mechanism of Si electrodes and the role of homogeneity on the cycle life and the nature of SEI, operando neutron depth profiling is further exploited (**Chapter 4**). Interestingly, the degradation of the Si electrode without any additive demonstrates a Li gradient as a function of electrode depth during the first cycles, thus indicating inhomogeneous lithiation of Si. Inhomogeneity of lithiation will cause large local volume changes, promoting capacity fading of Si electrodes. A higher Li concentration is observed close to the current collector at the onset of discharge, most likely caused by the limited electronic conductivity of Si particles at the beginning of the cycling. It is suggested that together with alloying of Si, SEI growth is promoted close to the current collector. Uncontrollable SEI formation compromises the electronic contacts between Si/carbons which supports the local lithiation near the current collector and limits lithiation of Si near the separator. This inhomogeneous lithiation as a function of electrode depth is strongly reduced upon the addition of fluoroethylene carbonate and vinylene carbonate electrolyte additives. These electrolyte additives are well-known to significantly improve cycling performance due to the electronically insulating and stable lithium fluoride, forming at the surface of the Si before electrolyte solvents. The high electronic resistivity of LiF is argued to be responsible for the more homogenous distribution of Li across the depth of the electrode, and lowers the accumulation of SEI products growing upon cycling close to the current collector. This demonstrates that the homogeneity of Li storage throughout the Si electrode in addition to the nature of the SEI is a key parameter for long cycle life of Si electrodes, and that charge transport properties already at initial cycling play a key role in this.

In order to gain insight in the role of electron and Li-ion transport, solid additives are introduced in the Si electrode cycled in half cells with a liquid electrolyte - the results of which are presented in **Chapter 5**. All cells

with solid additives show improved cycling performance with respect to bare Si. Of all studied additives,  $\text{Li}_{1.5}\text{Al}_{0.5}\text{Ge}_{1.5}(\text{PO}_4)_3$  being a good Li-ion conductor, demonstrates the highest capacity retention, charge efficiency and lowest overpotential. These ion conductive additives may facilitate ion transport vital for high capacity operation, which lowers the internal resistance during the (dis)charge process and thus leads to a more homogenous distribution of Li through the whole electrode, as indicated by operando neutron depth profiling measurements. This research highlights the critical role of an ionic network governed by an inorganic filler allowing to reach all the Si particles, therefore improving the Li capacity and charge efficiency. Analysis of the solid electrolyte interface species demonstrates the presence of decomposition products of  $\text{Li}_{1.5}\text{Al}_{0.5}\text{Ge}_{1.5}(\text{PO}_4)_3$ . These form at a higher potential as compared to the regular solid electrolyte interface products originating from electrolyte decomposition at 1V vs. Li/Li<sup>+</sup>. The amount of  $\text{Li}_{1.5}\text{Al}_{0.5}\text{Ge}_{1.5}(\text{PO}_4)_3$  used in the electrode material is very small (5 wt. %), and appears to have a large impact on the solid electrolyte interface formation. X-ray photoelectron spectroscopy indicates that the solid electrolyte interface is free from regular decomposition products such as LiF,  $\text{Li}_2\text{CO}_3$ ,  $\text{Li}_2\text{O}$ . Since the measurements are performed at low potentials, 10 mV vs. Li/Li<sup>+</sup>,  $\text{Li}_{1.5}\text{Al}_{0.5}\text{Ge}_{1.5}(\text{PO}_4)_3$  is expected to decompose towards  $\text{Li}_{15}\text{Ge}_4$ ,  $\text{Li}_3\text{P}$ ,  $\text{Li}_9\text{Al}_4$ ,  $\text{Li}_2\text{O}$ . Reduction of Ge (Ge3d) and Al (Al2p) is indeed observed using X-Ray Photoelectron Spectroscopy. It is speculated that the decomposition products of LAGP, such as Li-Ge and Li-Al alloys in the SEI improve the ionic and electronic pathway for the (de)-lithiation of the Si electrode. This would promote homogeneous activity throughout the electrodes and rationalise the improved Li capacity and charge efficiency observed.

**In summary, the role of the solid electrolytes redox activity, and its correlation with the electrochemical stability window, is established, providing a guide for interface and material design for all-solid-state batteries. The importance of homogenisation of (de)lithiation of the Si negative electrode is shown to be critical in designing Si negative**

electrodes for long term cycling. This can be achieved by changing the nature of the SEI by coatings, different liquid electrolyte additives, or/and by providing electronic and ionic pathways through the addition of solid additives. In-situ decomposition of liquid and/or solid additive, can provide stability of the interface and good conductivity by the nature of decomposition products. A recommendation for future research for next generation lithium batteries, aiming at safe and high energy density batteries, is to combine Si electrodes with solid electrolytes, providing a stable anodic matrix and avoiding the issues associated with Li-metal dendrites.

## Samenvatting

Heden ten dagen krijgen batterijen veel aandacht als gevolg van toenemende vraag naar energieopslag benodigd voor het opslaan van duurzame energy, het gebruik van draagbare elektronica en nieuwe toepassingen in de transport sector (**Hoofdstuk 1**). Voor de ontwikkeling van nieuwe materialen voor batterijen is het begrip van de fundamentele processen die plaatsvinden in batterijen cruciaal. Deze processen zijn vaak alleen waar te nemen met nieuwe geavanceerde technieken die de onderliggende elektrochemische processen kunnen meten op de relevante lengteschalen, hier van atomair tot macroscopisch niveau zoals beschreven in **Hoofdstuk 1**. Van de volgende generatie batterijen wordt verwacht dat ze meer energie op kunnen slaan (per gewicht en/of volume) en veilig zijn in gebruik. In principe zijn er al materialen die dit mogelijk kunnen maken en dat is waar dit proefschrift zich op zal focussen: (1) Silicium is een van de meest veelbelovende anodematerialen door zijn hoge lithium-opslagcapaciteit (tien keer meer dan de huidige grafietanodes) en (2) vaste stof elektrolyten die bij vervanging van vloeibare elektrolyten de veiligheidsproblemen kunnen ondervangen. Voor deze nieuwe batterijmaterialen is de uitdaging om een lange levensduur te bereiken, door decompositiereacties op de grensvlakken van elektrode en elektrolyt te onderdrukken of zelfs te voorkomen. Het gemeenschappelijke thema en de onderzoeksvraag van dit proefschrift is: welke decompositiereacties vinden er plaats en hoe kunnen deze voorkomen worden om een langere levensduur te bereiken. Dit wordt eerst onderzocht voor siliciumanodes (**Hoofdstuk 3, 4 en 5**) in combinatie met een vloeibare elektrolyt en vervolgens specifiek voor vaste stof elektrolyten (**Hoofdstuk 2**).

**Hoofdstuk 2** is gewijd aan de elektrochemische stabiliteit van vaste stof elektrolyten. Meer specifiek worden de Argyrodiet, Granaat en NASICON-achtige materialen onderzocht. Doorgaans is de elektrochemische stabiliteit gebaseerd op de vormingsenergie van decompositieproducten in

thermodynamisch evenwicht, waaruit het voltage voor decompositie kan worden berekend. In dit hoofdstuk wordt een reactiemechanisme voorgesteld waarbij de vaste stof elektrolyt vervalst naar zijn decompositieproducten via een indirecte route. Deze alternatieve route bepaalt uiteindelijk de voltages waarin de elektrolyt elektrochemisch stabiel is. De hierbij voorspelde elektrochemische stabiliteit komt overeen met galvanostatische testen. Röntgendiffractie en kernspinresonantie zijn gebruikt om de elektrochemische activiteit van Argyrodiet en de decompositieproducten te onderzoeken. De indirecte decompositie gaat tijdens oxidatie via het instabiele  $\text{Li}_4\text{PS}_5\text{Cl}$  ( $\text{S}/\text{S}^{2-}$  redox) bij 2,24 V vs.  $\text{Li}/\text{Li}^+$  en tijdens reductie via het onstabiele  $\text{Li}_{11}\text{PS}_5\text{Cl}$  ( $\text{P}/\text{P}^{5+}$  redox) bij 1,08 V vs.  $\text{Li}/\text{Li}^+$ . Deze redoxpotentialen van Argyrodiet bepalen de praktische elektrochemische stabiliteit. Dit is voorts bevestigd in een experiment waarbij dezelfde voltages voor de eerste oxidatie en reductie zijn waargenomen tijdens de eerste laad- en ontlaadcyclus. Als het voltage in de batterij buiten het voltagebereik van de vaste stof elektrolyt gaat, vervalst het snel in de verwachte stabiele decompositieproducten:  $\text{Li}_3\text{PS}_4$ , S en LiCl tijdens oxidatie en P,  $\text{Li}_2\text{S}$ , en LiCl tijdens reductie. Verdere decompositie levert  $\text{P}_2\text{S}_7^{4-}$  en  $\text{S}^0$  bij 2,9 V vs.  $\text{Li}/\text{Li}^+$  en  $\text{Li}_3\text{P}$  rond 0,8 V vs.  $\text{Li}/\text{Li}^+$ . Röntgendiffractie en kernspinresonantie laten ook de aanwezigheid van het metastabiele gelithieerde en gedelithieerde argyrodiet zien. Deze bevindingen ondersteunen de indirecte decompositieroute via de actieve Argyrodiet vaste stof elektrolyt en daarmee debepalen elektrochemische stabiliteit van vaste stof elektrolyten. De gegenereerde capaciteit van de decompositiereacties draagt bij aan de volledig gemeten capaciteit van het op- en ontladen van de batterij. Voor Argyrodiet zijn de decompositieproducten S,  $\text{Li}_2\text{S}$  en LiCl slecht ionisch geleidend en mede door volumeveranderingen zal de weerstand op het grensvlak toenemen tijdens op- en ontladen. Om dit indirecte decompositiemechanisme te veralgemeniseren zijn er twee andere vaste stof elektrolyten van verschillende origine getest, namelijk Granaat  $\text{Li}_x\text{La}_3\text{Zr}_2\text{O}_{12}$  en NASICON

$\text{Li}_{1.5}\text{Al}_{0.5}\text{Ge}_{1.5}(\text{PO}_4)_3$ . Voor  $\text{Li}_x\text{La}_3\text{Zr}_2\text{O}_{12}$  is de voorspelde en gemeten oxidatiepotentiaal rond 3,54 V vs.  $\text{Li}^+$  en dit is significant hoger dan de 2,91 V die voorspeld is door middel van vormingsenergieën van de decompositieproducten. Voor NASICON  $\text{Li}_{1.5}\text{Al}_{0.5}\text{Ge}_{1.5}(\text{PO}_4)_3$  is de voorspelde en gemeten reductie rond 2,31 V vs.  $\text{Li}/\text{Li}^+$  en dit is lager dan de 2,70 V die direct voorspeld is vanuit de decompositieproducten  $\text{Ge}$ ,  $\text{GeO}_2$ ,  $\text{Li}_4\text{P}_2\text{O}_7$  en  $\text{AlPO}_4$ . De resultaten bevestigen de indirecte decompositieroute via de ge(de)lithieerde vaste stof. In praktijk betekent dit een breder stabiliteitsbereik dan ten opzichte van de decompositieproducten. Het fundamentele karakter van dit mechanisme is in algemene zin een zeer belangrijk aspect voor vaste stof batterijen om zo begrip te krijgen over het interface en welke materialen er gebruikt kunnen worden voor deze batterijen.

**Hoofdstuk 3** concentreert zich op de rol van een beschermcoating van  $\text{TiO}_2$  die op siliciumdeeltjes aangebracht wordt om zo de oplaadbaarheid van een batterij te verbeteren, met als doel de parasitaire reacties aan het grensvlak te onderdrukken en de interessante bulkeigenschappen van Si te laten behouden. De optimale dikte van de coating is 5 nm, waarbij de balans tussen ionische geleiding en flexibiliteit optimaal is. Röntgendiffractie is uitgevoerd tijdens het op- en ontladen om het gedrag van de  $\text{TiO}_2$ -coating tijdens een diepe ontlading van Si te achterhalen. De lithiëring gaat via een vaste-stofoplossing naar uiteindelijk een samenstelling van  $\text{Li}_{x \sim 0.12}\text{TiO}_2$ . Deze fase heeft een redelijke Li-iongeleiding welke gunstig is voor het transport van Li-ionen door de elektroden, terwijl tegelijkertijd de elektronische geleiding gelimiteerd wordt door de vaste stof op het oppervlak, welke evenwel scheurvorming van het Si onderdrukt. Bovendien toont Neutron Diepte Profilering (NDP) tijdens het testen van de batterij aan dat de niet gecoate Si-elektrode geen homogene lithiëring laat zien als functie van de diepte, terwijl de met  $\text{Li}_{0.12}\text{TiO}_2$  gevormde coating een meer homogene lithiëring geeft als functie van de diepte. Dit geeft aan dat de verbeterde prestatie van de batterij niet alleen komt van het beschermende effect van



de coating, maar ook door de meer homogene Li-verdeling in het Si door de hogere ionische geleiding in de coating.

Om meer inzicht te verkrijgen in de degradatiemechanismes in Si-anodes met betrekking tot de rol van oplaadcycli, homogeniteit en de aard van de SEI (solid electrolyte interphase), wordt nog dieper ingegaan op de resultaten van NDP (**Hoofdstuk 4**). Een poreuze Si-elektrode zonder additief laat in de elektrode een gradiënt zien in de Li-concentratie over de diepte wat duidt op een inhomogene lithiëring van het Si over de elektrode. Inhomogeniteit veroorzaakt grote lokale volumeveranderingen met eventueel breuk tot gevolg waardoor de capaciteit zal worden beperkt. Een hogere Li-concentratie is waargenomen dicht bij de stroomcollector, dat wordt veroorzaakt door een gelimiteerde elektronische geleiding van Si-deeltjes aan het begin van het ontladen. Er wordt gesuggereerd dat SEI bij de stroomafnemer groeit tijdens het legeren van Li met Si. Ongecontroleerde vorming van SEI beperkt het elektronische contact tussen Si/C, draagt bij aan de lokale lithiatie bij de stroomafnemer en de beperkt lithiatie van Si aan de kant van het elektrolyt. Deze inhomogene lithiëring over de diepte van de elektrode wordt sterk gereduceerd door toevoegen van additieven zoals fluorethyleen carbonaat en vinyleencarbonaat aan de elektrolyt, welke ook in de poriën van de elektrode komen. Van deze elektrolyten is reeds bekend dat ze de herlaadbaarheid verbeteren door de vorming in een nevenreactie van het slecht elektronisch geleidende lithiumfluoride (LiF). Er wordt beargumenteerd dat de lage elektronische geleiding van dit LiF zorgt voor een homogene verdeling van Li over de diepte van de elektrode en dat het de vorming van SEI-producten ter plaatse van de stroomcollector vermindert gedurende het verdere verloop van op- en ontladen. Dit laat zien dat de homogeniteit van Li-opslag in een Si-elektrode tijdens het laden zeer belangrijk is voor de herlaadbaarheid van de batterij en dat het ladingstransport aan het begin van het op- en ontladen hier een belangrijke rol in speelt.

Om meer inzicht te krijgen in de rol van elektron- en Li-iontransport zijn vaste stof additieven toegevoegd aan de vloeibare elektrolyt waarin de poreuze Si-elektrodes zich bevinden en vervolgens worden deze getest in half-cellen op op- en ontladprestaties. De resultaten hiervan worden gepresenteerd in **Hoofdstuk 5**. Alle cellen met vaste stof additieven laten een prestatieverbetering zien. Van alle additieven is  $\text{Li}_{1.5}\text{Al}_{0.5}\text{Ge}_{1.5}(\text{PO}_4)_3$  de best presterende. NASICON  $\text{Li}_{1.5}\text{Al}_{0.5}\text{Ge}_{1.5}(\text{PO}_4)_3$  is een goede Li-iongeleider, levert de minste degradatie in capaciteit en de hoogste efficiëntie met de laagste overpotentiaal. De iongeleider faciliteert het transport van ionen, dat zeer belangrijk is voor reductie van de interne weerstand in de batterij en zorgt derhalve voor een homogene Li-distributie in de elektrode, wat wordt bevestigd met NDP experimenten. Dit onderzoek benadrukt de cruciale rol van een ionennetwerk dat wordt gegenereerd middels een anorganisch materiaal dat toegevoegd wordt aan de Si-elektrode, waardoor de Li-capaciteit en laad efficiëntie worden verbeterd. Op het grensvlak van de elektrode worden de decompositieproducten van  $\text{Li}_{1.5}\text{Al}_{0.5}\text{Ge}_{1.5}(\text{PO}_4)_3$  aangetroffen, welke bij een hogere potentiaal worden gevormd dan de decompositieproducten van het elektrolyt. De relatief kleine hoeveelheid  $\text{Li}_{1.5}\text{Al}_{0.5}\text{Ge}_{1.5}(\text{PO}_4)_3$  additief (5 massa %) heeft een relatief grote impact op de vorming van de SEI. Röntgen-foto-elektronenspectroscopie (XPS) toont aan dat er geen decompositieproducten van de elektrolyt zijn gevormd. Aangezien de elektrode op een zeer laag voltage wordt gemeten kan verwacht worden dat het additief  $\text{Li}_{1.5}\text{Al}_{0.5}\text{Ge}_{1.5}(\text{PO}_4)_3$  compleet reduceert naar  $\text{Li}_3\text{P}$ ,  $\text{Li}_9\text{Al}_4$ ,  $\text{Li}_2\text{O}$  en deze stoffen worden ook daadwerkelijk waargenomen met XPS. De gevormde decompositieproducten zoals de Li-Ge en Li-Al legeringen in de SEI verbeteren hierbij de ionische en elektronische geleiding in de Si-elektrode. Dit zorgt voor een meer homogene activering in de elektrode waardoor meer capaciteit behaald kan worden met een hogere efficiëntie.

**Samenvattend, de rol van redoxactiviteit in vaste stof elektrolyten en de correlatie met de bijbehorende elektrochemische stabiliteit is**

bepaald. Deze informatie is erg belangrijk voor het ontwikkelen van nieuwe materialen voor vaste-stofbatterijen. Het belang van homogeniciteit tijdens (de)lithiëring van Si-anodes is cruciaal voor de herlaadbaarheid. Dit kan worden bereikt door het aanbrengen van coatings om de SEI vorming te onderdrukken. Tevens kunnen vloeibare en vaste stof additieven gebruikt worden om elektronische en ionische netwerken te bewerkstelligen. Door decompositie van vloeibare en vaste additieven gecontroleerd te laten plaatsvinden kan een stabiel grensvlak met goede geleidbaarheid verkregen worden. In vervolgonderzoek naar veilige batterijen met een hoge energiedichtheid kan silicium gecombineerd met een vaste-stofelektrolyt een interessante richting zijn, waarbij een stabiele structuur kan worden aangebracht zonder dat problemen als Li-metaal dendrietenvorming zullen ontstaan.

## Acknowledgments

I would like to express my gratitude to all the people that contributed in my PhD journey which was a wonderful road.

First of all I would like to thank to my promotor Dr. Ir. Erik Kelder, who gave me the great opportunity to start my scientific career in Delft University of Technology under his supervision. He always supported me and encouraged me in all the steps during my PhD. He created the opportunities for me to develop further and being always enthusiastic about my new ideas, being involved in trying to understand in depth my results. I had always all his support in joining KIC Inno Energy school, he helped me to get a proposal for measurements in ESRF, which was a wonderful experience for me to have. Moreover, he always being worried if I return safe from the conference travels since I faced earthquake in Japan and massive flooding in Peru. Furthermore, I would like to thank my other supervisor Prof. Marnix Wagemaker. I started to work with him in the later stage of my PhD. Through discussions I got another angle on my projects and I could contribute in different topics and develop my skills in other techniques that are available in our institute. He encouraged me to try NDP measurements, which brought me very successful results included in my thesis. Also he inspired many of us to start bouldering during group activities, and I still need to improve and start climbing reds, luckily he let me graduate without that. I am incredibly thankful to dr. Swapna Ganapathy, that was my great scientific support and mentor. She had thought me ssNMR and how to solve all the problems related with the measurement, she has being very patient and always positive and enthusiastic about new measurements. She always encouraged me to try one more time, so I could successfully complete my measurements. Prof. Ekkes Brück for giving me opportunity to do PhD in FAME group where I started my project. Aron Ruszin for nice collaboration through Delft IMP, it was very helpful in my project. Marco Sommariva for helping me with

operando XRD in Almelo. Marcus Fehse for assisting me in measurements in ESRF and teaching data analysis. Prof. Ernst van Eck for helping me in NMR measurements in Nijmegen. Also to my students Ivan and Elise, for great collaboration. I would like to thank Frans Ooms. All the achievements in the lab, were successful thanks to him. I knew I could always have just 2 questions at once to keep the balance. Kees Goubitz, for helping me with XRD and being always patient and of course supporting us with coffee that was keeping us sharp. I am also thankful to the rest of academic and technical support, Niels van Dijk, Lambert van Eijck, Michel Steenvoorden, Jouke Heringa, Bert Zwart, Bart Boshuizen, Anton Lefering, Baukje Terpstra, Robert Dankelman, Esther Bijl, Ilse van der Kraaji-Quick, Nicole Banga. I would like to thank to my dear colleagues from FAME and SEE for constant support and fun times. Carlita and Peter-Paul, my favourite colleagues, and museum team. Countless Argentinian bbqs and drinking mate, playing ping pong, roller-skating and helping in making all my schematic figures and cover. Niek for fun time in Nijmegen where we were doing one week NMR measurements. Tomas for showing me NDP measurements and being very enthusiastic about that, and the fruitful discussions, and you were the binder of the group with all bbqs and other events. Zhaolong for helping me with operando XRD measurements, and being a nice colleague. Yaolin, for always being so helpful, I really enjoyed your company at work. Qidi and Chenglong for nice Chinese dinners together in Netherlands, France and China. Kun for being great team in operando XRD measurements and being always so positive and kind. Guorui for helping in opening the smallest rotors without breaking. Shiv for the nicest TEM images. Ming for showing us China and being cool office and lab mate. Always enjoyed scientific and life related topics. Zhu for sharing struggle with 2D NMR experiments and being always so positive in the lab. Chao, for helping me with solid state batteries and having nice conversations. Remco for showing us how to cook Roti. Alex for always having Greek lunches and countless coffee breaks. Chuang for sharing office together and showing that hard work always pays off. Xinmin

for nice talks after work, sharing experience. Eveline for being great boulder gym mate. Hanan always fun to talk and being always helpful and positive. Michi for all pizzas eves and all times with guys. Pierre for having fun trip to Argentina. Lars for helping me with XPS measurements and fruitful discussions. Susan for having nice talks and time travelling in NL. Anika, my polish mate in the institute, I enjoyed speaking polish, secret language. Angie for all the great talks and time outside of work, and constant support. Tammo for being my best friend. It was fun to publish great paper together and that you helped me with my measurements in Grenoble and unforgettable trip to China. And many more people that I had opportunity to meet and chat: Martijn, Mark, Pranav, Walter, Mark, Walter and new generation of people Victor, Theo, Shengnan, Pedro, Xuehang. Also to my Delft friends Romina, Clarissa, Julian, Timo, Aga for fun times with surfing, bouldering and other activities. I would like to extent my appreciation to my MESC family, Danita, Amansito, Vicky and Praveen (thank you for Sri Lankan wedding experience) for always being supportive to me even we are living in different countries, but we always keep our back and encourage each other in science and life! To my Uni friends, Ola, Agata, Gosia for always being there and nice trips together. To Marta for being the best travel mate I can ask for. To my polish friends Agata, Kasia, Marysia, Monica for keeping me updated with all important events happening in Podkowa and other places. I feel really acknowledged that even I live far away I could attend all the important moments in your life. Kocham Was dziewczyny! Also many thanks to my dutch family Mart, Reinier, Dirk, Hidde, Annika, Muriël, Henny and Harry for being wonderful to me and showing me beautiful NL.

And the last but not least to my mum, dad and to my brothers, my lovely aunt and uncle Joanna and Bill for being so supportive and loving all this time! Dziękuję Wam z całego serca, jesteście najlepszymi rodzicami na świecie. Kocham Was!



## List of publications and patent

**Violetta Arszewska**<sup>†</sup>, Tammo Schwietert<sup>†</sup>, Chao Wang, Chuang Yu, Alexandros Vasileiadis, Niek J. J. de Klerk, Jart Hageman, Thomas Hupfer, Ingo Kerkamm, Yaolin Xu, Eveline van der Maas, Erik M. Kelder, Swapna Ganapathy, Marnix Wagemaker, *Clarifying the relationship between redox activity and electrochemical stability of solid electrolytes*, **Nature Materials** 19, no. 4 (2020): 428-435 (**†co first author**).

Shibabrata Basak, Vadim Migunov, Amir H. Tavabi, Chandramohan George, Qing Lee, Paolo Rosi, **Violetta Arszewska**, Swapna Ganapathy, Ashwin Vijay, Frans Ooms, Roland Schierholz, Hermann Tempel, Hans Kungl, Joachim Mayer, Rafal E. Dunin-Borkowski, Rüdiger-A. Eichel, Marnix Wagemaker, and Erik M. Kelder, *Operando Transmission Electron Microscopy Study of All-Solid-State Battery Interface: Redistribution of Lithium among Interconnected Particles*, **ACS Applied Energy Materials** (2020).

Shibabrata Basak, Amir H. Tavabi, Krzysztof Dzieciol, Vadim Migunov, **Violetta Arszewska**, Hermann Tempel, Hans Kungl, Erik M. Kelder, Marnix Wagemaker, Chandramohan George, Joachim Mayer, Rafal E. Dunin-Borkowski, Rüdiger-A. Eichel, *Operando Transmission Electron Microscopy in Open cell: Thickness dependent breaking of Metal Oxide coating on Si/SiO<sub>2</sub> active particles (submitted)*.

Ming Liu, Chao Wang, Chenglong Zhao, Eveline van der Maas, Kui Lin, **Violetta A. Arszewska**, Baohua Li, Swapna Ganapathy and Marnix Wagemaker, *Quantifying the local Li-ion diffusion over the grain boundaries of a protective coating, revealing the impact on the macroscopic Li-ion transport in an all-solid-state battery (submitted)*.



**Violetta Arszewska**, Tomas Verhallen, Marnix Wagemaker, Erik Kelder, *Operando monitoring the Li-ion distribution in Silicon Anodes for Li-ion batteries (to be submitted)*.

**Violetta Arszewska**, Tomas Verhallen, Ivan Rene Soejatmiko, Erik Kelder, Marnix Wagemaker, *Operando study of the rate limiting mechanism in silicon anodes using solid ionic conductive additive for Li-ion batteries (to be submitted)*.

Patent: **Violetta Arszewska**, Tomas Verhallen, Marnix Wagemaker, *Solid ionic conductive additive in electrodes for lithium-ion batteries using liquid electrolyte*, 100449PC OCT-19-80.

## Conferences

*Operando monitoring the Li-ion distribution in silicon anodes for Li-ion batteries*, 3<sup>rd</sup> International Conference on Energy Storage Materials (ICEnSM2019), November 28<sup>th</sup> – December 1<sup>st</sup>, Shenzhen, China, (Oral presentation)

*Reversible capacity and decomposition mechanism in argyrodite  $\text{Li}_6\text{PS}_5\text{Cl}$  solid electrolytes for all solid state Li-ion batteries*, 9<sup>th</sup> Lithium Battery Discussions (LIBD2019), September 15<sup>th</sup>–20<sup>th</sup>, 2019, Arcachon, France, (Oral presentation)

3<sup>rd</sup> Bunsen Colloquium on Solid-State Batteries, November 14<sup>th</sup> – 16<sup>th</sup>, 2018, Frankfurt, Germany

*Towards high energy density silicon-based anodes in all solid-state lithium batteries*, Topic 19<sup>th</sup> International Meeting on Lithium Batteries (IMLB), June 17<sup>th</sup> – 22<sup>th</sup>, 2018, Kyoto, Japan, (Poster presentation)

*Graphite encapsulation of silicon particles using different metals as template for negative electrode in lithium-ion batteries*, 20<sup>th</sup> Topical Meeting of the International Society of Electrochemistry (ISE), March 19<sup>th</sup> – 22<sup>th</sup>, 2017, Buenos Aires, Argentina, (Poster presentation).

The 67<sup>th</sup> Annual Meeting of the International Society of Electrochemistry (ISE), 21<sup>st</sup>– 26<sup>th</sup> August, 2016, The Hague, The Netherlands

## **PhD graduate School, KIC Inno Energy**

Energy Economics, Grenoble Ecole Management Technology and Innovation,  
April 10<sup>th</sup> – 14<sup>th</sup>, 2017, Grenoble, France

Connecting the innovators of tomorrow, The 2018 InnoEnergy PhD School  
Conference, October 3<sup>rd</sup> – 5<sup>th</sup>, 2018, Budapest, Hungary

Managing Innovation and Entrepreneurship, ESADE Business School, May  
27<sup>th</sup> – June 7<sup>th</sup>, 2019, Barcelona, Spain

## Curriculum Vitae

Violetta Arszewska was born on 4<sup>th</sup> of February 1990 in Swindon, United Kingdom. She is undergraduate student of the Warsaw University of Technology which she finished on February 2013 with an Engineering Degree in Chemistry. The thesis diploma was carried out at the Institute of Biocybernetics and Biomedical Engineering (PAN). She is graduate of the Erasmus Mundus Joint Master Program on Materials for Energy Storage and Conversion (MESC#10) which she succeeded on September 2015 with Master Degree in Material Science and Electrochemistry. She completed her studies in Aix Marseille Université, Warsaw University of Technology, Universidad de Córdoba and master thesis project in Umicore. On December 2015 she started as PhD candidate at Delft University of Technology in the group of Fundamental Aspects of Materials and Energy under supervision of Ekkes Brück and Erik Kelder. Later in time she joined Storage of Electrochemical Energy under supervision of Erik Kelder and Marnix Wagemaker. This work was financially supported by ADEM, A Green Deal in Innovative Energy Materials of the Ministry of Economic Affairs of The Netherlands. During her PhD she was a part of PhD Graduate school funded by KIC Inno Energy and completed ESADE Business School for managing innovation and entrepreneurship.